UNIVERSITÀ
DI PAVIA

University of Pavia
Faculty of Engineering
Department of Electrical, Computer Science
and Biomedical Engineering

Smart micro-opto-fluidic sensing platforms for contactless chemical and biological analyses

Ph.D. Dissertation by Valentina Bello
Supervisor: Prof. Sabina Merlo

Ph.D. School in Electronics, Computer Science
and Electrical Engineering
XXXIV Cycle (2018-2021)

La fatica non è mai sprecata:
soffri, ma poi sogni.

Pietro Mennea

Two roads diverged in a wood, and I–
I took the one less traveled by,
And that has made all the difference.

"*The Road Not Taken*" by *Robert Frost*

A Rosella e Luigi,
nonni amati,
sempre nel mio cuore.

Acknowledgments

First of all, I want to express my sincere gratitude to my supervisor, Prof. Sabina Merlo, for her constant guidance, patience and strong dedication to her job. She always pushed me to do my best in every situation and to be eager to learn, and, above all, she keeps believing in me. I also thank her because she made our group an environment where I always felt comfortable and happy and proud to work in. I could not have asked for a better advisor than her.

A special thank also goes to Andrea for the technical support and for our coffee breaks: the Laboratory of ElectroOptics would not be the same without you.

Thanks to Elisabetta for her constant help and kindness and for spending with me many long hours in the lab. It's a pleasure to work together.

I want to acknowledge as well Prof. Ferdinando Auricchio, Dr. Fabrizio Tessicini and Dr. Rodrigo Romarowski, for the fruitful collaboration in the framework of the DSF Digital Smart Fluidic project. Thanks to Dr. Andrea Bratto for the support in designing the industrial prototypes. Thanks also to Prof. Stefania Marconi for the assistance in the realization of the 3D-printed components.

I also want to express my gratitude to Professor Silvano Donati for his precious support and for helping me with the managmenet of the IEEE Student Branch of Pavia.

I thank Prof. Kamil L. Ekinci for accepting me as visiting Ph.D. student at the Nanometer Scale Engineering Laboratory of Boston University.
Thanks also to my labmates Chaoyang, Levent and Atakan.
A special acknowledgment goes to Ezgi and Chuck, who helped and gave me strength in a very hard moment.

Thanks to all the amazing people that I met during my stay in Boston, that made my American experience something that changed me a lot and made me understand that, often, all we need is simply beyond our fears.
Special thanks go to my wonderful landlady Deborah: you have been like a mother to me and I will forever keep in my heart that time you said me "You can feel safe here: now this is your home, too". And thanks to Tommy, the sweetest (and laziest) cat of Brigthon.
My deep gratitude goes also to Marco, her wife Erika and their lovely daughters Giorgia and Anna. You welcomed me when I was completely alone and lost on the other side of the world and I am really glad for this.
And, eventually, thanks to Elisa, my Boston soulmate (and to bus 57 that made us meet). You taught me to be brave and confident and to intensely enjoy all the little good things. I cherish our friendship and I am sure it will last for a very very long time.

Voglio poi ringraziare tutte le persone che mi accompagnano e sostengono nella vita di tutti i giorni.

Grazie a Luisa e Antonio, per l'aiuto prezioso che da sempre offrono a me ed alla mia famiglia.

Grazie alle mie bellissime e simpaticissime discepole Dajana e Martina, che trovano sempre il modo di farmi sorridere e confortarmi. È bello sapere di poter contare sulla vostra amicizia.

Un ringraziamento speciale va a Gabriele, che ha vissuto insieme a me ogni gioia (e qualche dolore) di questi tre anni di dottorato.

Grazie al mio amico di infanzia Federico (detto Sui), per esserci in ogni occasione importante.

Grazie a Giulia, per avere sempre l'entusiasmo e la costanza di continuare a coltivare la nostra amicizia negli anni.

Grazie a Federico e Stop, i bellissimi più bellissimi che conosco.

Grazie alla mia cara amica Ilaria, sempre pronta a raggiungermi in qualsiasi parte del mondo io mi trovi. Insieme abbiamo vissuto tante avventure di vita e mille

altre ci stanno aspettando. Sono felice di come stiamo crescendo insieme e di tutti i traguardi che stiamo raggiungendo, sempre una al fianco dell'altra.

Voglio poi rivolgere un ringraziamento speciale a tutte le coinquiline con cui ho avuto la fortuna di condividere quel posto magico (e per me profondamente catartico) che è Casa Fagioli, dove ho imparato non solo il vero significato di parole come "condivisione", "comprensione" e "ascolto", ma anche a guardarmi dentro abbandonando ogni paura.
In particolare, ringrazio Elena, per la sua schiettezza e determinazione e per avermi insegnato l'importanza di fidarsi e affidarsi agli altri.
Ringrazio Sara, per la sua tranquillità e il suo solare ottimismo, per la sua spontaneità disarmante e per avermi insegnato a volermi bene un po' di più e prendermi cura di me stessa un po' di più.
A Valentina voglio invece dire grazie per essersi raccontata senza filtri e per aver reso la nostra amicizia un luogo dove mi sono sempre sentita libera di confidarmi, senza paura del giudizio. Ascoltare le persone e cercare di capirne davvero i timori e i desideri è una dote rara da trovare nelle persone, ma tu, Vale, la possiedi ed è questo uno dei molti motivi per cui ti stimo e ti voglio bene.
Ad Alessia, Chiara e Giulia lascio in eredità stanze colme di ricordi e vita: con la vostra spensierata allegria e la vostra freschezza, sono sicura che sarete delle perfette padrone di casa.

Il ringraziamento più importante va a Jacopo, per aver riportato il sorriso sul mio volto. Mi hai fatto riscoprire la gioia nella semplicità dei gesti quotidiani e la voglia di guardare al futuro. Grazie per la pazienza con cui sai accogliere le mie infinite fragilità e per la dolcezza con cui le sai lenire. Grazie perché quando perdo la bussola nel mio mare di preoccupazioni, tu sai ripescarmi con prontezza e mi ricordi chi sono e dove sto andando. Grazie per chiedermi sempre "Sei felice insieme a me?".

E infine, grazie a mia mamma Daniela e a mio papà Piero. Grazie per il vostro esempio, per il vostro amore e per i vostri insegnamenti preziosi: il tempo passa ed io imparo ad apprezzarne sempre di più il valore. Grazie per la premura con cui mi avete seguita (letteralmente) fino in capo al mondo e per la gioia con cui aspettate ogni mio ritorno a casa. Spero di rendervi sempre orgogliosi di me e di riuscire a ricambiare anche solo una piccola parte del bene con cui mi avete cresciuta. Vi amo tanto.

Abstract

In the last years, a strong interest has been oriented towards micro-opto-fluidics, nominally merging optic and microfluidic technologies, for sensing applications in the field of biology, medicine and chemistry. The research activity that I have carried out during my Ph.D. at the Laboratory of ElectroOptics of the University of Pavia is inserted in this framework and aimed to develop smart sensing platforms to analyze the optical properties of fluids for chemical and biological applications, exploiting label free, remote, contactless and non-invasive techniques. The solutions investigated are based on the use of well-established opto-electronic components, traditionally developed in the visible and near infrared optical regions for telecom applications. The first sensing platform I have designed and implemented exploits optical interferometry in an innovative manner for high sensitivity measurements of the refractive index (real part) of liquids. Rectangular glass micro-capillaries were considered as fluidic channels since they are low-cost commercial devices, suitable for optical analysis of ultra-low volumes of fluids. Moreover, they can be modelled as optical resonators, and, if illuminated by a broadband radiation, the reflection spectrum is characterized by a sequence of minima corresponding to the optical resonances. The wavelength position of the spectral minima depends on the refractive index of the sample filling the channel. In this sensing configuration, a micro-capillary was inserted at the end of the measurement path of a a free-space Michelson interferometer working in the near infrared region around 1550 nm. Optical resonances were recognized as steep phase variations of the interferometric signal, analyzed in the wavelength domain. Moreover, refractive index changes were measured monitoring the spectral shift of the phase variations. The interferometric measurements are surely very promising but they are non-specific, since the same change of refractive index can be due to various combinations of fluids. On the other hand, the absorption spectrum, which is related to the imaginary part of the refractive index according to the Beer-Lambert law, is a unique “fingerprint” of every molecule. For this reason, I have worked on the development of another innovative micro-opto-fluidic configuration for the

measurement of the near infrared absorption spectrum of sub-microliter quantities of liquids, again flowing in rectangular glass micro-capillaries, in the range 1.0–1.7 μm. The micro-devices were externally coated with a full-length bottom metallic layer and a shorter top one. The incident beam can be moved along the capillary surface in order to make the light bounce once on the bottom metallization or bounce multiple times, exploiting the zig-zag guiding effect provided by the top metallization. In this way, the interaction length between the radiation and the sample (and thus the measurement sensitivity) can be tuned. The sensing platform was used in particular to detect the presence of water in alcohols as polluting substance and, afterwards, for quality control of water content in alcoholic beverages and in hand sanitizer gels and its compliance with the composition reported on the labels. The third and last sensing platform was developed in collaboration with the company Fluid-o-Tech in the framework of the DSF (Digital Smart Fluidics) project that won the "Research and Innovation Hub" POR FESR 2014-2020 call for tender of Regione Lombardia. Main goal of the project is the creation of a standardized fluidics platform to develop smart biomedical devices and equipment for hospital and home infusion therapy. The expertise that I have acquired in the field of optical sensors allowed me to take part in this project working on the development of an opto-fluidic platform that is able to distinguish different types of fluids for parenteral artificial nutrition on the basis of their refractive index, with the aim of improving the quality of life of patients at home. The principle of operation is based on the observation that if a light beam enters a rigid fluidic channel at a certain angle and a mirror is located behind it, then the radiation is reflected and exits the channel in a different position with respect to the entrance point. In particular, if fluids with different refractive index flow in the fluidic device, the radiation is deflected at different angles inside the liquid (according to Snell law) and the light exit point shifts along the channel surface. This variation of position can be easily detected by means of a position sensitive detector. After investigation and characterization of different fluidic channels and optical components, industrial prototypes of the opto-fluidic platform for integration in commercial pumps for infusion were designed. They were successful exploited to simultaneously detect mixtures for artificial nutrition and dangerous air bubble that could generate along the fluidic path.

Abstract (Italian)

Negli ultimi anni, si è osservato un crescente interesse per la micro-opto-fluidica, che combina tecnologie ottiche e microfluidiche, per applicazioni sensoristiche nel campo della biologia, della medicina e della chimica. L'attività di ricerca che ho svolto durante il mio dottorato presso il Laboratorio di ElettroOttica dell'Università di Pavia si inserisce esattamente in questo contesto e si pone come obiettivo lo sviluppo di piattaforme sensoristiche per l'analisi delle proprietà ottiche di fluidi per applicazioni chimiche e biologiche, sfruttando tecniche *label free*, senza contatto e non invasive. Le soluzioni investigate si basano sull'utilizzo di componentistica opto-elettronica consolidata e sviluppata per operare tradizionalmente nelle regioni del visibile e del vicino infrarosso, nell'ambito delle comunicazioni ottiche. La prima piattaforma sensoristica che ho progettato ed implementato utilizza l'interferometria ottica in modo innovativo per misure ad elevata sensibilità dell'indice di rifrazione (parte reale) di liquidi. Micro-capillari in vetro a sezione rettangolare sono stati considerati come canali fluidici poiché sono dispositivi commerciali a basso costo, adatti per analisi ottiche di volumi ultra-piccoli di fluidi. Inoltre, possono essere modellizzati come risuonatori ottici e, se illuminati da radiazione ottica a banda larga, lo spettro della luce riflessa è caratterizzato da una sequenza di minimi che identificano le risonanze ottiche. La lunghezza d'onda dei minimi dipende dall'indice di rifrazione del campione nel canale. In questa piattaforma, un micro-capillare è stato inserito al termine del cammino di misura di un interferometro di Michelson che opera intorno a 1550 nm. Le risonanze ottiche sono state identificate come ripide variazioni di fase del segnale interferometrico, analizzato nel dominio della lunghezza d'onda. Inoltre, variazioni di indice di rifrazione sono state misurate monitorando la traslazione spettrale dei salti di fase. Queste misure interferometriche sono certamente promettenti, ma tuttavia non specifiche, poiché la stessa variazione di indice può essere indotta da diverse combinazioni di fluidi. D'altro canto, lo spettro di assorbimento, legato alla parte immaginaria dell'indice di rifrazione secondo la legge di Beer-Lambert, è "l'impronta digitale" caratteristica di ogni molecola. Per questo motivo, ho poi la-

vorato allo sviluppo di un'altra configurazione micro-opto-fluidica innovativa per la misura dello spettro di assorbimento nel vicino infrarosso (da 1.0 a 1.7 μm) di piccoli volumi di liquidi, sempre contenuti in micro-capillari rettangolari in vetro. I micro-dispositivi sono stati esternamente rivestiti con un strato metallico per tutta la lunghezza della parete inferiore e con una metallizzazione superiore più corta. Il fascio incidente può essere traslato lungo la superficie del micro-capillare per ottenere un singolo rimbalzo della luce sulla metallizzazione inferiore oppure più rimbalzi, sfruttando l'effetto di guida offerto dalla metallizzazione superiore. In questo modo, la lunghezza di interazione e quindi la sensibilità possono essere accordate opportunamente. La piattaforma è stata utilizzata per rivelare la presenza di acqua in alcol come agente diluente e, in seguito, per il controllo di qualità di gel igienizzanti per mani e di liquori contenenti alcol. La terza ed ultima piat-taforma sensoristica è stata sviluppata in collaborazione con l'azienda Fluido-Tech nell'ambito del progetto DSF (Digital Smart Fluidics) che ha vinto il bando "Research and Innovation Hub" POR FESR 2014-2020 finanziato dalla Regione Lombardia. Il principale obiettivo del progetto è la creazione di una piattaforma fluidica standardizzata per sviluppare dispositivi medici intelligenti per terapie infusionali in ospedale e a casa. Le competenze che ho acquisito nell'ambito dei sensori ottici mi ha consentito di prendere parte a questo progetto e di lavorare alla realizzazione di una piattaforma opto-fluidica che può identificare tipi diversi di miscele per nutrizione artificiale parenterale sulla base del loro indice di rifrazione, con l'obiettivo di migliorare le condizioni di vita di pazienti curati a casa. Il principio di funzionamento del sensore si basa sul fenomeno per cui, se un fascio luminoso incide su di un canale fluidico rigido ad un certo angolo e uno specchio è posizionato al di là del canale, la radiazione riflessa esce dal canale in una posizione diversa dal punto di ingresso. In particolare, se fluidi con diverso indice fluiscono nel dispositivo fluidico, il fascio di luce penetra nei fluidi con angoli diversi e la posizione di uscita del fascio riflesso trasla lungo la superficie. Questa variazione di posizione può essere facilmente misurata utilizzando un fotorivelatore di posizione commerciale. Dopo lo studio e la caratterizzazione di diversi canali fluidici e componenti ottici, sono stati progettati alcuni prototipi industriali per l'integrazione in pompe per infusione commerciali. I prototipi sono stati utilizzati con successo per distinguere miscele per nutrizione artificiale e, allo stesso tempo, per rivelare bolle d'aria potenzialmente pericolose che possono svilupparsi lungo il cammino fluidico.

List of Symbols and Abbreviations

a	Orthogonal projection of lightpath in the front wall
A	Absorbance
A_{H2O}	Water absorbance
Al	Aluminum
$A_{mixture}$	Absorbance of the mixture
AN	Artificial Nutrition
A_{sample}	Sample absorbance
Au	Gold
b	Orthogonal projection of lightpath in the channel
c	Orthogonal projection of lightpath in the back wall
C	Concentration of a substance
$C_6H_{12}O_6$	Glucose
C_{amino}	Concentration of an amino acid
CCD	Charge-Coupled Device
C_{el}	Concentration of an electrolyte
C_{glu}	Concentration of glucose
C_{H2O}	Concentration of water
$CO(NH_2)_2$	Urea
$COVID$-19	CoronaVirus Disease 2019
d	Channel depth
d_{sample}	Displacement of the nano-beam
$DICAr$	Dipartimento di Ingegneria Civile ed Architettura
DSF	Digital Smart Fluidic
EBS	Erbium-doped fiber Broadband Source
E_m	Electric field amplitude of measurement arm
$\overrightarrow{E_{measurement}}$	Electric field vector of measurement arm
E_r	Electric field amplitude of reference arm

$\overrightarrow{E_{reference}}$	Electric field vector of reference arm
f	Geometrical path for a single channel crossing
f_{res}	Resonance frequency
F	Total geometrical path
FSR	Free Spectral Range
$FTIR$	Fourier transform infrared
$FWHM$	Full width at half maximum
G	Autocorrelation function
He-Ne	Helium-Neon
i	Imaginary unit
I	Supply current
I_1	Photogenerated current 1
I_2	Photogenerated current 2
I_{cap}	Intensity signal due to the micro-capillary reflection
$InGaAsSb$	Indium gallium arsenide
$InGaAsSb$	Indium gallium arsenide antimony
I_{interf}	Intensity of the interferometric signal
$I_{interf\ exp}$	Intensity of the experimental interferometric signal
IIR	Infinite Impulse Response
I_m	Photodetected current for the measurement arm
I_{mirror}	Intensity signal due to the mirror reflection
I_{ph}	Overall interferometric photodetected current
I_r	Photodetected current for the reference arm
k	Wavenumber
k_{abs}	Imaginary part of the refractive index
L	Length of the fluidic channel
L_c	Coherence length
LED	Light Emitting Diode
L_m	Length of the measurement arm
$L_{n'}$	Transmission losses due to refractive index differences
L_{met}	Length of the metallization
L_{NEMS}	Length of the nano-beam
L_r	Length of the reference arm
L_t	Total transmission losses
LoD	Limit of Detection
L_{PSD}	Length of the position sensitive detector active area

m	Order of the resonant mode
M	Odd integer number
$MEMS$	Micro-electro-mechanical systems
n	Refractive index
N	Number of bounces
n'	Real part of the refractive index
$NaCl$	Sodium chloride
$n_{AF\ fluid}$	Refractive index of an artificial nutrition mixture
n_{air}	Refractive index of air
$N_{a\ tot}$	Total number of amino acids
$Nd:YAGS$	Neodymium-doped yttrium aluminium garnet
$NEMS$	Nano-electro-mechanical systems
n_{etoh}	Refractive index of ethanol
$N_{e\ tot}$	Total number of electrolytes
n_{glass}	Refractive index of glass
n_{H2O}	Refractive index of water
n_{iso}	Refractive index of isopropanol
n_{saline}	Refractive index of saline solution
$n_{mixture}$	Refractive index of a mixture
NIR	Near Infared
OCT	Optical Coherence Tomography
OSA	Optical Spectrum Analyzer
p	Distance travelled by the light along the x-direction at each bounce
P	Dissipated power
PBS	Polarized beam splitter
PD	Photodiode
$PDMS$	Polydimethylsiloxane
PID	Proportional integrative-derivative
P_{in}	Incident power
$P_{interferometric}$	Responsivity parameter for interferometric readout
$P_{out\ air}$	Output power in presence of air
$P_{out\ blank}$	Output power in presence of blank solution
$P_{out\ sample}$	Output power in presence of a sample
p_{PSD}	Position of the light beam measured by the position sensitive detector

PSD	Position Sensitive Detector
$P_{spectral}$	Responsivity parameter for spectral readout
r	Reflection coefficient for the electric field
R	Reflection coefficient for the power
R^2	Coefficient of determination
RB	Resolution Bandwidth
r_{cap}	Reflection coefficient for the electric field for the whole micro-capillary
R_{cap}	Reflection coefficient for the power for the whole micro-capillary
RI	Refractive Index
RIU	Refractive Index Unit
R_{met}	Reflection coefficient for the power of the metallic layer
S	Sensitivity
SiN	Silicon nitride
$S_{multiple}$	Sensitivity of multiple bounce configuration
S_{single}	Sensitivity of single bounce configuration
$SARS\text{-}CoV\text{-}2$	Severe Acute Respiratory Syndrome CoronaVirus 2
$SLED$	Superluminescent Light Emitting Diode
SPR	Surface Plasmon Resonance
$SWIR$	Short-wave infrared
t	Transmission coefficient for the electric field
T	Transmission coefficient for the power
T_{abs}	Fraction of radiation transmitted through an absorbing medium
$T_{abs\ mixture}$	Fraction of radiation transmitted through a mixture
T_{air}	Spectral transmittance through the channel filled with air
t_b	Thickness of the back wall
t_{cap}	Transmission coefficient for the electric field for the whole micro-capillary
T_{cap}	Transmission coefficient for the power for the whole micro-capillary
t_f	Thickness of the front wall
t_{NEMS}	Thickness of the nano-beam
t_p	Transmission coefficient for p-polarized electric field
t_s	Transmission coefficient for s-polarized electric field

T_{sample}	Spectral transmittance through the channel filled with a sample
v	Air bubble velocity
V	Fringe visibility
$V_1 + V_2$	Sum signal of position sensitive detector
$V_1 - V_2$	Difference signal of position sensitive detector
V_{AC}	Amplitude of the actuation signal
V_{air}	Average amplitude detected by the photodiode in presence of air in the channel
W	Width of the fluidic channel
V_{sample}	Average amplitude detected by the photodiode in presence of a sample in the channel
W_{NEMS}	Width of the nano-beam
x	Lightpath
X	Theoretical shift of the light beam
$X_{experim}$	Experimental shift of the light beam
α	Absorption coefficient
$\alpha_{thermal}$	Thermal expansion coefficients
Δn	Refractive index variation
Δs	Difference between measurement and reference paths
$\Delta s_{optical}$	Generic variation of the optical path
$\Delta\lambda$	Spectral wavelength shift
$\Delta\lambda_{source}$	Emission bandwidth
$\varepsilon_{glucose}$	Molar extinction coefficients of glucose
ε_{H2O}	Molar extinction coefficients of water
ε_s	Molar extinction coefficients of solute
ε_{urea}	Molar extinction coefficients of urea
θ	Angle
λ	Wavelength
λ_e	Central emission wavelength
ν	Ratio of amplitude responsivities
ρ	Responsivity
σ	Standard deviation on experimental data
σ_{ph}	Responsivity of the photodetector
τ	Time
ϕ_{cap}	Phase due to the micro-capillary

ϕ_{interf}	Interferometric phase
ϕ_m	Electric field phase of measurement arm
ϕ_r	Electric field phase of reference arm
ϕ_{tot}	Total phase
Ψ	Amplitude responsivity
ω	Pulsation
$\frac{\partial n}{\partial C_{glu}}$	Refractive index increment coefficient for glucose
$\frac{\partial n}{\partial C_{amino}}$	Refractive index increment coefficient for an amino acid
$\frac{\partial n}{\partial C_{el}}$	Refractive index increment coefficient for an electrolyte

List of Figures

List of Tables

Contents

Introduction

Opto-fluidics, nominally the technological area where optics and fluidics merge, is a relatively new research field that, in the last decade, is catching the attention of both the worlds of academia and industry. Indeed, there is a growing interest for the development of innovative opto-fluidic devices for a wide plethora of applications in the field of biology, nanomedecine, physics, chemistry, material science and nanotechnology [1]. On the other hand, opto-fluidics is surely a challenging field because it has a strongly interdisciplinary origin: thus, in order to develop suitable solutions, a combination of knowledge in different fields, ranging from materials science to photonics, from fluidics to molecular biology, is required. The "young age" of opto-fluidics is proved by the fact that the first works reported in the Web of Science database containing the word "opto-fluidics" are quite recent and date back to the year 2005 [2, 3]. Since then, the number of publications on opto-fluidic rapidly increased, going from 0 to more than 500 in a range of 12 years (2005-2016). Moreover, also the number of Ph.D. schools on topics related to opto-fluidics is growing as well as the number of topical conferences organized by important scientific associations. In the very last years, the newest trend is to move to micro-opto-fluidic devices, based on the integration of optical technologies and micro-fluidics [4] that allows the analysis of ultra-low volumes of sample, a feature particularly important when dealing with biological fluids [5]. Another important challenge is the necessity of achieving high performance and sensitivity while using low-cost, or disposable, systems. Such an achievement could boost the diffusion of opto-fluidic solutions in many environments where complex laboratory instrumentation is not available. Moreover, the creation of user-friendly and easy-to-use platforms could help promote the use of such devices also by non-technically-expert personnel. In the literature several works on opto-fluidics are reported, focusing on many different research field. A particularly interesting and urgent application is the exploitation of opto-fluidics for medical and biological sensing [6]. Opto-fluidics solutions are reported for sample detection based on absorbance and fluorescence [7], refractive index measurement of biological fluids

[8], protein and DNA analysis [9], cell imaging and sorting [10], immunoassays. Moreover, the latest trend is to combine optics and micro-fluidics to realize miniaturized lab-on-chip platforms where light sources and detectors, waveguides and fluidic channels can be integrated in a single chip using innovative microfabrication techniques and innovative materials [11].

The research activity that I have carried out during my Ph.D. places itself exactly in this framework and aims to develop smart sensing platforms to analyze the optical properties of fluids for chemical and biological applications, exploiting label free, remote, contactless and non-invasive opto-fluidics techniques.

In the following, a brief summary of this Ph.D. dissertation is reported.

In **Chapter 1**, I introduce the first micro-opto-fuidic platform that I designed for high sensitivity refractive index measurements in rectangular glass micro- capillaries in the near infrared region, exploiting optical interferometry in an innovative manner. In particular, the interferometric signal is analyzed in the wavelength domain to detect the position of optical resonances. The theoretical background and principle of operation of the measuring technique, as well as the developed instrumental configuration, are discussed. Experimental results are presented and compared with the method based of reflectivity and transmissivity analysis previously investigated.

In **Chapter 2**, I describe the micro-opto-fuidic platform that I developed for characterization of the absorption spectrum of fluids in the near infrared range from 1.0 to 1.7 μm in micro-fluidic channels with selectable pathlength. Spectroscopic measurements are necessary to identify the composition of a sample, since detection of the real part of refractive index is non-specific. I introduce the theoretical model developed to describe light propagation in the channel and the instrumental configuration, then I compare theoretical and experimental results. In the end, two specific real-life sensing applications are described: quality control of hand sanitizer gels and quality control of alcoholic beverages.

In **Chapter 3**, I present the activity carried out in the framework of DSF Digital Smart Fluidics project to develop a smart opto-fluidic platform that identifies commercial mixtures for artificial nutrition. The features and performances of different fluidic channels are investigated and compared, both theoretically and experimentally. Then, I describe the opto-electronic and fluidic components chosen to realize industrial prototypes for integration in commercial pumps for infusion

and I present the outcome of experimental testing of artificial nutrition mixtures. Eventually, preliminary results about the detection of air bubbles along the fluidic path are given.

In **Chapter 4**, I report the overall conclusions and future work.

In **Appendix A**, I present the research activity carried out at the Nanometer Scale Engineering Laboratory of Boston University, demonstrating the exploitation of a more conventional type of high-coherence interferometry in the time domain for characterization of nano-electro-mechanical systems. After describing the features of doubly-clamped suspended nano-resonators that I analyzed, I present the results of electro-thermal actuation and thermal noise characterization using a sophisticated laser Michelson interferometer.

In **Appendix B**, I describe the side activity carried out on absorption spectroscopy analysis using short-wave infrared LEDs for multiwavelength detection of urea concentration. I present the results of spectral analysis, as well as the results of amplitude detection obtained with photodiodes. Then I describe the parameters that were extracted for specific sensing of urea in water and dialysate solution.

In **Appendix C**, I report the detailed composition of each mixture for artificial parenteral nutrition used for experimental testing, as indicated on the product leaflets.

Chapter 1

Spectral phase interferometry for high-sensitivity refractive index sensing in rectangular glass micro-capillaries

This Chapter is devoted to the presentation of spectral phase interferometry operating in the near infrared wavelength range for refractive index monitoring of liquid samples in micro-capillaries. First, the features of such micro-devices and the theoretical equations that allow to describe them as optical resonators are presented. Afterwards, few general results about optical reflectometry to identify the optical resonances of the capillary are described. Then, a brief introduction about the theory of interferometry, how it can be used for resonances detection and the most common instrumental configurations is provided. An important Section is then devoted to the presentation of the results of theoretical simulations carried out first considering an empty micro-capillary, and then filled with fluids for refractive index monitoring. Eventually, after the description of the micro-opto-fluidic setup, the experimental results about resonances recognition and refractive index detection of different types of liquids are presented and discussed in detail. The results of this work were published in [12, 13, 14].

1.1 Features of rectangular glass micro-capillaries

Rectangular glass micro-capillaries are low-cost disposable micro-channels, commercially available in a wide variety of formats. All the micro-capillaries investigated during the researches presented in this doctoral thesis, known as Rectangle –

Miniature Hollow Glass Tubings (VitroTubes^{TM}), were purchased from VitroCom (NJ, USA). The inner channel has depth indicated with d, while the front and back wall have thickness t_f and t_b, respectively. Capillaries with length L = 50, 100, 300, 600 mm can be purchased, while different combination of wall thicknesses and channel depths are available, ranging from 7 to 700 µm. The channel width W is usually one order of magnitude larger than its depth d. Moreover, the manufacturer ensures a tolerance of ±10% for the channel depth and of ±20% for thickness of the walls. VitroTubes^{TM} capillaries are realized in 3.3 borosilicate glass with a refractive index (RI) of about 1.51 across the visible and near infrared spectral region. Figure 1.1 reports a schematic representation of the micro-capillary and a picture of three micro-devices with different dimensions in comparison with a 50-cent euro coin.

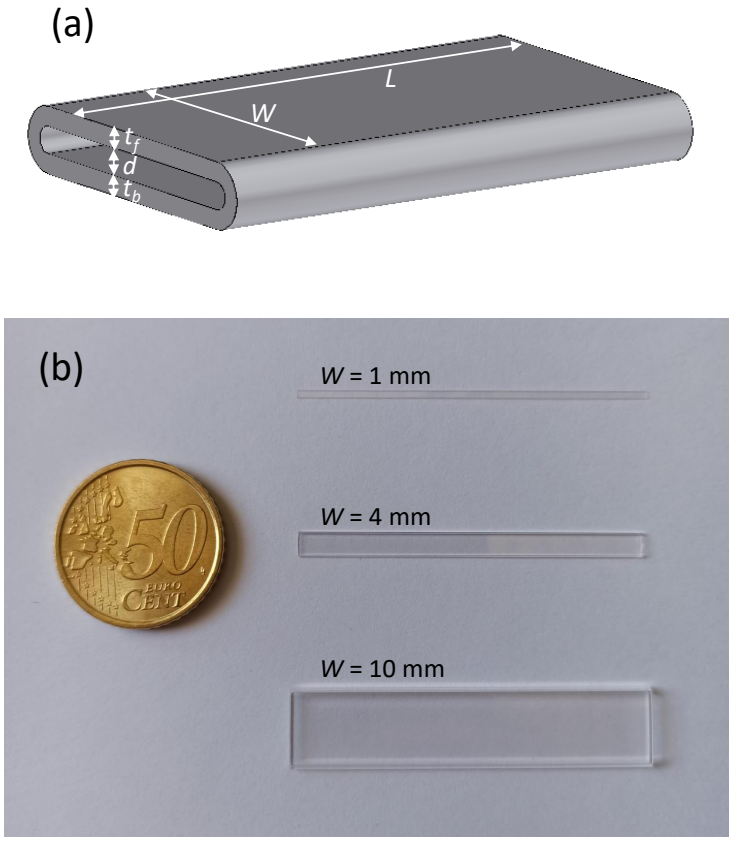

Figure 1.1: Rectangular glass micro-capillaries. (a) Schematic representation of the micro-capillary. (b) Picture of three micro-capillaries with different dimensions.

Rectangular glass micro-capillaries exhibit many interesting features that make them highly suitable for optical investigation of liquids and biological fluids. First,

they are transparent and they offer a flat surface for remote contactless non-invasive optical readout, also reducing scattering phenomena that typically arise when using circular section capillaries. Then, borosilicate glass is a biocompatible material that can be easily functionalized for biological analyses; it also offers a good adhesion for the deposition of thin metallic layers. Moreover, thanks to their micrometric dimensions, micro-capillaries allow the analysis of ultra-low volumes of liquid samples, of the order of few µL or even nL, an important feature in the field of biological analyses, where often just very small quantities of fluids are accessible. Eventually, they can be easily connected with fluidic paths and inserted into fluidic circuits to perform both static and in-flow measurements.

1.2 Rectangular glass micro-capillaries as optical resonators

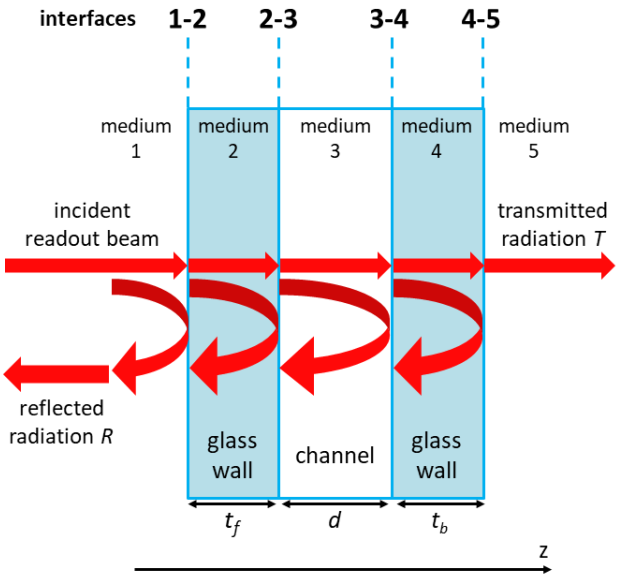

Figure 1.2: Schematic representation of the layered structure constituting the rectangular glass micro-capillaries. At each interface between different media, incident light is partially reflected and partially transmitted.

Rectangular glass micro-capillaries can be envisioned as optical resonators [15, 16, 17], composed of a sequence of three layers with different refractive index: the front wall, the inner channel and the back wall. As reported in Figure 1.2, when a light beam (plane wave) is shined orthogonally to its flat surface along the z-direction, it encounters four different interfaces: interface 1-2 between air and

glass, interface 2-3 between glass and the material filling the channel, that can be air or a liquid sample, interface 3-4 between the channel and glass and interface 4-5 between glass and air. At each separation surface, the radiation is partially transmitted and partially reflected. Supposing a condition of perpendicular incidence, light is transmitted along the same direction of the incident beam, while the reflected beam travels in the backward direction. In condition of perpendicular incidence, the amount of transmitted and reflected field amplitude at each interface, r_{jl} and t_{jl} respectively, is equal for the two polarizations of the electric field and it can be calculated by applying the Fresnel formulas:

$$r_{jl} = \frac{n_j - n_l}{n_j + n_l} \tag{1.1}$$

$$t_{jl} = \frac{2n_j}{n_j + n_l} \tag{1.2}$$

where the subscripts *j* and *l* indicate the origin and destination medium, respectively, while n_j and n_l are the refractive indices of the two media. The overall reflectivity and transmissivity of 2D and 3D structures are usually calculated by transfer matrix method; however, in this situation a simpler approach based on electromagnetic field propagation can be adopted. Indeed, being the width and the length of the capillary larger than the diameter of the incident light spot, the micro-capillary can be modeled as a cascade of Fabry-Pèrot etalons (each layer is an etalon). This method consists in recursively applying the Fresnel formulas starting from the back etalon in order to take into account the contribution given by each layer [18]. Starting by considering the back glass wall of the capillary, two interfaces are identified: 3-4 between the channel and back glass wall and 4-5 between back glass wall and air. Considering a plane wave propagating and applying the Fresnel formulas, it holds that:

$$r_{3-4} = \frac{n_{channel} - n_{glass}}{n_{channel} + n_{glass}} \tag{1.3}$$

$$r_{4-3} = -r_{3-4} \tag{1.4}$$

$$r_{4-5} = \frac{n_{glass} - n_{air}}{n_{glass} + n_{air}} = \frac{n_{glass} - 1}{n_{glass} + 1} \tag{1.5}$$

$$t_{3-4} = \frac{2n_{channel}}{n_{channel} + n_{glass}} \tag{1.6}$$

$$t_{4-3} = \frac{2n_{glass}}{n_{channel} + n_{glass}} \tag{1.7}$$

$$t_{4-5} = \frac{2n_{glass}}{n_{air} + n_{glass}} = \frac{2n_{glass}}{1 + n_{glass}} \tag{1.8}$$

where n_{glass} is the glass RI, $n_{channel}$ is the RI of the substance filling the channel and n_{air} = 1 is the RI of air. Afterwards, the equivalent electric field reflection coefficient r_{3-4eq} and the equivalent electric field reflection coefficient t_{3-4eq} that take into account the overall effect of the back wall are given by

$$r_{3-4eq} = r_{3-4} + \frac{t_{3-4} \cdot t_{4-3} \cdot r_{4-5} \cdot e^{-i \cdot 2 \cdot k \cdot n_{glass} \cdot t_b}}{1 - r_{4-3} \cdot r_{4-5} \cdot e^{-i \cdot 2 \cdot k \cdot n_{glass} \cdot t_b}} \tag{1.9}$$

$$t_{3-4eq} = \frac{t_{3-4} \cdot t_{4-5} \cdot e^{-i \cdot k \cdot n_{glass} \cdot t_b}}{1 - r_{4-3} \cdot r_{4-5} \cdot e^{-i \cdot 2 \cdot k \cdot n_{glass} \cdot t_b}} \tag{1.10}$$

where i is the imaginary unit, k = 2·π/λ is the wavenumber and λ is the wavelength. The calculations have to be iteratively repeated also when considering the other layers. When considering the capillary channel, defined by the interface 2-3 between the front glass wall and the channel and the interface 3-4 between the channel and the back glass wall, the equivalent electric field reflection coefficient r_{2-3eq} is given by

$$r_{2-3eq} = r_{2-3} + \frac{t_{2-3} \cdot t_{3-2} \cdot r_{3-4eq} \cdot e^{-i \cdot 2 \cdot k \cdot n_{channel} \cdot d}}{1 - r_{3-2} \cdot r_{3-4eq} \cdot e^{-i \cdot 2 \cdot k \cdot n_{channel} \cdot d}} \tag{1.11}$$

and the equivalent electric field reflection coefficient t_{2-3eq} is obtained as:

$$t_{2-3eq} = \frac{t_{2-3} \cdot t_{3-4eq} \cdot e^{-i \cdot k \cdot n_{channel} \cdot d}}{1 - r_{3-2} \cdot r_{3-4eq} \cdot e^{-i \cdot 2 \cdot k \cdot n_{channel} \cdot d}} \tag{1.12}$$

where

$$r_{2-3} = \frac{n_{glass} - n_{channel}}{n_{channel} + n_{glass}} \tag{1.13}$$

$$r_{3-2} = -r_{2-3} \tag{1.14}$$

$$t_{2-3} = \frac{2n_{glass}}{n_{channel} + n_{glass}} \tag{1.15}$$

$$t_{3-2} = \frac{2n_{channel}}{n_{channel} + n_{glass}} \tag{1.16}$$

Eventually, considering the cavity constituted by the front glass wall, similarly to the previous calculations, the equivalent electric field reflection coefficient for the whole structure r_{1-2eq}, that is the reflection coefficient for the whole micro-capillary r_{cap}, is given by

$$r_{cap} = r_{1-2eq} = r_{1-2} + \frac{t_{1-2} \cdot t_{2-1} \cdot r_{2-3eq} \cdot e^{-i \cdot 2 \cdot k \cdot n_{glass} \cdot t_f}}{1 - r_{2-1} \cdot r_{2-3eq} \cdot e^{-i \cdot 2 \cdot k \cdot n_{glass} \cdot t_f}} \tag{1.17}$$

and the the equivalent electric field transmission coefficient for the whole structure t_{1-2eq}, that correspond to the transmission through the entire micro-capillary t_{cap}, can be calculated as

$$t_{cap} = t_{1-2eq} = \frac{t_{1-2} \cdot t_{2-3eq} \cdot e^{-i \cdot k \cdot n_{glass} \cdot t_f}}{1 - r_{2-1} \cdot r_{2-3eq} \cdot e^{-i \cdot 2 \cdot k \cdot n_{glass} \cdot t_f}} \tag{1.18}$$

where

$$r_{1-2} = \frac{n_{air} - n_{glass}}{n_{air} + n_{glass}} = \frac{1 - n_{glass}}{1 + n_{glass}} \tag{1.19}$$

$$r_{2-1} = -r_{1-2} \tag{1.20}$$

$$t_{1-2} = \frac{2n_{air}}{n_{air} + n_{glass}} = \frac{2}{1 + n_{glass}} \tag{1.21}$$

$$t_{2-1} = \frac{2n_{glass}}{n_{air} + n_{glass}} = \frac{2n_{glass}}{1 + n_{glass}} \tag{1.22}$$

The spectral reflectivity for the power R_{cap} as a function of the wavelength and the spectral transmissivity for the power T_{cap} as a function of the wavelength for the overall micro-capillary are obtained as

$$R_{cap}(\lambda) = n_{air} \cdot |r_{cap}|^2 = |r_{cap}|^2 \tag{1.23}$$

$$T_{cap}(\lambda) = n_{air} \cdot |t_{cap}|^2 = |t_{cap}|^2 \tag{1.24}$$

1.3 Refractive index sensing based on spectral shift monitoring of transmissivity over reflectivity ration

In a previous work carried out at the Laboratory of ElectroOptics of the University of Pavia [19], refractive index monitoring in micro-capillaries was carried out in the near-infrared range through reflectometry measurements, by collecting the reflection spectrum $R_{cap}(\lambda)$ from the capillary illuminated with a broadband radiation and monitoring its minima: indeed, they wavelength position undergoes a redshift when the sample RI increases. Afterwards, also the transmitted $T_{cap}(\lambda)$ light was collected and the T_{cap}/R_{cap} ratio was computed and the refractive index was measured by following the wavelength shift of its spectral maxima [18]. Acquisition of both reflected and transmitted spectra represents undoubtedly an advantage with respect to standard reflectometry, since the evaluation of the T_{cap}/R_{cap} ratio allows to compensate for intensity fluctuations of the readout source, with no need of an additional monitoring system of the emitted optical power. The most significant results of this research are briefly discussed in this Section.

1.3.1 Theoretical results

In [18] the model presented in Section 1.2 describing how light propagates in a layered structures such as that of the micro-capillary was implemented in MATLAB environment and simulations were performed considering a micro-device with geometrical parameter $t_f = t_b = 21$ µm and $d = 30$ µm. With the explained method, the overall optical reflection R_{cap} and transmission T_{cap} by the capillary were calculated considering first an empty capillary (i.e. filled with air), as reported in Figure 1.3. R_{cap} minima correspond to T_{cap} maxima, and vice versa, and their spectral location identifies the position of the micro-capillary resonances. Moreover, the wavelength location of minima and maxima depends on the geometrical dimensions of the micro-device as well as on the RI of the walls and of the substances filling the channel. As a consequence, spectral measurements of reflected and trasnmitted power by the capillary can be used for refractive index sensing.

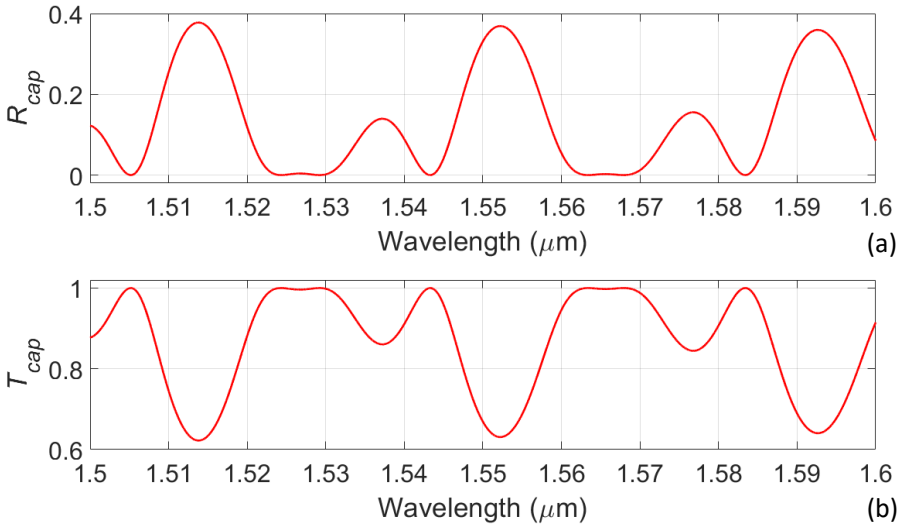

Figure 1.3: Theoretical results calculated through numerical simulations for an empty capillary with $t_f = t_b = 21$ µm and $d = 30$ µm. (a) Reflectivity R_{cap}. (b) Transmissivity T_{cap}.

Hence, to observe the response of the device to flowing media RI changes, numerical simulations were repeated for increasing RI values of the fluid inside the channel. Figure 1.4 shows the theoretical spectral reflectivity and transmissivity obtained for three different water-glucose dilutions with concentration 0 (water), 5 and 10% corresponding to RI values equal to 1.3340, 1.3413 and 1.3485 RIU, respectively. Afterwards, the T_{cap}/R_{cap} ratio was computed (Figure 1.5): it is clear that the resonances are located in correspondence of the maxima of this ratio signal. Moreover, the T_{cap}/R_{cap} ratio shifts towards longer wavelength as the RI in the channel increases. By monitoring the wavelength shift of the T_{cap}/R_{cap} peaks, theoretical values of RI sensitivity were found in the range 290-500 nm/RIU. Moreover, it is important to notice that the maximum refractive index difference that can be detected without ambiguity depends on the so called free spectral range (FSR), that is the distance between two consecutive maxima of the same T_{cap}/R_{cap} spectrum. As reported in detail in [18], the FSR depends on he geometrical features of the micro-capillary.

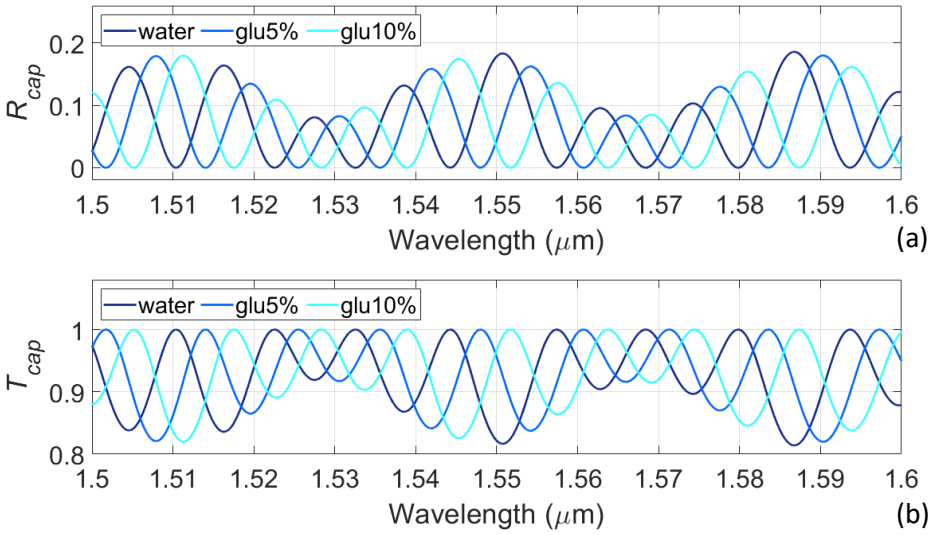

Figure 1.4: Theoretical results calculated through numerical simulations and obtained supposing the micro-capillary filled with samples with RI of 1.3340, 1.3413 and 1.3485 RIU. (a) Reflectivity R_{cap}. (b) Transmissivity T_{cap}.

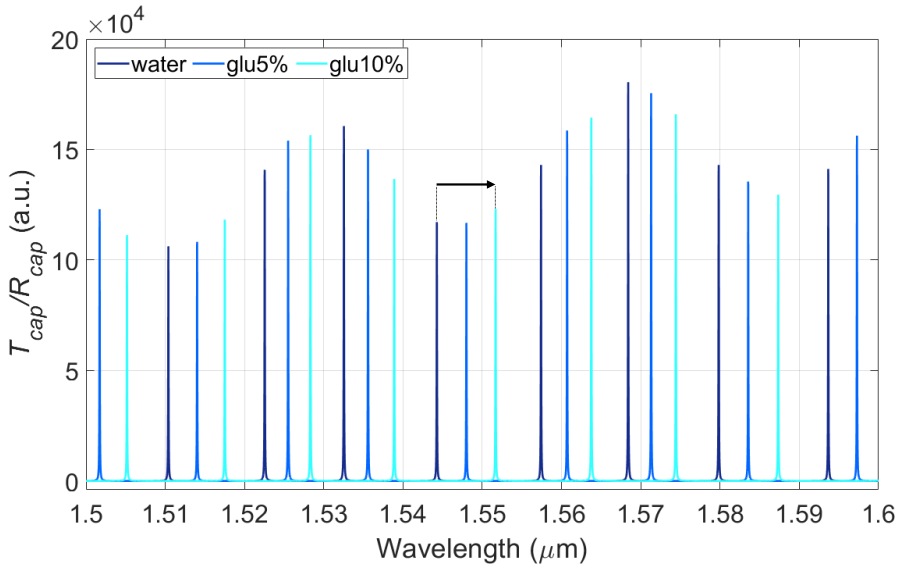

Figure 1.5: Theoretical T_{cap}/R_{cap} ratio. The RI difference with respect to a reference fluid can be reconstructed by monitoring the spectral shift of the ratio peaks as indicated by the black arrow.

1.3.2 Optical setup

Figure 1.6 shows the instrumental configuration employed to perform spectral reflectivity and transmissivity measurements. Readout radiation in the near-infrared range is provided by a Superluminescent Light Emitting Diode (SLED) source

(EXS1510-2111, Exalos, Switzerland) with peak emission wavelength of 1549 nm, Full Width at Half Maximum (FWHM) bandwidth of 57 nm and optical power coupled in standard single-mode optical fibers of approximately 1.8 mW when driven by a pumping current of $I = 180$ mA (current driver LDX-3207B, ILX Lightwave, MT, USA) at a temperature of 20 °C (temperature controller, LDT-5910, ILX Lightwave, MT, USA). The SLED is protected from unwanted optical feedback with a fiber optical isolator. Radiation is carried toward the capillary under test through a 2×2 fiber coupler with 50:50 splitting ratio (10202A-50-FC, Thorlabs, NJ, USA). A pigtail style focuser with aspheric lens (LPF-04-1550-9/125-S-5-23.5-3.9AS-60-3A-3-1, OzOptics, Canada) is used to shine light (with orthogonal incidence) on the flat side of the micro-capillary, placed at a distance of approximately 23.5 mm, and at the same time to couple the back reflected light from the device under test. Transmitted optical power is as well coupled in the fiber by means of a second lens (equal to the first one) placed on the opposite side of the capillary. Fluids enter the devices just by capillary action dipping the free ending of the capillary into an Eppendorf tube containing the fluid to be tested. A peristaltic pump (Minipuls2, Gilson, WI, USA) is employed to push the fluids out of the device channel after the optical detection. Reflected and transmitted optical powers are redirected to an optical spectrum analyzer (OSA Agilent 86142B, Agilent Technologies, CA, USA) for acquisition with a resolution bandwidth RB = 0.1 nm by a laptop.

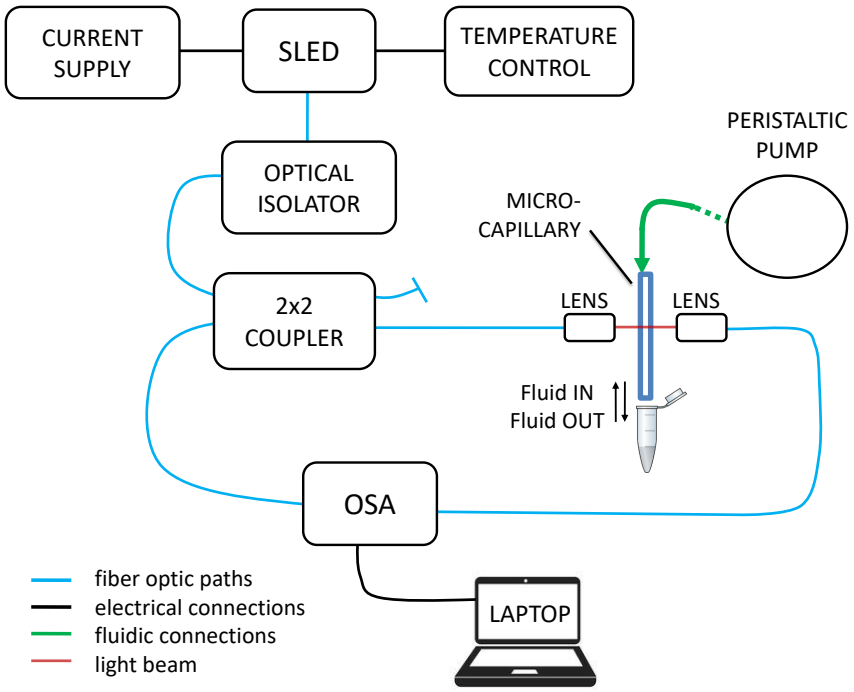

Figure 1.6: Schematic representation of the optical setup for T_{cap}/R_{cap} measurements. SLED: Superluminescent Light Emitting Diode. OSA: Optical Spectrum Analyzer.

1.3.3 Experimental results

The aim of the experimental study was to demonstrate that the spectral shift of the T_{cap}/R_{cap} ratio depends on the refractive index of water-glucose solutions flowing through the micro-capillary, and thus can be proposed as a method for refractive index sensing. A micro-capillary with geometrical dimensions $t_f = t_b = 21$ µm, $d = 30$ µm, $W = 300$ µm and $L = 5$ cm was tested by flowing water-glucose dilutions in concentration from 0 (water) to 16.5%, corresponding to RI values from 1.3340 to 1.3579 RIU. For every sample, the reflected and the transmitted power spectra were acquired. All the signals were processed with a low-pass digital filter. Then, since the SLED has a Gaussian-shaped emission spectrum, the reflected spectrum was normalized to the spectrum of the optical signal incident on the capillary, whereas the transmitted spectrum was normalized with respect to a reference spectrum captured in transmission without the capillary. Finally, for every sample the T_{cap}/R_{cap} ratio was calculated as reported in Figure 1.7. Figure 1.7(a) shows the sequence of T_{cap}/R_{cap} spectra acquired for all the solutions tested. As the RI of the filling solution increased, a shift of the spectral peaks toward longer wavelengths was observed in agreement with the theoretical predictions, as better

highlighted in the zoomed view of Figure 1.7(b) by the black arrow. Reporting the wavelength position of the maxima as a function of the solution RI, the calibration curves of the refractive index sensor were obtained and values of experimental sensitivity S were found in the range 290-485 nm/RIU (Figure 1.7(c)). These results are comparable with data reported in the literature [20, 21, 22] for more complex devices, sometimes attainable only with expensive and lengthy microfabrication techniques. The best calculated value for the LoD is $3.6 \cdot 10^{-5}$ RIU.

In conclusion, this work demonstrated the feasibility of using rectangular glass micro-capillaries for RI sensing. Since they have flat transparent walls and the have micrometric dimensions, they can be exploited for label free optical analyses of ultra-low volumes of fluids. Moreover, the possibility of collecting both transmitted and reflected spectra allows to calculate their ratio and eliminates the need of an external monitoring system for the emitted optical power in amplitude-based sensors.

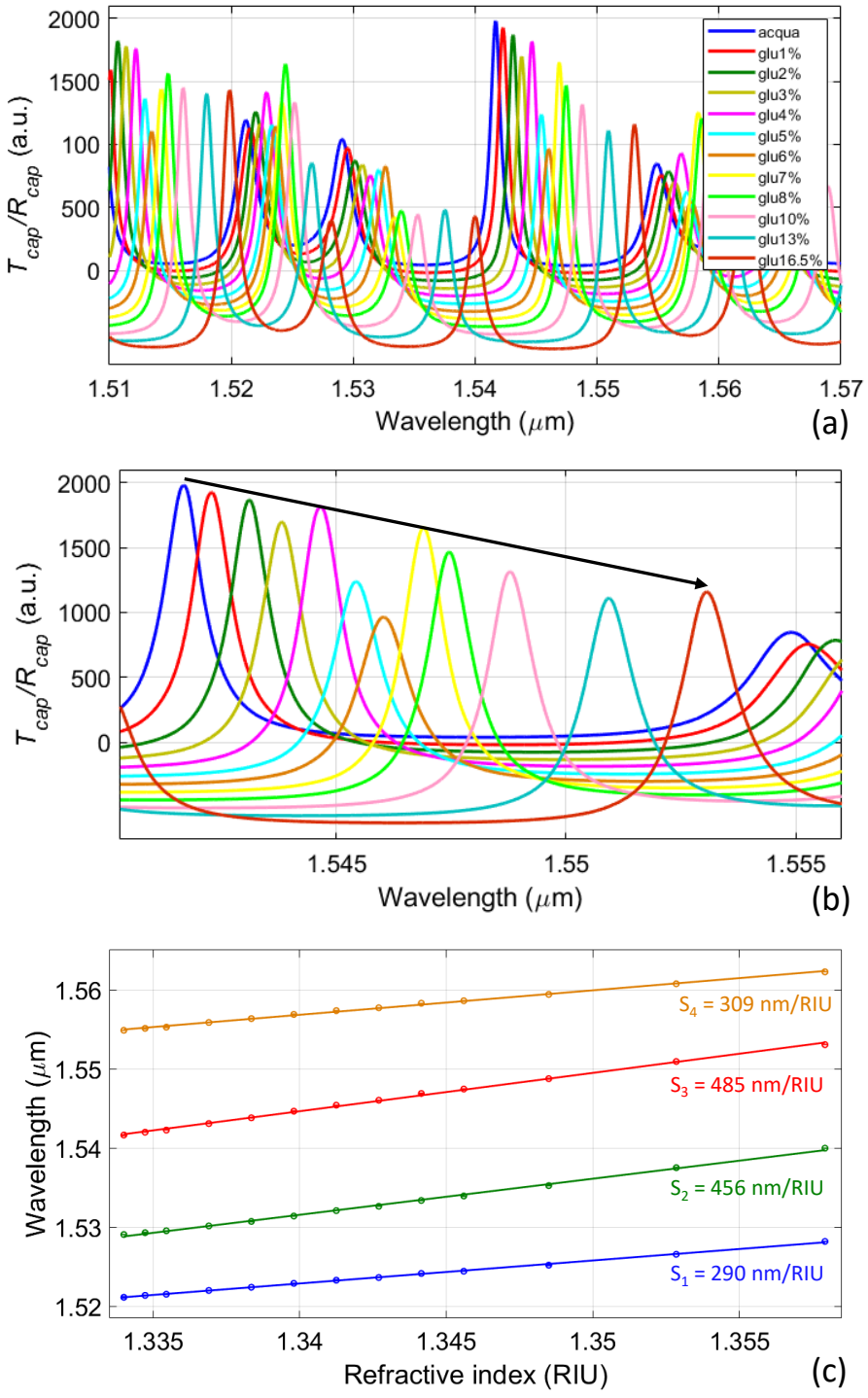

Figure 1.7: Experimental results of T_{cap}/R_{cap} measurements. (a) T_{cap}/R_{cap} spectra relative to water-glucose dilutions with RI from 1.3340 to 1.3579 RIU. Traces have been vertically shifted for a better visualization. The absolute scale, on the y-axis, refers only to the trace relative to water. (b) Zoomed view. (c) Experimental calibration curves of T_{cap}/R_{cap} peaks.

1.4 Principles of optical interferometry and features of spectral phase interferometry

Optical interferometry is a widely employed technique, relying on the well-known physical phenomenon of light interference, demonstrated for the first time in 1803 by Thomas Young [23]: when two coherent light waves (in space and time) with the same frequency interact, the resultant is a wave with amplitude that can range from zero to the sum of the amplitudes of the two waves. During the Nineteenth century, even though a good understanding of interference was reached, interferometry had only few relevant applications because of the limited availability of sources with very narrow emission bandwidth. With the invention of laser in the 1960s, many powerful instruments based on interferometry were developed, able to measure displacement, vibrations and velocity with sub-micrometric resolution [24]. Nowadays, optical laser interferometry is widely exploited in many application fields, ranging from astronomy to engineering metrology, from telecommunications to medicine and biology.
On the other hand, low-coherence interferometry relies on the use of broadband light sources (hence with a short coherence length) to perform measurements of relative distance and relative optical paths. Optical Coherence Tomography (OCT) is a bright example of a well-established technology based on low-coherence interferomtry [25]. It is an imaging technique used to capture two- and three-dimensional images of media constituted of several layers with micrometer-resolution and it is typically exploited for investigation of biological tissues.

1.4.1 Laser interferometry

Figure 1.8 shows the basic scheme of a laser interferometer [26].

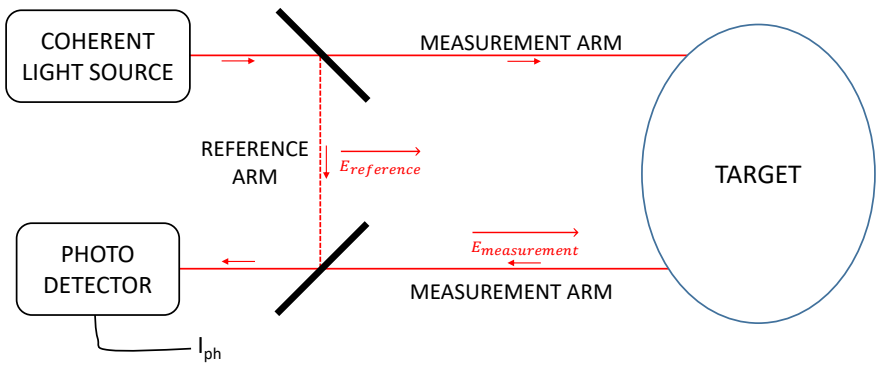

Figure 1.8: General scheme of a laser interferometer.

Light emitted by a highly coherent source in space and time is directed towards the target object or the physical ambient to be sensed (measurement beam). On the other hand, a fraction of the radiation is kept inside the instrument to be used as reference beam. Light reflected by the target is superimposed to the reference radiation onto a photodetector so that the two associated electric field ($\overrightarrow{E_{measurement}}$ and $\overrightarrow{E_{reference}}$, respectively) can interfere. The photogenerated current is given by:

$$\begin{aligned} I_{ph} &= \sigma_{ph} \cdot |\overrightarrow{E_{measurement}} + \overrightarrow{E_{reference}}|^2 = \sigma_{ph} \cdot |E_m \cdot e^{i \cdot \phi_m} + E_r \cdot e^{i \cdot \phi_r}|^2 \\ &= \sigma_{ph} \cdot |E_m \cdot e^{i \cdot (\omega \cdot \tau + k \cdot L_m))} + E_r \cdot e^{i \cdot (\omega \cdot \tau + k \cdot L_r)}|^2 \end{aligned} \tag{1.25}$$

where σ_{ph} is the photodetector responsivity, E_m and E_r are the electric field amplitudes, ϕ_m and ϕ_r are the electric field phases, ω is the pulsation, τ is time and L_m and L_r are the lengths of the measurement arm and reference arm, respectively. Developing Equation 1.25 yields:

$$\begin{aligned} I_{ph} &= \sigma_{ph} \cdot [E_m^2 + E_r^2 + 2 \cdot E_m \cdot E_r \cdot Re\{e^{i(\phi_m - \phi_r)}\}] \\ &= I_m + I_r + 2 \cdot \sqrt{I_m \cdot I_r} \cdot \cos(\phi_m - \phi_r) \end{aligned} \tag{1.26}$$

where I_m and I_r are the currents that the measurement and reference fields would provide individually and the last cosinusoidal term is the interference signal. If the reference phase ϕ_r is kept constant and equal to a know value, then by measuring the variations of the cosine signal it is possible to retrieve how the phase ϕ_m (and hence the measurement path L_m) varies in time.

Laser interferometry is used to measure displacement of a target, surface roughness, surface planarity, angle rectangularity. Another important application is vibrometry, that is the measurement of very small vibrations of a solid body with zero-average around an equilibrium point with a resolution down to fractions of the wavelength. Laser vibrometry allows to study mechanical resonances of bodies and to identify unwanted vibrations that may lead to breaks. It is exploited, for example, in construction industry to monitor the state of maintenance of buildings and in acoustics, to study the features of music instruments. Thanks to its great resolution, laser interferometry is also highly suitable to characterize the mechanical response of nano-resonators (see Appendix A). Last, laser interferometers have been exploited also in the worldwide known LIGO and Virgo experiments for the detection of gravitational waves [27].

1.4.2 Low-coherence interferometry

Another important optical interferometric technology is the low-coherence interferometry, also known as white light interferometry. The general instrumental configuration is the same of Fig. 1.8, but this technique makes use of a broadband radiation such as an LED (Light Emitting Diode) or a SLED or even a white lamp. In white light interferometry, the coherence length L_c of the source plays a fundamental role because it defines the possibility or not of having an interference term in the photodetected current. In particular, it is defined as the value of the difference Δs between the measurement and reference paths that leads to halving of the height of the interferometric fringes and it can be calculated as

$$L_c = \frac{\lambda_e^2}{n \cdot \Delta\lambda_{source}} \tag{1.27}$$

where λ_e is the central emission wavelength, n is the RI of the propagation medium (n = 1 for a free-space interferometer) and $\Delta\lambda_{source}$ is the FWHM emission bandwidth, supposing a source with a Gaussian-like emission spectrum. While the coherence length L_c of a laser source is of several meters, for LEDs and SLEDs $L_c \sim$ 5-50 µm. From a rigorous point of view, the effect of the coherence length for a low-coherence source is taken into account by modifying Equation 1.25 as follows:

$$I_{ph} = I_m + I_r + 2 \cdot \sqrt{I_m \cdot I_r} \cdot |G(\tau)| \cdot \cos(\phi_m - \phi_r) \tag{1.28}$$

where $G(\tau)$ is the autocorrelation function, also called "fringe visibility". The autocorrelation function modulates the amplitude of the cosine signal and according to the Wiener-Khinchin theorem it is related to the emission spectrum of the light source through the Fourier transform [28]. For highly coherent sources, the autocorrelation function can be considered constant and always equal to 1. On the other hand, in white light interferometry, the value of the fringe visibility depends on the value of Δs. In particular, if $\Delta s \gg L_c$, then the value of the autocorrelation function is almost equal to 0: no interferometric fringes are generated and photodetector measures only a constant signal that is the sum of the intensities provided by the reference and measurement beams. On the opposite, if $\Delta s \ll L_c$ (that is, the two interferometer arms are nearly balanced), then the autocorrelation function can be considered equal to 1 and the interferometric cosine signal does appear. In a low-coherence interferometer, the reference mirror is usually mounted on a translation stage, so that it can be moved farther or closer to the target (Figure 1.9).

When the reference path matches the measurement one (i.e. $\Delta s = 0$) the interferometric fringes are generated. Hence, the interferometer can be used to measure the relative distances of the sample.

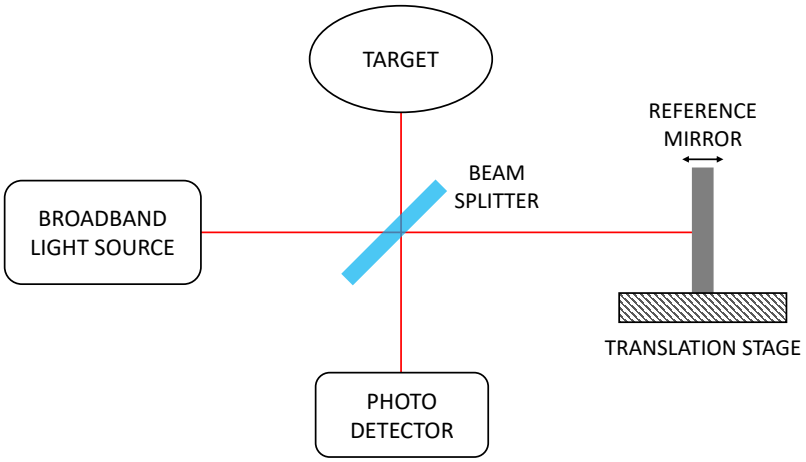

Figure 1.9: Schematic representation of a low-coherence interferometer. Reference mirror is mounted on a translation stage and it can be moved farther or closer to the target.

The low-coherence interferometry is an excellent technique also for the detection of the interfaces or layers that compose the sample under test. For example, Rigamonti et al. exploited an all-fiber Michelson interferometer to detect the glass walls and the inner channel constituting the rectangular glass micro-capillaries presented in Section 1.1 [29, 30]. Measuring the optical path related to the different interfaces and knowing the refractive index of the borosilicate glass, they were also able to measure the wall thickness and the channel depth and check the compliance with the manufacturing tolerances reported by the producer (see Section 1.1).

1.4.3 Instrumental configurations for optical interferometers

Many different instrumental configurations can be considered for the practical implementation of an optical interferometer. Figure 1.10 reports the most common instrumental schemes that are used in commercial products and gave rise also to several variants to improve the final performances. In every scheme the element $\Delta s_{optical}(f)$ represents a generic variation of optical path happening along the measurement arm of the interferometer (that is the variable to be measured) caused by the phenomenon f. f could be a displacement, a vibration, a rotation, a variation of refractive index, for example.

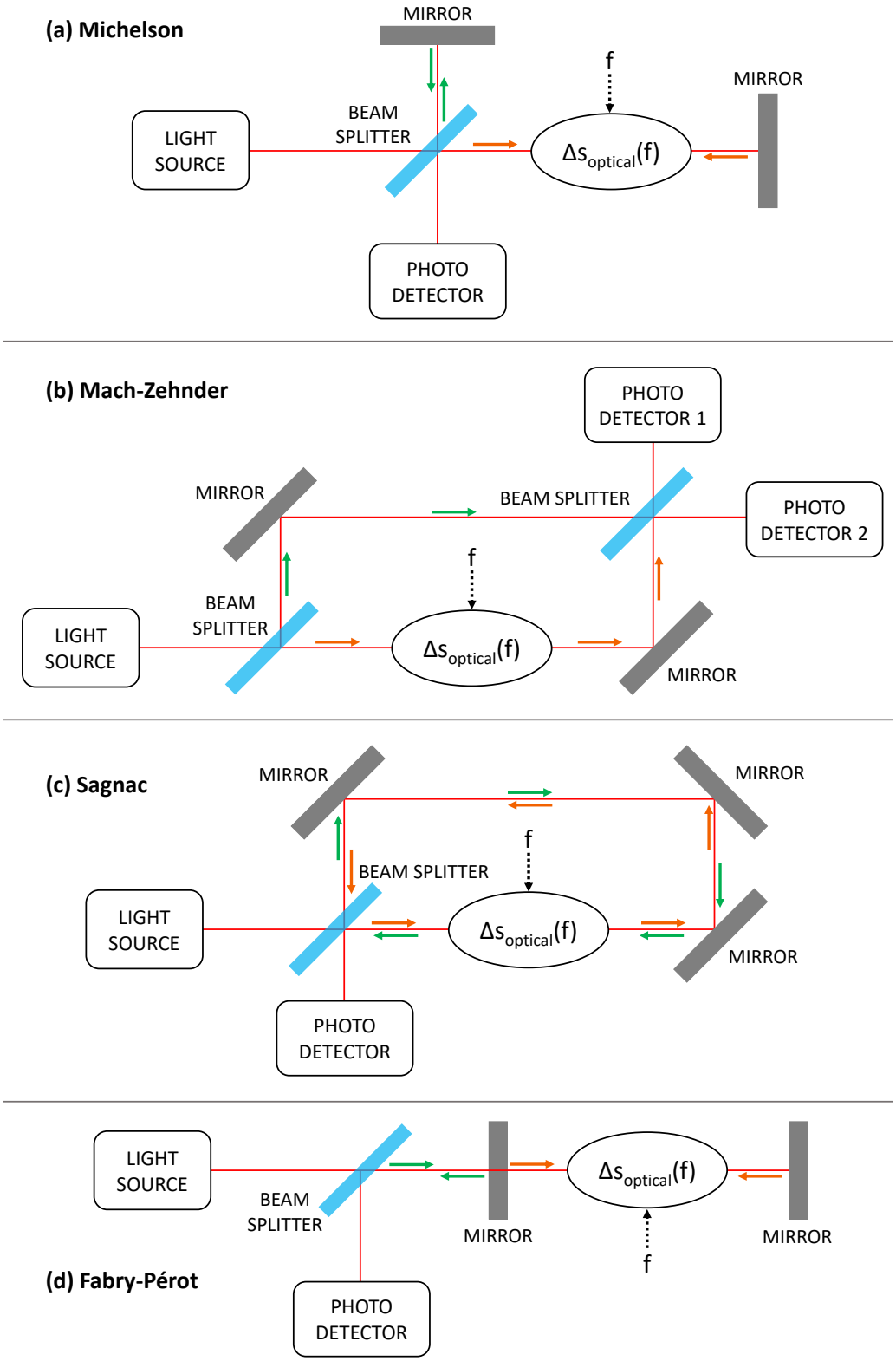

Figure 1.10: Most common optical interferometers and their bulk optics implementation schemes. From these basic configurations, many others have been developed for performance improvement or specific applications. The orange and green arrows indicate the path of measurement and reference beams, respectively.

Widely used today, the Michelson interferometer is the first type of interferometer invented by Albert Michelson in 1887 (Figure 1.10(a)). All modern interferometers have evolved from this first one since it demonstrated how light can be used to make the most sensitive of measurements. In a Michelson interferometers, a beam splitter is used to split light between the reference and the measurement path where the target (or sample) is located. Back-reflected light from the target and the reference mirror is recombined and a photodetector records the interference pattern. The variation of optical path of the target is measured with $\lambda/2$-resolution and, in order to get a precise measurement, the angular alignment of both mirrors and target has to be ensured, which is often a critical point. To solve this issue, the Twyman-Green interferometer, that is a variant of Michelson scheme, can be implemented by substituting the mirrors with corner cubes: here, the reflected beam is returned parallel to the impinging one, regardless of the incidence angle. Similarly, the beam splitter is replaced with a glass cube beam splitter. The Mach-Zehnder interferometer shown in Figure 1.10(b) is a sort of unfold Michelson scheme, where the reference and measurement beam are split and recombined by two different beam splitters. The second beam splitter divides the superposed beams in two halves that are detected by two different photodetectors. In the Sagnac interferometer (Figure 1.10(c)), light is split into two beams by a beam splitter and the reference and measurement beams travel along the same path but in opposite directions (clockwise and counterclockwise). Then, they are recombined by the original beam splitter and interfere on the photodetector. Since the two paths have the same length, the Sagnac interferometer is insensitive to any movements of its optical components: hence it is totally unsuited to measure length variations. However, when the interferometer system is put in rotation, one light beam takes a longer time than the other in order to travel the whole path, resulting in a non-reciprocal phase shift between the two beams. Hence, the Sagnac configuration is used in gyroscopes to measure angular velocity and in magnetic field sensors. Last, the Fabry-Pérot interferometer (Figure 1.10(d)) features two parallel mirrors that define a cavity inside which the optical path variation happens. The first mirror has a reflectivity much smaller than 100% so that a fraction of light (measurement beam) can reach the second mirror. Light that is reflected is kept as reference beam. A typical application of a Fabry–Pérot interferometer is to check whether a laser operates on a single resonator mode or on multiple modes.

1.4.4 Spectral phase interferometry for detection of optical resonances

In this Ph.D dissertation, an innovative interferometric detection method was developed to identify the optical resonances of rectangular glass micro-capillaries presented in Section 1.1 with the goal of monitoring refractive index variations of fluids flowing in the micro-channel. It is based on the study of the spectral phase of the cosine signal in the wavelenght domain generated during the interferometric measurement. Traditional interferometry provides interference signals that are analyzed in the domain of time or temporal frequency: for example, in high-coherence interferometry, the displacement of a target can be estimated by counting the number of the interferometric "fringes", that are the semi-periods of the cosine signal recorded in the time domain. In vibrometry, the vibrations of a body can be studied looking at the interferometric signal in the domain of temporal frequency. Here, a different approach is adopted and the cosine signal is studied in the domain of optical wavelength. Indeed, by analyzing the shape of the spectral cosine signal, it is possible to retrieve the wavelength location of the micro-capillary optical resonances [12, 14]. In particular, the technique based on interferometric phase interrogation was demonstrated for the first time in 1996 at visible wavelengths for measuring the wavelength position of surface plasmon resonances (SPRs) in SPR-based sensors [31]: using a He-Ne laser, the detection was based on the measurement of the relative phase shift of the TM polarized component of the electric field compared with the TE polarized one. Since then, the phase detection method has been widely employed for the investigation of both prism- [32, 33] and fiber-based SPR sensor [34, 35]. Moreover, the configuration presented in this thesis differs from both high-coherence and low-coherence traditional interferometers: indeed, the instrumental configuration set up in this research work does not make use of a light source with a very narrow emission bandwidth (such as a laser), nor a broadband radiation emitted by a lamp. As explained in further details in Section 1.6, here a light source with an emission bandwidth around 40 nm was exploited, but the actual bandwidth to be considered is the resolution bandwidth RB = 0.1 nm set by the optical spectrum analyzer.
In order to detect the wavelength position of the optical resonances of micro-capillaries, the interferometric signal in the wavelength domain must be considered. When having a Michelson interferometer with the micro-device placed at the end of the measurement path and a mirror at the end of the reference path, the interference between the two back-reflected fields yields the typical interferometric signal $I_{interf}(\lambda)$ with a cosine-like profile [26]

$$I_{interf}(\lambda) \propto \cos[\phi_{tot}(\lambda)] = \cos[\phi_{interf}(\lambda) + \phi_{cap}(\lambda)] \tag{1.29}$$

where the total phase $\phi_{tot}(\lambda)$ is given by the sum of $\phi_{cap}(\lambda)$, which is the phase shift related to the capillary reflection coefficient, and $\phi_{interf}(\lambda)$, which is the phase shift contribution due to the difference Δs between the optical path of the interferometer arms, given by

$$\phi_{interf}(\lambda) = 2 \cdot k \cdot \Delta s \tag{1.30}$$

where k is the wavevector as previously defined. Moreover, $\phi_{cap}(\lambda)$ can be retrieved by performing the following calculations:

$$e^{i \cdot \phi_{cap}(\lambda)} = \frac{r_{cap}(\lambda)}{|r_{cap}(\lambda)|} \tag{1.31}$$

$$\phi_{cap}(\lambda) = Im\{\ln \frac{r_{cap}(\lambda)}{|r_{cap}(\lambda)|}\} \tag{1.32}$$

where ln denotes the natural logarithm and Im the imaginary part of a complex number. As explained in further details in the following Sections, from the analysis of the phase of the spectral cosine signal it is possible to clearly detect the number and the wavelength position of the optical resonance of the micro-capillary structure.

1.5 Results of theoretical analysis

In order to better understand the principle of operation of the spectral interferometric method and its theoretical performances, the model explained in Section 1.2 was further extended in MATLAB environment with the addition of the equations presented in Section 1.4.4: numerical analyses were performed to calculate the line-shape of the cosine signal when spectral phase interferometry is used for the recognition of optical resonances and to obtain a theoretical estimation of the sensitivity when the micro-opto-platform is exploited for RI sensing. Moreover, simulations for an empty capillary were also repeated by adding a Gaussian noise term to the data, in order to better simulate a laboratory condition.

1.5.1 Theoretical evaluation of spectral phase interferometry for resonances detection

Theoretical studies were carried out by first considering a micro-capillary with nominal dimensions $t_f = d = t_b = 50$ μm and empty channel (i.e. filled with air). Simulations were carried out supposing an infinitely small (ideally equal to 0) resolution bandwidth; glass RI dependence on the wavelength has been taken into account through interpolation of data obtained from the literature [36]. RI of air was considered constant and equal to 1.The spectral reflectivity $R_{cap}(\lambda)$ calculated for this micro-device is reported in Figure 1.11(a) in the wavelength range from 1.52 to 1.58 μm. The spectrum exhibits maxima and minima at wavelength positions that depend on the geometrical parameters of the micro-device and on the RI of the walls and of the substance filling the channel. In particular, for an empty channel, each spectral minimum is located exactly at a wavelength position that corresponds to a resonance of the capillary structure. Making a comparison with the results reported in Section 1.3 and obtained for a capillary with the same structure but with different dimensions ($t_f = t_b = 21$ μm, $d = 30$ μm), it can be noticed that the line-shape and the number of resonances of the reflectivity signal is very different for the two micro-devices: indeed, it was demonstrated that these features depends on the dimensions of the wall and of the inner channel [18, 19]. In particular, the number of optical resonances increases for thicker micro-devices. Since the actual dimensions could be different from the nominal values, the simulations were repeated also considering the highest error tolerances reported by the manufacturer. Figure 1.11(b) shows how the shape of the spectral reflectivity does change when considering two extreme cases corresponding to geometrical dimensions far from nominal values: +20% for both wall thicknesses and +10% for channel depth (dashed trace) or –20% for both wall thicknesses and −10% for channel depth (dotted trace). The solid black trace corresponds to the result obtained by considering nominal dimensions as in Figure 1.11(a). Figure 1.11(c) compares the spectral behavior of the interferometric cosine signal (black trace) provided by Equation 1.25, assuming $\Delta s = 140$ μm, with the capillary reflectivity (red trace). From the comparison, it can be noticed that the interferometric signal exhibits very steep jumps corresponding to sharp phase changes at wavelengths where reflectivity minima are located. In order to enhance the steep variations, the derivative of the cosine signal with respect to the wavelength was computed and its absolute value is plotted as a function of the wavelength in Figure 1.11(d). Hence, the wavelength position of the resonances can be identified as narrow peaks of the derivative signal rather than as broad minima of the spectral reflectivity signal.

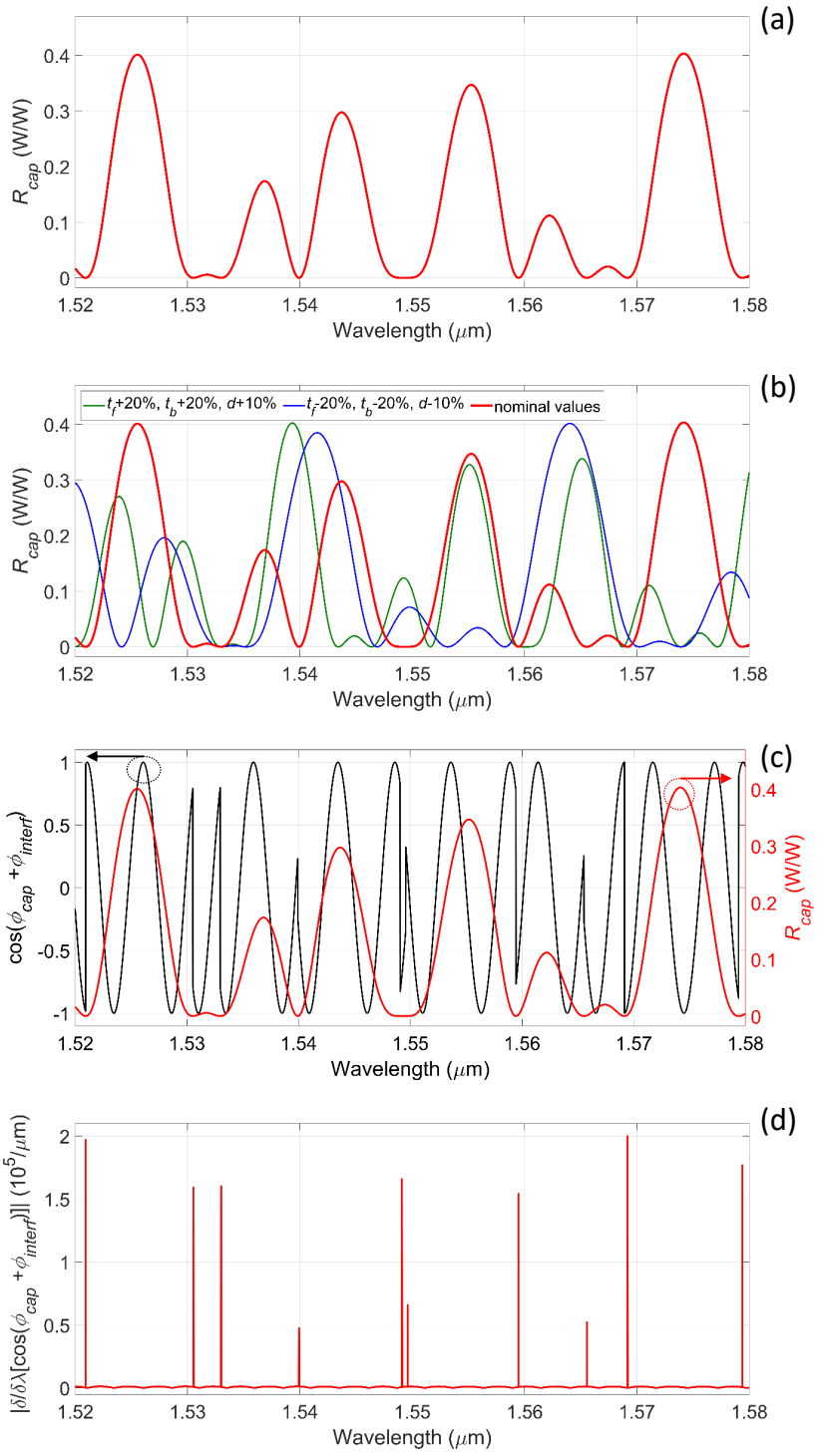

Figure 1.11: Results of theoretical analysis carried out on an empty micro-capillary with t_f = d = t_b = 50 µm. (a) Spectral reflectivity $R_{cap}(\lambda)$ of the capillary. (b) Comparison between spectral reflectivities $R_{cap}(\lambda)$ of capillaries with different geometrical parameters: t_f = d = t_b = 50 µm (red trace), t_f = t_b = 50 µm 50 µm + 20% variation and d = 50 µm + 10% variation (green trace),t_f = t_b = 50 µm - 20% variation and d = 50 µm - 10% variation (blue trace). (c) Cosine interferometric signal (black trace), characterized by steep phase jumps (red trace). (d) Absolute value of the cosine derivative with respect to the wavelength.

1.5.2 Effect of Gaussian noise addition

In order to better model an experimental situation, the theoretical analysis on the empty micro-capillary (with same nominal dimensions) was also repeated by adding a term of random white Gaussian noise to the overall reflection coefficient of the capillary itself $R_{cap}(\lambda)$, using the MATLAB function $awgn$ [13] and specifying as inout parameter a signal-to-noise ratio of 30 dB. Results are shown in Figure 1.12.

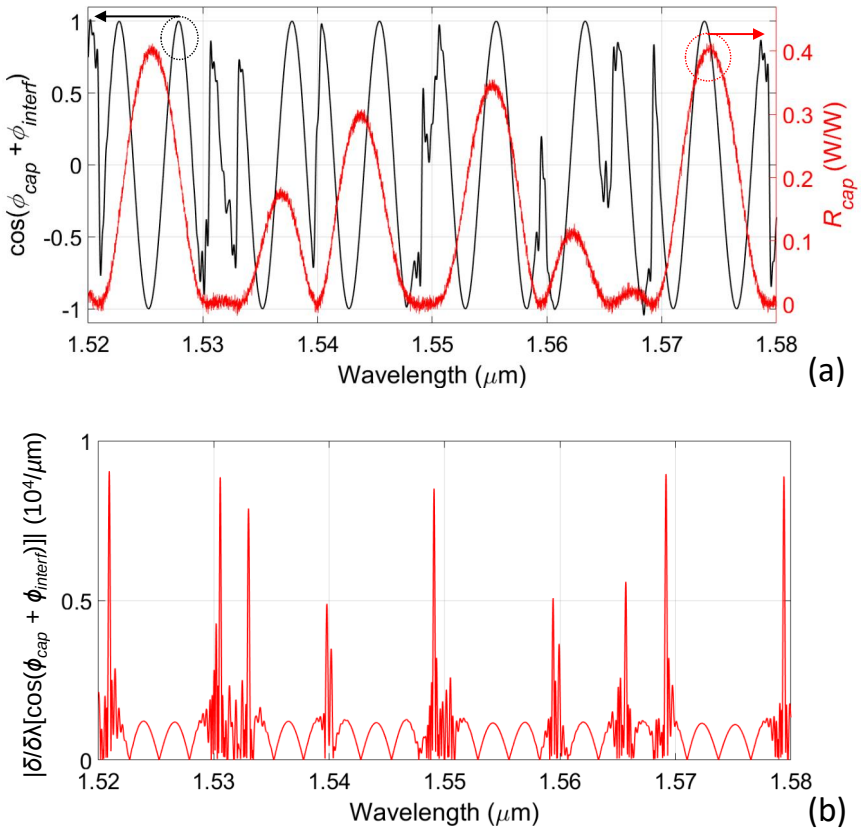

Figure 1.12: Results of analytical simulations obtained by adding white Gaussian noise to the reflectivity spectrum R_{cap}. (a) "Noisy" capillary reflection (red trace) in comparison with "noisy" cosine signal (black trace). (b) "Noisy" derivative signal: the position of the resonances is still clearly detectable.

Figure 1.12(a) shows the "noisy" capillary reflectivity (red trace) in comparison with the "noisy" cosine signal (black trace) that has been processed with a digital low-pass Butterworth filter, by analogy to the data processing that was done on experimental data. Amplitude fluctuations affect now the R_{cap} signal and the position of its minima is now less easy to identify with respect an ideal situation, in particular for very close resonances. On the other hand, the cosine signal

still exhibits well-defined phase jumps in correspondence of almost all the micro-capillary resonances. Computing the derivative (Figure 1.12(b)), it can be noted that the amplitude of the peaks is only one order of magnitude smaller than in the ideal case when no noise is considered (Figure 1.11(d)). In addition, the FWHM of the theoretical derivative peaks before and after considering the presence of noise was computed. For the theoretical maxima obtained before adding the white Gaussian noise, the FWHMs are limited by the wavelength step (10 pm) used to carry out the simulations. Supposing an ideal sampling with an infinite number of points, the FWHM of each peak would be equal to 0. On the other hand, for the theoretical peaks obtained after adding the noise, the FWHMs have finite values (due to the noise effects) of the order of 200 pm.

1.5.3 Theoretical evaluation of spectral phase interferometry for refractive index sensing

Since the main goal of this research was the exploitation of spectral phase interferometry for refractive index sensing of liquids in rectangular micro-capillaries, theoretical simulations were repeated by considering the same micro-device filled with liquid samples, in order to investigate the performances of such innovative readout technique. For the fluids filling the channel, RI were considered equal to 1.33400, 1.33545, 1.33690, 1.33835, 1.33980, 1.34270, 1.34560 and 1.34850 RIU, values that can be obtained by means of water-glucose solutions with concentration 0, 1, 2, 3, 4, 6, 8 and 10%, respectively. The refractive index of the samples where considered constant with the wavelength because of the complexity of finding reliable values in the literature. Theoretical results are reported in Figure 1.13. Figure 1.13(a) shows the theoretical cosine signals for different sample RIs. As stressed by the black arrow, they undergo a spectral red-shift as the sample RI increases; moreover, the line-shape of the phase jumps can change for different samples. The steep phase variations can be better detected by computing the absolute value of the cosine derivative with respect to the wavelength (Figure 1.13(b)). As it can be better observed in the zoomed view of Figure 1.13(c), the derivative peaks can have a very different absolute amplitude due to the different shape of the phase jumps: nevertheless, the automatic detection of the derivative peaks is not negatively affected. By linearly fitting the wavelength position of the derivative peaks as a function of the sample refractive index, the theoretical calibration curves of the micro-opto-fluidic platform for RI sensing based on spectral phase interferometry were retrieved (Figure 1.14). Theoretical values of sensitivity S, defined as the spectral shift of the derivative peak $\Delta\lambda$ for a certain variation

of refractive index Δn ($S = \Delta\lambda/\Delta n$), were found in the range 324-412 nm/RIU.

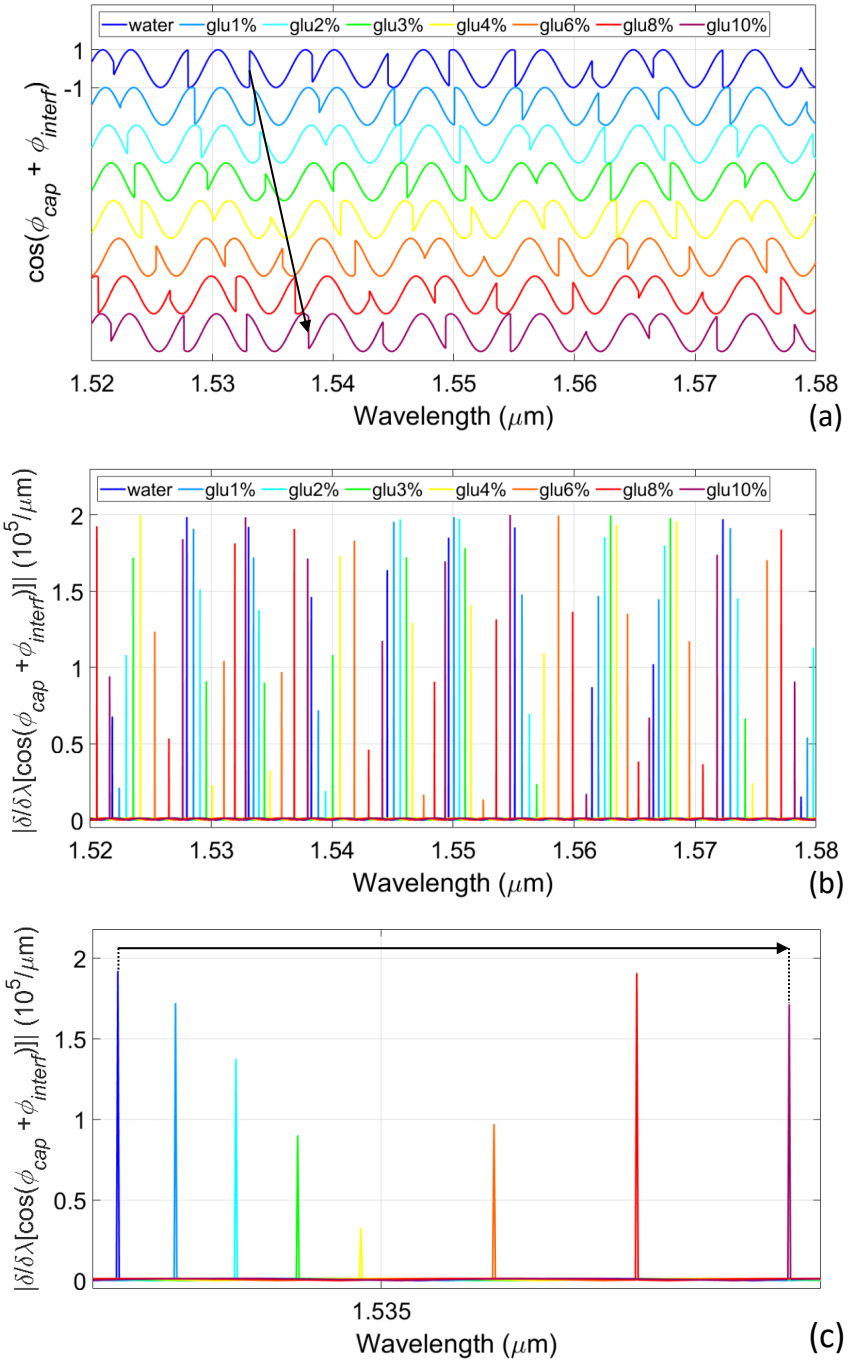

Figure 1.13: Theoretical results obtained by simulation of a micro-capillary with $t_f = t_b = d =$ 50 µm filled with samples with RIs varying from 1.3340 to 1.3485 RIU. (a) Cosine signals shift towards higher wavelength when the sample RI increases. (b) Derivative signals with respect to the wavelength with a zoomed view (c): the spectral shift of phase jumps can be monitored more easily.

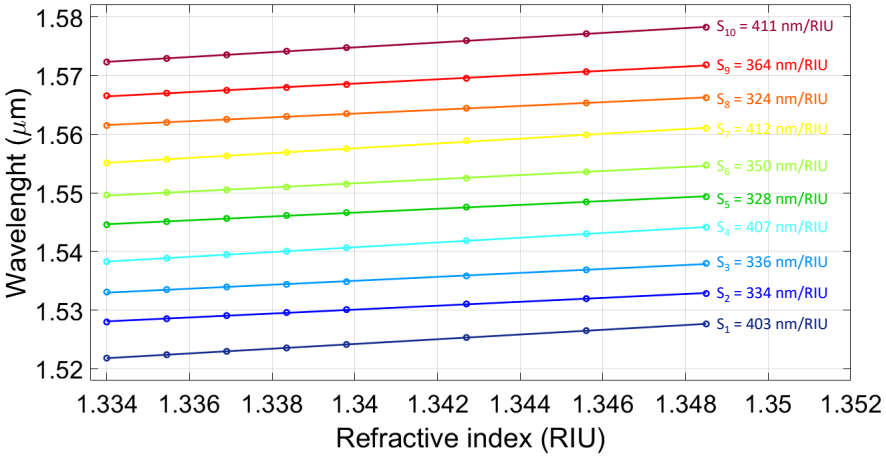

Figure 1.14: Theoretical calibration curves.

1.6 Micro-opto-fluidic configuration for experimental measurements

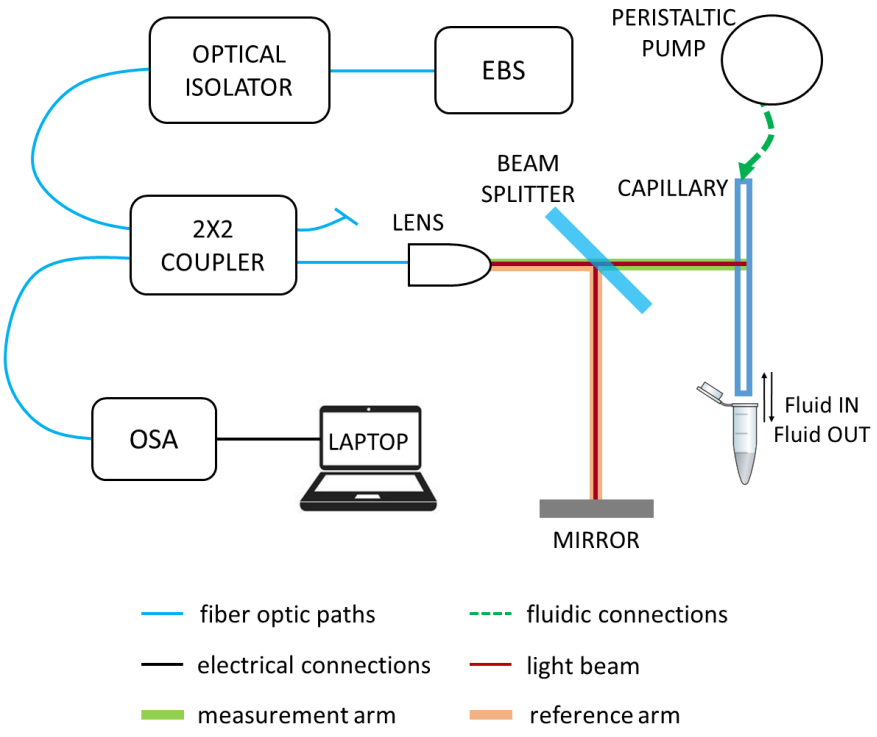

Figure 1.15: Block diagram of the instrumental configuration including a Michelson interferometer for experimental testing. EBS: broadband source. OSA: optical spectrum analyzer.

Experimental measurements were performed in order to verify the theoretical analysis. First, the interferometric spectral readout configuration was exploited to detect and measure the wavelength positions of the optical resonance of micro-capillaries. Afterwards, simply by adding one component for liquid sample handling, the same setup was used also to carry out refractive index measurements in micro-capillaries with high sensitivity. Figure 1.15 reports the block diagram of the micro-opto-fluidic configuration employed for experimental measurements. The micro-capillary is positioned vertically and glued to a metallic frame support to improve its rigidity and avoid unwanted vibrations of the micro-device. Light in the near-infrared region with average power density of 0.12 mW/0.1 nm is emitted by a diode-pumped Er3+-doped fiber Broadband Source (EBS-4022, MPB Technologies Inc., Canada). Its output spectrum (shown in Figure 1.16) is characterized by a 40-nm emission bandwidth, as FWHM, centered at the wavelength of 1550 nm.

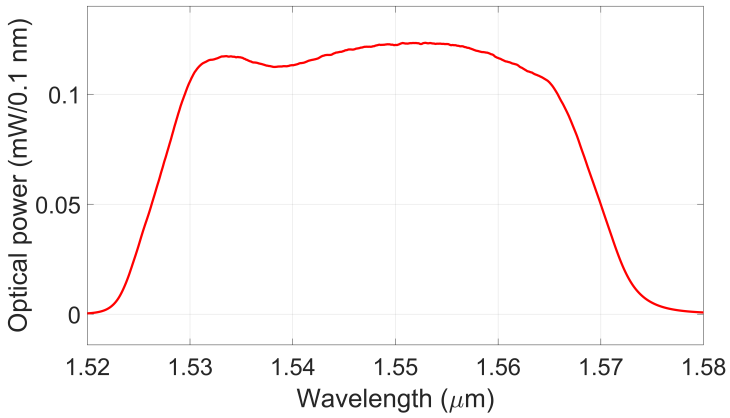

Figure 1.16: Emission spectrum of the EBS light source.

The emitted radiation is coupled into a standard telecommunication single-mode optical fiber (9/125 core/cladding diameter, SM-R/KR, Pirelli Cavi, Italy) and guided through a fiber optical isolator (to protect the source from unwanted back-reflections) towards an input port of a 2×2 fiber-optic coupler (BXC15, Thorlabs, NJ, USA) with 50:50 splitting ratio. One output port of the coupler ends with an aspherical lens (LPF-04-1550-9/125-S-5-23.5-3.9AS-60-3A-3-1, OzOptics, Canada) with working distance of 23 mm. The unused output port of the coupler was terminated with an angled connector to avoid spurious back reflections. The low-divergence beam travels in free space and reaches a 4-mm-thick glass slab acting as a beam splitter since it is oriented at 45° with respect to the incoming beam axis. About 96% of light is transmitted at each interface of the beam

splitter: consequently, about 92% (96% $\times$ 96% $\approx$ 92%) of the readout radiation crosses the glass slab and reaches the flat side of the micro-capillary, traveling along the measurement path of the Michelson interferometer. A small fraction (approximately 4%) of the radiation that is shined onto the beam splitter is reflected by the first air–glass interface at an angle of 90° and it is redirected along the reference arm of the interferometer toward an Al-coated mirror (ME05S-G01, Thorlabs, NJ, USA). The light reflected from the second glass–air interface of the slab does not reach the mirror. During the experiments with liquid samples, the fluids fill the channel by capillary action and they are then discarded with the aid of a peristaltic pump connected to the upper end of the micro-device with a luer adapter and a plastic tube. Beams back-reflected by the capillary and the mirror are recombined on the same axis by the beam splitter and redirected toward the lens for fiber coupling. Collected light is detected with an optical spectrum analyzer (OSA Agilent 86142B, Agilent Technologies, CA, USA) that allows recording of amplitude spectra as well as of interferometric signal due to beating between the measurement and reference beams, with a resolution bandwidth RB = 0.1 nm. The OSA is connected to a laptop for data acquisition via a LabVIEW interface. Data are acquired as Excel files and subsequently processed through a MATLAB routine.

1.7 Experimental results

In order to verify the validity of the theoretical analyses and demonstrate the principle of operation of the spectral phase interferometry as well as its suitability for refractive index monitoring of liquids, experimental measurements were performed on a rectangular glass micro-capillary using the instrumental configuration presented in Section 1.6. First the optical resonances of the micro-devices were identified. Afterwards, by filling the micro-channel with liquid samples and following the wavelength shift of the abrupt phase jumps, the phase interferometry technique was exploited for the measurement of refractive index changes with respect to a reference fluid.

1.7.1 Detection of the optical resonances of the micro-capillary

First, the optical resonances of a glass micro-capillary with nominal dimensions $t_f = t_b = d$ = 50 μm were measured exploiting spectral phase interferometry. The wavelength dependence of the experimental photodetected interferometric signal is given by the expression

$$I_{interf\ exp}(\lambda) = I_{cap}(\lambda)+I_{mirror}(\lambda)+2\cdot V\cdot[I_{cap}(\lambda)\cdot I_{mirror}(\lambda)]^{1/2}\cdot\cos[\phi_{tot}(\lambda)] \quad (1.33)$$

where $I_{cap}(\lambda)$ is the signal intensity only due to the capillary reflection, $I_{mirror}(\lambda)$ is the signal intensity only due to the mirror reflection, $\phi_{tot}(\lambda)$ is the total phase as mentioned in Equation 1.29 and V is the fringe visibility, a parameter that is controlled by the autocorrelation function of the readout light, as previously explained. V can be assumed to be equal to 1 if the unbalance between the lengths of the two interferometer arms Δs is much shorter than the coherence length L_c of the photodetected light. L_c can be computed substituting in Equation 1.27 the values λ_e = 1550 nm and n = 1; moreover, $\Delta\lambda$ to be considered in the calculation is the resolution bandwidth of the OSA RB = 0.1 nm. In this condition, L_c = 24 mm. Since in the experimental measurements the Michelson interferometer is operated in quasi-matching condition (i.e. $\Delta s \approx 0$), then $L_c \gg \Delta s$ and V can be considered equal to 1. Signals were acquired by the OSA in the following sequence. First, $I_{cap}(\lambda)$ was collected by blocking the reflection coming from the reference mirror. Then, the signal $I_{mirror}(\lambda)$ was recorded by blocking the signal coming back from the capillary. Eventually, the overall interferometric signal $I_{interfexp}(\lambda)$ containing the interference contribution was collected. During each measurement the position of the mirror was kept fixed to maintain the quasi-matching condition. After acquisitions, data were processed and the cosine signal was retrieved as

$$\cos[\phi_{tot}(\lambda)] = \frac{I_{interf\ exp}(\lambda) - I_{cap}(\lambda) - I_{mirror}(\lambda)}{2\cdot[I_{cap}(\lambda)\cdot I_{mirror}(\lambda)]^{1/2}} \quad (1.34)$$

The results of the experimental measurements carried out on an empty micro-capillary are reported in Figure 1.17 and Figure 1.18. All the signals were acquired with wavelength steps of 10 pm and resolution bandwidth of 0.1 nm. Figure 1.17(a) reports the power spectrum $I_{cap}(\lambda)$ due to the capillary only (red trace), the interferometric signal $I_{interfexp}(\lambda)$ (black dotted trace), and the power spectrum $I_{mirror}(\lambda)$ (blue trace) due to the reference mirror only with constant amplitude over the spectral range of interest. The spectral line-shape of the experimental power reflected by the capillary is in substantial agreement with the theoretical behavior, shown in Figure 1.11(a), in terms of the number of minima and maxima in the selected span and the sequences of peaks with different amplitudes. Discrepancies between experimental and theoretical spectra are due to the effective values of the capillary dimensions, very likely not coincident with the nominal values considered in the simulations, due to fabrication tolerances. Moreover,

the interferometric signal is very similar to the reflectivity spectrum since the inteferometer was operated in quasi-matching condition (i.e. with short mismatch between arm lengths): hence the period of the interferometric signal is quite large and comparable to the periodicity at which the resonances of the $I_{cap}(\lambda)$ signal occur. Figure 1.17(b) and Figure 1.17(c) reports two examples of interferometric cosine signal retrieved by applying Equation 1.34 (black traces). The two signals exhibit a different number of fringes since they were obtained by slightly translating the position of the mirror: in particular, the trace of Figure 1.17(c) has a lower number of fringes and it was retrieved by slightly reducing the mismatch Δs. Figure 1.17(c) reports also a filtered version of the cosine signal (blue trace): indeed, a digital low-pass filter was implemented to get rid of spurious spectral ripple, very likely coming from unwanted internal reflections. The applied filter, implemented in MATLAB code, is an infinite impulse response (IIR) Butterworth low-pass filter with a cut-off λ^{-1} at 3000 μm^{-1} and an order of 10. The cosine signals are directly compared with the power spectrum $I_{cap}(\lambda)$ (red trace) due to the capillary only. In both examples, the interferometric cosine signals exhibit sharp amplitude jumps due to steep phase changes at the same wavelength positions where reflectivity minima, and thus resonances, are located, in agreement with the theoretical hypotheses. Hence, it was demonstrated that the presence of the phase jumps is not a spurious or random interferometric effects, but they are due to the presence of the optical resonances. Moreover, the position of the abrupt phase variation for a certain resonance is always the same and does not change for different periods of the fringes, meaning that it does only depend on the resonance wavelength.

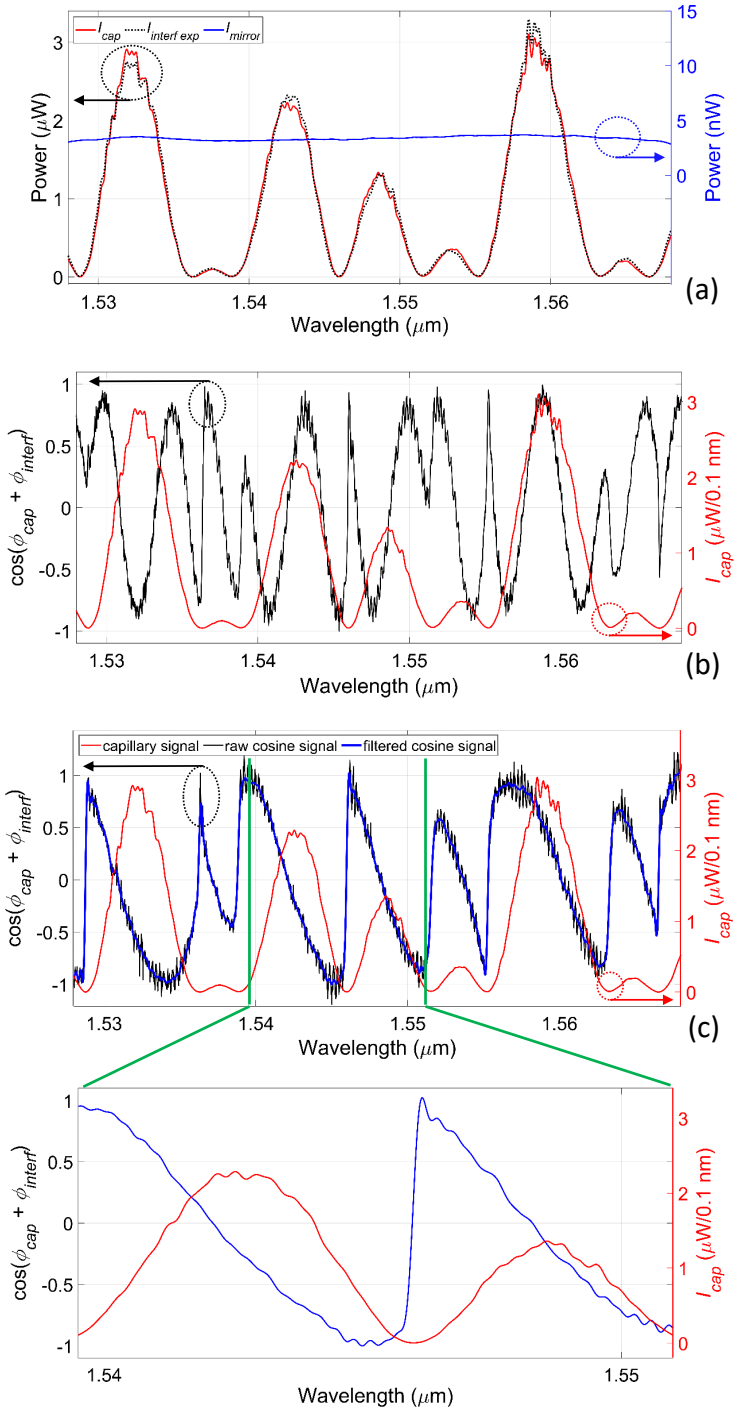

Figure 1.17: Experimental results for an empty micro-capillary with $t_f = t_b = d = 50$ µm. (a) Typical experimental signals: reflectivity spectrum of the capillary (red trace), interferometric signal (black dotted trace) and reflection from the reference mirror (blue trace). (b) Example of a cosine interferometric signal (black trace) with visible fringes directly compared with the capillary spectral reflectivity (red trace). (c) Example of a cosine interferometric signal (black trace) with a lower number of fringes (with a zoomed detail) obtained by reducing the arm mismatch compared with capillary spectral reflectivity (red trace); the blue trace is a filtered version of the same interferometric signal.

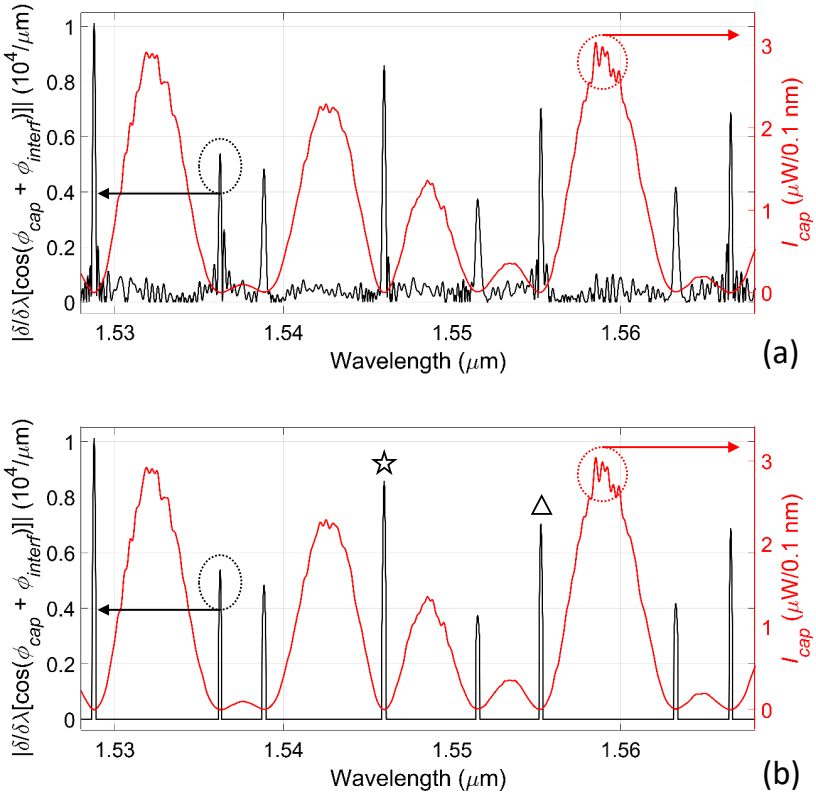

Figure 1.18: Experimental results for an empty micro-capillary with $t_f = t_b = d = 50$ µm. (a) Absolute value of the derivative (black trace) with respect to the wavelength of the filtered cosine signal reported in Figure 1.17(c): very sharp peaks are located in correspondence of the optical resonances. Red trace: capillary spectral reflectivity. (e) Absolute value of the derivative (black trace) after thresholding to better visualize the sharp peaks. Red trace: capillary spectral reflectivity.

By calculating the derivative of the cosine signals with respect to the wavelength and computing the absolute value, the steep amplitude variations due to phase jumps are strongly enhanced, appearing as sharp peaks as a function of the wavelength (Figure 1.18(a), black trace). The sharp peaks allows to clearly and easily identify the resonances of the capillary reflection spectrum (red trace). To eliminate low amplitude components of the derivative (not relevant for the phase detection of the resonances), a threshold was set to 2700 µm^{-1} and the signal components lower than the threshold were zeroed (Figure 1.18(b)). To check the reliability of the phase-based detection method, the wavelength positions of the spectral minima and of the derivative peaks were calculated and compared. For example, the derivative peak indicated by the star in Figure 1.18(b) and the corresponding reflectivity minimum are both found at $\lambda = 1546.0$ nm. Again in Figure 1.18(b), for the resonance indicated by the triangle, the derivative peak is found at $\lambda = 1555.25$

nm, while the wavelength position of the reflectivity minimum on the spectrum is found at $\lambda = 1555.27$ nm. The comparison was studied for all the micro-capillary resonances in the wavelength range of interest, revealing a high level of agreement between the results obtained by applying the two methods (the spectral one and the interferometric one, respectively). Thus, it was demonstrated that the spectral phase interferometry is a reliable method for detection of the optical resonances.

1.7.2 Application of spectral phase shift interferometry for refractive index sensing

After the characterization of the micro-device resonances, the same capillary with geometrical dimensions $t_f = t_b = d = 50$ μm previously tested with empty channel was used to perform experimental measurements on liquid samples in order to develop a spectral phase interferometric readout to measure variations of real part of the refractive index of fluids with respect to a reference substance. As described in Section 1.6, the fluid enters the channel simply by capillary action thanks to its micrometric depth and then it is discarded with the aid of a peristaltic pump (Minipuls2, Gilson, WI, USA) connected to the upper end of the capillary. All tests were carried out in static conditions, that is, with the fluid in steady condition inside the micro-channel. It is important to stress that this readout method is remote, non-invasive, contactless and totally safe for the sample under test. Moreover, the choice of working in the NIR region allows to use well-established standard optical components (such as optical fibers and sources) that have been traditionally developed for telecommunication applications and are now available at reasonable costs. First, to obtain a calibration of the micro-opo-fluidic platform, water-glucose dilutions were tested in concentration of 0 (water), 1, 2, 3, 4, 5, 10% and corresponding to RI values of 1.3340, 1.3351, 1.3363, 1.3372, 1.3387, 1.3398, and 1.3468 RIU, respectively. The solutions were obtained by diluting a glucose-water mixture of 10% concentration (Eurospital S.p.A., Italy) with deionized water. The interferometric signal $I_{interf\ exp}(\lambda)$, the capillary signal $I_{cap}(\lambda)$, and the mirror signal $I_{mirror}(\lambda)$ were acquired for every sample filling the micro-device and the cosine signal was retrieved by applying Equation 1.34. Experimental results of water-glucose solution testing are shown in Figure 1.19, Figure 1.20 and Figure 1.21. Figure 1.19(a) reports the capillary reflected power $I_{cap}(\lambda)$ for glucose–water dilutions at concentrations 1% and 5% (black trace and blue trace, respectively) and the interferometric signal $I_{interf\ exp}(\lambda)$ for both concentrations (gray dotted trace: glucose 1%; cyan dotted trace: glucose 5%): in particular, the signals related to the higher concentration sample are shifted toward higher wave-

length values (as highlighted by the red arrow in the figure), since the resonance positions depend on the geometrical dimensions of the micro-capillary and on the RI of the liquid filling the channel. Hence, by following the wavelength shift of the resonance positions, it is possible to retrieve the RI variation of the sample with respect to the reference fluid. For every sample analyzed, the interferometric cosine signal was retrieved and filtered with the same IIR Butterworth filter previously described: in particular, Figure 1.19(b) shows the cosine signal for a sample with 2% glucose concentration (black trace) in comparison with the correspondent capillary signal (red trace). In agreement with the behavior observed for the empty capillary, abrupt phase variations occur at the same wavelength positions where reflectivity minima of the signal $I_{cap}(\lambda)$ are located.

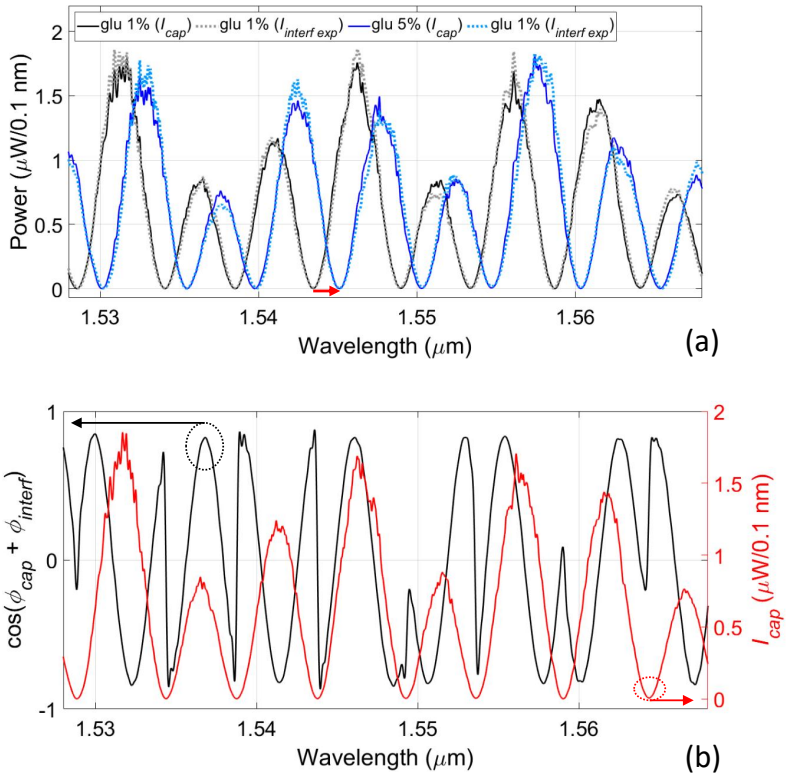

Figure 1.19: Experimental results obtained by filling the capillary channel with glucose–water dilutions. (a) Capillary signal for glucose 1% and glucose 5% (black trace and blue trace) and interferometric signal for glucose 1% and glucose 5% (gray dotted trace and cyan dotted trace). (b) Example of a cosine signal (black trace) directly compared with the capillary spectral reflectivity (red trace). Both signals were obtained with a water–glucose sample in concentration 2% filling the micro-capillary. The steep phase jumps are clearly recognizable in correspondence of the reflectivity resonances.

In Figure 1.20(a), the cosine signals related to the tested samples are reported

(traces would be all superposed, but they have been vertically shifted for a better visualization). The position of the phase jumps shifts toward higher wavelength when the sample concentration increases. In view of a better automatic recognition, the derivatives of the cosine signals with respect to the wavelength was computed and its absolute value was calculated: they are reported in Figure 1.20(b). Here, the steep phase jumps are converted in sharp peaks that can be easily recognized also by an automatic algorithm. Figure 1.20(c) reports a 2D view of the 3D representation of the cosine derivatives, where the signal amplitude is expressed in false color scale. This graph offers a better visualization of the derivative peak shifts when the concentration (and thus also the RI) of the sample increases.

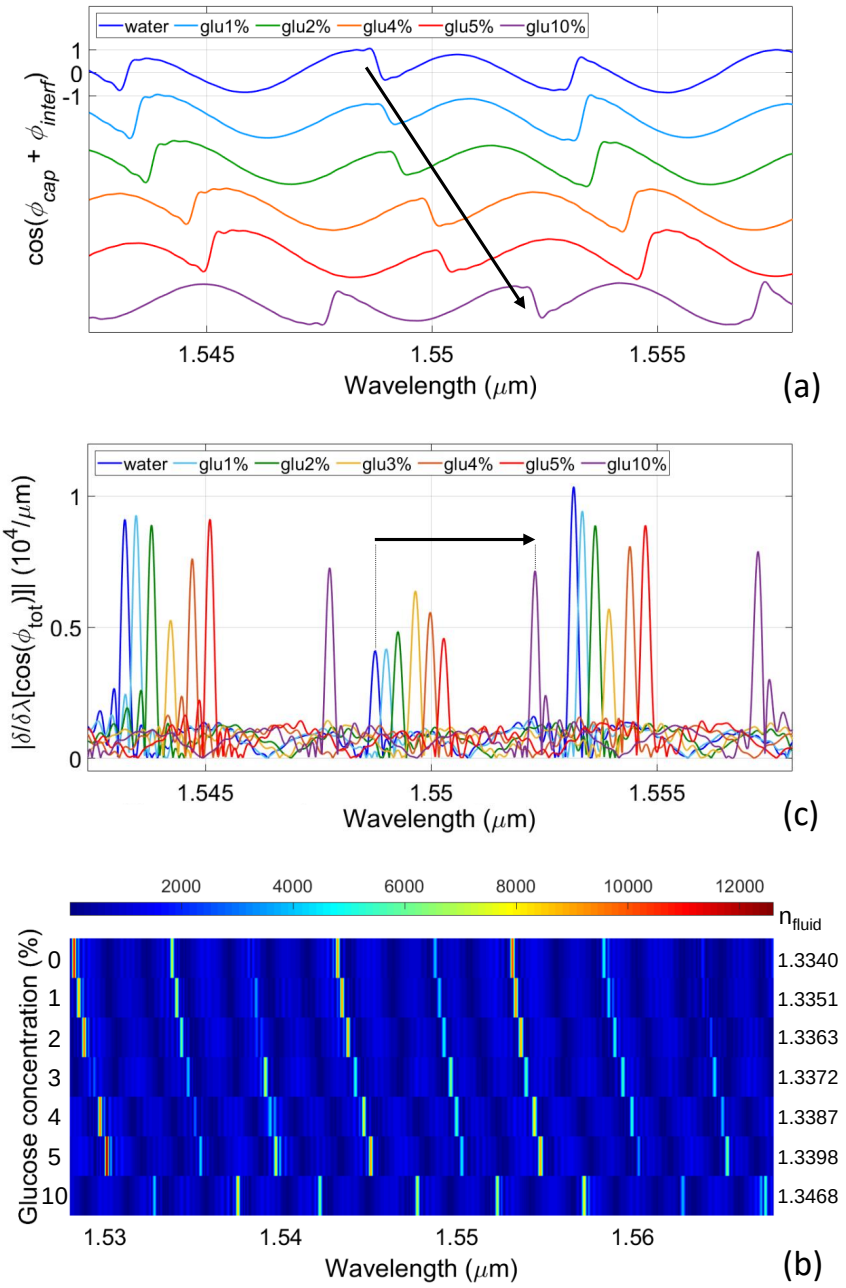

Figure 1.20: Experimental results obtained by filling the capillary channel with glucose–water dilutions. (a) Cascade of the cosine interferometric signals acquired by flowing in the micro-capillary glucose dilutions in water. The scale on the y-label refers only to the water cosine signal; all the other traces were vertically shifted for a better visualization. The black arrow indicates the shift underwent by phase jumps for increasing values if RI. (b) Absolute value of the cosine derivatives with respect to the wavelength. The black arrow indicates the shift of the derivative peaks for increasing values of RI. (c) 2D view of the 3D plot of the cosine signals derivatives. Amplitude values are represented using false colors, indicated on the top of the graphs.

By best fitting the wavelength position of the derivative peaks as a function of the

sample RI with a linear relation, the calibration curves of the micro-opto-sensing platform with spectral interferometric readout were obtained and they are reported in Figure 1.21 together with their equation and coefficient of determination R^2. Sensitivity S values in the range of 284–362 nm/RIU were obtained and the smallest LoD was found equal to $9.72 \cdot 10^{-5}$ RIU. The values of experimental sensitivity are slightly lower than the theoretical value reported in Section 1.5.3. This small mismatch could be due to the fact that the actual dimension of the micro-capillary likely differ from the nominal values that were considered in the analytical simulations.

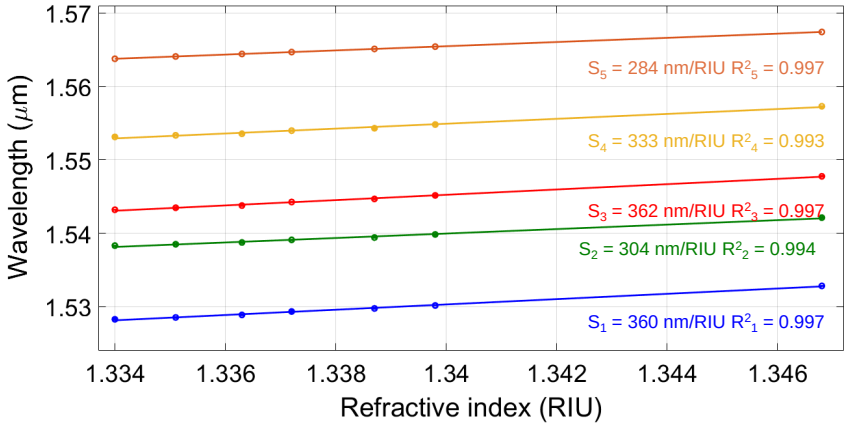

Figure 1.21: Linear calibration curves obtained by filling the micro-channel with water-glucose dilutions. Sensitivity was found in the range 284-362 nm/RIU, in agreement with the theoretical predictions.

Afterwards, to empirically verify the reliability of the measured LoD, other experiments were carried out by filling the capillary channel with distilled water and saline solution (Alcon Laboratories, Inc., FortWorth, TX, USA) [13]. The RIs of these samples, measured at room temperature by means of an Abbe refractometer at a wavelength of 566 nm, were found to be n_{H2O} = 1.3340 RIU and n_{saline} = 1.3345 RIU: thus, their RI difference is very small and equal to $\Delta n_{sal} = 5 \cdot 10^{-4}$ RIU, value that is very close to the LoD that was previously found equal to $9.72 \cdot 10^{-5}$ RIU. Even if in the NIR region the absolute RI values are not exactly the same as in the visible region, their RI difference is very likely of the same order of magnitude. The results of this test are reported in Figure 1.22. Figure 1.22(a) reports the spectral power reflected from the capillary for water and saline solution (black trace and dotted black trace, respectively) in comparison with the filtered cosine signals retrieved by applying Equation 1.34 (red trace: water; blue trace: saline solution). The cosine signal related to saline solution is slightly red-shifted

with respect to the same kind of signal achieved with water filling. The shift can be better appreciated by computing the cosine derivative, shown in figure 1.22(b), and in the zoomed view of Figure 1.22(c).

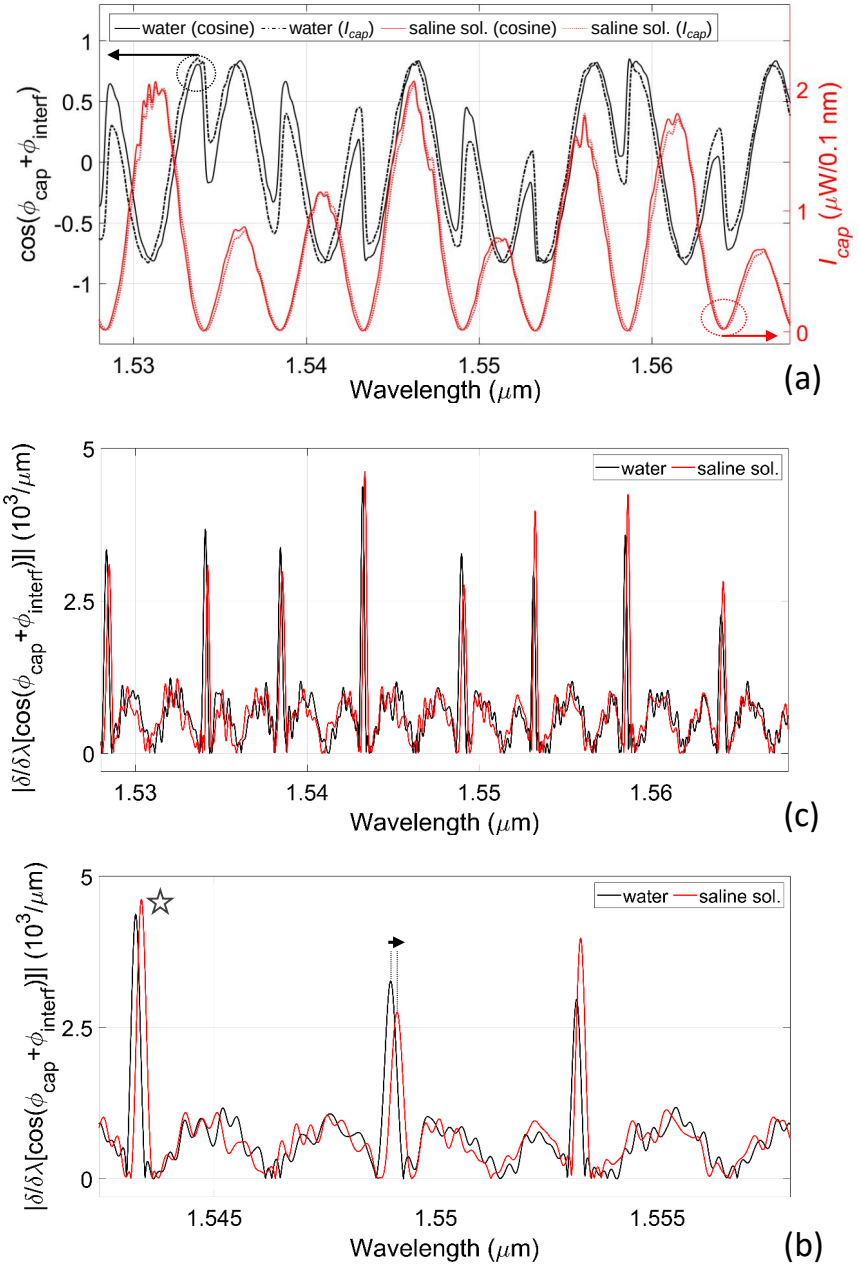

Figure 1.22: Experimental results obtained by filling the capillary channel with water and saline solution. (a) Filtered cosine signals obtained when the capillary is filled with water (black solid trace) and saline solution (black dotted trace) in comparison with the capillary reflectivity I_{cap} (red solid trace: water; red dotted trace: saline solution). (b) Derivative signal and a zoomed view (c): even if the RI difference between the two fluid is very small, it is still possible to distinguish the spectral shift.

These results are very interesting and promising because they are the experimental proof that the spectral phase shift readout technique is able to measure and distinguish fluids with a RI difference very close to the LoD value calculated during the procedure of calibration of the micro-opto-fluidic platform. Moreover, the sensitivity S for the derivative peak indicated by the star in Figure 1.22(c) was calculated. The position of the resonance for water filling the channel is λ_1 = 1543.21 nm, while for saline solution it is found λ_2 = 1543.40 nm. Hence the sensitivity is $S = (\lambda_2 - \lambda_1)/\Delta n_{sal} \approx 360$ nm/RIU and thus it is in agreement with the values found for the calibration curves of Figure 1.21.
Eventually, experimental analyses were repeated by filling the capillary with two alcohols, ethanol and isopropanol (both by Carlo Erba Reagents S.r.l., Italy), to further investigate the potentiality of spectral phase-shift interferometry for monitoring very large RI variations [13]. The RIs of these samples, measured at room temperature by means of an Abbe refractometer at a wavelength of 566 nm, were found to be n_{etoh} = 1.3640 and n_{iso} = 1.3772, thus, the RI difference is $\Delta n_{alcohol}$ = $13.2 \cdot 10^{-3}$ RIU. Considering a sensitivity of the order of 360 nm/RIU, previously calculated from the experimental results attained with water and saline solutions, when testing ethanol and isopropanol we expect a spectral shift of the order of 5 nm—as large as the typical wavelength separation between consecutive minima relative to resonances of the same order. Note that it was already demonstrated in previous works [19] that the separation between consecutive minima differs from one to another. This set of experiments with alcohols was performed to demonstrate that phase-sensitive detection is feasible and suitable also for large RI variations, close to the limit of the unambiguous range. Data were collected and processed following the same procedures previously described. The main results of this analysis are reported in Figure 1.23. Figure 1.23(a) reports the power spectra reflected from the capillary itself when the channel is filled with ethanol (black trace) and isopropanol (red trace). The absolute values of the derivatives of the cosine signals (as a function of the wavelength), obtained with phase-sensitive detection, are shown in Figure 1.23(b). As expected, the peaks undergo a wide red-shift, almost as large as the separation between consecutive resonances, when ethanol is substituted by isopropanol in the capillary channel. In this case, the wavelength shift of the resonance indicated by the arrow is $\Delta\lambda_{alcohol}$ = 5.15 nm.

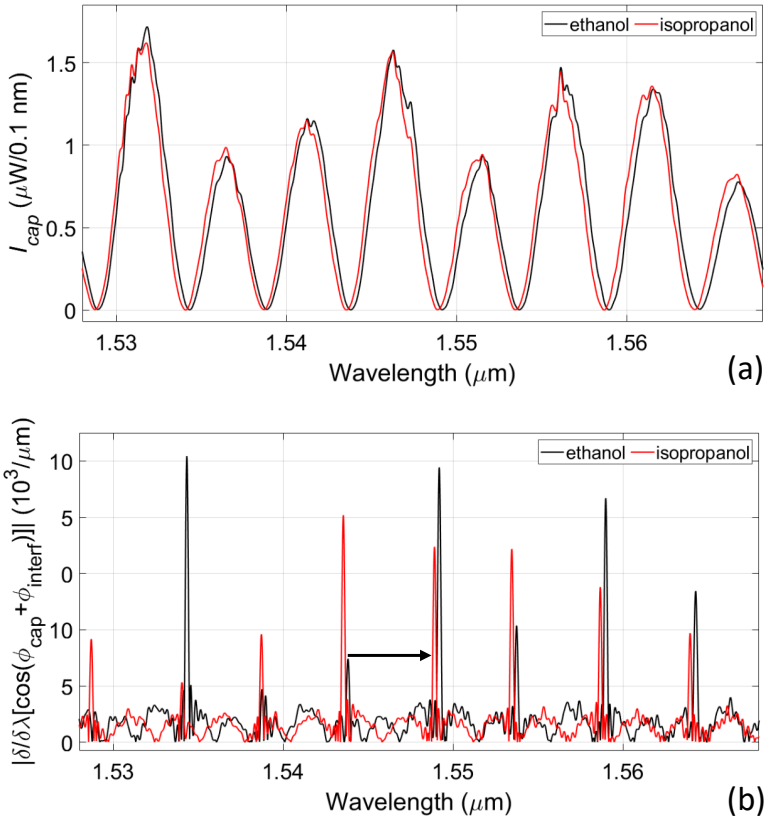

Figure 1.23: Experimental results obtained by filling the capillary channel with ethanol and isopropanol. (a) I_{cap} signal obtained when the capillary is filled with ethanol (black solid trace) and isopropanol (black dotted trace). (b) Derivative signals.

1.8 Discussion and conclusions

In this Chapter, a micro-opto-fluidic platform in combination with an innovative spectral phase interferometric readout technique was presented for refractive index monitoring in rectangular glass micro-capillaries in the near infrared region. An accurate theoretical model was implemented for carrying out theoretical predictions. Then, the micro-opto-fluidic setup was used first to detect the optical resonances of the micro-capillaries and then for measuring the real part of the RI of liquids. All the measurements performed are non-invasive, remote and contactless. The experimental results are in good agreement with the theoretical ones and the experimental testing proved that the micro-opto-fluidic platform is suitable for measuring different types of liquids, including alcohols.

A comparison can be made between this sensing platform and the performances of other solutions reported in the literature. In [37], with a three-level-gradient

interferometer based on a custom-fabricated S-tapered fiber, authors obtained a sensitivity of 51.17 nm/RIU that is significantly lower than the value we observed with our configuration (284–362 nm/RIU). Zhang et al. [38] realized a fiber-optic Fabry–Pérot interferometer for wide-range RI measurement, reporting a sensitivity value of 1260 nm/RIU. This value is roughly four times higher than our typical sensitivity but it is obtained with a complex fiber-spliced sensor structure. Moreover, this kind of probe is highly invasive for the sample since it is put in direct contact with the fluid. Zhao et al. [39] reported a temperature and RI fiber-optic sensor based on the cascade of a reflected Fabry–Pérot interferometer and a transmitted Mach–Zehnder interferometer, obtaining an RI sensitivity of 178.7 nm/RIU that is slightly lower compared with the sensitivity range (284–362 nm/RIU) demonstrated in our work. For the prism-based system, reported in [33], the declared range of linearity is 1.333–1.336 RIU, while in our work, we reported a linear response of the sensor for sample with RI in a bigger range (1.3340–1.3468 RIU). Gasior et al. [35] report a sensitivity of 2700 nm/RIU. This value is higher than the sensitivity of our sensor but it is obtained with a complex birefringent D-shaped fiber obtained with complex micromachining fabrication steps.

In previous researches carried out at the Laboratory of ElectroOptics, RI detection in micro-capillaries was carried out first measuring the minima of the $R_{cap}(\lambda)$ and then the maxima of the $T_{cap}(\lambda)/R_{cap}(\lambda)$ ratio (as described in Section 1.3) [18, 19, 29]. The advantage of finding the wavelength positions of the narrow peaks of the ratio signal was, however, at the expenses of a more complex instrumental setup. In this new work, by adding a few optical components to the instrumental configuration previously demonstrated for the spectral amplitude detection of resonances, we have achieved phase-sensitive detection of the wavelength positions of the resonances and thus of the fluid RI. The main advantage of the interferometric method over the spectral amplitude readout consists in measuring the wavelength position of narrow and well-defined maxima of the cosine signal derivative, instead of broad minima of the capillary reflection spectrum. Moreover, minima are more sensitive than maxima to amplitude oscillations due to the detection of noise or fluctuations in the source-emitted power that could even be wavelength dependent. Therefore, the interferometric method is less affected by all these spurious fluctuations. Furthermore, even if the sensitivity is comparable for both detection techniques, because it is an intrinsic feature of the transduction method based on resonance shift, the spectral phase technique could provide better performances. Indeed, in the neighborhood of a resonance, we can define a responsivity parameter P for both measurement methods given, for phase interferometric readout, by $P_{interferometric} = \Delta\cos[\phi_{tot}(\lambda)]/\Delta n = S \cdot \Delta\cos[\phi_{tot}(\lambda)]/\Delta\lambda$

and, for spectral amplitude readout, by $P_{spectral} = \Delta I_{cap}/\Delta n = S \cdot \Delta I_{cap}(\lambda)/\Delta\lambda$. As is evident, $P_{interferometric}$ is much higher than $P_{spectral}$. Finally, it is also underlined in the literature that the performance is better when using phase-sensitive detection [40].

Future work could be devoted to the investigation of a more compact instrumental setup that does not require the use of the OSA. By sweeping the emission wavelength of a semiconductor laser across an optical resonance and simultaneously introducing a higher frequency amplitude modulation, phase detection of the resonance shift induced by small refractive index variations could be carried out with a photodiode outside the base-band. Moreover, since the proposed sensing platform allows to perform safe and non-invasive analyses, it could be exploited also for the measurement of biological samples.

Chapter 2

Near infared absorption spectroscopy in rectangular glass micro-capillaries with selectable pathlength for alcohol-water mixtures detection

In this Chapter, I introduce another micro-opto-fluidic platform based on rectangular glass micro-capillaries with the selectable pathlenght for NIR absorption spectroscopic analysis of fluids. First, the goal of the work and the features of the absorption spectroscopy technique are presented. Then, a brief description of the state of the art is given. The theoretical model used to simulate the features of the platform and the instrumental configuration used for experimental measurements are described. Afterwards, spectral results (both theoretical and experimental) are presented. Then, the analysis on responsivity and sensitivity parameters is illustrated. Eventually, two real-life sensing applications for quality control of alcohol-based fluids are proposed and investigated.

2.1 Goal of the work

The Michelson scheme and the sophisticated spectral phase detection method presented in Chapter 1 allow to recover the real part of the RI of fluids inside the capillary with high sensitivity. However, this kind of measurement is non specific: indeed, if a solution contains many compounds, the same variation of RI can be due to various combinations of fluids. On the other hand, the absorption spec-

trum, which is related to the imaginary part of the RI, is a "fingerprint" of every molecule. For this reason, I have worked on the development of another innovative micro-opto-configuration for the measurement of the NIR absorption spectrum of sub-microliter quantities of liquid substances, again flowing in rectangular glass micro-capillaries (presented in Section 1.1), but with different geometrical dimensions and provided with integrated reflectors to guide light inside the channel, obtained by coating the glass walls with ultra-thin Aluminum layers. In this way, it is possible to guide radiation inside the capillary channel to increase the interaction length with the sample. In particular, the length of integrated mirrors can be tailored in order to adjust the lightpath according to the requirements desired. The micro-opto-fluidic platform was in particular exploited for specif measurements of water in mixtures of alcohols and water and, afterwards, for quality control of hand sanitizer gels and beverages for dietary use. The results of this work were published on international journals with referees [41, 42] and presented at international conference [43, 44].

2.2 Hints of absorption spectroscopy

Spectroscopy is the study of the interaction between matter and electromagnetic radiation as a function of the wavelength or frequency of the radiation [45, 46]. In particular, optical absorption spectroscopy measures the absorption of radiation in the ultra violet-visible-infrared region, as a function of frequency or wavelength, due to its interaction with a sample [47, 48, 49]. The fraction of radiation that is transmitted (and thus not absorbed) through a sample depends on the characteristics of the medium and the wavelength through the Beer-Lambert formula [50]

$$T_{abs}(\lambda) = e^{-\alpha(\lambda)\cdot x} \tag{2.1}$$

where λ is the wavelength, x is the path travelled by light in the sample. $\alpha(\lambda)$ is the so-called absorption coefficient that can be expressed as

$$\alpha(\lambda) = \frac{4 \cdot \pi \cdot k_{abs}(\lambda)}{\lambda} \tag{2.2}$$

where k_{abs} is the imaginary part of the RI of the medium. Moreover, the transmittance T_{abs} is related to the absorbance A through the formula

$$A(\lambda) = \text{Log}\left[\frac{1}{T_{abs}(\lambda)}\right] = -\text{Log}[T_{abs}(\lambda)] \tag{2.3}$$

where Log indicates the base-10 logarithm. The behavior of k_{abs} as a function of the wavelength is a characteristic fingerprint of every molecule. Indeed, different molecules exhibit a different absorption spectrum. In particular, Figure 2.1 reports the spectral behaviour in the NIR region of the RI imaginary part k_{abs} of water and three alcohols (ethanol, isopropanol and ethylene glycol) that have been investigated in this work. The four fluids present absorption peaks at different wavelengths and with different amplitude. Data have been taken from the literature [51, 52, 53]. In particular, water absorbs more than alcohols around 1450 nm and the shape of $T_{abs}(\lambda)$ for a mixture depends on its concentration on the sample. Hence, NIR absorption spectroscopy is a powerful technique used to identify the composition of alcoholic mixtures. Indeed, it is accessible, robust, versatile, non destructive and it does not require pre-treatment of the sample [54].

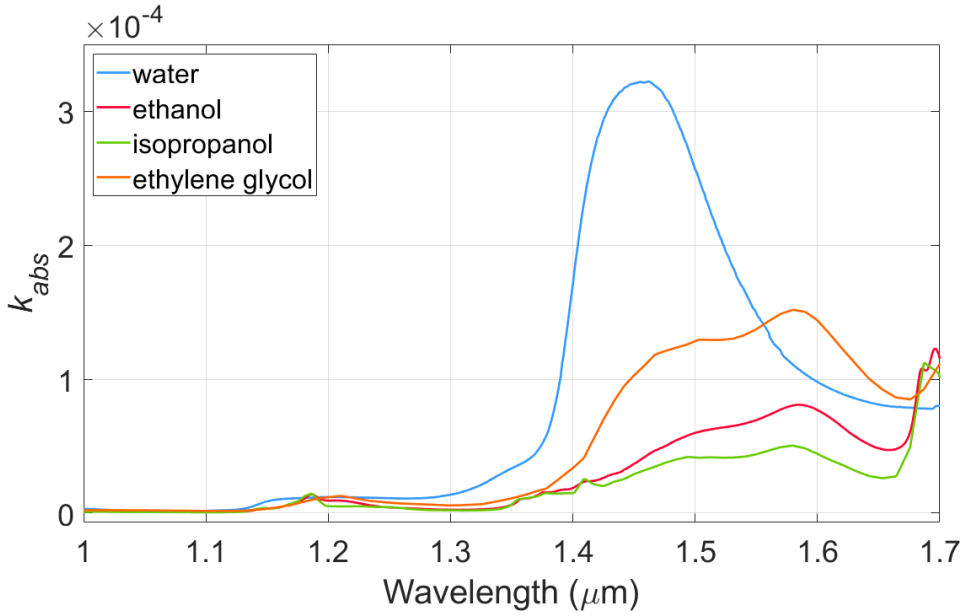

Figure 2.1: Lineshape of the the RI imaginary part k_{abs} as a function of the wavelength for water (light-blue trace), ethanol (pink trace), isopropanol (green trace) and ethylene glycol (orange trace).

2.3 Existing approaches from the literature

Several solutions for absorption spectroscopy based on waveguides, optrodes or resonators are reported in the literature. For example, in [55], Puyol et al. designed an integrated waveguide absorbance optrode membrane that acts as sensing element and light guiding medium at the same time. The resulting optrode aims at coupling the technological developments achieved by the communication industry in passive and active components for light transmission with the advantages of

conventional spectroscopic techniques. Light emitted at 670 nm by an LED propagates through the membrane that changes its absorption spectrum while interacting with the analyte. In [56], the authors proposed a PDMS microfluidic channel with a spiral geometry waveguide constituted of a photosensitive polymer core. Radiation emitted at 650 nm by a laser diode is coupled in the waveguide by means of an optical fiber. A power meter is used for absorbance measurements on fluids. In [57], the authors realized a miniaturized disposable polymer waveguide with sensing film and multiple reflections for absorption-based chemical sensing. An LED and a photodiode are used. Hu et al. demonstrated the first micro-fluidic device monolithically integrated with planar chalcogenide waveguides on a silicon substrate for N-methylaniline detection exploiting the absorption fingerprint of the N-H bond near 1496 nm [58]. In [59], the authors presented a miniaturized spectrometer with elastomeric micro-channels for absorption and fluorescent spectroscopy. In [60], a compact low-cost photometer based on stainless steel capillaries was developed for ultra-sensitive absorbance detection. The optical-path can be greatly enhanced because the light scattered by the sidewall can be confined inside the capillary regardless of the incident-angle.The absorbance measurements were performed using an LED emitting at 505 nm and a photodiode.

Other solutions based on absorption spectroscopy for analysis of fluids reported in the literature rely on the use of round-section glass or quartz capillaries. For example Wei et al. used Pyrex glass capillaries of one meter in length in different configurations (straight, coiled) with laser and lamps to perform sensitive measurement of absorbance [61]. NIR spectrophotometry for the analysis of alcoholic solution in circular PDMS capillaries is proposed in [62]: the determination of ethanol in a liquor sample contained in a capillary with a six-port valve was demonstrated. Absorbance is monitored by measuring the transmitted intensity through the sample the wavelengths of 2305 nm and 2636 nm, the first corresponding to a strong absorption band of ethanol. A multi-reflection flow cell suitable for flow analysis is described in [63]. Light from an LED is directed through an optical fibre into a silver coated glass capillary through a sidewall aperture, and emerges through a similar aperture 10 mm along the capillary after undergoing an estimated 19 reflections. The capillary has a length of 10 mm and a diameter of 0.80 mm This process provides a sensitivity enhancement of approximately 2.5 compared with a conventional cell of the same nominal path length. Absorbance measurements are carried out using a 652-nm-LED for application to the determination of reactive phosphorus in estuarine waters with wide variation in salinity. In [64], the same authors proposed a total internal reflection flow-through cell based on a 6-cm-long circular quartz capillary. Quartz optical fibres were used to in-

troduce light and to collect emergent light. A red LED was used as light source, and the absorbance was measured with a CCD (Charge-Coupled Device) detector. The system was exploited for determination of reactive phosphorus in marine water. In [65], a silica capillary was used as a waveguide. Light from a LED is coupled in the capillary through a fiber and it absorbed by the medium in the channel according to Beer-Lambert law.

The literature also reports some works based on absorption spectroscopy in various types of fluidic channels for solvents identification and recognition of water-based fluids. These specific topics are attracting a wide interest for several applications, from pharmaceutics to biofuel to food and beverage industry. In [66, 67], an imaging method for simultaneous detection of temperature and concentration of water-ethanol mixtures and other alcohols in PDMS channel was reported. Absorbance images at two wavelengths (1905 nm and 1935 nm) were acquired with a NIR camera. Gomez et al. proposed an integrated fiber-optic sensor that uses incoherent broadband cavity enhanced absorption spectroscopy for sensitive detection of aqueous samples in nanoliter volumes [68]. NIR absorption is measured in a 100 μm gap between the ends of two short segments of multimode fiber The other ends of the fibers were coated with dielectric mirrors to form a 9.5 cm optical resonator. Light from a fiber-coupled SLED is directly coupled into one end of the cavity, and transmission was measured using a fiber-coupled photodiode. In [69], Neil et al. reported a broadband cavity-enhanced absorption spectroscopy to record in real-time the absorption spectrum of microliter volume aqueous phase droplets within a micro-fluidic chip assembly. Channels of width 1 mm and depth 320 μm were fabricated in ultraviolet-curing optical adhesive, sandwiched between two microscope cover slides. In [70], the authors used a coiled fiber-optic sensor and an infrared source to determine the low-level water content in ethanol conducting absorption measurements. Tantawi et al. realized a glass micro-cuvette and measured the full absorption spectrum of liquid ethanol in the NIR region from 300 to 2900 nm [71]. The configuration allows in-plane transmission measurements.

Although many interesting solutions are reported in the literature for NIR absorption measurements in micro-fluidic devices, there is still the need for improvements. Indeed many platforms rely of fluidic channels that need to be custom realized with complex and expensive micromachining technologies. Moreover, often they are not suitable for in-flow measurements. Last, when using circular waveguides or capillaries, substantial light loss can occur due to scattering in the walls.

2.4 Theoretical model

A detailed theoretical model was developed in MATLAB enviroment to describe light travelling inside the micro-capillary and predict the sensor spectral response to different samples. The path followed by light in the micro-capillary and all the important geometrical parameter are depicted in Figure 2.2.

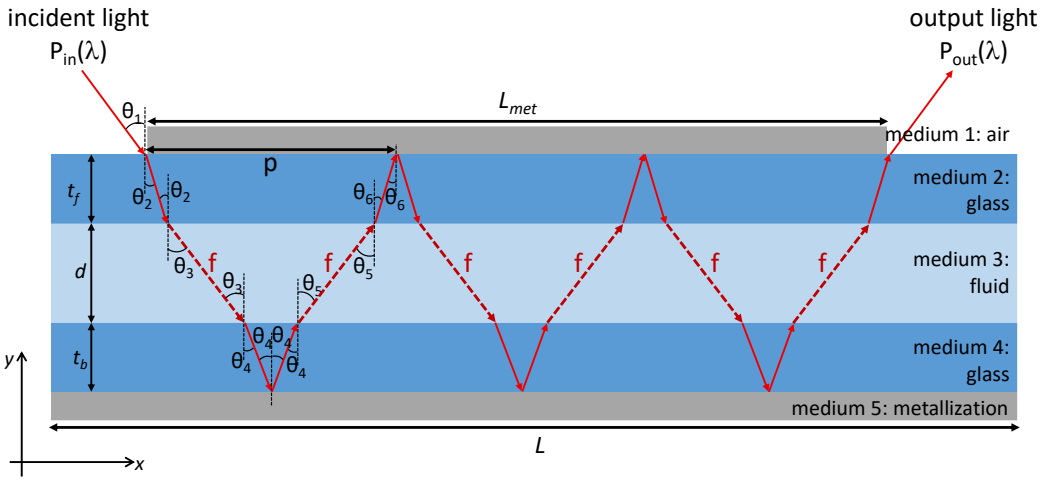

Figure 2.2: Schematic representation of the path travelled by the light in the micro-capillary. In this scheme, a number of bounces $N = 3$ is considered. The incident beam can be moved along the surface of the capillary in order to make light bounce once on the bottom reflector or multiple times, exploiting the presence of the top reflector.

The geometrical ray optics approximation was applied to study the path followed by the light inside the micro-capillary since its dimensions are much larger than the considered wavelength values. The model was developed by considering the micro-capillary as a multi-layer structure composed of three layers with finite thickness (upper glass wall, channel and bottom glass wall) inserted between two infinite media (either air/aluminum or aluminum/aluminum). The presence of the top aluminum layer was considered for modelling the multiple bounce configuration. The thickness of the reflector was considered infinite, providing specular reflectivity with a coefficient for the power $R_{met} \approx 0.99$. The aluminum layers were deposited on the glass using standard industrial method. As reported in the literature [72], even for high deposition rates the roughness height of the metal layer is of the order of a few nm, thus much shorter than the wavelength and the total path travelled by light in the capillary channel, in both cases of single and multiple bounce configuration. Hence, in the model it was possible to neglect scattering effects due to residual roughness. The refractive index of air n_1 was considered equal to 1 and hence constant for every wavelength, while for the refractive index

of glass n_2, assumed to be purely real, its dispersion relation was included. The refractive index of the sample filling the channel was modeled as

$$n_3(\lambda) = n'(\lambda) - i \cdot k_{abs}(\lambda) \tag{2.4}$$

where $n'(\lambda)$ is the real part, λ is the wavelength, i is the imaginary unit and $k_{abs}(\lambda)$ is the imaginary part. The behaviour of k_{abs} as a function of the wavelength determines the absorption properties of each molecule, which are a unique characteristic of every substance. In this way, the absorption features of the fluid can be accounted for. When the light beam crosses the separation surface between two different media, it is deflected according to Snell law:

$$n_j \cdot \sin\theta_j = n_l \cdot \sin\theta_l \tag{2.5}$$

where the subscripts j and l indicate the origin and destination media, respectively, n_j and n_l refer to the real part of the refractive indices and θ_j and θ_l are the angle of incidence and the angle of transmission, respectively. Moreover, at each interface, the electric field is partially transmitted and partially reflected. Here, we are interested only in the transmission coefficients that can be calculated with the Fresnel relations. For an incidence angle of 35°, the coefficients for the s-polarized and the p-polarized field are significantly different. Moreover, since in the experimental setup the beam travels in a multimode fiber and no control of the polarization is applied, it can be supposed that the radiation is equally distributed between the two polarizations. The transmission coefficient for the field with s-polarization is given by

$$t_{s,jl} = \frac{2 \cdot n_j \cdot \cos\theta_j}{n_j \cdot \cos\theta_j + n_l \cdot \cos\theta_l} \tag{2.6}$$

while the transmission coefficient for the p-polarized field is calculated as

$$t_{p,jl} = \frac{2 \cdot n_j \cdot \cos\theta_j}{n_l \cdot \cos\theta_j + n_j \cdot \cos\theta_l} \tag{2.7}$$

Then, the overall field transmission coefficient t_{jm} is retrieved computing the mathematical average between $t_{s,jl}$ and $t_{p,jl}$:

$$t_{jl} = \frac{t_{s,jl} + t_{p,jl}}{2} \tag{2.8}$$

From the overall field transmission coefficient, the power transmission coefficient at each interface is obtained by applying the formula:

$$T_{jl} = \frac{n_l \cdot \cos\theta_l}{n_j \cdot \cos\theta_j} \cdot |t_{jl}|^2 \tag{2.9}$$

Every time the beam crosses the channel containing the sample, it travels along a distance f equal to

$$f = \frac{d}{\cos\theta_3} \tag{2.10}$$

Because of the presence of the top metallization, the beam makes N bounces inside the micro-channel and the total geometrical path F is given by

$$F = 2 \cdot f \cdot N = \frac{2 \cdot N \cdot d}{\cos\theta_3} \tag{2.11}$$

N can be geometrically found by computing

$$N = CEIL(L_{met}/p) \tag{2.12}$$

where p is the distance travelled by the light along the x-direction at each bounce in the structure and $CEIL$ is the MATLAB function that returns the smallest integer value that is bigger than or equal to L_{met}/p. In the single bounce configuration, $N = 1$. As explained in Section 2.2, the overall attenuation $T_{abs}(\lambda)$ due to fluid absorption can be calculated by applying the Lambert-Beer formula, considering the total lighpath F travelled in channel

$$T_{abs}(\lambda) = e^{-\alpha(\lambda)\cdot F} \tag{2.13}$$

To simulate the absorption effect of mixtures of two pure substances and its dependence on concentration, the law of additivity of the absorbance has to be considered:

$$A_{mixture}(\lambda) = A_I(\lambda) \cdot C_I + A_{II}(\lambda) \cdot C_{II} \tag{2.14}$$

where $A_I(\lambda)$ and $A_{II}(\lambda)$ are the absorbances of the two substances and C_I and C_{II} are the corresponding fractional volume concentration. The transmittance for the mixture $T_{abs\ mixtures}$ can be retrieved as

$$T_{abs}(\lambda) = T_{abs\ mixture}(\lambda) = \frac{1}{10^{A_{mixture}(\lambda)}} \tag{2.15}$$

For the mixtures, also the real part of the RI is modified according to the formula

$$n_{mixture}(\lambda) = n_I(\lambda) \cdot C_I + n_{II}(\lambda) \cdot C_{II} \tag{2.16}$$

where n_I and n_{II} are the RI real part of the fluids, supposing no interaction at molecular level. Eventually, the spectral behavior of the output light $P_{out\ sample}(\lambda)$ is found by multiplying all the contributions of transmission. In particular, the spectral transmittance is given by

$$T_{sample}(\lambda) = \frac{P_{out\ sample}(\lambda)}{P_{in}(\lambda)} = T_{12} \cdot T_{23}^N \cdot T_{34}^N \cdot T_{43}^N \cdot T_{32}^N \cdot T_{21} \cdot R_{met}^{2N-1} \cdot T_{abs}(\lambda) \tag{2.17}$$

where $P_{in}(\lambda)$ is the optical power that enters the capillary, in the model considered a constant as a function of the wavelength. The same computation has to be done also when the micro-capillary is empty, considering air as medium filling the channel. In this case, no attenuation due to absorption is considered. Hence, the transmittance for the empty capillary is

$$T_{air}(\lambda) = \frac{P_{out\ air}(\lambda)}{P_{in}(\lambda)} = T_{12} \cdot T_{23}^N \cdot T_{34}^N \cdot T_{43}^N \cdot T_{32}^N \cdot T_{21} \cdot R_{met}^{2N-1} \tag{2.18}$$

Moreover, in order to compare the analytical simulations with the experimental results, for the single bounce configuration the spectral response was defined as

$$spectral\ response\ (\lambda) = \frac{T_{sample}(\lambda)}{T_{air}(\lambda)} = \frac{P_{out\ sample}(\lambda)}{P_{out\ air}(\lambda)} \tag{2.19}$$

2.5 Experimental configuration

A micro-opto-fluidic instrumental configuration was designed to carry out experimental measurements. A schematic representation of the experimental configuration is reported in Figure 2.3(a).

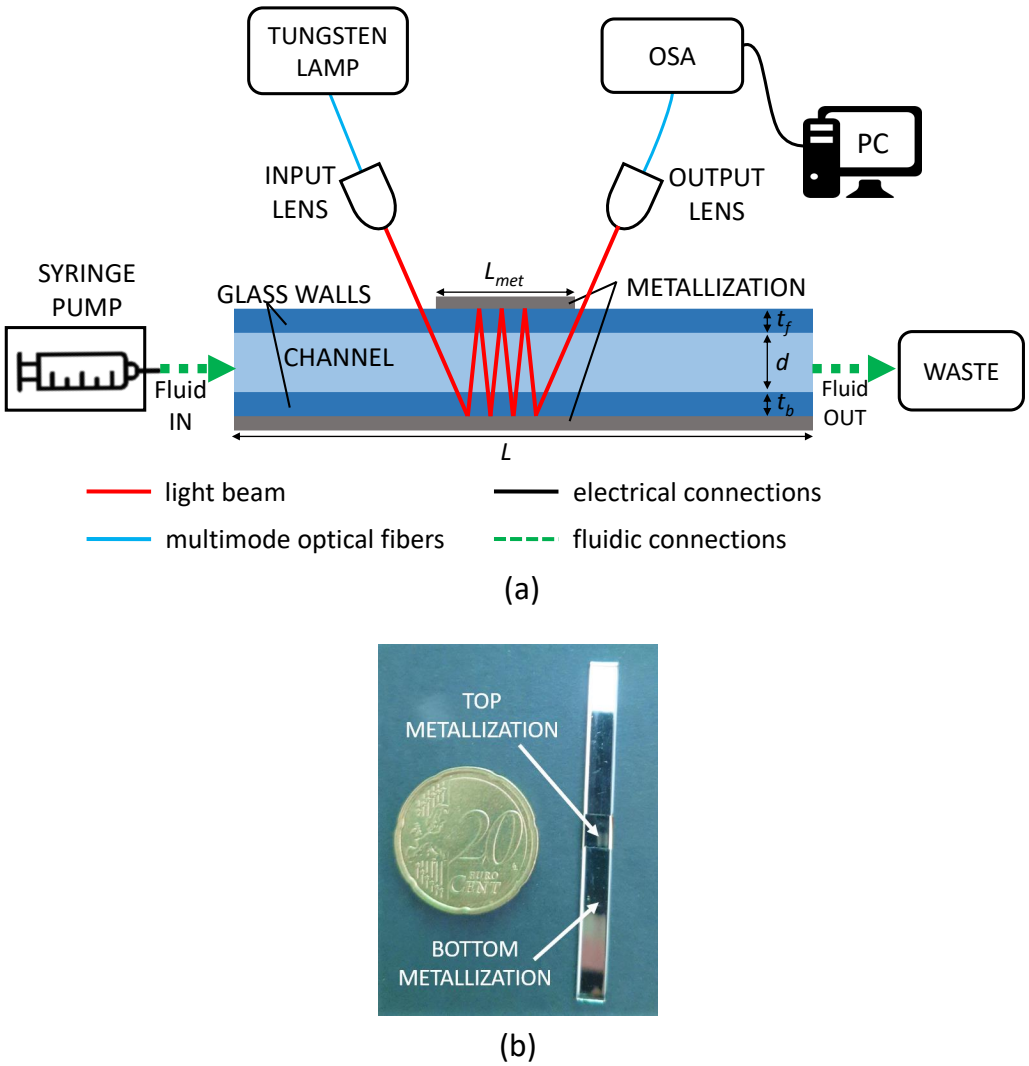

Figure 2.3: Micro-opto-fluidic configuration and rectangular glass micro-capillary. (a) Schematic representation of the instrumental setup for experimental measurements. The incident beam can be moved along the capillary surface to make it bounce once on the bottom reflecting layer or multiple times, exploiting the guiding effect provided by the top reflecting layer. OSA: Optical Spectrum Analyzer. (b) Picture of the aluminum-coated micro-capillary in comparison with a 20-cent coin: the bottom and top metallizations are clearly recognizable.

Glass micro-capillaries with rectangular section purchased from VitroCom (NJ, USA) and already described in detail in Section 1.1 are the core elements of the instrumental setup. The micro-capillaries investigated in this work have nominal thickness of the glass walls $t_f = t_b = 280$ µm and nominal inner channel depth $d = 400$ µm. Moreover, they have width $W = 4$ mm and length $L = 5$ cm. Tolerances reported by the manufacturer are 10% for the channel depth and 20% for the wall thickness. The capillary is laid horizontally onto a metallic support to ensure its

stability and improve its rigidity. The external side of the capillary bottom wall is fully coated with a 50-nm-thick aluminum layer, while on the upper external wall a layer with same thickness but length L_{met} = 4 mm or 5 mm is deposited. The aluminum depositions, realized in high vacuum environment, were performed by VAQUARZ (Italy). In a previous version of the work, only a bulk aluminum mirror was used in place of the bottom metallization [41]. Here, the deposition of thin metallic layer allows to obtain an integrated and more compact micro-fluidic device. A picture of a micro-capillaries with metallizations is shown in Figure 2.3(b). Both tips of the capillary are inserted in heat-shrink tubes provided with luer connections to fill and drain the channel with the aid of manual syringes or of a programmable syringe pump (NE-100 MUlti-Phaser, NH, USA). The sample volume required for the measurement is of the order of 18 µL. Light from a tungsten lamp (Agilent, CA, USA) with an average spectral power density of 4 nW/10 nm (Figure 2.4) is coupled into a multimode fiber cable (50 µm/125 µm core/cladding diameter) and shone onto the surface of the micro-capillary under test at an angle of approximately 35° using a pigtailed lens (LPF-04-1550-50/125-QM-6-26-3.9AS-3S-30-1, OzOptics, Canada). The lens generates a light spot of unpolarized light with a diameter of 300 µm at a working distance of 26 mm. The incident beam can be moved along the micro-capillary surface in order to make the light bounce once on the bottom metallization in the single bounce configuration or bounce multiple times, exploiting the zig-zag guiding effect provided by the top and bottom reflecting layers in the multiple bounce configuration. The output light is collected by another multimode pigtailed lens identical to the input one and it is directed toward the monochromator input of an optical spectrum analyzer (OSA Agilent 86142B, CA, USA) connected to a laptop for data acquisition via a dedicated LabVIEW interface. Spectra are acquired in the wavelength range 1.0–1.7 µm with a resolution bandwidth RB = 10 nm. Signal processing is performed in MATLAB environment.

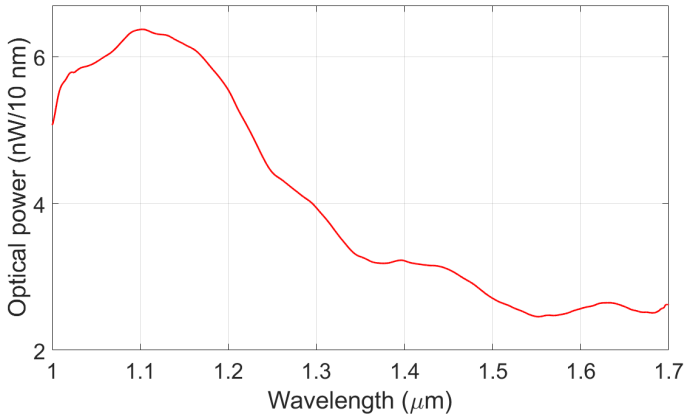

Figure 2.4: Emission spectrum of the tungsten lamp in the considered wavelength range.

2.6 Spectral results

The micro-opto-fluidic configuration presented in Section 2.5 was exploited to test mixtures of alcohols and water and mixtures of different types of alcoholic fluids. First, a full spectral analysis was carried out by by testing samples containing different concentrations of water and alcohols and analyzing the spectrum of the output light reflected from the micro-capillary. Then, the experimental results were compared with those theoretical obtained by performing simulations on micro-capillaries filled with the liquids. The following two Sections, Section 2.6.1 and Section 2.6.2, report the spectral results regarding the single and multiple bounce configuration, respectively.

2.6.1 Results obtained with the single bounce configuration

Experimental measurements were carried out first exploiting the single bounce configuration ($N = 1$) and testing solutions containing an alcohol, as main component, and deionized water, as polluting substance, present in high concentrations. Fluids were flown in the micro-capillary channel and then measurements were carried out in static conditions. First, mixtures of ethanol and deionized water were tested (Figure 2.5). The ethanol used for these experiments is a food-grade ethyl alcohol with agricultural origin (Dilmoor S.p.A., Italy), that contains 96% of alcohol in volume and 4% of water: the exact content of ethanol and water were calculated and taken into account in the theoretical simulations carried out to be compared with the experimental results. Figure 2.5(a) shows then experimental transmitted power output spectra $P_{out}(\lambda)$ collected by testing solutions of water

diluted in ethanol in volume concentrations equal to 4% (dark-green trace), 8.8% (blue trace), 13.6% (thick red trace), 18.4% (light-green trace), 23.2% (pink trace), 52% (orange trace), 71.2% (dark-red trace) and 100% (light-blue trace). The black trace is the spectrum of the output radiation collected with the empty capillary (i.e. channel filled with air). It is possible to observe that the transmission dip at 1450 nm, where the absorption band of water due to OH- ions is located, becomes deeper for increasing concentrations of water. In general, this absorption band of water is not exploited for sensing purposes, due to its weakness but it turned out to be very interesting to exploit optical sources and detector that were traditionally developed for telecomunication applications. For the single bounce configuration, the experimental spectral response, as defined by Equation 2.19, was calculated for every sample by normalizing each spectrum to that obtained with the empty micro-capillary; then, it was compared with the theoretical spectral response. The experimental spectral responses turned out to be in agreement with the theoretical simulations obtained considering a micro-capillary with channel depth $d = 440$ μm, as reported in Figure 2.5(b). Indeed as explained in Section 1.1, the manufacturer reports a tolerance of ±10% for the channel depth and thus the actual dimension could be different from the nominal one.

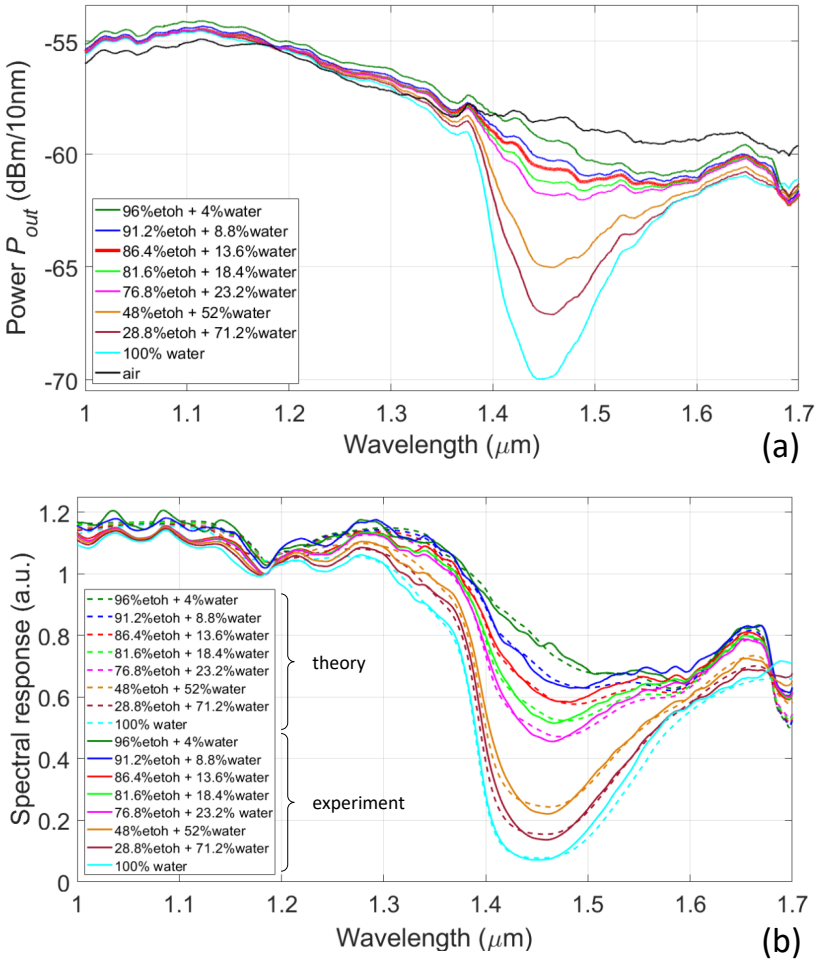

Figure 2.5: Spectral results for ethanol-water mixtures tested in the single bounce configuration (N = 1). (a) Experimental power spectra. For increasing concentrations of water, the minimum around 1450 nm becomes deeper. (b) Comparison between theoretical (dotted traces) and experimental (solid traces) spectral responses.

To further validate the operation of the micro-opto-fluidic platform, the theoretical and experimental analyses were repeated considering mixtures of isopropanol, (RS Components, United Kindom) as main component, and deionized water, as polluting substance present in high concentrations (Figure 2.6). Figure 2.6(a) reports the power spectra of $P_{out}(\lambda)$ obtained testing sample with a water content of 0% (pure isopropanol, blue trace), 10% (pink trace), 20% (red trace), 50% (orange trace), 70% (green trace) and 100% (light-blue trace). It is possible to observe that the spectral minimum located around 1450 nm, due to the presence of water, becomes deeper for increasing concentration of water. This observation is in agreement with the results obtained by testing water-ethanol dilutions and proves that analysis of the spectral results around 1450 nm is specific for measur-

ing the concentration of water, regardless the other substances that are contained in the mixture. Figure 2.6(b) shows the comparison between the experimental (solid traces) spectral responses and the theoretical ones (dotted traces), obtained simulating the effect of a channel depth $d = 440$ µm. The high level of agreement is a further confirmation of the correctness of the model implemented.

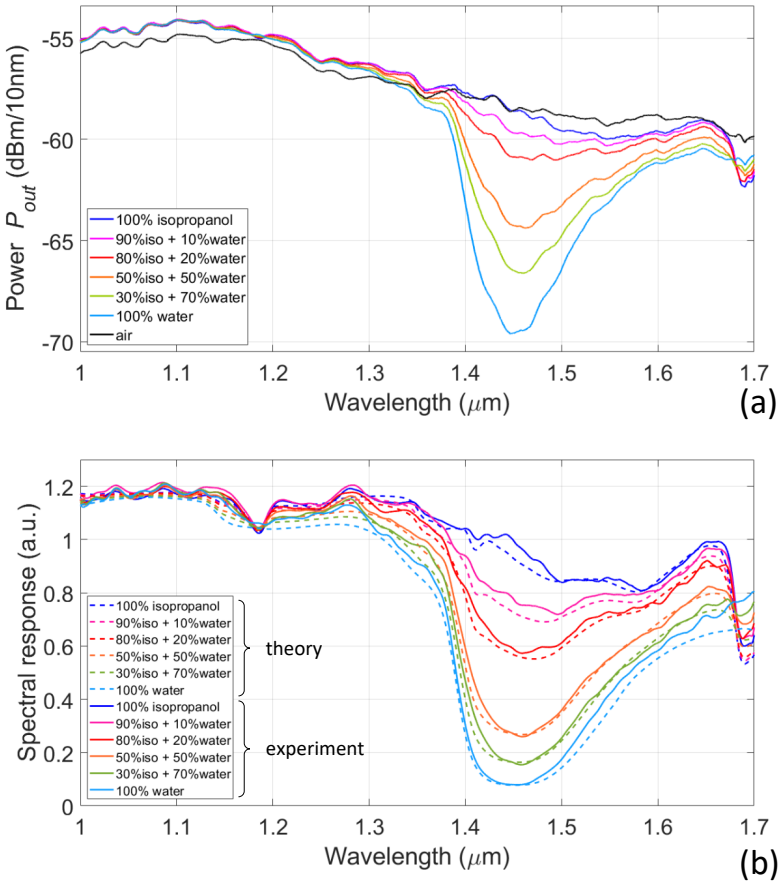

Figure 2.6: Spectral results for isopropanol-water mixtures tested in the single bounce configuration ($N = 1$). (a) Experimental power spectra. For increasing concentrations of water, the minimum around 1450 nm becomes deeper. (b) Comparison between theoretical (dotted traces) and experimental (solid traces) spectral responses.

2.6.2 Results obtained with the multiple bounce configuration

The single bounce configuration is suitable for the analysis of solutions with high water content. However, to detect also the presence of very small quantities of water with higher sensitivity, it is necessary to increase the interaction length between the light and the sample: hence, the multiple bounce configuration was exploited to measure mixtures with a difference in concentration of substances smaller than

1%. First, a micro-capillary with L_{met} = 5 mm was used to test ethanol-water mixtures. With such a length of the front metallization, the theoretical model allowed to estimate a number of bounces N = 7. Figure 2.7(a) reports the power spectra $P_{out}(\lambda)$ obtained for water in ethanol in concentration of 4% (black trace), 4.96% (blue trace), 5.92% (pink trace), 6.88% (green trace), 7.84% (light-blue trace), 8.8% (purple trace), 13.6% (thick red trace), 18.4% (yellow trace) and 23.2% (orange trace). Exploiting this configuration, the effect of water absorption around 1450 nm is strongly enhanced thanks to the longer lightpath. Moreover, also the absorption band of ethanol centered at 1185 nm is here clearly recognizable. Figure 2.7(b) shows the comparison between the output power spectrum obtained testing a sample with a concentration of water equal to 13.6%, in the single and multiple bounce configuration, respectively. It is possible to note how the spectral shape of the absorption profile can be detected with a greater level of detail exploiting the multiple bounce configuration, thanks to the longer lightpath. In the case of multiple bounce configuration, the spectral response was not computed: indeed, it would be meaningless since the number of bounces that the light undergoes in the micro-capillary containing the sample is different from that in air (i.e., with the empty channel) due to their huge RI difference. To compare experimental and theoretical results, Figure 2.7(c) reports the transmittance $T_{sample}(\lambda)$, as defined by Equation 2.17, for a sample with 4.96% concentration of water in ethanol. The blue trace is the theoretical $T_{sample}(\lambda)$, while the orange trace is the experimental one. In the multiple bounce configuration, the ray tracing model neglects additional losses due to the non-ideal guiding properties of the capillary channel that have an impact on the experimental results. In practice, guided propagation of the beam (due to multiple reflections) occurs only in the vertical plane (orthogonal to the wide flat surfaces of the capillary) whereas no guiding is ensured in the horizontal plane. This discrepancy between the model and the experimental situation has an almost negligible impact for the single bounce configuration, but in the case of multiple bounces real losses become much larger. Thus, the theoretical results are based on a model that neglects losses that are not due to fluid absorption or to partial transmission/reflection at the interface. Although this assumption does not hold in the experimental conditions, additional losses are observed as almost constant with the wavelength for $\lambda > 1350$ nm.

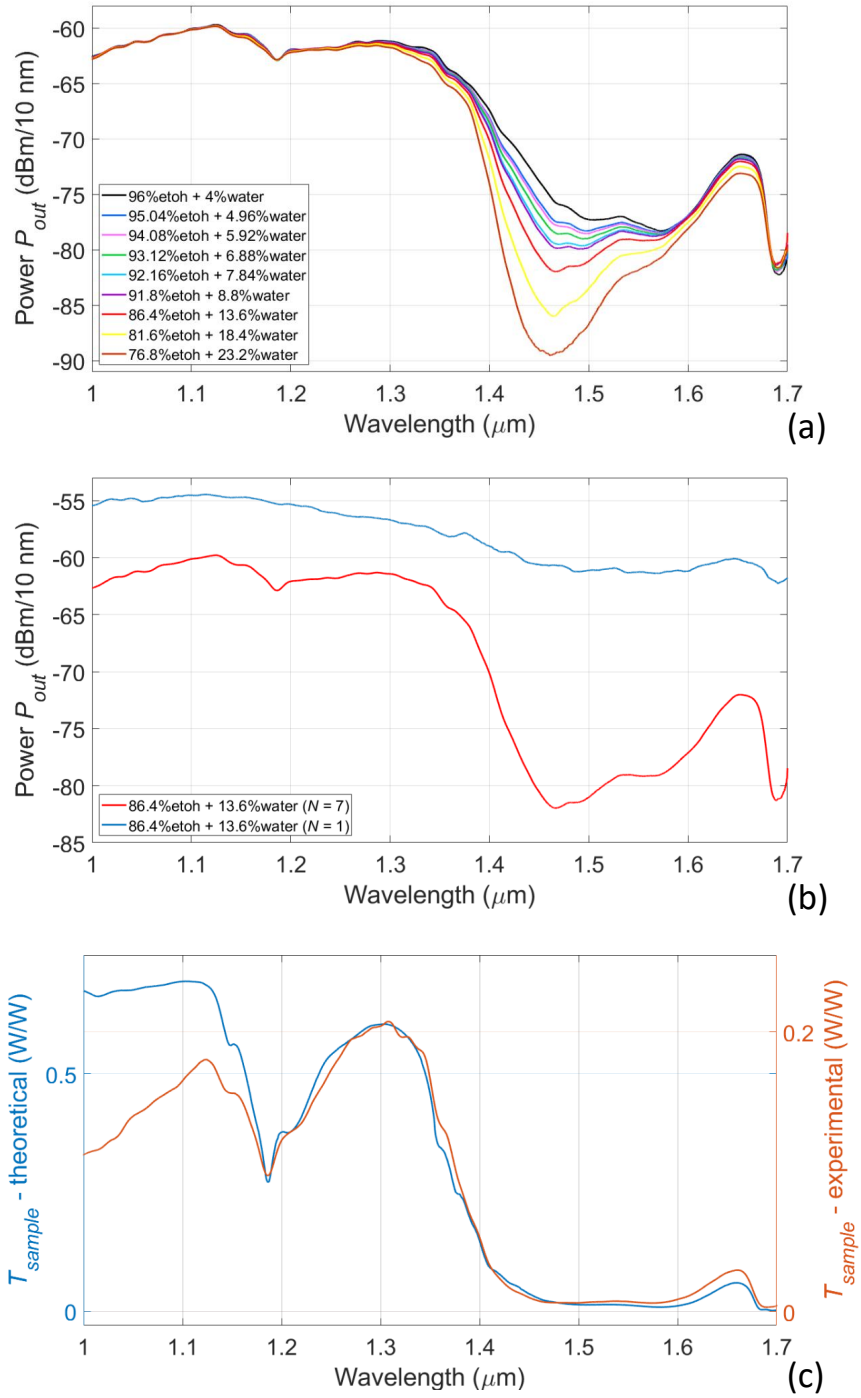

Figure 2.7: Spectral results for ethanol-water mixtures tested in the multiple bounce configuration, with $N = 7$. (a) Experimental power spectra obtained by testing water-ethanol dilutions with a difference in concentration lower than 1%. (b) Comparison between spectra related to the same sample tested in the single bounce (blue trace) and multiple bounce (red trace) configuration. (c) Comparison between theoretical (blue trace) and experimental (orange trace) $T_{sample}(\lambda)$ for a solution containing the 4% of water.

The same micro-capillary with $L_{met} = 5$ mm leading to $N = 7$ was exploited in the multiple bounce configuration also to detect low concentrations of water in isopropanol-water mixtures (Figure 2.8). Figure 2.8(a) reports the power spectra $P_{out}(\lambda)$ for samples with a concentration of water equal to 0% (isopropanol, black trace), 1% (light-blue trace), 2% (red trace), 3% (light-green trace), 4% (pink trace), 5% (blue trace), 10% (yellow trace), 15% (purple trace), 20% (orange trace) and 25% (green trace). As already underlined when testing ethanol-water mixtures, the effect of water absorption around 1450 nm is strongly enhanced thanks to the extension of interaction length between light and sample. Furthermore, also the absorption band of the alcohol around at 1185 nm becomes here clearly recognizable. Figure 2.8(b) reports the comparison between the theoretical (blue trace) and experimental (orange trace) $T_{sample}(\lambda)$ for a mixture of isopropanol and water containing the 1% of water. Also in this case, the spectral shapes are in agreement but the values of $T_{sample}(\lambda)$ are different because of the additional losses, which have an impact when considering the multiple bounce configuration, but are neglected in the theoretical model.

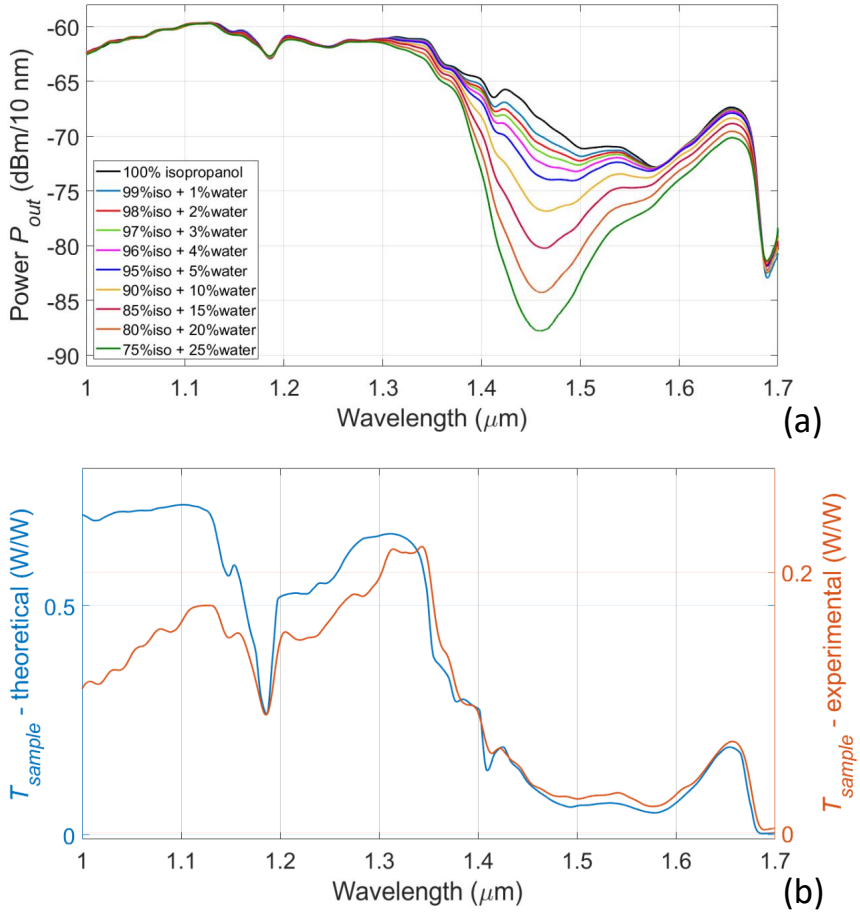

Figure 2.8: Spectral results for isopropanol-water mixtures tested in the multiple bounce configuration, with $N = 7$. (a) Experimental power spectra obtained by testing samples with a difference in concentration down to 1%. (b) Theoretical (blue trace) and experimental (orange trace) $T_{sample}(\lambda)$ for a solution containing the 1% of water.

Eventually, experimental measurements with the multiple bounce configuration (L_{met} = 5 mm and N = 7) were carried out considering mixtures of two alcohols: isopropanol and ethylene glycol (Figure 2.9). Ethylene glycol is a diol, well known for applications in various fields, such as an antifreeze and coolant in automobiles, a raw material in the manufacture of polyester fibers and an ingredients in detergents and cosmetics [73, 74]. Moreover, if ingested, this compound can be toxic and led to poisoning [75], hence its correct identification is a particular interesting issue. Ethylene glycol presents a lower absorption with respect to water (see Figure 2.1), thus it was possible to detect higher concentrations of this substance mixed with isopropanol. The experimental spectrum of the output light $P_{out}(\lambda)$ is reported in Figure 2.9(a) for mixtures with a concentration of ethylene glycol equal to 0% (isopropanol, black trace), 5% (blue trace), 10% (red trace), 20% (orange

trace), 30% (green trace), 50% (pink trace), 70% (grey trace) and 100% (light-blue trace). When the concentration of ethylene glycol increases, the absorption peak at 1185 nm (due to isopropanol) disappears and the absorption peak at 1210 nm (related to ethylene glycol) appears. Moreover, the double absorption band between 1450 nm and 1600 nm becomes more evident. Figure 2.9(b) reports the comparison between the theoretical (blue trace) and experimental (orange trace) $T_{sample}(\lambda)$ for a sample containing the 5% of ethylene glycol. Also in this case, the spectral shapes are in a quite good agreement but the values of $T_{sample}(\lambda)$ are different because of the additional losses that have an impact when considering the multiple bounce configuration but are neglected in the theoretical model.

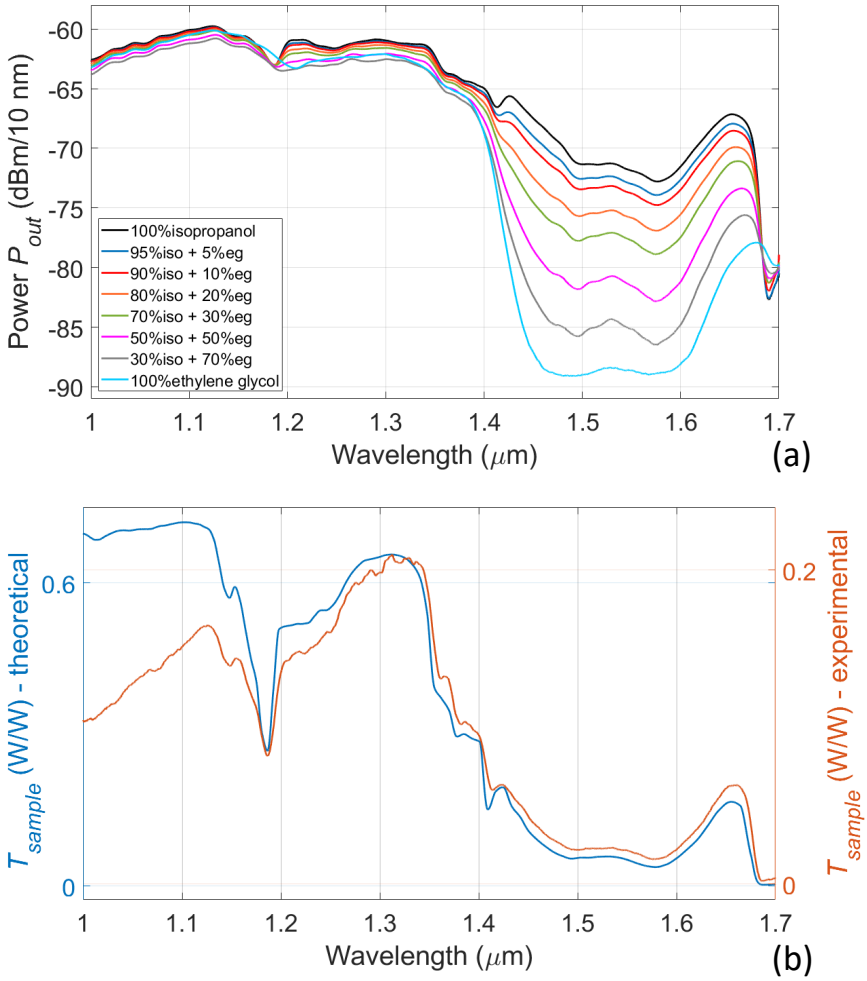

Figure 2.9: Spectral results for isopropanol-ethylene glycol mixtures tested in the multiple bounce configuration, with $N = 7$. (a) Experimental power spectra obtained by testing samples with difference concentrations. (b) Theoretical (blue trace) and experimental (orange trace) $T_{sample}(\lambda)$ for a solution containing 95% of isopropanol and 5% of ethylene glycol.

2.7 Responsivity and sensitivity results

Further analyses were carried out to extract some sensor parameter that are independent from the power (Figure 2.10). Indeed, when designing an optical sensor based on amplitude measurements, a reliable response parameter, or responsivity, is the ratio of the output signal collected at two wavelengths, to compensate for spurious amplitude fluctuations that could arise during the measurement but are not induced by the variation of the parameter under test. For this reason, the responsivity was defined as

$$\rho = \log_{10}\left[\frac{T_{sample}(\lambda = 1450\ nm)}{T_{sample}(\lambda = 1300\ nm)}\right] \tag{2.20}$$

where $T_{sample}(\lambda = 1450\ nm)$ and $T_{sample}(\lambda = 1300\ nm)$ indicate the average values calculated over a range of 101 data points (corresponding to a 10-nm-bandwidth) around the wavelength of 1450 nm and 1300 nm, respectively. The wavelength of 1450 nm corresponds to the center wavelength of the water absorption band in this region, whereas the wavelength of 1300 nm was chosen as a reference since water and ethanol are only weakly absorbing at that wavelength value. Hence, the responsivity, as defined by Equation 2.20, is a specific parameter for water detection. ρ was calculated for all water-ethanol mixtures investigated (considering both experimental and theoretical spectra) and then linearly fitted as a function of the water concentration C in the solution (expressed in % of volume). Thus, the theoretical and experimental calibration curves were retrieved. They are reported in Figure 2.10(a) for the single bounce configuration (N = 1) and for the multiple bounce configuration (N = 5 and N = 7). Results for N = 5 were obtained testing another micro-capillary coated with a top metallization with L_{met} = 4 mm. The theoretical values of ρ and of its linear fitting are in good agreement with the experimental results, proving that the number of bounces calculated with the theoretical model matches the actual one. Moreover, the sensitivity S, which corresponds to the slope of the fitting curves, was defined as

$$S = \frac{\Delta\rho}{\Delta C} \tag{2.21}$$

It was verified that it is approximately directly proportional to the number of bounces. In particular, we found that the experimental sensitivity for N = 1, 5 and 7 is equal to -0.010, -0.049 and -0.069 $\%^{-1}$, respectively, very well matching the theoretical values (-0.010, -0.050 and -0.070 $\%^{-1}$, respectively). Moreover, the LoD values (defined as $LOD = 3\sigma/S$, where σ is the standard deviation on

data) were found equal to 3.03% for N = 1, 0.73% for N = 5 and 0.29% for N = 7. It can be observed that the LoD decreases (thus improving) when N increases. The computation of responsivity and sensitivity parameters was repeated also for the experimental and theoretical spectra related to isopropanol-ethanol mixtures. Results are shown in Figure 2.10(b) for the single bounce configuration ($N = 1$) and for the multiple bounce configuration with $N = 7$. The experimental values of sensitivity are in agreement with the predicted theoretical values (reported in the Figure). Again, a direct proportionality between the number of bounces N and the sensitivity S is observed. Indeed, for $N = 1$, experimental S = -0.010 $\%^{-1}$ and theoretical S = -0.011 $\%^{-1}$; for $N = 7$, experimental S = -0.074 $\%^{-1}$ and theoretical S = -0.071 $\%^{-1}$. Moreover, the $LoDs$ were found equal to 3.19% for $N = 1$ and 0.50% for $N = 7$. In the case of multiple bounce configuration, the LoD correctly appears reduced of a factor $N = 7$.

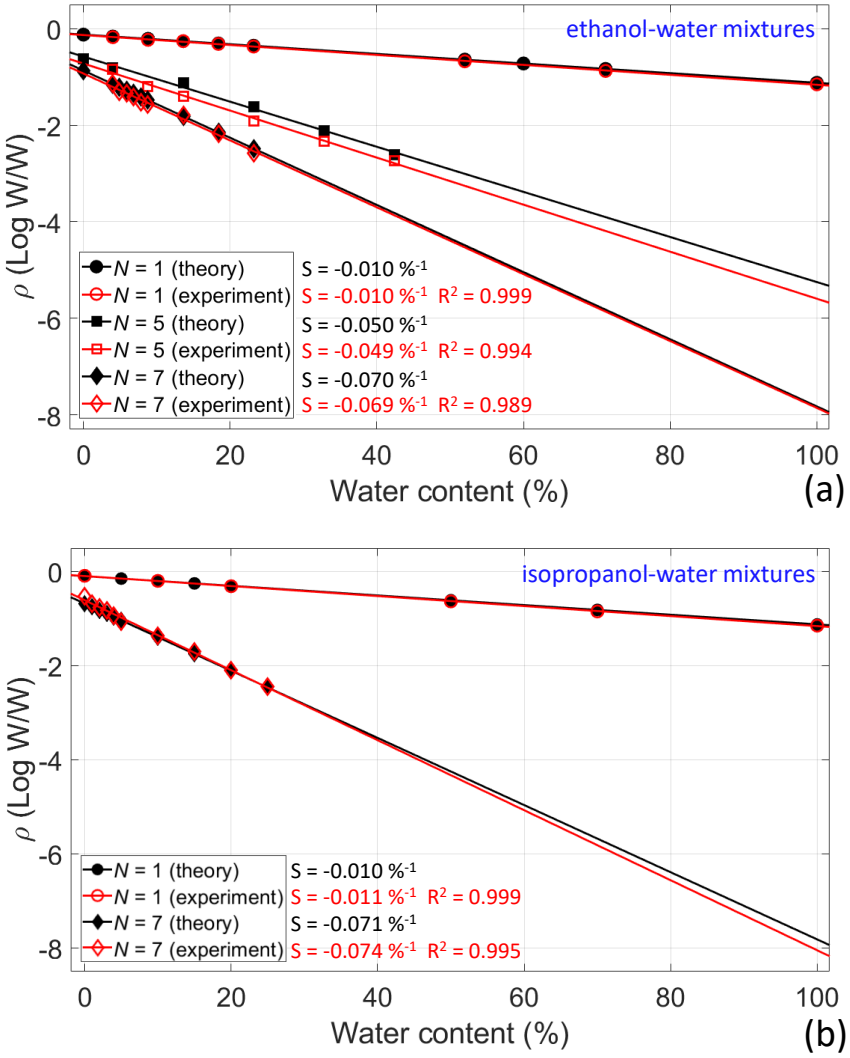

Figure 2.10: Responsivity and sensitivity results. (a) Experimental and theoretical ρ data points for single bounce ($N = 1$, circles) and multiple bounce ($N = 5$, squares, and $N = 7$, diamonds) configuration, obtained testing ethanol-water mixtures. Red and black lines: linear fitting curves as a function of the water content. (b) Experimental and theoretical ρ data points for single bounce ($N = 1$, circles) and multiple bounce ($N = 7$, squares) configuration, obtained testing isopropanol-water mixtures. Red and black lines: linear fitting curves as a function of the water content.

All the experiments described so far were carried out with fluids in static conditions inside the micro-channel. In order to verify if the proposed readout method could be applied also to more complex fluidic circuits where the fluid is in motion inside the channel and thus if the flow rate had an impact on the performances of the sensing method, the responsivity analysis on water was repeated in dynamic conditions. Hence, a programmable syringe pump was used to infuse water in the micro-capillary with different flow rates (0, 100, 200, 300, 400, 500 and 600 ml/h). These values correspond to velocity of fluid of 0, 15, 30, 45, 60, 75 and

90 mm/s. The single bounce configuration was exploited. The ρ parameter as a function of the fluid velocity is reported in Figure 2.11: its value, with an average value around -1.2, is not significantly affected by the increasing flow velocity of the sample.

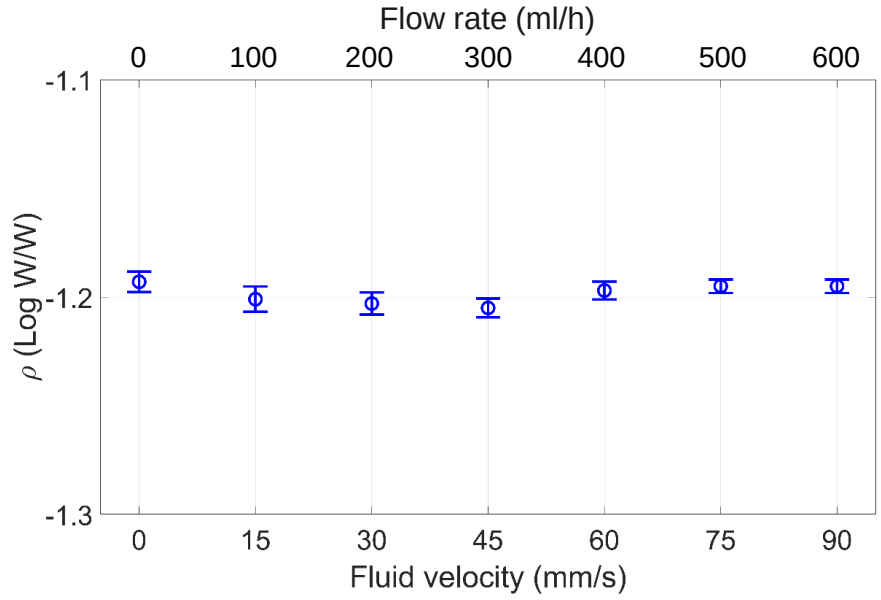

Figure 2.11: In-flow measurements: ρ parameter calculated considering water filling the micro-capillary in stationary conditions and non-stationary conditions.

2.8 Real-life sensing applications

After preliminary testing to prove its principle of operation, the proposed micro-opto-fluidic platform was exploited for real-life sensing applications. In particular, it was used for quality control of commercial hand sanitizer gels and and alcoholic beverages.

2.8.1 Quality control of hand sanitizer gels based on ethanol

Since the research activity described in this Chapter was carried out during the SARS-CoV-2 (COVID19) pandemic, the micro-opto-fluidic platform was investigated for quality control of ethanol-based hand sanitizer gels and, in particular, for the specific measurement of the water content in sanitizer gels. Ethanol-based hand sanitizer gels contain mainly water and ethanol, but also other excipients (such as hydrogen peroxide, glycerol, propylene glycol, perfumes and others). Nevertheless, their concentration is very small with respect to that of ethanol and

water: hence, by detecting with high specificity the percentage of water, it possible to obtain also a rough indirect esteem of the ethanol content. This analysis is particularly important since, at present, alcohol-based handrubs are the only known means for rapidly and effectively inactivating a wide array of potentially harmful microorganisms on hands [76, 77] and knowing the actual alcohol content is fundamental in determining the effective antibacterial action of the gel [78]. For example, the Food and Drug Administration (FDA) recommends a concentration of 60% to 95% of alcohol to ensure the germicidal efficacy [79]. On the other hand, the World Health Organization (WHO) reports that alcohol solutions containing 60–80% alcohol are most effective [80]. Moreover, for hand sanitizers, it recommends a formulation containing 80% of ethanol [81].

The experimental measurements on hand sanitizer gels were carried out exploiting the micro-capillary with L_{met} = 4 mm in the multiple bounce configuration (N = 5). Four commercial hand sanitizer gels from different brands were tested. On the labels, the composition and the percentage of alchol are reported:

- gel 1: ”Gel igienizzante mani” (PARISIENNE ITALIA S.p.A., Italy). Ingredients: ethanol, water, carbomer, parfum (fragrance), triethanolamine, propylene glycol, hexyl cinnamal, limonene, linalool, citral, citronellol, geraniol. Alcohol content declared: > 60%;

- gel 2: ”Gel mani igienizzante Fresh & Clean” (Sodalis Group, Italy). Ingredients: ethanol, water, glycering, PEG-75 lanolin, propylene glycol, benzyl alcohol, parfum, acrylates/C10-30, alkyl acrylate crosspolimer, PEG-40 hydrogenated castor oil, trydeceth-9, aminomethyl propanol, BHT, citral, citronellol, geraniol, limonene, linalool. Alcohol content declared: 60%;

- gel 3: ”Gel mani” (Farmacia San Matteo Pharmacy di Pavia, Italy). Composition: ethanol, water, excipients. Alcohol content declared: 74.2%;

- gel 4: ”Disinfect Puravir Gel” (PharmaMillenium srl, Italy). Ingredients: ethanol (CAS 64-17-5) 80g, water and excipients to reach 100 g. Alcohol content declared: 83.4%.

After experimental measurements of the transmitted power through the micro-capillary, the parameter $T_{sample}(\lambda)$ as a function of the wavelength, defined by Equation 2.17, was retrieved for every gel: it is reported in Figure 2.12(a) (color traces, shown in base-10-logarithmic scale), in comparison with the data obtained by testing some ethanol-water mixtures (black traces). The four gel spectra do exhibit a minimum at 1450 nm with different amplitude, meaning that the content

of water is different in the four fluids. Figure 2.12(b) reports the calibration curve (blue trace), obtained by linear fitting the responsivity parameter ρ as a function of water content C after testing ethanol-water solutions, with equation

$$\rho = -0.049 \cdot C - 0.721 \tag{2.22}$$

The colored dots are the data related to the tested gels: the value of the ρ parameter was computed for each gel from the experimental measurements and it was substituted in Equation 2.22 to retrieve the experimentally measured value of the water content C.

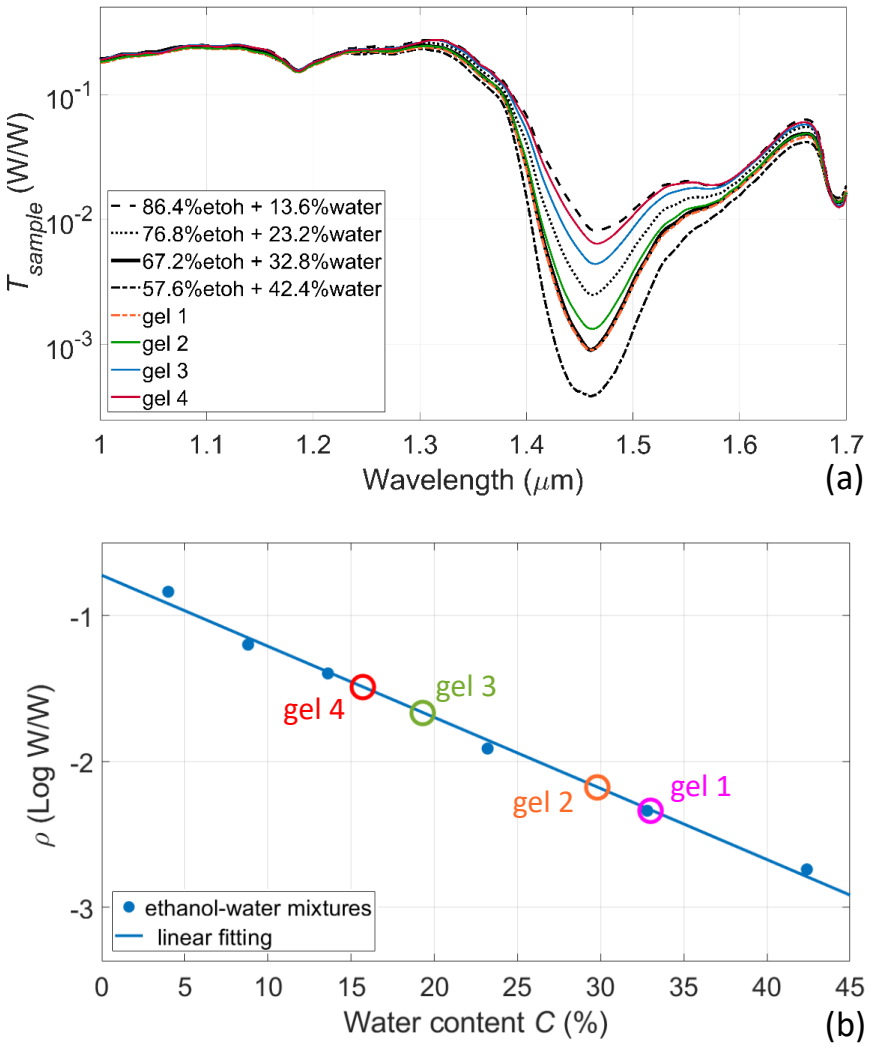

Figure 2.12: Quality control of hand sanitizer gels. (a) Spectral $T_{sample}(\lambda)$ for ethanol-water mixtures (black traces) and gels (colored traces). (b) Responsivity analysis.

Eventually, the concentration of the other excipients, that is never specifically re-

ported on the labels, can be calculated by subtraction (i.e. subtracting form the total volume of 100% the volume percentage of alcohol declared by manufactures and that of water, retrieved through the experimental analysis). Table 2.1 summarizes the results of the quality control analysis and confirms that the alcohol values reported by the manufacturers could be very close to the actual values. It was observed that the lowest content of excipients is actually found for the gel that declares explicitly on the label only alcohol and water as main components (Disinfect Puravir Gel), whereas the gel with the highest content of excipients is the product with the higher number of components declared on the label (Gel mani igienizzante Fresh & Clean). This investigation shows that the composition of the hand sanitizer gels that are commercially available can be very different and that the labels are often not completely precise.

Gel	Alcohol content declared on label (vol/vol %)	Water content C experimentally measured (vol/vol %)	Excipients content retrieved by subtraction (vol/vol %)
1	> 60	33	< 7
2	60	29.8	10.2
3	74.2	19.3	6.5
4	83.4	15.7	0.9

Table 2.1: Results of quality control on commercial ethanol-based hand sanitizer gels. The alcohol content is reported on the labels, while the water content C is retrieved by experimental measurements. The concentration of excipients is retrieved by subtraction.

These results are promising and very interesting. Indeed, they demonstrated the suitability of the micro-opto-fluidic platform for the testing of gels that have different density and viscosity from simple alcohol-water mixtures. Moreover, these measurements proved the suitability of the proposed readout method for specific detection of water content in complex fluids containing also several others ingredients.

2.8.2 Quality control of alcoholic beverages

Last, the micro-opto-fluidic platform was exploited for specific measurement of the water content in Scottish whisky, hence an alcoholic beverage used in the food industry. The sample analyzed comes from a bottle of whisky (Laphroaig Distillery, Isle of Islay, United Kindom). It contains water and ethanol; the color is adjusted by addition of a negligible quantity of caramel. The concentration of alcohol declared on the label is equal to 40%. In this situation, because of the high

water concentration to measure, experimental testing was carried exploiting the single bounce configuration (N = 1). Results are shown in Figure 2.13. The spectral output power $P_{out}(\lambda)$ (Figure 2.13) obtained by testing whisky (black dotted trace) is reported in comparison with the spectra obtained for some ethanol-water mixtures (colored traces). The spectrum for whisky is almost perfectly overlapped to that referring to a ethanol-water mixture containing 40% of water. Eventually the linear calibration curve with equation

$$\rho = -0.011 \cdot C - 0.158 \tag{2.23}$$

was retrieved (Figure 2.13(b)). The experimental value ρ for whisky was retrieved from experimental measurements and inverting Equation 2.23, the measured value of water content was found C = 65.6 %. The successful test carried out on commercial whisky proves that the proposed readout method can be applied also to liquids for dietary purposes since it is a remote, contactless and non-invasive technique that does not cause adulteration of the samples. Moreover, the liquid flows in a channel made up of glass that is a non-toxic safe material.

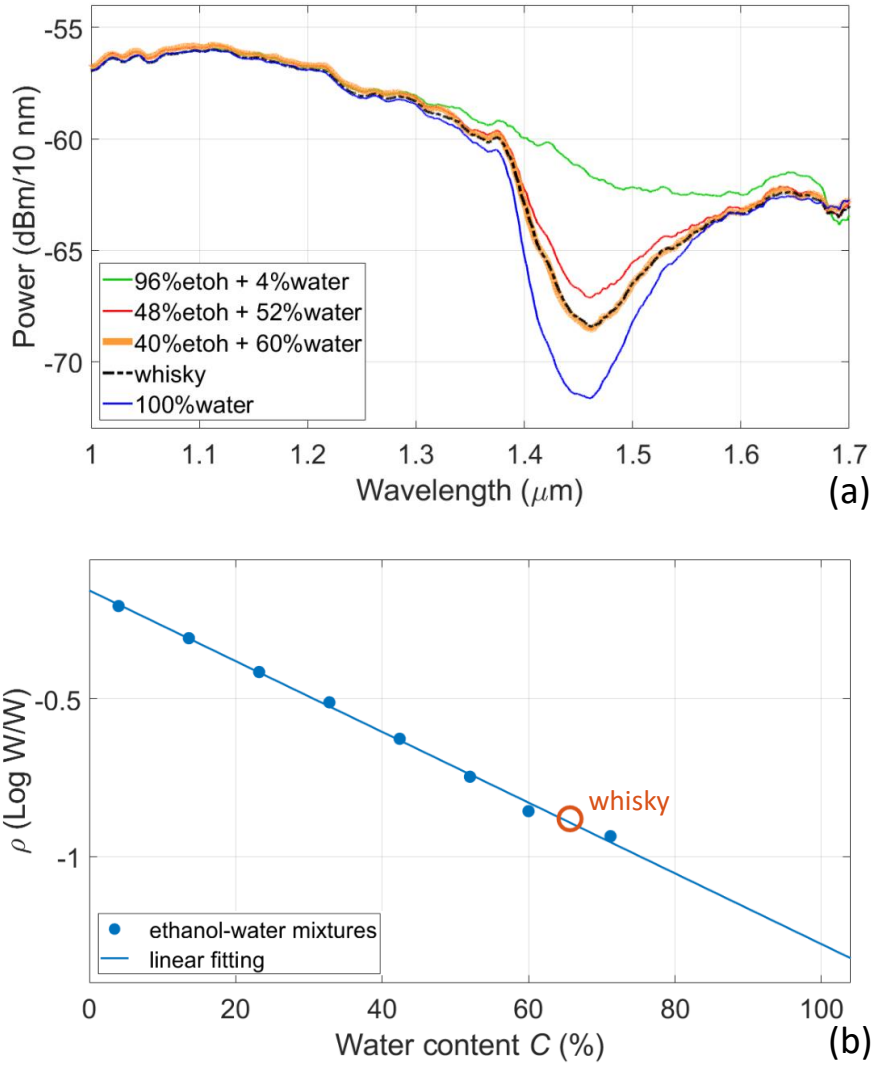

Figure 2.13: Quality control of Scottish whisky. Spectral $T_{sample}(\lambda)$ for ethanol-water mixtures (colored traces) and whisky (black dotted trace). (b) Responsivity analysis.

2.9 Conclusions and future perspectives

The research presented in this Chapter demonstrated the integration of rectangular glass micro-capillaries in a micro-opto- fluidic setup for detecting the spectroscopic features of water-alcohol mixtures in the near infrared region. The micro-capillaries were coated with a top and a bottom ultra-thin aluminum layer. This simple and low-cost technology allows to fabricate smart devices provided with integrated reflectors, so that they can be exploited to arrange a single or a multiple bounce configuration: light can bounce once or multiple times inside the capillary channel to obtain different pathlengths of the light beam in the sample. The di-

mension of the top metallization can be custom-designed according to the desired application. The single bounce configuration was employed to test water-ethanol dilutions with a high content of water; on the other hand, the multiple bounce scheme was exploited to measure solutions containing a small percentage of water with higher resolution and allowed to reconstruct the spectral absorption profile of the samples in more detail. The measurement of solutions containing two different alcohols was also possible. The experimental results were demonstrated to be in good agreement with the predictions provided by the theoretical model. To extract a parameter independent from amplitude fluctuations, the responsivity ρ, defined as the power ratio at two wavelengths, was studied as a function of the water content. Moreover, it was observed that the sensitivity S is proportional to the number of bounces. The platform was also successfully exploited fro two real-life sensing applications: quality control of hand sanitizer gels and of alcoholic beverages. The proposed readout does not require to insert a probe in the sample, as it is necessary with optrodes, but sensing can be performed remotely, contactless and non-invasively along the flow line. The rectangular section capillary could be exploited as a shunt micro-cuvette, with respect to the main flow-path. Moreover, input and output beams, on the same side with respect to the micro-channel, do not interfere with the flow or any fluidic connection.

In the future, a more compact setup can be realized exploiting two LEDs emitting at 1300 nm and 1450 nm and a photodiode (instead of the OSA) for direct power detection in the two selected bands. A similar configuration was investigated in the Laboratory of ElectroOptics, after the work presented in this Chapter, for a different application (i.e. urea detection): it is presented in Appendix B. Moreover, since the proposed sensing method is non-invasive and employs low power, future work will be devoted also to the analysis of biological fluids and samples. In particular, since we demonstrated that our readout method is specific for water detection, it could be applied to verify if a sample has been diluted with water, for example, to reveal milk adulteration.

Chapter 3

Towards an industrial real-world application: a smart opto-fluidic platform for identification of fluids for artificial nutrition at home

This Chapter is devoted to the detailed presentation and description of the research activity that was carried out at the Laboratory of ElectroOptics in the framework of the Digital Smart Fluidic project with the aim of designing and implementing an opto-fluidic platform to correctly identify mixtures used for artificial parenteral nutrition at home. The expertise and skills that I acquired in the field of optical sensing of the physical and chemical properties of fluids allowed to realize a compact prototype of a smart opto-fluidic device that can be integrated in pumps for infusion of liquids. First, the features of artificial nutrition and the goals of the projects are illustrated. The principle of operation of the sensor is described. Then, a theoretical analysis is carried out in detail. Afterwards, the instrumental configuration for preliminary experimental testing is described and the performances of different fluidic devices are compared. Then, an important Section is devoted to the presentation of the industrial prototypes that were developed and to the testing of the mixtures for artificial nutrition. Eventually, preliminary results about the detection of air bubbles in the fluidic circuit are presented.

3.1 Artificial nutrition at home and the Digital Smart Fluidic project

Every human being needs nutrition and hydration to live. When a person cannot eat or drink anymore or does not get enough nutrients or liquids, because of serious medical conditions, then nursing and medical procedures are needed to cover the individual's vital need for nutrition as well as fulfill these natural requirements with the purpose of enabling the individual to participate optimally in his/her social environment. In this framework, the expressions "artificial nutrition" (AN) and "medical nutrition therapy" are used to indicate the medical techniques and treatments applied to satisfy the nutritional needs of patients who are, temporarily or permanently, unable to feed themselves naturally [82]. Even if it is not a medical topic very often discussed, artificial nutrition plays a fundamental role in the life of a large number of patients affected by different diseases. For example, artificial nutrition is often administered to patients with inflammatory bowel disease to treat the deficiency of iron, folic acid, zinc, magnesium, calcium and vitamins [83]. Moreover, AN is fundamental to oncology patients that suffer from malnutrition as a consequence both of the cancer itself and of surgeries and anti-tumor drugs [84]. Eventually, during the COVID-19 pandemic, for subjects intubated in the intensive care unit for more than 48 hours, it has been shown that a correct AN with the supplementation of amino acids helps to lower the hyperinflammatory state and promotes normal physiological recovery [85, 86]. Also, it must be stressed that AN is highly common among children and teenagers: to them, being under AN is usually very hard from a psychological point of view since they are highly concerned about their body image and being accepted by other young people [87, 88]. Two main methods to artificially deliver nutrition to patients exist, according to the path followed inside the body (Figure 3.1). "Enteral nutrition" refers to the delivery of substances into the gastrointestinal tract using tubes. One type of tube can be placed through the nose into the stomach or small intestine (nasogastric or nasoenteral feeding tube). Other times the tube is placed directly into the stomach or small intestine through a cut in the skin (gastrostomy or jejunostomy tube). In "parenteral nutrition", instead, liquid nutrients are infused through a vein (intravenously) by inserting a central catheter into the superior vena cava or into an arm vein. In both cases (enteral and parenteral nutrition), the nutrition mixtures are administered using automated programmable pumps for infusion.

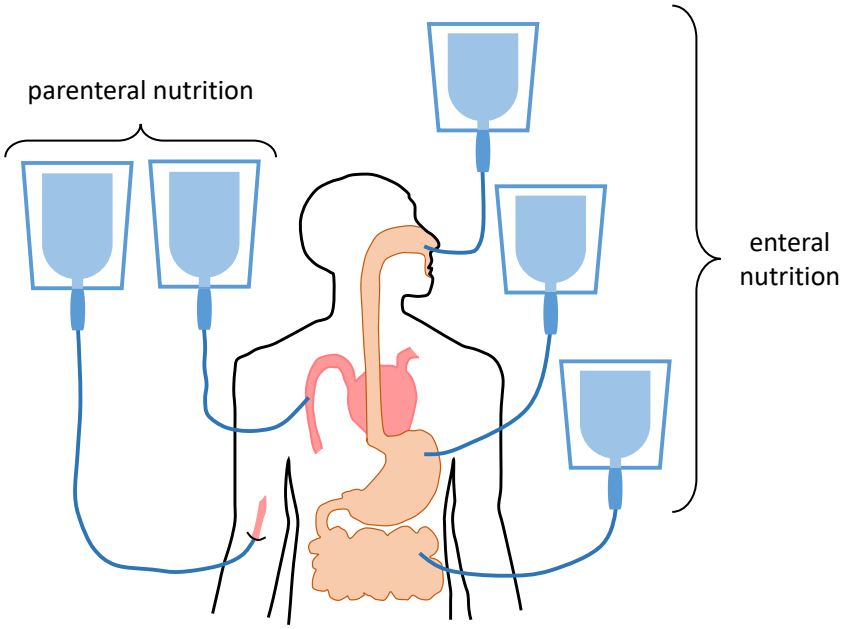

Figure 3.1: Two main types of artificial nutrition systems exist: parental nutrition, which consists in delivering nutrients to the body through the veins, and enteral nutrition, where the nutrients are administered via the gastrointestinal apparatus.

When hospitalization is not strictly necessary, to allow patients to recover in a more familiar environment, AN nutrition can be administered also at home ("artificial nutrition at home"). In this situation, a daily control by a qualified nurse is usually required and the basic steps of managing the nutrition (correct storage of liquids, cleaning of the tubes, use of the pump) have to be taught to patients. Hence, there is still a long way to go and many advancements in the AN procedures and instrumentation can be done to improve the life conditions of patients at their houses. Artificial nutrition at home is a research topics that the Digital Smart Fluidic (DSF) project focuses on. The DSF project is one of the winners of the "Research and Innovation Hub" POR FESR 2014-2020 call for tender of Regione Lombardia, that provides financial support to the of development of new technologies and facilities on the territory. The project is headed by Fluid-o-Tech, with the strong collaboration of University of Pavia, Fondazione I.R.C.C.S. Policlinico San Matteo and other companies. The DSF ultimate goal is the creation of a standardised fluidics platform to develop smart biomedical devices and equipments for hospital and home infusion therapy. The innovation promoted in this project aims to overcome the technological limits of existing biomedical devices that are bulky, expensive, non-user-friendly and often not remote-controlled. The DSF project focuses on four main therapeutic/care areas: hospitalisation, artificial nutrition at home, chemotherapy and palliative therapies and intensive care.

In particular, in the field of artificial nutrition at home, the aim of the project is to manufacture a miniaturised and intelligent artificial fluidic device that can monitor the administration of nutritive substances to patients out of the hospital. Indeed, the device could be interfaced with a web app for an efficient remote communication between patient and caregiver. Moreover, it will have a compact and light-weight design and it will be portable with rechargeable battery for a wireless use that can considerably improve the quality of life of the patients.

The Laboratory of ElectroOptics of the University of Pavia is taking part in the DSF project as research partner working on the development of an opto-fluidic device to be applied to artificial parenteral nutrition at home. This activity, presented in detail in this thesis chapter, focuses on the development of a smart optical sensor that recognizes the type of AN fluid that is being delivered to the patient's body and checks its compliance with the nutrition mixture prescribed by the doctor team. This sensor will be integrated in a smart commercial delivery pump (as shown in Figure 3.2) and, if needed, will communicate an alert message to the patient, constituting a security check system that can make artificial nutrition at home safer. In this way, the patients will be able to manage themselves the AN system at home without the constant intervention of the nursing staff, making feel them more autonomous and comfortable with AN.

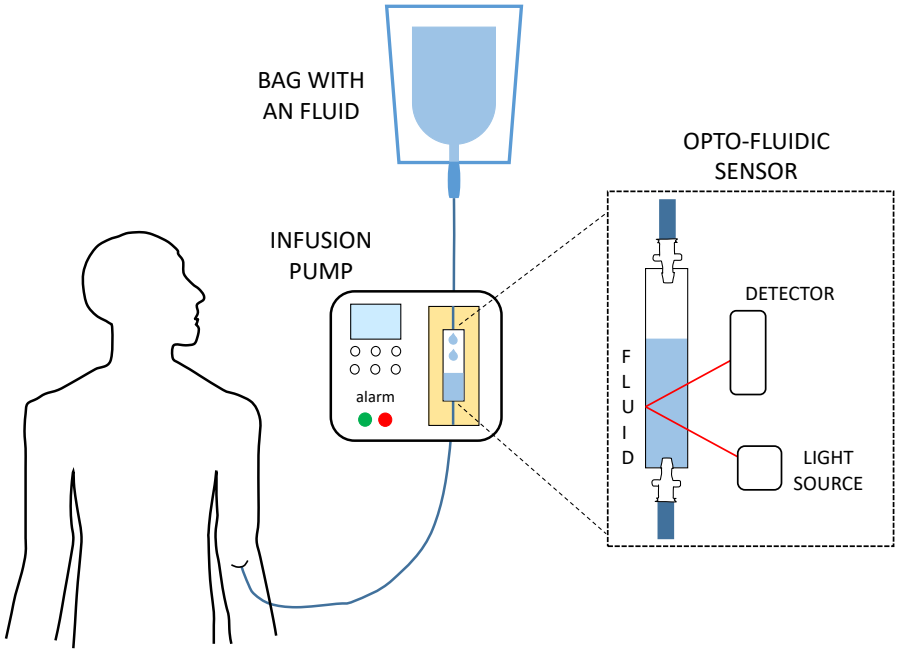

Figure 3.2: Schematic representation of the smart opto-fluididc sensor developed at the Laboratory of ElectroOptics for recognition of AN fluids and integration in commercial infusion pumps.

The composition of the AN fluids investigated and the principle of operation of the opto-fluidic sensor for recognition of the nutrients are described in detail in the following two Sections.

3.2 Fluids for enteral artificial nutrition: chemical composition and refractive index

In this work, liquid mixtures for artificial parenteral nutrition only were considered and investigated. In particular, two different types of mixtures can be administer through the veins: fluids containing amino acids, glucose and electrolytes (salts) and fluids containing amino acids, glucose, electrolytes and lipids. The lipidic component is constituted by an emulsion of suspended particles: hence, the AN fluids containing lipids have a milk-like white appearance because incident light is strongly scattered. For this reason, this kind of liquids is not suitable to be measured with the optical sensor developed during this research activity. On the other hand, AN fluids containing amino acids, glucose and electrolytes only are transparent and they were investigated and considered for experimental testing in this work. Samples of transparent AN fluids were provided by the pharmacy of the San Matteo hospital and have commercial name CLINIMIX (Baxter S.r.l., Italy) and AMINOMIX (Fresenius Kabi, Germany). The amino acids with the electrolytes and the glucose are initially contained in two different sections divided by a plastic membrane. The membrane can be easily broken to mix the liquids just before administering the AN fluid to the patient. Every type of CLINIMIX and AMINOMIX contains amino acids and glucose in variable concentrations, resulting in different amounts calories. Hence, it is reasonable to suppose that every mixture has a different refractive index, that can be considered as the characteristics parameter to distinguish the liquids. Thus, the theoretical RI value of every AN fluids ($n_{AN\ fluid}$) was estimated by computing the formula

$$n_{AN\ fluid} = n_{H2O} + \frac{\partial n}{\partial C_{glu}} \cdot C_{glu} + \sum_{q_a=1}^{N_{a\ tot}} \frac{\partial n}{\partial C_{amino}(q_a)} \cdot C_{amino}(q_a) + \sum_{q_e=1}^{N_{e\ tot}} \frac{\partial n}{\partial C_{el}(q_e)} \cdot C_{el}(q_e) \tag{3.1}$$

where n_{H2O} is RI of water, C_{glu} is the glucose concentration expressed in g/100 mL, $\frac{\partial n}{\partial C_{glu}}$ = 0.00143 100 mL/g is the RI increment coefficient for glucose [89], $C_{amino}(q_a)$ is the concentration of the qa-th amino acid expressed in g/mL, $\frac{\partial n}{\partial C_{amino}(q_a)}$ is the RI increment coefficient due to the qa-th amino acid expressed in mL/g, $N_{a\ tot}$

is the total number of amino acids contained in the AN mixture, $C_{el}(q_e)$ is the concentration of the qe-th electrolyte expressed in g/mL, $\frac{\partial n}{\partial C_{el}(q_e)}$ is the RI increment coefficient due to the qe-th electrolyte expressed in mL/g and $N_{e\,tot}$ is the total number of amino acids in the mixture. Values of the RI increment coefficient for every amino acid and electrolyte are tabulated in the literature in [90] and [91], respectively. Moreover, the exact concentration of each substance in every AN fluid is clearly reported on the leaflet (see Appendix C for details). Hence, the RI of every available AN fluid could be theoretically estimated at a wavelength of 670 nm that is the emission wavelength of the source used for optical readout (see Section 3.8 and Section 3.9), as reported in the second column of Table C.6. Then, to verify the reliability of the calculation, the RI was measured with a digital commercial refractometer (PCE-DRB 1, PCE Italia s.r.l, Italy). Results are reported in the third column of Table C.6. Since the refractometer performs the measurement at 589 nm, the RI esteem was repeated also at this wavelength (second column of Table C.6).

AN fluid commercial name	Estimated $n_{AN\ fluid}$ @670 nm (RIU)	Estimated $n_{AN\ fluid}$ @589 nm (RIU)	Measured $n_{AN\ fluid}$ @589 nm (RIU)
CLINIMIX N9G15E	1.3481	1.3503	1.3497
CLINIMIX N12G20E	1.3531	1.3554	1.3548
AMINOMIX 12%	1.3601	1.3624	1.3608
CLINIMIX N14G30E	1.3617	1.3640	1.3633
CLINIMIX N17G35E	1.3667	1.3689	1.3681
AMINOMIX 20%	1.3716	1.3738	1.3720

Table 3.1: List of the AN mixtures provided by the pharmacy of the San Matteo hospital for testing. Commercial names (first column); theoretical RI values estimated by Equation 3.1 at the wavelength of 670 nm (second column); theoretical RI values estimated by Equation 3.1 at the wavelength of 589 nm (third column); RI values measured at the wavelength of 589 nm using the commercial digital refractometer (fourth column).

From the analysis of the Table, it is possible to conclude that Equation 3.1 allows to get a reliable esteem of the AN mixtures RI, in agreement with the values experimentally measured with a standard refractometer. Moreover, C.6 shows that every AN mixture is characterized by a different RI values: therefore, refractive index is a suitable parameter to be checked to distinguish the AN fluids.

3.3 Principle of operation of the sensor

The principle of operation of the proposed opto-fluidic sensor for recognition of AN fluids is very simple and intuitive. It is based on the observation that if a light beam enters a rigid fluidic channel at a certain angle and a mirror is located behind it, then the radiation is reflected and exits the channel at a different position with respect to the entrance point. Reflectors can be located on both sides of the fluidic cell to guide light inside the channel and increase the interaction length between the radiation and the sample. In particular, if fluids with different refractive index are contained in the fluidic device, the radiation is deflected at different angles inside the liquid (according to Snell law, as explained in further detail in Section 3.4) and the light exit point shifts along the channel surface. This change of position can be easily detected by means of a Position Sensitive Detector (PSD). Hence, by a proper calibration, it is possible to retrieve the RI of the fluids in the channel after measuring the shift of the light beam position. This readout method was implemented in this work considering different types of fluidic devices, as described in detail in Section 3.3.1.

Some interesting works relying on similar principles of operation have been proposed in the literature. In 1992, Nemoto presented a simple method for measuring the refractive index of liquids [92]. A laser beam impinges obliquely on quartz cell filled with the sample: the transmitted beam is deviated from the incident one and the beam axis is determined by the knife-edge scanning method. Few years later, Docchio et al. developed a similar apparatus with the purpose of controlling the adulteration of liquids based on their RI [93]. In this system, the RI is determined by measuring the lateral displacement of a He-Ne beam, that is obliquely transmitted through a rectangular cell filled with the liquid under characterization. Here, the lateral displacement is accurately determined by a PSD. In [94], the authors demonstrated an experimental setup for measuring the refractive index of saline water, and thus its salinity, that exploited the beam deviation of a He-Ne laser caused by refraction at the receiving end face of a specifically designed fluid holder, that was partitioned into two parts by an oblique optical transmission plate: one part is filled with reference liquid, and the other is filled with saline water. Beam deviation caused by salinity change is detected by a PSD. This system is very similar to that proposed previously by Minato et al., but based on semiconductor laser [95]. In 2005 Yeh et al. proposed a high-precision yet complex measurement technique based on a double laser beam, a rectangular glass cell and a PSD to determine the concentration of glucose in aqueous solutions and their RI, with an error of 0.000444 [96]. In an other work [97], an optoelectronic sys-

tem with a red laser diode was used to measure RI variations during the alcoholic fermentation of wine in a non-invasive manner. The laser beam crosses the cell containing the sample, it is deflected according to its RI and it shifts on the active area of a PSD used for measurements. Nasibov et al. realized a non-invasive imaging-based apparatus for measuring the RI of liquids inside a cell with a precision of 10^{-4} RIU [98]. The proposed method makes use of a line structured laser beam and simultaneously probes the media at several points along the laser stripe, instead of probing at a single point when a spot laser beam is used. The main benefit is that it is possible to retrieve RI variations across a certain direction with a CCD camera by properly aligning the laser stripe in that direction. In another work, the authors realized a non-contact measuring method for obtaining the RI of a solution based on an inverse ray tracing technique [99]. They used a laser diode and an optical angle sensor constructed by two linear CCD image sensors. Then, they placed the sample in a transparent beaker and installed a reflector on the bottom of the beaker and they measured the two light rays reflected at the liquid surface and the bottom of the beaker. To meet the challenges of miniaturization of refractive index sensors, Seow et al. exploited the partial refraction phenomenon at the solid core-liquid cladding interface in an opto-fluidic planar device based on PDMS, produced on a silicon wafer by standard soft-lithography method [100].

These solutions, surely very interesting, still present some drawbacks: for example, many of them require that the sample is stored in a closed cell, thus without the possibility of in flow measurements. Moreover, large volumes of fluids are often needed for the measurement, making these systems not suitable for the analysis of ultra-low volumes. To reduce the sample volume, several works in the literature propose custom designed micro-fluidic channels requiring dedicated micro-fabrication facilities. Also, bulk and expensive instrumentation (as CCD cameras) is sometimes required. The present work aims to overcome these technological limitations: indeed, it allows both static and in flow measurements and makes use of extremely small volumes of sample (of the order of few µL or even nL). Moreover, it makes use of cheap fluidic and optoelectronic instrumentation. The proposed readout method is label free, contactless, non invasive and remote.

3.3.1 Choice of the fluidic channel

In the course of our studies, three fluidic channels with different dimensions and features were considered (Figure 3.3).

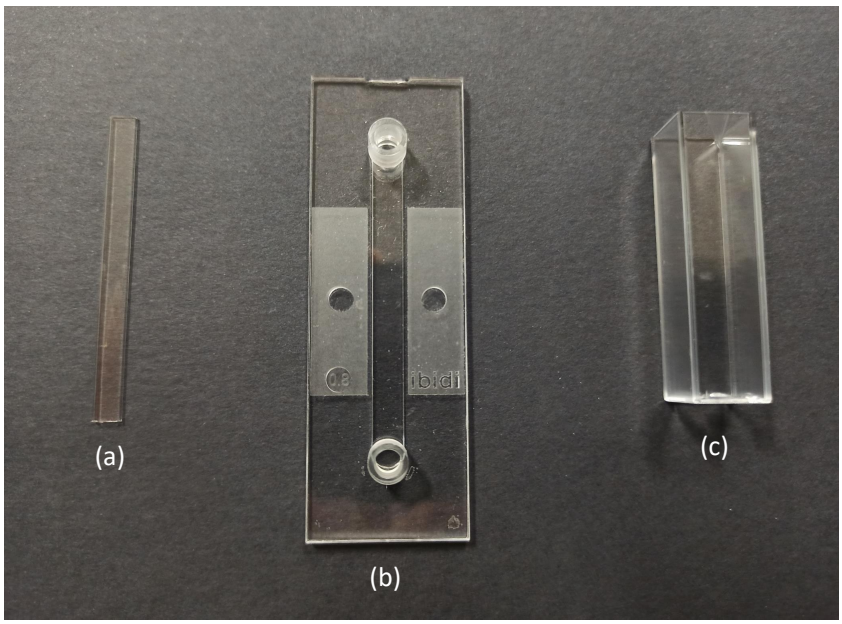

Figure 3.3: Picture of the three fluidic channels investigated in this work. (a) Rectangular glass micro-capillary. (b) Plastic IBIDI µ-Slide I Luer. (c) Polysterene standard square-section cuvette.

First, micro-capillaries by VitroCom (NJ, USA), already described in detail in Section 1.1, were investigated (Figure 3.3(a)). They are constituted of borosilicate glass with RI of 1.51 RIU. As presented in Chapter 2, they were coated with thin aluminum layers on the external sides of the glass wall to realize integrated reflectors (see Figure 2.3(b)). The back wall was fully coated, while on the front wall a few-mm long metallization was deposited. Micro-capillaries investigated in this work have nominal dimensions $d = 400$ µm and $t_f = t_b = 280$ µm. Other interesting micro-fluidic devices that were exploited are IBIDI µ-Slide I Luers, commercialized by IBIDI™ (Germany) and shown in Figure 3.3(b). They consist of a channel with length L and width W equal to 50 mm and 5 mm, respectively. Devices with channel depth d of 200, 400, 600 or 800 µm are commercially available: the small internal dimensions allow to deal with small quantities of fluids. The channel ends at both sides with standard luer connections, enabling an easy and efficient interconnection with the external fluidic system. The sample can be introduced in the channels just by means of a syringe or a micropipette or can be integrated in a more sophisticated fluidic system able to reproduce specific flow conditions. The µ-Slides are realized in polymeric material with excellent optical properties, comparable to that of glass [101], and refractive index of 1.52 RIU at 589 nm. Moreover, they are highly suitable for high-end microscopic analyses, fluorescence experiments and cell culture under perfusion and flow. In previous works

carried out at the Laboratory of ElectroOptics of the University of Pavia, IBIDI devices were exploited for RI measurements combined with low-coherence interferometry [102]. For this research, IBIDI devices with d = 800 µm were chosen, in order to consider a channel depth doubled with respect that of micro-capillaries previously described in this Section. The polymer coverslip has a thickness t_f = 180 µm, while the thickness of the front wall, measured with a Palmer tester (406-350, Mitutoyo, Japan) is $t_f \simeq 1060$ µm. As micro-capillaries, also the IBIDI devices were coated with external metallic reflectors. Eventually, standard plastic cuvettes, purchased from Cheimika S.A.S. (Italy), were considered as third fluidic channel suitable for RI measurements (Figure 3.3(c)). They have standard channel depth d of 1 cm, width $W = 1$ cm and length $L = 5$ cm. Moreover, each cuvette has four optical sides, meaning that every side wall (with thickness of 1 mm) is realized in highly transparent polysterene plastic with RI of 1.5862 RIU and high optical transmission in the wavelength range 340-900 nm [103]. Thanks to the 1-cm-by-1-cm-section of the cuvettes, it was possible to strongly increase the path travelled by the light in the fluid. Hence, only the single bounce configuration was here considered, obtained depositing only one metallic layer on the back wall, without the need of implementing a multiple bounce scheme, thus making the whole design simpler and easier to handle. On the other hand, because of the dimensions of cuvette channel, the volume of fluid required for the test is of 5 mL, that is clearly much higher than that required to perform measurements with micro-capillaries of IBIDI µ-Slides. However, this does not appear as a severe drawback since AN mixtures are administered to the patient in large volumes (0.5-2 L). Moreover, cuvettes would be a suitable device to realize a low-cost and easy-to-fabricate disposable, to be integrated in a commercial device.

3.4 Theoretical model of light propagation in the fluidic channel

Similarly to the the theoretical analysis carried out in Chapter 2, also for this research line a detailed theoretical model was implemented in MATLAB environment to study light propagation through the investigated fluidic devices (micro-capillaries, IBIDI µ-Slides, cuvettes) with different geometrical parameters. It predicts the displacement of the output beam position onto the sensitive surface of the PSD when the considered device is filled with samples with different RIs. The same theoretical model, taking into account just few adjustments, can be applied to study either the single bounce or the multiple bounce configuration. Some of

the formulas of this model (e.g. those to calculate the number of bounces) are exactly identical to the equations of the theoretical analysis presented in Chapter 2. However, all the equations are here written and explained again for sake of completeness. A schematic representation of light travelling inside the fluidic channel in case of single bounce configuration is reported in Figure 3.4.

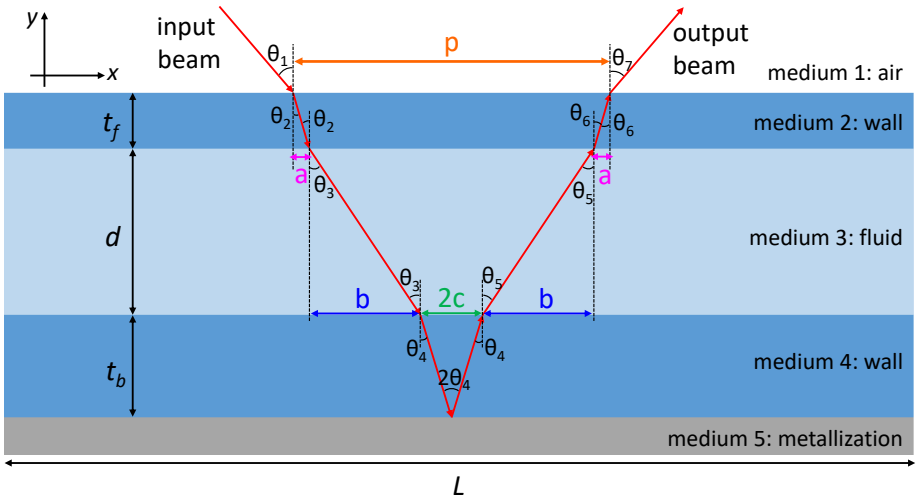

Figure 3.4: Schematic representation of the path travelled by the light in the fluidic device, considering the single bounce configuration.

As previously explained in Chapter 2, to study the path travelled by light in the fluidic devices, the geometrical ray optics approximation can be applied since the dimensions of the channels are much larger than the considered wavelength values and the beam has a very limited divergence. Each fluidic device was considered as a multi-layer structure composed of three layers with finite thickness (front wall with thickness t_f, channel with depth d and back wall with thickness t_b) inserted between two infinite media (either air/metallization in the single bounce scheme or metallization/metallization in the multiple bounce configuration). The front metallization (when present) was considered for modelling the multiple bounce configuration (Figure 3.6). The metallic layers act as mirrors, specularly reflecting the incident light. The RI of air is equal to 1, while the absorption effect of the samples was neglected since it does not affect the path travelled by the light. Moreover, at the wavelengths emitted by the considered laser diodes (around 650 nm) the absorption of water (that is the main component of the tested fluids) is very weak. As it is well known, when light crosses the separation surface between two different media, it is partially reflected and partially transmitted. Here, only the transmission is relevant and the deflection of the transmitted beam can be cal-

culated computing the Snell law:

$$n_j \cdot \sin\theta_j = n_l \cdot \sin\theta_l \tag{3.2}$$

where the subscripts j and l indicate the origin and destination medium, respectively, n_j and n_l are the refractive indices of the two dielectric media and θ_j and θ_l are the incidence and transmission angles, respectively. When radiation encounters the metallization, it undergoes a specular reflection. By recursively applying the Snell formula, it is possible to calculate the effective pathlength inside the overall structure. In particular, the geometrical distance p between the entrance and exit positions of the light beam in the fluidic device depends on the sample RI and can be computed as

$$p = 2a + 2b + 2c \tag{3.3}$$

where a, b and c are the orthogonal projections of the path that light travels in the front wall, channel and back wall, respectively. They can be retrieved as

$$a = t_f \cdot \tan\theta_2 \tag{3.4}$$

$$b = d \cdot \tan\theta_3 \tag{3.5}$$

$$c = t_b \cdot \tan\theta_4 \tag{3.6}$$

If $t_f = t_b$ (i.e. for the micro-capillaries and cuvettes), then $2a = 2c$. In the single bounce configuration (that is when no top metallization is present or when the light is shone far from it, so that its guiding effect is not present) light bounces once on the back metallization and it crosses the fluidic channel containing the sample twice. If fluids with different RI are tested (Figure 3.5), then the light beam exits the channel always with an output angle equal to the incidence angle (indeed, in the figure the green, blue and red output arrows are all parallel), but its exit position along the fluidic device surface does change: in particular, for increasing values of RI, it is moved closer to incident input beam and the value of p decreases. Figure 3.5 highlights this feature: if the green, blue and red lines corresponds to the paths of light when the channel is filled with sample with RI equal to n_1, n_2 and n_3, respectively, and $n_3 > n_2 > n_1$, then $p_3 < p_2 < p_1$.

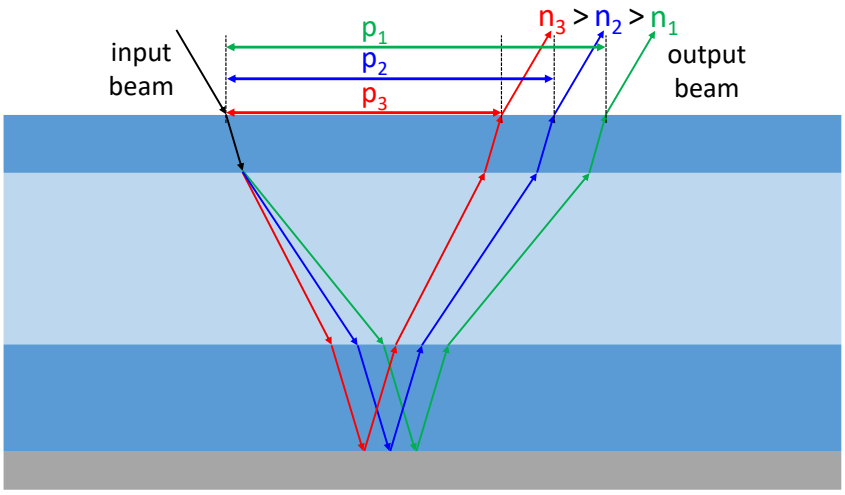

Figure 3.5: Schematic representation of light beam crossing the channel in the single bounce configuration when different samples with increasing RI are considered in the channel.

The same model is also exploited to study the multiple bounce configuration (Figure 3.6). In this particular case, thanks to the presence of the front metallization, the light beam is zig-zag guided inside the fluidic channel and it crosses the sample multiple times. The number of bounces N, as already explained in Chapter 2, depends on the length of the front metallization L_{met} and it is given by

$$N = CEIL(L_{met}/p) \tag{3.7}$$

where $CEIL$ is the MATLAB function that returns the smallest integer value that is larger than or equal to L_{met}/p. In the single configuration, $N = 1$. With the multiple bounce configuration, the shift of the output beam is strongly enhanced: the higher the number of bounces N, the longer the distance p. For the multiple bounce configuration the model can also be used to predict the exact length of the front metallization, after the number of bounces has been chosen, simply inverting Equation 3.7.

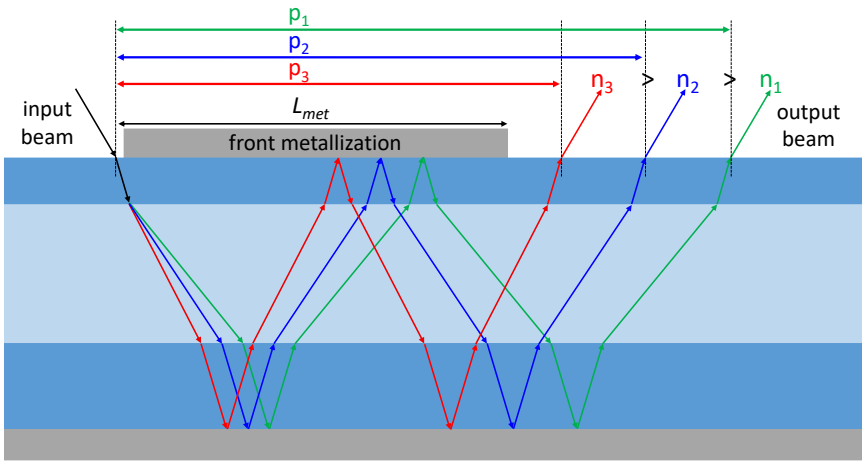

Figure 3.6: Schematic representation of light beam crossing the channel in the multiple bounce configuration when different samples with increasing RI are considered in the channel.

3.5 Results of theoretical analysis

Theoretical simulations were carried out in MATLAB environment by implementing the model presented in Section 3.4, in order to estimate how the channel depth and the number of bounces (in case of multiple bounce configuration) affect the relationship between the geometrical distance p and the refractive index n of the tested fluid. Moreover, the theoretical analysis allowed to compare the performances of the different fluidic channels (micro-capillaries, IBIDI µ-Slides and cuvettes).

3.5.1 Achievable theoretical performances with glass micro- capillaries

Simulations for a micro-capillary with external metallization on the back wall and with nominal geometrical parameters d = 400 µm and $t_f = t_b$ = 280 µm were first carried out considering the single bounce configuration. The angle of incidence (θ_1 in Figure 3.4) has been selected θ_1 = 45°. Such value was chosen because it ensures a good trade-off between increase of the light path inside the channel and limitation of the losses due to reflection at the interfaces. The RI of the glass wall was considered equal to 1.51 RIU: glass RI dispersion was not kept into account since only laser sources with narrow emission spectrum were used for experimental measurements in this work. Moreover, since VitroCom declares a tolerance of ±10% for the channel depth, simulations were repeated also considering the

two extreme cases $d = 360$ µm and $d = 440$ µm. Indeed, if the channel depth changes, also the interaction length between the radiation and the sample is modified. Initially, the theoretical analysis was carried out by calculating the geometrical distance p between the entrance and exit positions of the light beam in the fluidic device (given by Equation 3.4), for the single bounce configuration, as a function of the sample RI in the range 1-2 RIU, corresponding to the refractive index of real fluids (Figure 3.7(a)). It can be observed that the value of p decreases for increasing RIs. Moreover, its behaviour is not linear but it can be linearized when considering smaller RI intervals, for example between 1.30 and 1.39 RIU, as shown in the zoomed plot of Figure 3.7(b). This simulation also demonstrates that the single bounce configuration can be exploited for absolute measurement of a sample RI by comparing the position p obtained with fluid in the micro-capillary with that obtained with the empty channel. Absolute RI measurements are not possible with the multiple bounce configuration, since high values of RI could lead to a different number of bounces from that obtained with air in the channel. Hence, the multiple bounce configuration is suitable only to detect small RI variations with respect to a reference fluid.

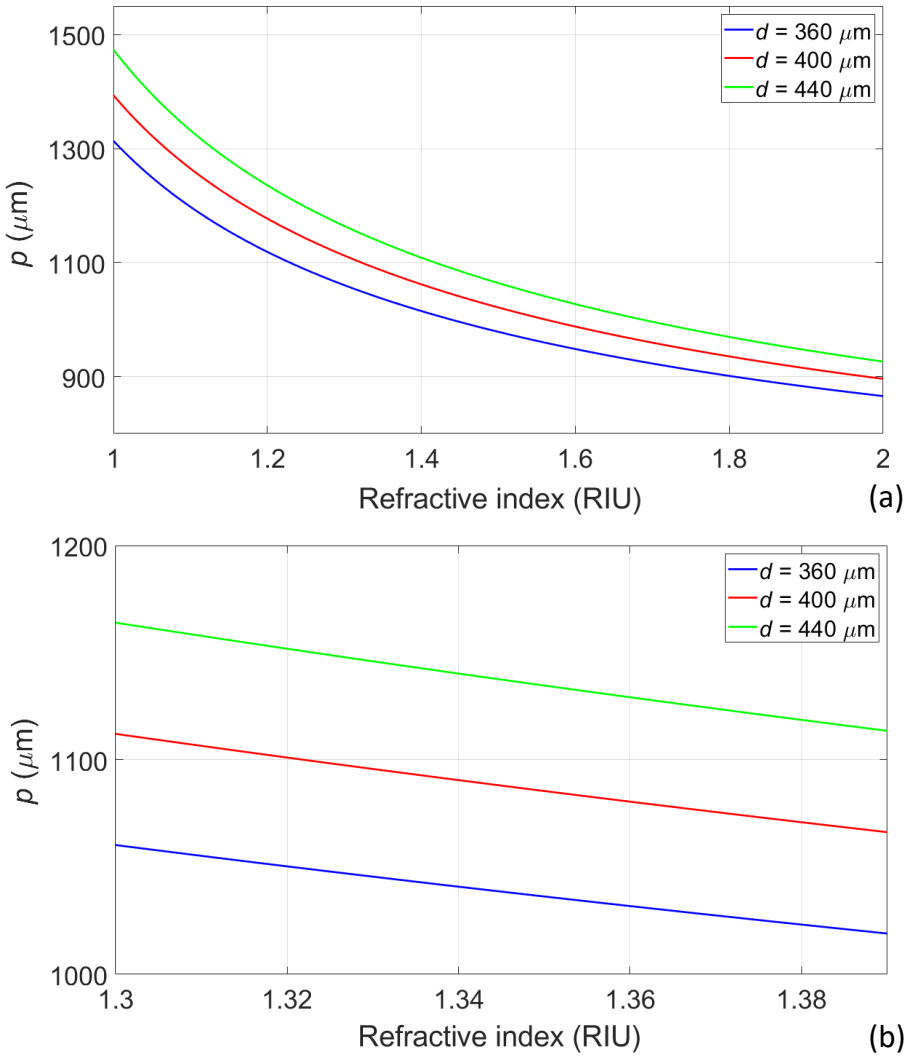

Figure 3.7: Results of the theoretical analysis obtained for a micro-capillary with channel depth d = 360, 400 or 440 µm in the single bounce configuration (N = 1). (a) Calculated geometrical distance p as a function of RI in the range 1-2 RIU. (b) Zoomed view: p can be linearized in the smaller interval from 1.30 to 1.39 RIU.

The theoretical analysis was then carried on by considering fluids filling the micro-capillary with RI of 1.3314, 1.3386, 1.3459, 1.3553, 1.3604, 1.3676 and 1.3792 RIU. Such values correspond to water-glucose dilutions in concentration of 0 (water), 5, 10, 16.5, 20, 25 and 33% respectively. For every considered sample, the shift X of the light beam along the micro-capillary was obtained by computing the difference

$$X = |p_{fluid} - p_{water}| \tag{3.8}$$

where p is calculated with Equation 3.3 and $|\,|$ indicates the absolute value. The exit

position of the beam obtained simulating the presence of water in the channel was chosen as reference. By linearly fitting the shift X as a function of the liquid RI the theoretical calibration curves were obtained (Figure 3.8). The shift X of the laser spot is maximum for the sample with the highest RI. Moreover, the sensitivity S, defined as $S = \Delta X/\Delta n$, which corresponds to the slope of the calibration curves, depends on the channel depth d and increases for higher values of d, taking values between about 450 and 550 µm/RIU.

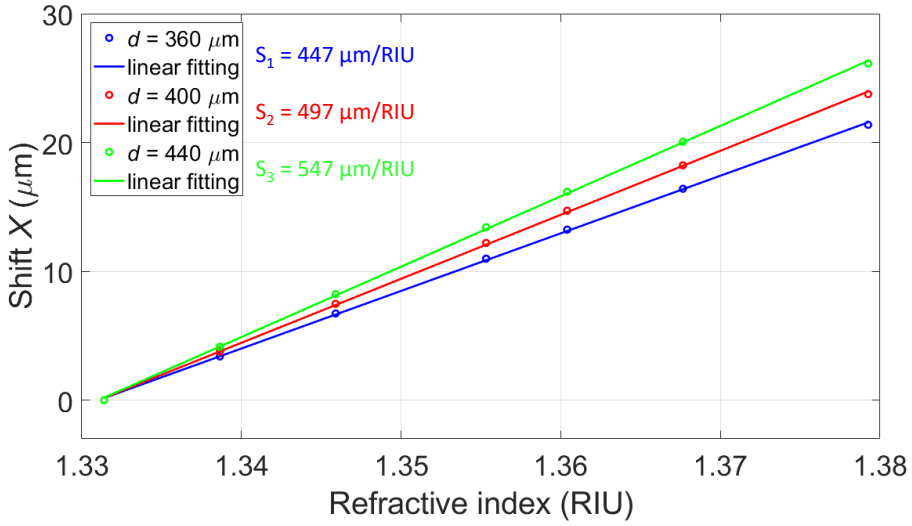

Figure 3.8: Theoretical calibration curves for a micro-capillary with channel depth d = 360, 400 or 440 µm, considering the single bounce configuration (N = 1).

Afterwards, the theoretical analysis was repeated considering the same micro-capillary with the presence of a front metallization with length L_{met} = 6 mm in order to simulate the multiple bounce configuration. The considered angle of incidence is the same, $\theta_1 = 45°$ and also in this case the simulations were repeated considering d = 360, 400 or 440 µm. The theoretical model allowed to estimate a number of bounces N = 6 for all the three cases. The theoretical calibration curves are reported in Figure 3.9. Since the interaction length between light and sample is here strongly increased with respect to the single bounce configuration, higher sensitivity values were found. The sensitivity S varies between around 2680 µm/RIU (d = 360 µm) and 3280 µm/RIU (d = 440 µm). For the same value of d, it can be observed that the multiple bounce sensitivity $S_{multiple}$ is increased by a multiplying factor N (number of bounces) with respect to the single bounce configuration:

$$S_{multiple} \simeq N \cdot S_{single} \tag{3.9}$$

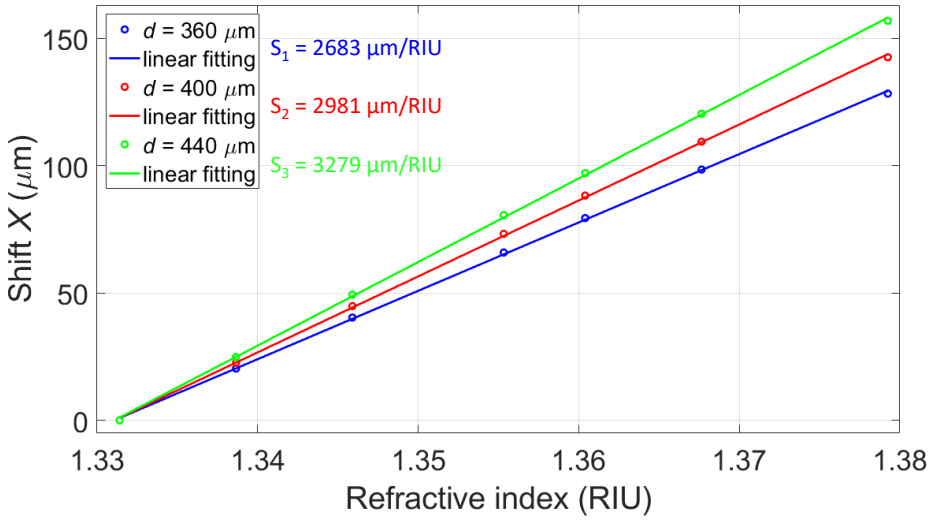

Figure 3.9: Theoretical calibration curves for a micro-capillary with channel depth d = 360, 400 or 440 µm, considering the multiple bounce configuration (N = 6).

3.5.2 Achievable theoretical performances with IBIDI µ-Slides

The theoretical simulations were then performed considering an IBIDI µ-Slide with back external metallization and dimensions t_f = 180 µm, d = 800 µm and t_b = 1060 µm, exploited in the single bounce configuration. The angle of incidence (θ_1 in figure 3.4) is of 45°. The refractive index of the polymeric layers was considered equal to 1.52 RIU, as reported on the device datasheet. The theoretical analysis was carried out considering samples filling the micro-capillary with RI of 1.3314, 1.3386, 1.3459, 1.3553, 1.3604, 1.3676 and 1.3792 RIU, corresponding to water-glucose dilutions in concentration of 0 (water), 5, 10, 16.5, 20, 25 and 33% respectively. No tolerance is reported by the manufacturer for channel depth and wall thickness, but it is reasonable to suppose that the IBIDI µ-Slide actual dimensions could slightly differ from the nominal ones. Moreover, due to the pressure exerted by the fluids on the plastic walls of the channel, the IBIDI µ-Slide could be slightly deformed during the measurements. Hence, also for the IBIDI device a deviation of ±10% on the parameter d was considered and the theoretical study was carried out for d = 720, 800 and 880 µm. The theoretical calibration curves are shown in Figure 3.10. As already observed in Section 3.5.1, the sensitivity S increases for higher values of the channel depth d and is equal to 894, 994 and 1093 µm/RIU. Moreover, making a comparison with the performances obtained with the micro-capillary, the sensitivity is here multiplied by a factor 2 since the channel depth of the IBIDI µ-Slide is twice that of the micro-capillary.

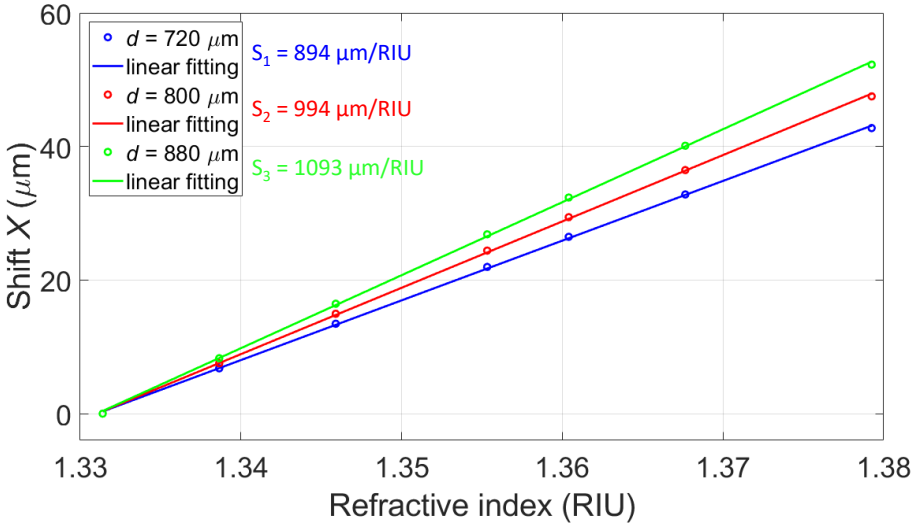

Figure 3.10: Theoretical calibration curves for an IBIDI µ-Slide with channel depth d = 720, 800 or 880 µm, considering the single bounce configuration (N = 1).

The theoretical analysis was then repeated for the configuration of multiple bounces, considering a front metallization with length L_{met} = 5 mm. Results are reported in Figure 3.11. It has to be noted that the number of bounces N, which turned out to be equal to 3, is here much-smaller than in the case of the micro-capillary even if the length of the front metallization is only 1 mm shorter. This feature is due to the deeper channel d, but also to the fact that the back polymeric layer of the IBIDI device is much thicker (1060 µm) with respect to the back wall of the capillary (280 µm). It is important to stress that the thickness of the walls does not have a direct effect on the light path in the channel, but it does affect the number of bounces and thus, indirectly, also the sensitivity of the multiple bounce configuration. As already observed for the micro-capillary, in the multiple bounce configuration the sensitivity is N-times the sensitivity of the single bounce configuration.

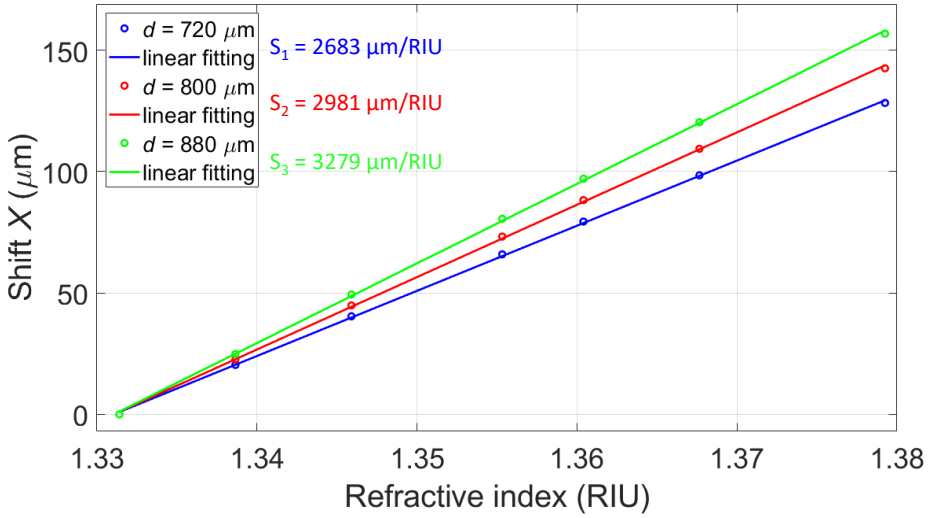

Figure 3.11: Theoretical calibration curves for an IBIDI μ-Slide with channel depth d = 720, 800 or 880 μm, considering the multiple bounce configuration (N = 3).

3.5.3 Achievable theoretical performances with standard square section cuvettes

Numerical simulations were eventually carried out considering a standard cuvette made of polysterene with RI of 1.5862 RIU and geometrical parameters $d = 1$ cm and $t_f = t_b = 1$ mm. Since the optical path offered by the cuvette is more than 10 times larger than that provided by the μ-Slide in the single bounce configuration, the theoretical study was carried out considering the presence of a back metallization only. Hence, the multiple bounce scheme has not been investigated. Moreover, cuvettes are well-established standard devices that have to be manufactured with reliable dimensions (1-cm-by-1-cm section), since they are mainly produced for spectroscopic analysis in commercial spectrophotometers. Hence, it is reasonable to believe that the actual dimensions well match the nominal ones. For this reason, only the nominal dimension for the channel depth d was considered in the simulation. On the other hand, the theoretical analysis was carried out considering different values of the angle of incidence θ_1 (40, 45 and 50°). Indeed, during the experimental testing, while the micro-capillary and the IBIDI channel were glued to a flat metallic support, the cuvette was simply located vertically but not pushed towards a flat support: hence, the alignment of the cuvette at an exact angle was a critical point. For this reason, different angles of incidence were considered. Also for the cuvette, samples with RI of 1.3314, 1.3386, 1.3459, 1.3553, 1.3604, 1.3676 and 1.3792 RIU, corresponding to water-glucose solutions with

concentration equal to 0 (water), 5, 10, 16.5, 20, 25 and 33% respectively, were simulated. Figure 3.12 shows the theoretical calibration curves. The sensitivity S, varying in the range 10271-14884 µm/RIU, is strongly enhanced with respect to the case of micro-capillaries and IBIDI devices thanks to the very long optical path in the sample. Moreover, the simulations proved that the angular position of the cuvette (i.e. different angle of incidence) has a remarkable effect on the value of sensitivity.

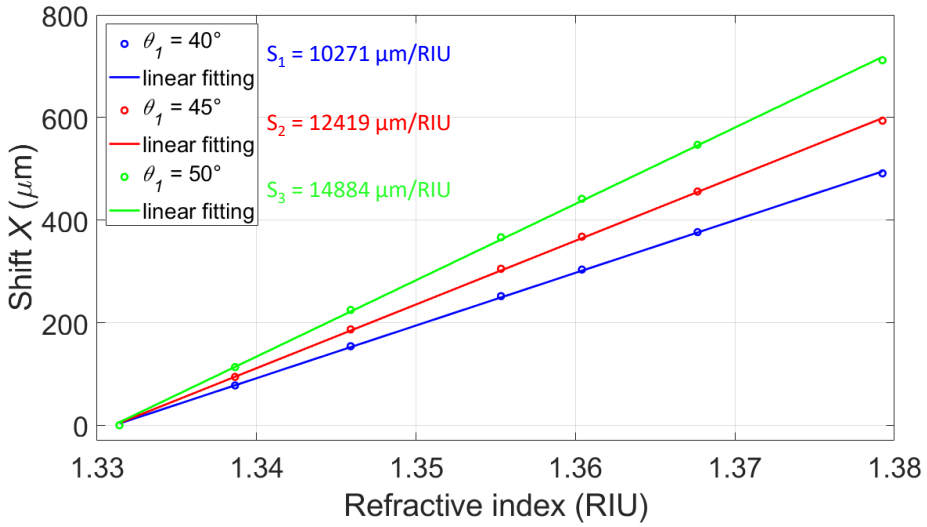

Figure 3.12: Theoretical calibration curves relative to a cuvette with variable angle of incidence (θ_1 = 40, 45 or 50°), considering the single bounce configuration (N = 1).

3.6 Opto-fluidic sensing platform for experimental testing

An opto-fluidic platform was designed and implemented to perform preliminary experiments with water-glucose dilutions. The general scheme of the instrumental configuration is reported in Figure 3.13.

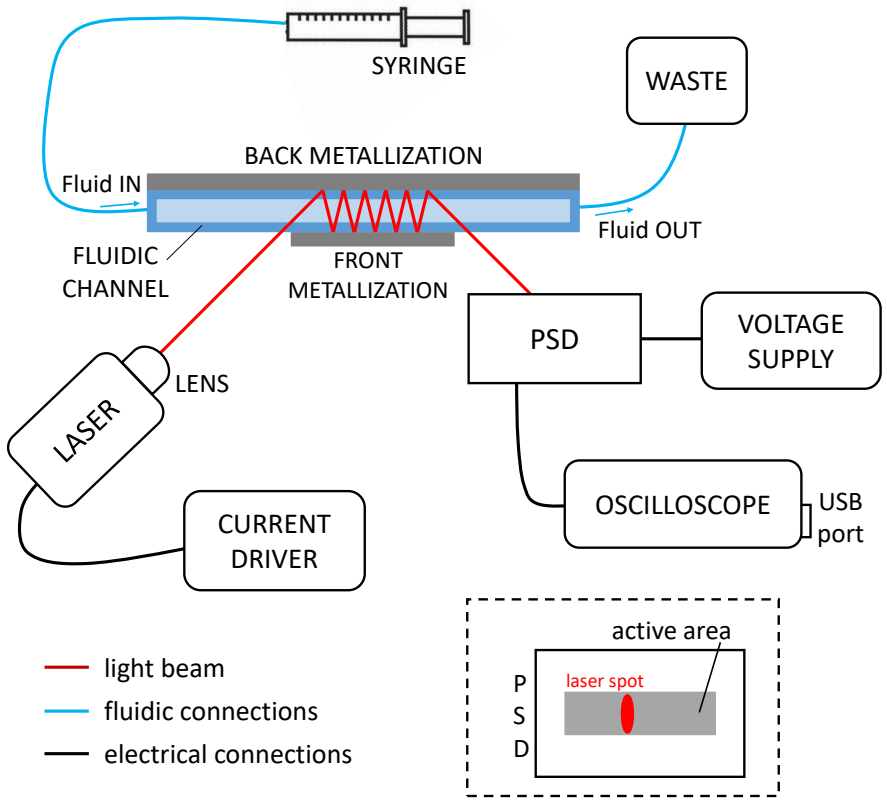

Figure 3.13: Schematic representation of the opto-fluidic platform for experimental testing. Inset: orientation of laser spot with respect to the PSD.

The readout beam is provided by a semiconductor laser diode (DL3147-060, Sanyo, Japan) emitting visible light at a wavelength of 650 nm with a maximum optical power of 7 mW and nominal threshold current of 20 mA. The source is controlled by a current driver (LDC 500, Thorlabs, NJ, USA). Light beam is shined onto the flat surface of the fluidic channel with an angle of incidence of 45°. A lens (LTN330-B, Thorlabs, NJ, USA) with focal length of 3.1 mm, numerical aperture equal to 0.68 and anti-reflection coating from 600 to 1050 nm is placed in front of the source and the light beam is focused in order to obtain the smallest light spot onto the surface of the photodetector. The readout beam crosses the fluidic channel only twice, bouncing on the back metalizzation, or multiple times when also a front metallization is deposited on the external side of the front wall. All the metal layers (in aluminum) were realized by sputtering deposition in high vacuum environment by VAQUARZ (Italy). The ending parts of the channel are connected to plastic tubes, so that the liquid sample is flowed inside using a syringe. In particular, minor adjustments have been made to adapt the fluidic connections to the different types of channel. For example, while the IBIDI devices are already provided with luer connectors, the micro-capillary ends were inserted in heat-shrink

tubings for connection with luer adapters. On the other hand, the cuvettes, that have one open side and the other closed, were customized with the addition of plastic connectors 3D printed by the Proto-Lab of the DICAr (Dipartimento di Ingegneria Civile ed Architettura) of the University of Pavia. After the interaction with the fluid, the light beam reaches a 1-dimensional linear PSD that is oriented parallel to the flat surface of the channel, at a distance of few millimeters. The PSD is a peculiar light detector that allows to measure the position of the light spot reaching its sensitive area and its variations with a resolutions of few micrometers. It has to be noted that the light spot generated by the semiconductor laser diode has an elliptical shape because of the different divergence of the beam in the x and y variation due to the rectangular section of the laser chip. Also, the radiation is polarized along the main axis of the ellipse. Hence, the laser spot is carefully oriented orthogonally with respect to the direction of the longer dimension of the PSD active area (as shown in the inset of Figure 3.13). The PSD is powered with a voltage supply (PS283, Tektronix, OR, USA). After the measurement, the sample is discarded by pushing air in the channel in the case of the micro-capillary and the IBIDI device, while the cuvette, vertically positioned, is emptied simply by gravity force. All the measurements were performed with fluids in static conditions in the channels. The output signals supplied by the PSD are visualized in real-time and then acquired with an oscilloscope (MDO3034, Tektronix, OR, USA) with USB connection. Eventually, data are processed in MATLAB environment.

3.6.1 Features of the Position Sensitive Detector

The 1-dimensional linear Position Sensitive Detector is a photodetector able to measure the position of the centroid of the impinging light spot along one spatial dimension. The PSD used in this work (1L10-SU74-SPC02), shown in Figure 3.14, was purchased from SiTek Electro Optics AB (Sweden) and is constituted by a sensitive area with length L_{PSD} = 10 mm and width of 2 mm. The chip has a total area of 20.5 mm $\times$ 20.5 mm. It is powered with ±15 V voltage supply and has a transimpedance gain of 10^5 V/A and a bandwidth of 400 kHz. This PSD is provided with attached signal processing circuit and provides two voltage signals:
- the difference signal $V_1 - V_2$, which carries information about the position of the light spot along the sensor area;
- the sum signal V_1+V_2, which is proportional to the total optical power that reaches the detector.
V_1 and V_2 are proportional to the currents that are photogenerated at the extremities of the sensitive region and depend on the position of the light spot: if it is located

at the center of the sensing region, then $V_1 = V_2$ and $V_1 - V_2 = 0$. The light spot position on the PSD p_{PSD}, with respect to the center of the sensitive area, can be retrieved by computing the formula

$$p_{PSD} = \frac{L_{PSD}}{2} \cdot \frac{V_1 - V_2}{V_1 + V_2} \tag{3.10}$$

This specific PSD was chosen for the preliminary steps of this study because the quite long length of its sensitive area (10 mm) allows to measure light beam displacements without any kind of limitations. Hence, even if the larger predicted displacement (obtained in this work with the cuvette, according to the theoretical simulations) is roughly between 500 µm and 1 mm, also much larger shifts of the laser spot (that could be obtained with different fluidic channels) could be detected with the same PSD. Moreover, the PSD datasheet reports that position linearity is valid within 80% of the detector length (equal to 8 mm) [104]. Hence, the PSD was aligned in such way to shine the laser spot always in the central part of the sensitive area, where the linear operation of the devices is guaranteed for measurement of a displacements typically smaller than 1 mm. About noise performances, a good signal-to-noise ratio is always ensured since the laser light is not strongly attenuated and the power level reaching the PSD is always of the order of 1-2 mW.

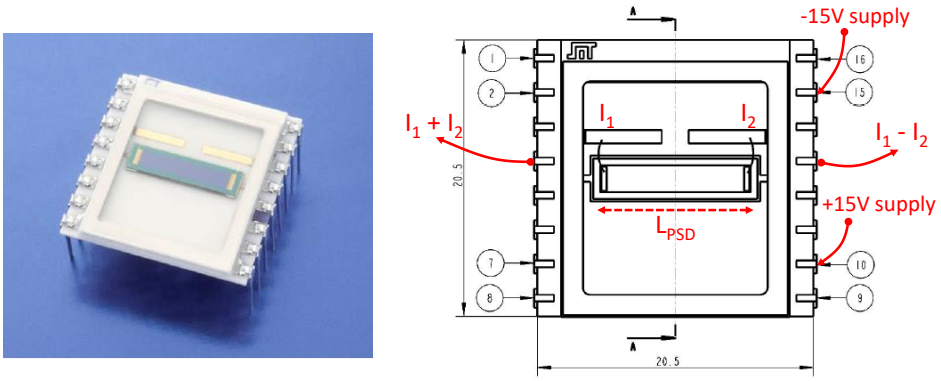

Figure 3.14: Position Sensitive Detector. (a) Picture of the device. (b) Schematic representation of the sensor with electrical connections.

3.7 Experimental results

In order to prove the suitability of the proposed readout method for refractive index monitoring, preliminary experimental measurements were performed by flowing

mixtures of glucose in deionized water in different concentration in the considered fluidic channels. Thus, it was possible to compare the performances offered by micro-capillaries, IBIDI µ-Slides and cuvettes and to study the compliance of the experimental results with the expected behaviour predicted by the theoretical model.

3.7.1 Experimental measurements on micro-capillaries

Experimental measurement were first carried out on a micro-capillary with nominal geometrical dimensions d = 400 µm and $t_f = t_b =$ 280 µm and front aluminum metallization with length L_{met} = 6 mm. The back side of the device was externally coated along its entire length. Experiments were performed by filling the channel with solutions of glucose in distilled water in concentration equal to 0, 5, 10, 16.5, 20, 25 and 33% corresponding to RI values of 1.3314, 1.3386, 1.3459, 1.3553, 1.3604, 1.3676 and 1.3792 RIU. The experimental analysis was performed first considering the single bounce configuration and shining the readout beam far from the front metallization. Then, it was repeated in the multiple bounce configuration, thus exploiting the guiding effect provided by both metallic layers deposited on the external walls. The laser current was set to 22.4 mA and 25.5 mA in the single and multiple bounce configuration, respectively, to ensure a good signal-to-noise ratio and avoid output signal saturation. When different fluids flow in the channel, the position of the output beam changes as explained in Section 3.4. Hence, using a PSD detector it is possible to measure this variation of position. In particular, as explained in Section 3.6.1, the PSD provides the difference ($V_1 - V_2$) and sum ($V_1 + V_2$) voltage signals. An example of $V_1 - V_2$ and $V_1 + V_2$ signals acquired while testing the single bounce configuration is reported in Figure 3.15. The difference signal carries information about the beam position and, thus, its value changes for different RIs of the sample. The spikes between the almost constant-amplitude regions occur when the channel is emptied and a new sample is injected: so, during the transient, air temporarily fills the channel. The sum signal is proportional to the total optical power reaching the PSD sensitive surface and it stays almost constant for every sample, but it is necessary to normalize the difference signal and compensate for spurious changes of light intensity on the detector.

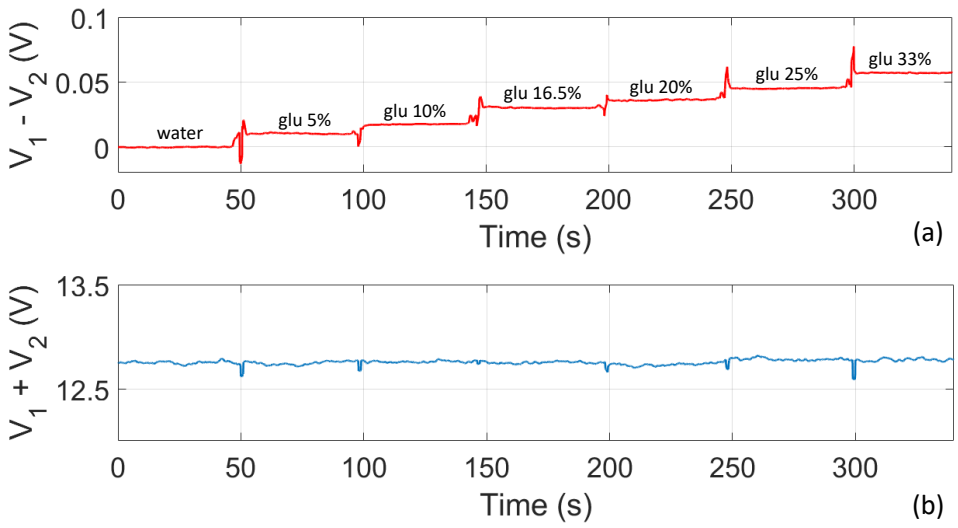

Figure 3.15: Example of typical difference $V_1 - V_2$ (a) and sum $V_1 + V_2$ (b) signals in the time domain acquired with the PSD.

The position p_{PSD} of the light beam measured by the PSD is then retrieved by applying Equation 3.10. Figure 3.16 shows the variations of the beam position p_{PSD} impinging on the PSD as a function of time when water-glucose dilutions are tested in the single bounce (Figure 3.16(a)) and multiple bounce (Figure 3.16(b)) configuration. From the comparison between the two traces, it can be observed that, for a given sample, the shift of the beam position is much higher in the multiple bounce configuration due to the longer path travelled by light in the sample.

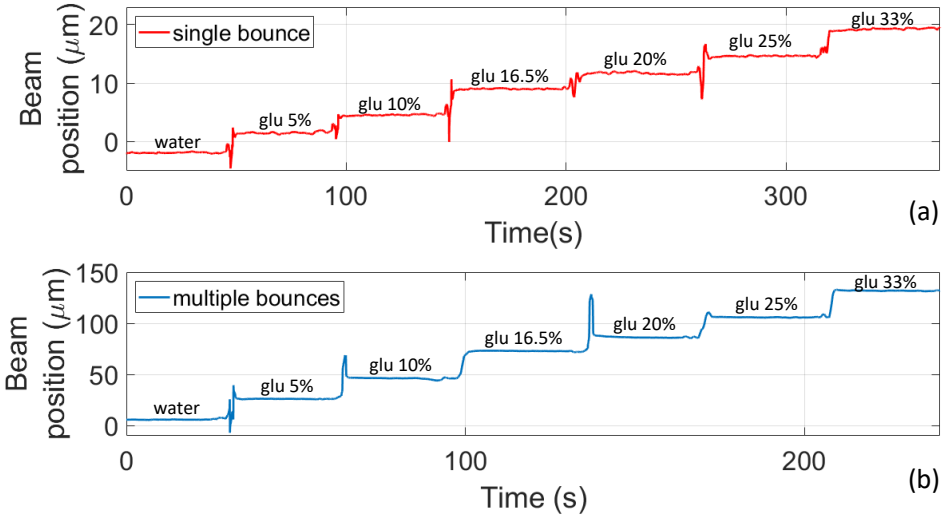

Figure 3.16: Variation of the beam position p_{PSD} detected by the PSD as a function of time when water-glucose solutions with different concentration are tested in the single bounce (a) and in the multiple bounce configuration (b).

Afterwards, the experimental shift $X_{experim}$ of the light beam position with respect to that measured when water, chosen as reference fluid, flows in the channel was recovered, for all the samples investigated, by applying the formula

$$X_{experim} = |p_{PSD-fluid} - p_{PSD-water}| \tag{3.11}$$

The values of $X_{experim}$ can be compared with the theoretical values of X provided by the model and given by Equation 3.8. The experimental data were then reported as a function of the sample RI with the best linear fitting that represents the calibration curves of the RI sensor. Figure 3.17 shows the comparison between experimental and theoretical curves. The experimental calibration curves (dotted traces) were found to be in extremely good agreement with the experimental ones (solid traces) obtained for a micro-capillary with channel depth d = 360 µm. Also, the number of bounces in the multiple bounce scheme was confirmed to be N = 6. The theoretical sensitivities (448 and 2669 µm/RIU, for the single and multiple bounce configuration, respectively) are very close to the theoretical values.

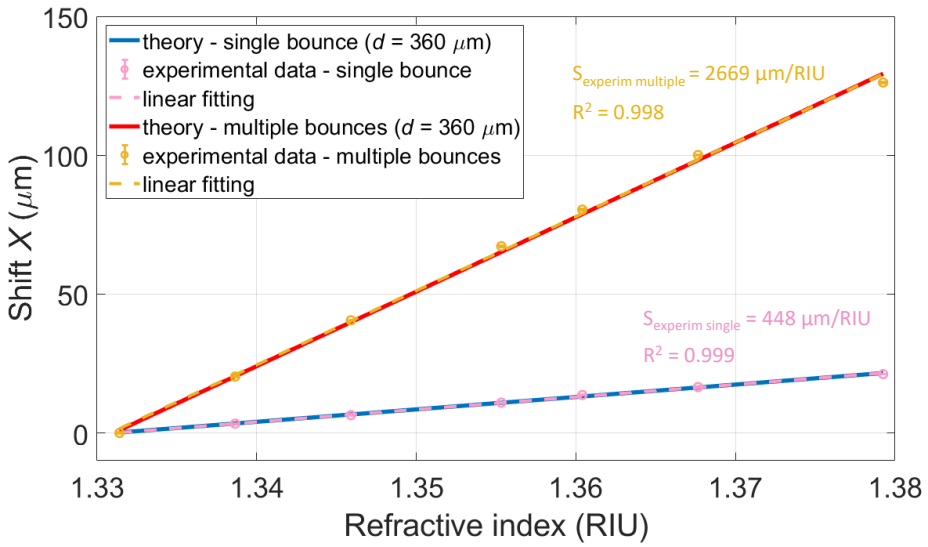

Figure 3.17: Experimental calibration curves (dotted traces) for single (N = 1) and multiple (N = 6) bounce configuration with the micro-capillary. They are almost perfectly overlapped to the theoretical calibration curves (solid traces).

3.7.2 Experimental measurements on IBIDI µ-Slides

After the micro-capillary, an IBIDI µ-Slide channel was considered for experimental testing. It has nominal dimensions t_f = 180 µm, d = 800 µm and t_b = 1060 µm. As the micro-capillary, also the IBIDI device was coated on one side with an Al

layer along the whole length of the channel and on the other side with a shorter layer with L_{met}= 5 mm. Water-glucose solutions with concentration 0, 5, 10, 16.5, 20, 25 and 33% and RI values of 1.3314, 1.3386, 1.3459,1.3553, 1.3604, 1.3676 and 1.3792 RIU, respectively, were tested first in the single bounce configuration. The laser current was set equal to 22.3 mA. Following the same procedure already explained in detail for the micro-capillary (Section 3.7.1), the $V_1 - V_2$ and $V_1 + V_2$ signals from the PSD were acquired and the beam position p_{PSD} and beam shift $X_{experim}$ were retrieved applying Equation 3.10 and 3.11, respectively. Then, the experimental data were linearly fitted as a function of the sample RI and further compared with the theoretical prediction. The experimental calibration curve (pink dotted trace in Figure 3.18) is overlapped to the theoretical curve (blue solid trace) obtained supposing a channel with depth of 800 μm (hence equal to the nominal value declared by the manufacturer). The experimental sensitivity (982 μm/RIU) is in good agreement with the value estimated by the model (994 μm/RIU). Experiments were then repeated in the multiple bounce scheme, setting the laser current to 23 mA. Current was here increased to obtained a significant level of optical power reaching the PSD: indeed, in the multiple bounce configuration losses increase because of the higher number of interfaces between different materials met by the light beam. The experimental calibration curve (green dotted trace) is in good agreement with the theoretical curve obtained with a number of bounces N =3 and a channel depth d = 880 μm and the value of sensitivity was correctly predicted by the theoretical analysis. It has to be noted that there is a mismatch on the value of d predicted in the single and multiple bounce configuration (800 μm vs 880 μm). This discrepancy could be justified by channel depth variations of the IBIDI μ-Slide along its length. Indeed, the front cover layer is extremely thin (t_f = 180 μm) and could be pretty flexible (surely, less rigid that glass). Hence, when the liquid flows into the channel, it applies a pressure in the walls and it could cause an expansion of IBIDI μ-Slide. Reasonably, the deformation is more evident at the center of the device and this seems to be confirmed by the fact that the value of d appears larger for the multiple bounce configuration that was tested about halfway along the channel. On the other hand, tests on the single bounce configuration were performed shining light close to the luer connection, where the device is sealed and the deformation is likely very limited.

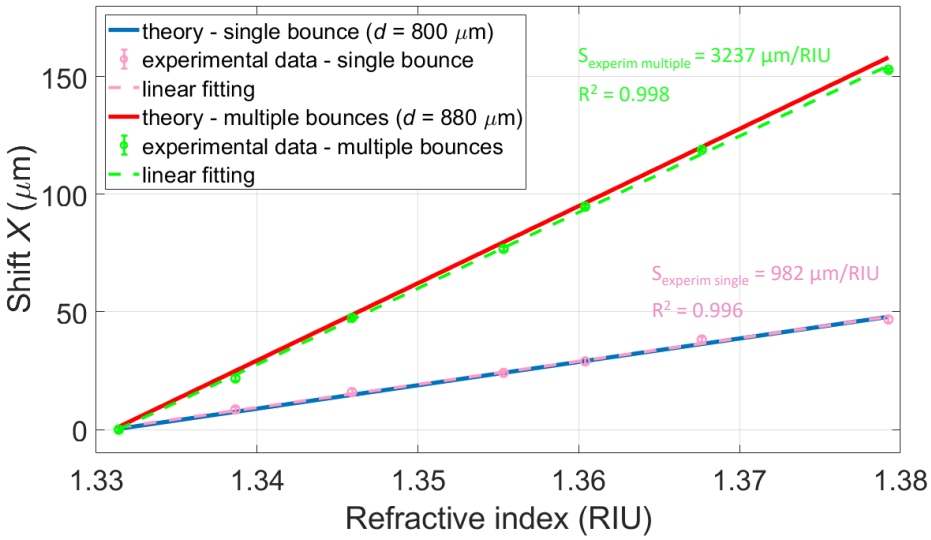

Figure 3.18: Experimental calibration curves (dotted traces) obtained with the IBIDI channel tested in single ($N = 1$) and multiple bounce ($N = 3$) configuration. They are almost perfectly overlapped to the theoretical calibration curves (solid traces). To be noted is the mismatch between the values of d predicted in the two configuration, very likely to be ascribed to the deformation of the channel because of the force applied by the liquids.

3.7.3 Experimental measurements on plastic cuvettes

Eventually, experimental measurements were carried out flowing the fluid samples in a plastic cuvette. The device has thickness of the walls $t_f = t_b = 1$ mm and channel depth $d = 1$ cm, thus much deeper than that of micro-capillaries and IBIDI µ-Slides. The back wall of the cuvette is fully coated with the aluminum layer, but no front metallization was realized since, using the cuvette, the light path in the channel is expected to be long enough to ensure high sensitivity even in the single bounce scheme. Water-glucose solutions with concentration 0, 5, 10, 16.5, 20, 25 and 33% and RI values of 1.3314, 1.3386, 1.3459,1.3553, 1.3604, 1.3676 and 1.3792 RIU, respectively, were tested. The laser current was set to 22.5 mA. Then, following the same procedure already explained in detail for the micro-capillary (Section 3.7.1), data from the PSD were acquired and processed. Beam position p_{PSD} and beam shift $X_{experim}$ were extracted. Then, as reported in Figure 3.19, the beam shift was linearly fitted as a function of the sample RI and the experimental calibration curve (green dotted trace) was obtained. Moreover, it was compared with the theoretical results reported in Figure 3.12. The comparison demonstrated good agreement between the experimental and the theoretical curve obtained simulating an angle of incidence $\theta_1 = 40°$. Also the experimental sensitivity (10455 µm/RIU) well matches the value estimated by the model (10271 µm/RIU).

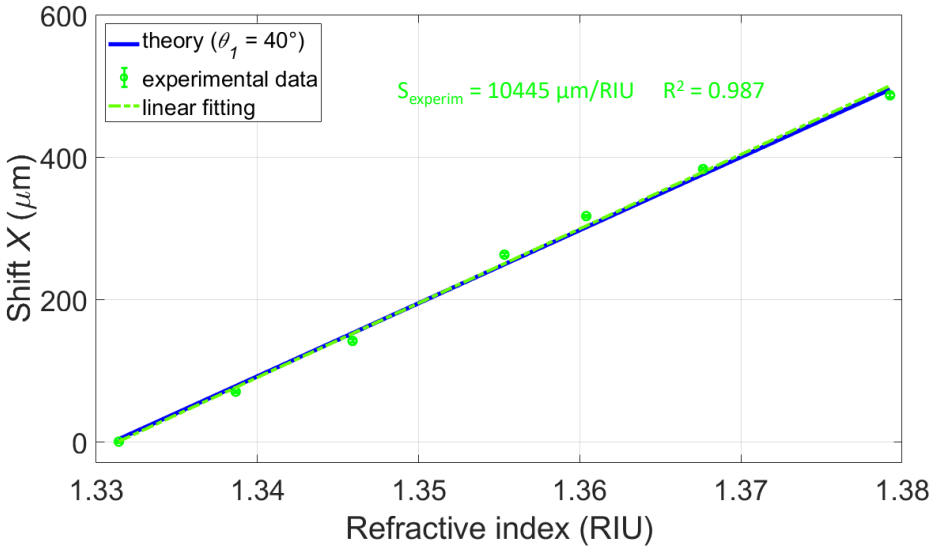

Figure 3.19: Experimental calibration curves (green dotted trace) for single bounce configuration ($N = 1$) in comparison with the theoretical curve (blue solid trace) related to a plastic cuvette.

3.8 Realization of industrial prototypes

After experimental demonstration of the principle of operation of the platform and and analysis of the features and performances obtained with the three fluidic channels, further work was made to realize industrial prototypes of an opto-fluidic sensor that can be easily integrated into commercial pumps for infusion of AN fluids. In particular, choices were made to use electro-optical and fluidic components that are low-cost and allow to realize a compact configuration. A first generation prototype and, later, a second generation prototype were designed and implemented during my Ph.D..

3.8.1 First generation prototype

To realize the first generation prototype, standard plastic cuvettes described in Section 3.3.1 were adopted as fluidic channels. Indeed, they are easy to handle and have to be operated only in the single bounce configuration (that results less critical in term of alignment) thanks to their long optical path that significantly increases the measurement sensitivity, as explained in Section 3.5.3. The bottom part of the each cuvette was polished away and plastic connectors were 3D-printed by Proto-Lab (Figure 3.20(a)) to insert the device along the fluidic path connecting the bags of AN mixtures to the vein of the patient (Figure 3.20(b)). Moreover, the external metalizzation was substituted with the use of a commercial cheap bulk mirror (12.5

mm $\times$ 50 mm, thickness of 1 mm) purchased from Amazon (WA, USA) (Figure 3.20(c)). In this way, the reflector can become part of the fixed setup and the cuvette with connectors and plastic tubes becomes the only low-cost consumable of the system.

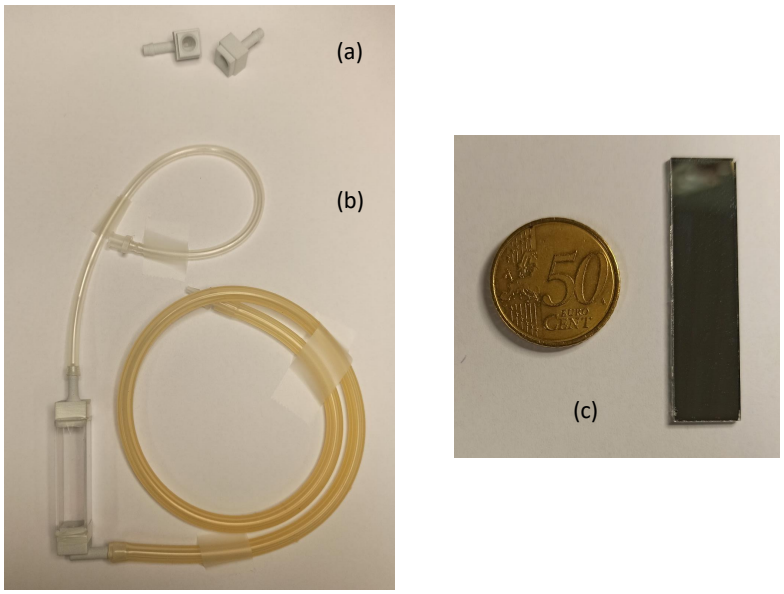

Figure 3.20: Choice of components for the first generation prototype. (a) 3D-printed connectors for cuvettes. (b) Plastic cuvettes with connectors and tubes. (c) Low-cost mirror.

The laser source of the previous configuration (see Section 3.6) was obsolete and out of production: hence, it was substituted by another semiconductor laser diode with emission centred at 670 nm (HL6748MG, Thorlabs, NJ, USA) and maximum optical power of 10 mW, still powered by the bench Thorlabs current driver (LDC 500). A different PSD (1L10_CP2, SiTek Electro Optics AB, Sweden) with respect to that previously employed (see Section 3.6.1) was chosen: the two detectors have the same active area (10 mm (L_{PSD}) $\times$ 2 mm), but the new PSD chip has smaller overall dimensions (19.6 mm $\times$ 7.4 mm), thus resulting less bulky (see Figure 3.21)(a). The new PSD needs to be supplied with ±15 V voltages (similarly to the previous one) and provides as outputs the two currents photogenerated at the extremities of the sensitive region, I_1 and I_2. Hence, a transimpedance circuit was designed and implemented to convert the current signals in voltage signals and amplify them. The circuit scheme is shown in Figure 3.21(b). The circuit provides the voltage signals V_1 and V_2, which are also amplified according to the value of the feedback resistors (15.05 kΩ) by means of the two operational amplifiers contained in a TL082 dual-in-line chip circuital element (Texas Instruments, TX, USA). The position of the light beam p_{PSD} is then retrieved by applying Equation

3.10. The capacitors between the supplies and ground are used to filter noise.

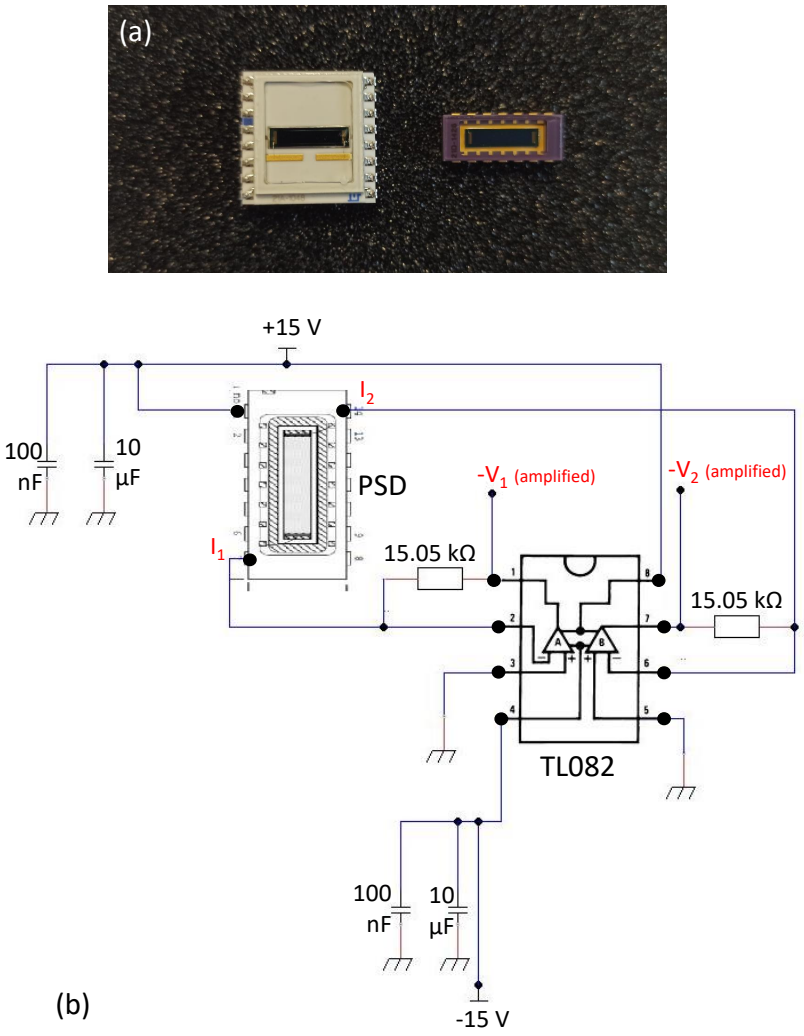

Figure 3.21: New SiTek PSD chosen for the first generation prototype. (a) Picture with comparison between the previous PSD (on the left) and the new one (on the right), which is clearly more compact. (b) Schematic of the transimpedance circuit.

3.8.2 Second generation prototype

Eventually, a second generation prototype was designed with the aim of making the sensing platform compact and optimized to be inserted in a commercial pump for infusion of fluids. Thus, Fluid-o-Tech and Proto-Lab provided a 3D-printed plastic shell purposely designed to replace the bench mechanical mountings previously used (purchased from Thorlabs, NJ, USA) and to integrate all the optical, electronic and fluidic components (Figure 3.22). The cuvette with the connectors, blocked against the mirror by means of two springs, is the only component

that needs to be changed after every use. The bulky and expensive bench current driver was substituted by a smaller programmable electronic board (provided by Fluid-o-Tech) with an area of about 4 cm $\times$ 7 cm, which provides a fixed value of current. Moreover, a small and compact Analog Discovery 2 (Digilent, WA, USA) was used instead of the oscilloscope. It is a multi-function electronic board, which also includes a two-channel input oscilloscope option. USB-connected to a computer, it is driven by the WaveForms software and it is also be used as analog-to-digital converter to acquire experimental data. The glass lens previously used (see Section 3.6) was replaced with a low-cost plastic lens (CAY033, Thorlabs, NJ, USA) with similar characteristics (focal length of 3.3 mm, numerical aperture equal to 0.40), allowing to reduce the overall cost. The distance between the laser and lens can be adjusted thanks to the presence of a spring.

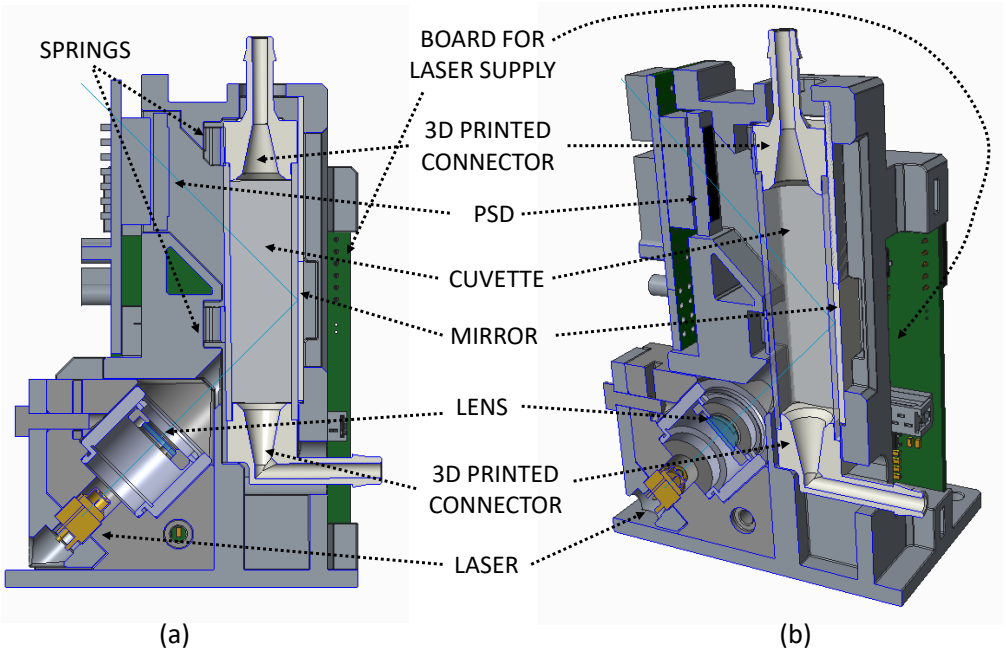

Figure 3.22: Second generation prototype. (a) 2D section of the 3D-printed polymeric shell containing all the components. (b) 3D section of the configuration.

3.9 Prototype testing

The first generation prototype was employed to carry out experimental measurements to detect and distinguish the six commercial AN mixtures with different RI presented in Section 3.2 (see Table C.6).

3.9.1 Calibration

First, the sensor was conveniently calibrated by testing solutions of glucose and water, according to the usual procedure, also to verify the performances of all opto-electronic components and in particular of the low-cost mirror, that is not specifically manufactured for optical sensing. The laser current was set equal to 23.7 mA. The V_1 and V_2 signals were directly acquired using the Digilent board and the light beam position measured by the PSD was retrieved by applying Equation 3.10. Then, the shift $X_{experim}$ for every glucose-water dilution tested was retrieved through Equation 3.11 and fitted as a function of the solution RI, considered at the emission wavelength of the laser (670 nm). The linear calibration curve, reported in Figure 3.23 (black trace), has equation

$$X_{experim} = 13960 \cdot RI - 18600 \tag{3.12}$$

and the sensitivity S = 13690 µm/RI is in agreement with the theoretical predictions (see Section 3.5.3).

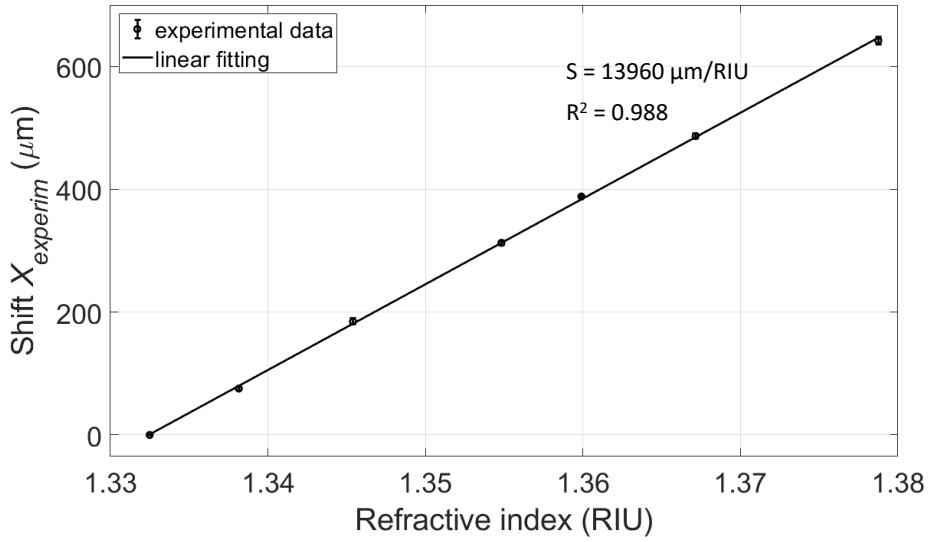

Figure 3.23: Experimental calibration curves obtained testing the first generation prototype with water-glucose solutions.

3.9.2 Test of AN fluids

After the calibration procedure, AN fluids were tested. Samples were prepared by mixing amino acids and electrolytes with glucose (initially contained in different compartments of the bag) few minutes before starting the experiments. Test mea-

surements were repeated in three different day within a week from the preparation of the samples, following the recommendation of the pharmacy of San Matteo hospital. After opening, bags with AN mixtures were stored in a refrigerator at 4 °C. To simulate a realistic situation where the sensing platform is initially calibrated using a reference fluid, measurements were carried out by first flowing in the cuvette a solution of 0.9% sodium chloride (NaCl) in distilled water (also known as injectable physiological solution) and then an AN fluid. The procedure was repeated for all the six AN mixtures. The position of the light beam p_{PSD} measured by the PSD for all the samples tested is reported in Figure 3.24(a). The position stays almost constant when testing NaCl solution, while it varies when testing AN fluids with increasing RI. Then, the experimental shift of the light beam position $X_{experim}$ was retrieved for every AN fluid: it is reported as a function of the theoretical RI (see Table C.6) in Figure 3.24(b) and its behaviour is compared with the calibration curve previously obtained (see Figure 3.23). The experimental data are well distributed along the calibration curve meaning that it can be correctly used to detect the RI of the AN fluids. Testing of the AN mixtures was repeated 4 times, as can be better appreciated in the zoomed inset of Figure 3.24(b): the repeatability of the measurement is good.

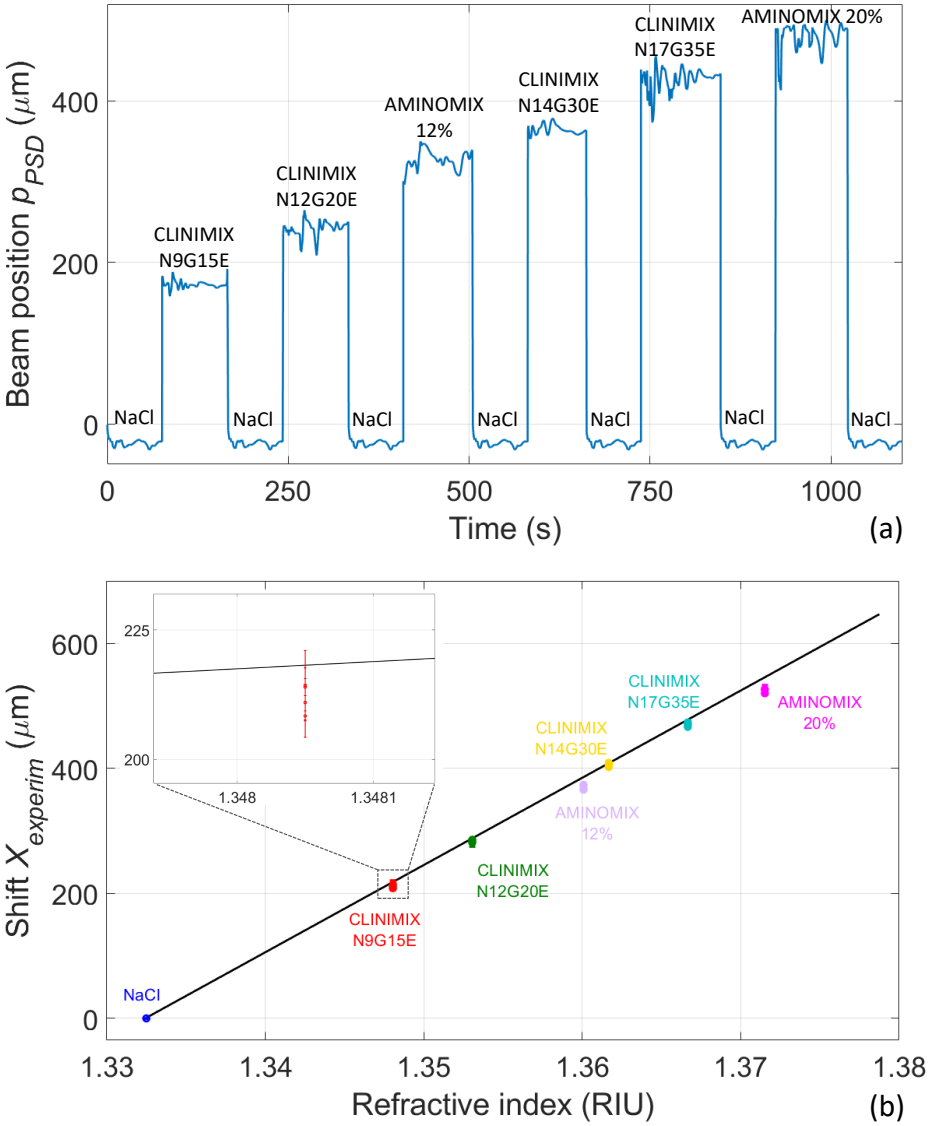

Figure 3.24: Experimental testing of AN mixtures. (a) Beam position p_{PSD} for reference NaCl solution and AN fluids. (b) $X_{experim}$ for the tested AN fluids in comparison with the calibration curve. In the inset, a zoomed view is reported, showing the four repetitions of the measurement.

The experimental shift obtained for the six AN fluids is reported in the barchart of Figure 3.25(a): the height of each bar represent the average value of $X_{experim}$, while the black segments have a length that is equal to twice the standard deviation. The barchart highlights that every AN mixture can be perfectly distinguished from all the others since the values of the experimental shift are significantly different, also considering their standard deviations. Eventually, the RI of the AN mixtures measured with the opto-fluidic sensor was retrieved by inverting the equation of the calibration curve (Equation 3.12). These values were then compared with the theoretical values estimated at 670 nm (reported in Table C.6, as reported in Figure

3.25(b). Each couple of values measured RI-estimated RI is well located on the black line that represent the bisector, meaning that the measured values of RI are in a very good agreement with the predictions obtained computing Equation 3.1.

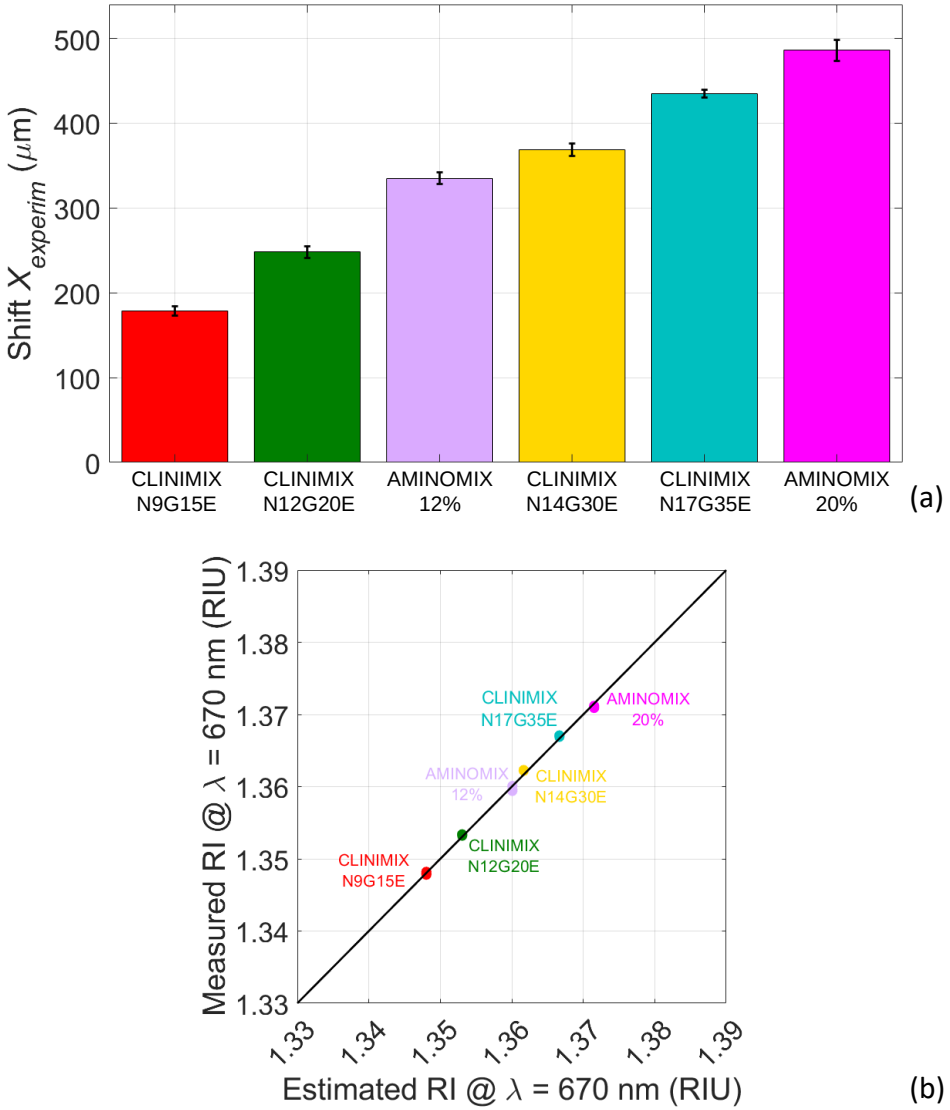

Figure 3.25: Results of experimental testing of AN mixtures. (a) Barchart representing the experimental shift $X_{experim}$ for every AN fluid. (b) Comparison between the RIs measured by the sensor and the estimated RIs.

3.10 Preliminary investigation for air bubble detection

One of the main complications that can arise when artificial parenteral nutrition is administered to a patient is the formation of air bubbles along the fluidic path that can eventually flow inside the blood vessel [105, 106, 107]. This phenomenon is known as embolism and can lead to very dangerous consequences for the patient: indeed, air bubbles can clog up the vessels and prevent blood from flowing in a the correct way and can cause stroke, heart attack, pleural effusion. For this reason, preliminary work has been done to verify if the opto-fluidic platform that identifies the AN mixtures is also able to detect the presence of air bubbles in the cuvette, thus eventually present along the fluidic path connecting the bag to the patient's vein. In this Section, preliminary results about air bubble identification are presented.

3.10.1 Optical-based solutions for air bubble detection reported in the literature

The literature reports some works that present optical-based solutions that can be implemented for air bubbles recognition in fluids. In [108, 109], the authors developed a laser optical tomography system to detect the existence of bubbles inside a vertical column pipeline. Sixteen couples of laser pointers-photodetectors are mounted in a jig around the circumference of the pipe. The voltage signals generated by the detectors are acquired and fed to a back projection algorithm that is able to reconstruct the tomographic images. From the analysis of the images it is possible to detected the bubbles and estimate their diameter. Jamaludin et al. proposed a similar optical tomography configuration based on four laser diodes and eight CCD sensors to detected air bubbles in crystal clear water [110]. Here, the images of captured data are reconstructed based on filtered image of linear back projection with hybrid algorithms. In another work [111], the authors realized a dip-in optical probe with an LED and a CCD camera. This solution was patented: however, this is an invasive approach because the probe needs to be immersed in the fluid. In [112], the authors proposed two setups for optical counting and sizing of air bubbles in a clear blood analogue sample. In the configuration for bubble counting, a laser light is shone onto a transparent cuvette and scattered radiation is captured by means of a camera located at 30° with respect to the incident beam. On the other hand, bubble sizing is achieved by using a backlight shadowgraphy

technique. This technique sizes bubbles based on images of their shadows. The transparent cuvette is illuminated on the back by a pulsed laser, while a high speed camera on the opposite side acquires images of the bubble shadows. The performances of the proposed methods are then compared with those of two commercial instruments based on ultrasounds, revealing better precision and accuracy in particular for high flow rates. In 2020, Alfarraj et al. measured the air bubble size and velocity in diesel using an optical method [113]. They use a 532 nm-Nd:YAG double-pulse laser with cylindrical lenses to expand the 2-D sheet beam impinging on a cuvette and a CCD camera to acquire pictures. They were able to measure number, velocity and size of micro-air bubbles. The proposed optical methods often rely on complex image processing and bulk cameras or on invasive probes. Hence, there is still the need for further investigations of smarter and more compact systems.

3.10.2 Experimental configuration

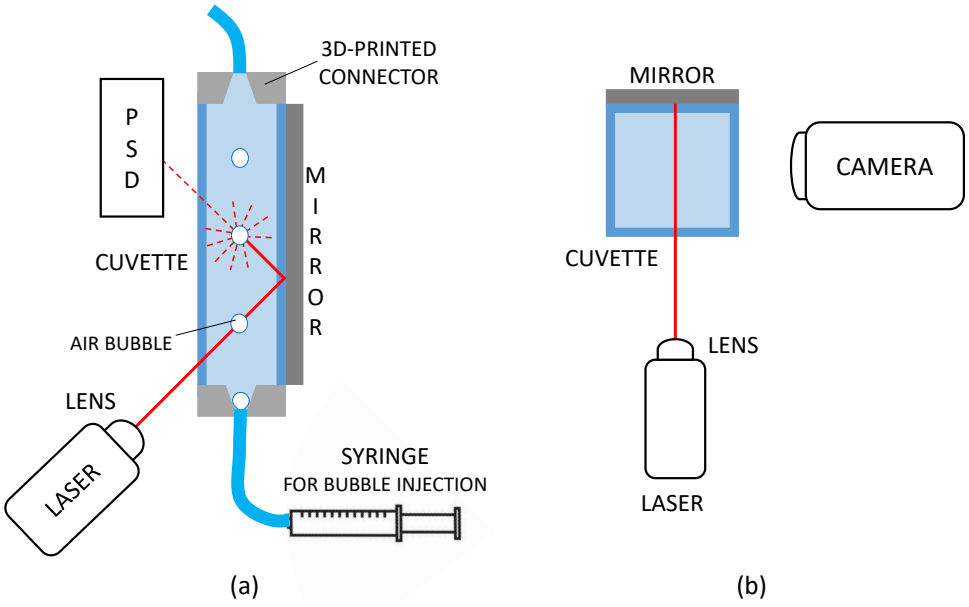

Figure 3.26: Experimental detection of air bubbles. (a) Bubbles injected by means of a syringe interrupts the laser beam twice (front view). (b) Preliminary setup for bubble detection including a camera (top view).

In the opto-fluidic platform described in this Chapter, the detection of air bubbles (represented in Figure 3.26) is based on the observation that when a bubble crosses the fluidic channel (i.e. the cuvette) in the direction of the liquid flow, it encounters the laser beam twice (once the incident beam and once the beam re-

flected by the mirror), causing scattering of light in all directions (Figure 3.26(a)). Hence, the optical power density radiation that reaches the PSD temporarily becomes extremely small (almost equal to 0) and also the photocurrent becomes 0. Experimental identification of bubbles was carried out using the instrumental configuration, described in Section 3.6, which includes the plastic cuvette vertically positioned, with minor modifications. Here, the metallization is replaced by a bulk Al-coated mirror (ME1S-G01 Thorlabs, NJ, USA) and a grey-scale CMOS camera (FLIR Grasshopper GS3-U3-41C6NIR-C, FLIR Systems, OR, USA) was added on one side of the cuvette, at 90° with respect to the incident beam (Figure 3.26(b)). The camera is here used just to acquire videos of the passage of the air bubbles in the fluidic channel and compare them with the voltage signals provided by the PSD. The camera is exploited only for preliminary testing and is not meant to be included in the final configuration, where the bubble detection can be made just exploiting the PSD. Air bubbles are injected using a syringe connected to the bottom connector by means of a plastic tube. The laser beam is shined towards the bottom part of the cuvette, close to the connector aperture the bubbles exit from, in order to detect all the travelling bubbles.

3.10.3 Experimental results

Air bubbles were injected in the cuvette filled with distilled water. The output signals provided by the PSD (difference $V_1 - V_2$ and sum $V_1 + V_2$) and videos recorded by the camera were acquired simultaneously in order to compare them. The signals provided by the PSD when an air bubble interrupts the laser beam were then analyzed. Figure 3.27 reports the sum (blue trace) and difference (orange trace) signals obtained during experimental testing. Both signals become equal to 0 V exhibiting sharp spikes when an air bubble crosses the light beam. The video acquired with the camera shows that a total number of 10 bubbles were generated during the experiment: all of them can be correctly detected by the PSD. Indeed, the signals of Figure 3.27 features a total of 10 sharp spikes.

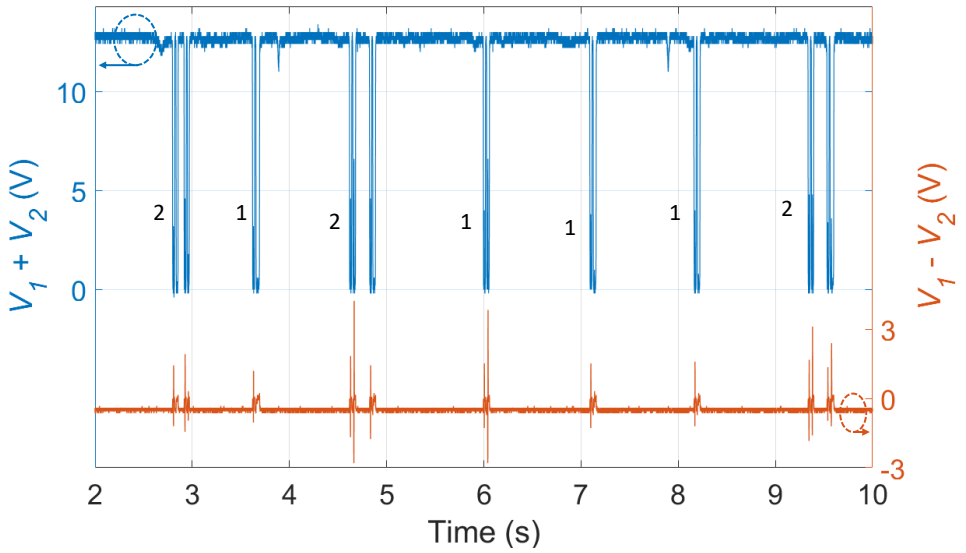

Figure 3.27: Experimental results relative to detection of air bubbles.

Moreover, it is particularly interesting to analyze the $V_1 - V_2$ and $V_1 + V_2$ signals generated during the crossing of a single bubble and make a detailed comparison with the video frames recorded by the camera. The graphs in the following are zoomed views of Figure 3.27 and they corresponds to the detection of only one air bubble, which crosses the light beam twice. Figure 3.28 shows the situation in which an air bubble generated by the syringe is leaving the connector and entering the cuvette. The laser beams (both incident and reflected by the mirror) are not interrupted by the bubble and thus the PSD measures values equal to about 12.4 V and –0.5 V for $V_1 + V_2$ and $V_1 - V_2$, respectively, as expected in the presence of water in the cuvette.

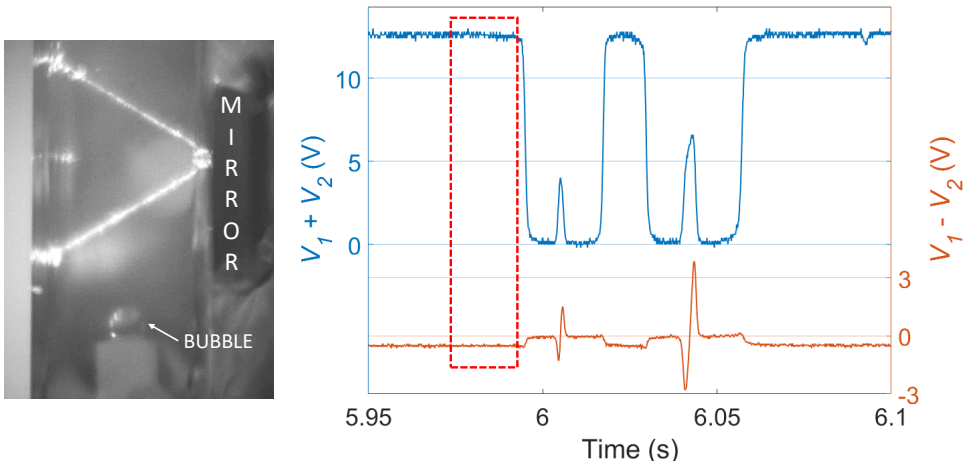

Figure 3.28: Video frame (left) and PSD signals (right, highlighted by the box) acquired when the air bubble is leaving the connector and the laser beams are not interrupted yet.

Afterwards, the bubble starts to cross the channel and it first encounters the incident laser beam (Figure 3.29). As highlighted by the red rectangle, the sum signal ($V_1 + V_2$) drops to 0 V, it stays constant at this value for few ms, it then exhibits a narrow peak (indicated by the black star) reaching a value (4 V) much lower than 12.4 V and, then, it drops to 0 V again for few ms. Finally, it jumps back to the initial value of 12.4 V. On the other hand, the difference signal ($V_1 - V_2$) has a different shape. It also drops to 0 V when the sum signal does but it is then characterized by a double-negative-positive peak, going from –1.3 V to 1.5 V (indicated by the green stars). The described transient behaviour of the sum and difference signals is likely due to the fact that, for a very short interval of time, the laser beam that meets the bubble goes through a different medium, i.e. air.

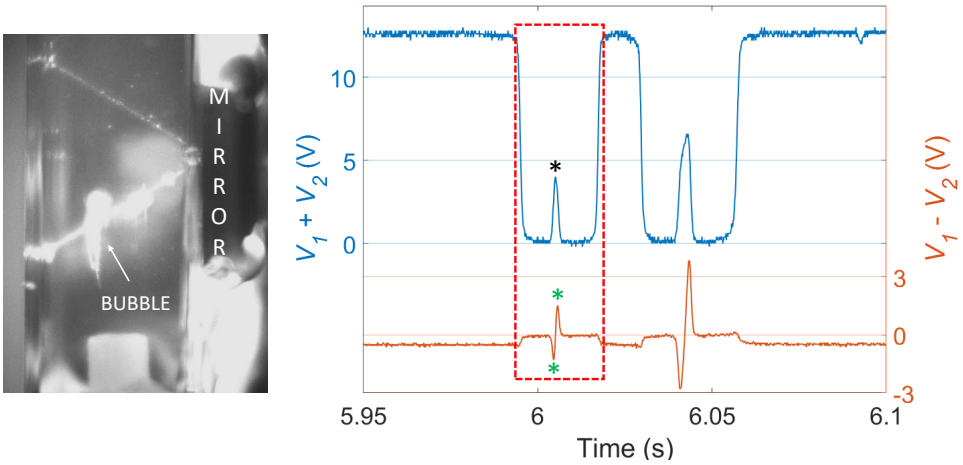

Figure 3.29: Video frame (left) and PSD signals (right, highlighted by the box) acquired when the air bubble is crossing the incident laser beam.

Then, as shown in Figure 3.30, the bubble travels between the incident and reflected laser beams, which therefore are not crossed. The sum and difference signals have the values of 12 V and –0.5 V, respectively, corresponding to the usual situation in which the light beam is simply travelling in water and does not go through the bubble, as already stressed in Figure 3.28.

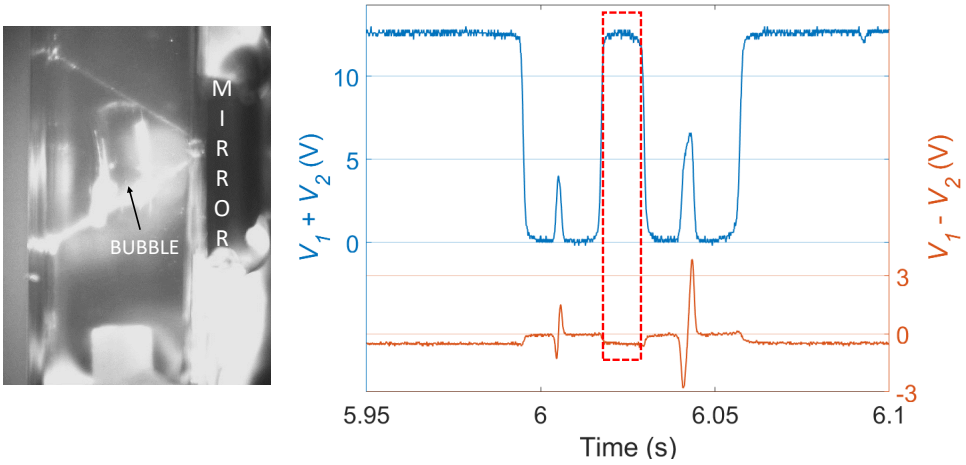

Figure 3.30: Video frame (left) and PSD signals (right, highlighted by the box) acquired when the air bubble is passing between incident and reflected laser beams.

Eventually, the air bubble crosses the laser beam reflected by the mirror (Figure 3.31). In this situation, the shape of the signals provided by the PSD is fully comparable to that observed during the first crossing of the incident beam (Figure 3.29). However, now the transient peaks of $V_1 + V_2$ and $V_1 - V_2$ signals have higher amplitudes (from 0 to 6.6 V and from –2.7 to 3.8 V, respectively). Moreover the time interval of the bubble crossing (indicated by the green arrow) is now longer with respect to that of the first crossing, indicated by the black arrow (29.2 ms vs 24.1 ms). This features can be due to the fact that the air bubble seems to undergo a slight elongation (that can also be appreciated in the image), thus taking more time to fully cross the laser beam.

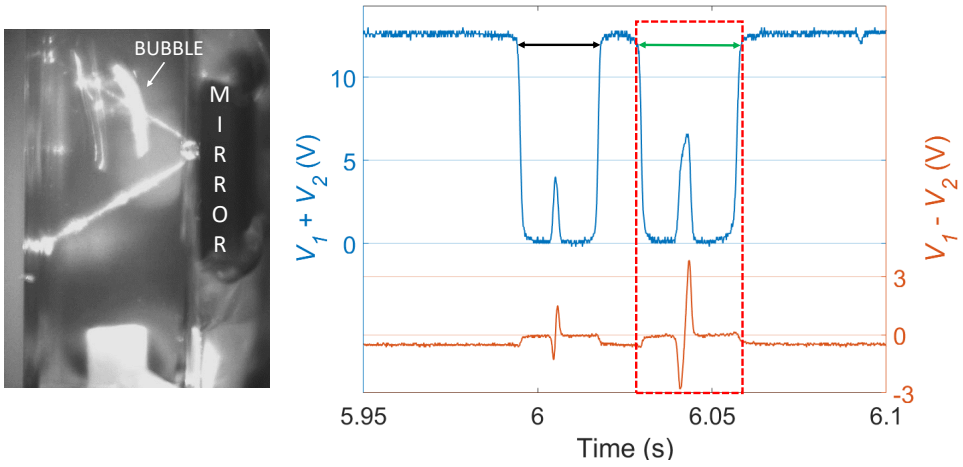

Figure 3.31: Video frame (left) and PSD signals (right, highlighted by the box) acquired when the air bubble is crossing the laser beam reflected by the mirror.

Eventually, the bubble keeps moving towards the upper part of the cuvette thus exiting from the region illuminated by laser light (Figure 3.32). Hence, the sum signal jumps back to 12 V and the difference signal drops again to –0.5 V.

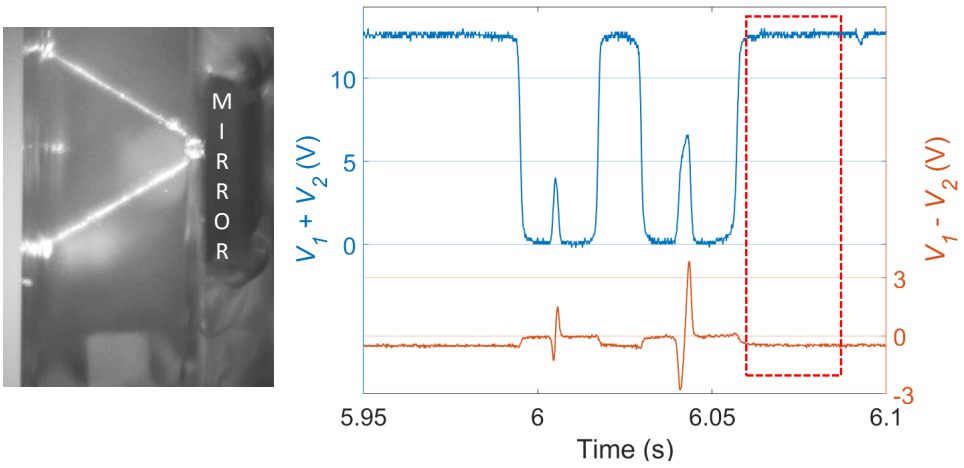

Figure 3.32: Video frame (left) and PSD signals (right, highlighted by the box) acquired when the air bubble is leaving the cuvette. Neither the incident nor the reflected laser beam are interrupted.

This particular shape of the sum and difference signals was reproducible and was found for almost all the bubbles during the experiments, suggesting it is a characteristic fingerprint of its crossing. Eventually, it was also possible to retrieve the velocity of the air bubble (Figure 3.33). First, the distance Δx between the incident and reflected laser beams (indicate by the black arrow in Figure 3.33(a)) was retrieved by theoretical computations through the theoretical model, supposing the bubble crossing the cuvette at its center. It resulted $\Delta x = 0.502$ cm. Then, the time interval $\Delta\tau = \tau_1 - \tau_2$ necessary to travel the distance Δx was retrieved from the analysis of the $V_1 + V_2$ signal. In particular, the values of τ_1 and τ were retrieved looking for the half value of the $V_1 + V_2$ jumps from 12.4 V to 0 V (Figure 3.33(b)), resulting $\Delta\tau = 0.0348$ s. Then, the bubble speed was retrieved as $v = \Delta x/\Delta\tau = 14.4$ cm/s. Then, for further validation of the result, the computation was repeated considering the video acquired by the camera and the $\Delta\tau$ between the two frames showing the bubble crossing the incident and reflected beams. With this method, $\Delta\tau = 0.0342$ s and $v = 14.7$ cm/s. The two experimental techniques lead to the same result.

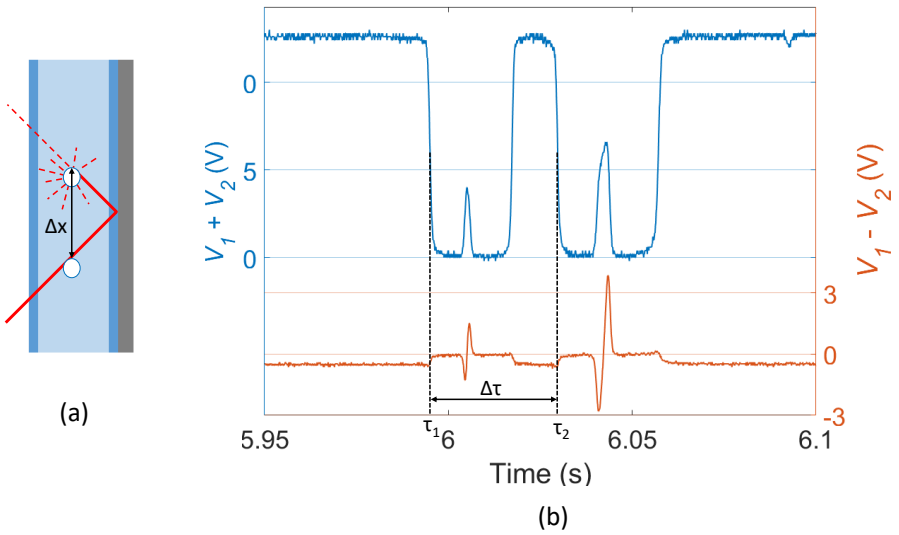

Figure 3.33: Calculation of air bubble velocity. (a) Representation of the distance Δx travelled by the bubble between the incident and reflected laser beams. (b) Calculation of the time interval $\Delta\tau$ from the sum signal.

3.11 Conclusions and future work

In this Chapter, I illustrated the research carried out at the Laboratory of ElectroOptics in the framework of the DSF project, founded by Regione Lombardia, to realize an opto-fluidic platform that correctly distinguishes mixtures used for artificial parenteral nutrition. The AN mixtures considered in this work contains water, glucose, amino acids and electrolytes in different concentration and they can be distinguished on the basis of their RI. The final goal is the realization of a smart opto-fluidic sensor that can be integrated into commercial pumps for infusion and used to improve the quality of life of patients treated with AN at home. The principle of operation of the sensors is based on the use of a semiconductor laser beam that crosses a fluidic channel, provided with reflectors, containing the fluid under test: thus, the beam is deflected according to the RI of the sample and its position is detected using a PSD. The performances of different types of fluidic channels (glass micro-capillaries, IBIDI µ-Slides and cuvettes) were investigated, both theoretically and experimentally. Exploiting the technology previously developed and already described in Chapter 2, single and multiple bounce configurations were considered. It was demonstrated that the sensitivity of the measurements depends on the length of the optical path and it is directly proportional to the number of bounces N. After preliminary testing with water-glucose dilutions, industrial prototypes of the opto-fluidic sensing platform were designed. Cuvettes

were chosen as fluidic channels since they are easy to handle and can be simply exploited in the single bounce configuration. Indeed, the much longer optical path allows to strongly enhance the sensitivity even with a single bounce. After testing a first generation prototype, a second generation prototype was realized by choosing low-cost electro-optical and fluidic components to optimize the instrumental configuration and realize a compact cost-effective platform that can be integrated in pumps for infusion. The first generation prototype was successfully exploited to test six AN mixtures: they can be distinguished without ambiguity. Moreover, by properly calibrating the sensor with a reference fluid (NaCl) it is also possible to retrieve the RI of each fluid. The measured values were found to be in good agreement with the estimated theoretical values. Eventually, preliminary work was started to use the opto-fluidic platform also for detection of air bubbles. Indeed, they can originate along the fluidic path causing embolism with dangerous consequences for the patient. Since every particle that intercept the laser beam produces a strong scattering effect, air bubbles can be detected by looking for sharp variations of the signals detected by the PSD. Air bubbles were correctly counted and their velocity was estimated.

Lot of work can be still done in the framework of this project. For example, future measurements on AN mixtures will be repeated in dynamic conditions (i.e. with the samples flowing in the fluidic circuit) to simulate a realistic situation where the fluids are infused to the patient. Afterwards, in order to further simplify the system, the PSD could be replaced by a photodiode and the readout could be done based on the observation that when the laser beam is deflected, the laser spot onto the photodiode is partialized. Furthermore, here I did not consider AN mixture containing also lipids since they strongly scatters light and they can not be identified with the developed readout method. Hence, future work will be devoted to the investigation of new techniques to identify this type of liquids. For example, imaging methods based on speckle pattern analysis could be investigated. Moreover, further analyses can be done on bubble detection to gather more precise information on velocity, shape, size and movement of the bubble. The technique could also be applied to detect different types of particles.

Chapter 4

Conclusions and future works

The research that I have carried out at the Laboratory of ElectroOptics of the University of Pavia during my Ph.D. focused on the design and realization of smart micro-opto-fluidic sensing platforms for chemical and biological analyses, exploiting label free, remote, contactless and non-invasive techniques. Moreover, a important goal was the use of well-established opto-electronic instrumentation, traditionally developed in the visible and near infrared spectral regions for telecom applications, and low-cost commercial fluidic and micro-fluidic channels. Three sensing platforms were investigated to detect the RI real part and the absorption spectrum of fluids.

The first sensing platform I developed is based on rectangular glass micro- capillaries for high sensitivity measurements of the RI (real part) of liquids in the near infrared. The readout method exploits spectral interferometry. A Michelson interferometry was set up using a broadband (40 nm) source with central emission wavelength of 1550 nm. The micro-capillary was located at the end of the measurement arm, while a mirror was positioned at the end of the reference arm. The interferometric signal was detected in the wavelength domain and optical resonances of micro-capillaries were identified as steep phase jumps. Monitoring the wavelength shift of the phase drops, RI variations with respect a reference fluids were detected. Sensitivity in the range 284-362 nm/RIU was found; these values are comparable with those obtained with more complex systems or sophisticated micro-fluidic devices, realized with expensive micro-fabrication facilities. Moreover, with respect to the method previously investigated, based on the analysis of the T_{cap}/R_{cap} ratio, the interferometric technique could provide better performances. Future work could be devoted to the realization of a more compact instrumental setup based on laser diodes and photodiodes, thus not requiring the use of the optical spectrum analyzer. Moreover, since the proposed analyses are safe

and non-invasive, also biological samples could be investigated.
I also demonstrated the integration of rectangular glass micro-capillaries in another micro-opto-fluidic configuration for detecting the spectroscopic features of water-alcohol mixtures in the near infrared region from 1.0 to 1.7 μm. Indeed, the absorption spectrum is a characteristics "fingerprint" that identifies molecules is a unique way. The micro-capillaries were customized with sputtering deposition of thin metallic layers. This simple and low-cost technology allows to fabricate smart devices provided with integrated reflectors, so that they can be exploited to arrange single or multiple bounce configurations. Thus, light can bounce once or multiple times inside the channel to obtain different pathlengths of the light beam in the sample. The multiple bounce configuration allowed to distinguish alcoholic mixtures polluted by adding concentrations of water smaller than 1%. In future advancements, the same readout method could be applied using different optical sources (such as lasers and LEDs) to study the absorption features of new molecules that exhibits interesting absorption peaks in the SWIR region (such as creatinine and salicylic acid). An initial step in this direction was made studying the absorption of urea at 2150 nm, as I presented in Appendix B as side activity of my Ph.D.
My research activity was then focused on the demonstration of an opto-fluidic platform for the identification of mixtures used in parenteral artificial nutrition. This activities was carried out in collaboration with the DICAr of the University of Pavia and the company Fluid-o-Tech, within the DSF project founded by Regione Lombardia. The principle of operation of the sensor is based on the use of a red laser beam that crosses a fluidic channel, provided with reflectors, containing the fluid under test: thus, the beam is deflected according to the RI of the sample and its position is detected using a PSD. The performances of different types of fluidic channels (glass micro-capillaries, plastic IBIDI μ-Slides and and standard polystyrene cuvettes) were investigated, both theoretically and experimentally. Afterwards, square-section cuvettes were chosen to realize compact low-cost industrial prototypes, suitable for integration in commercial pumps for infusion. One prototype was successfully exploited to distinguish six different type of AN fluids. Moreover, preliminary work was done for simultaneous detection and counting of dangerous air bubble that can generate along the fluidic path using the same optical configuration. Lot of work must still be done in the framework of this project. Surely, future measurements on AN mixtures will be done in dynamic conditions to simulate a realistic condition of infusion of the liquids to the patient's veins. Then, identification of scattering AN mixtures containing lipids must be pursued using a different optical technique, for example based on

laser speckle pattern. Moreover, the platform could be further miniaturized by realization of an integrated lab-on-chip that includes all opto-electronic and fluidic components. This device could be large-scale produced using silicon technologies. Eventually, an additional part of my research was conducted at Nanometer Scale Engineering Laboratory of Boston University. In particular, I applied traditional laser interferometry to characterize the mechanical properties of NEMS resonators, both in-thermal noise conditions and under electro-thermal actuation, in particular, demonstrating that different actuation patterns were able to excite odd or even resonant modes with different amplitude.

Appendix A

Measurement and characterization of nano-electro-mechanical systems using laser interferometry

During my Ph.D. program, I spent six months at the Photonics Center of Boston University (Boston, MA, USA) as visiting researcher. There, I worked in the Nanometer Scale Engineering Laboratory under the supervision of Prof. Kamil L. Ekinci. In particular, I focused my attention on the exploitation of laser interferometry to measure and characterize the mechanical properties of nano-electro-mechanical systems (NEMS). The resonant mechanical modes of doubly-clamped nano-beam resonators were first characterized using their thermal fluctuations in air. Afterwards, the NEMS devices were electro-thermally actuated, and their frequency responses were measured, also in air. The main novelty in this work is the simultaneous use of two electro-thermal actuators integrated on opposite ends of the NEMS, which could selectively actuate higher order modes based on the relative phase difference (of 0°, 45° or 90°) applied between the two actuators. All the measurements were carried out with a homodyne Michelson interferometer, allowing for ultrasensitive contactless, non invasive, remote, and nondestructive analysis. The results of this research were published in [114].

A.1 Introduction

In recent years, nano-electro-mechanical systems have attracted much interest from the scientific community [115, 116]. They are similar to micro-electro-mechanical systems (MEMS), but are able to attain even better performance limits by virtue of their sub-micron dimensions. Because of their interesting characteristics, NEMS

have found applications in several fields of science and technology, in particular as sensors and actuators. In sensing, they have been used for analyzing gas properties [117], mass spectrometry [118, 119], force detection [120], and inertial imaging [121]. Moreover, higher order modes have recently been exploited in some applications, such as mass and stiffness sensing [122] and quality factor control [123]. Since these nano-devices are often operated in their resonant modes, characterization and measurement of the resonance frequencies are of fundamental importance. Laser interferometry is a powerful measurement technique based on the use of highly-coherent light for the detection of displacements on the order of femtometers [26]. An optical interferometer offers several advantages: it allows for non-invasive, non-contact, and remote analysis of the device of interest without applying any type of external stimulus or stress. Moreover, an interferometric measurement is nondestructive, allowing the same device to be tested many times and in different conditions without damaging the device. Because of these features, optical interferometry has already been widely exploited for the characterization of MEMS [124, 125, 126]. In this work, a He-Ne-based Michelson interferometer was used for characterizing the frequency response of suspended doubly-clamped nano-beams. First, the NEMS devices were characterized by their thermal fluctuations in air, and mechanical resonances up to the fifth harmonic were detected. Subsequently, the nano-beams were driven electrothermally, using a double drive scheme based on phase-shifted voltage signals, and their responses were studied in air.

A.2 Doubly-clamped suspended beams

The nano-electro-mechanical systems investigated in this work are suspended doubly -clamped beams, fabricated on a silicon nitride layer over a silicon substrate [127]. Each beam has two nano-fabricated gold electrodes (one at each extremity) that are used for actuation of the device. The beams have width W_{NEMS} = 950 nm, thickness t_{NEMS} = 100 nm and length L_{NEMS} varying in the range 5-60 μm. Figure shows a scanning electron microscope image of an entire chip with 16 devices (a), a single NEMS suspended beam (b), and the area of a single device where one of the gold electrodes is fabricated (c).

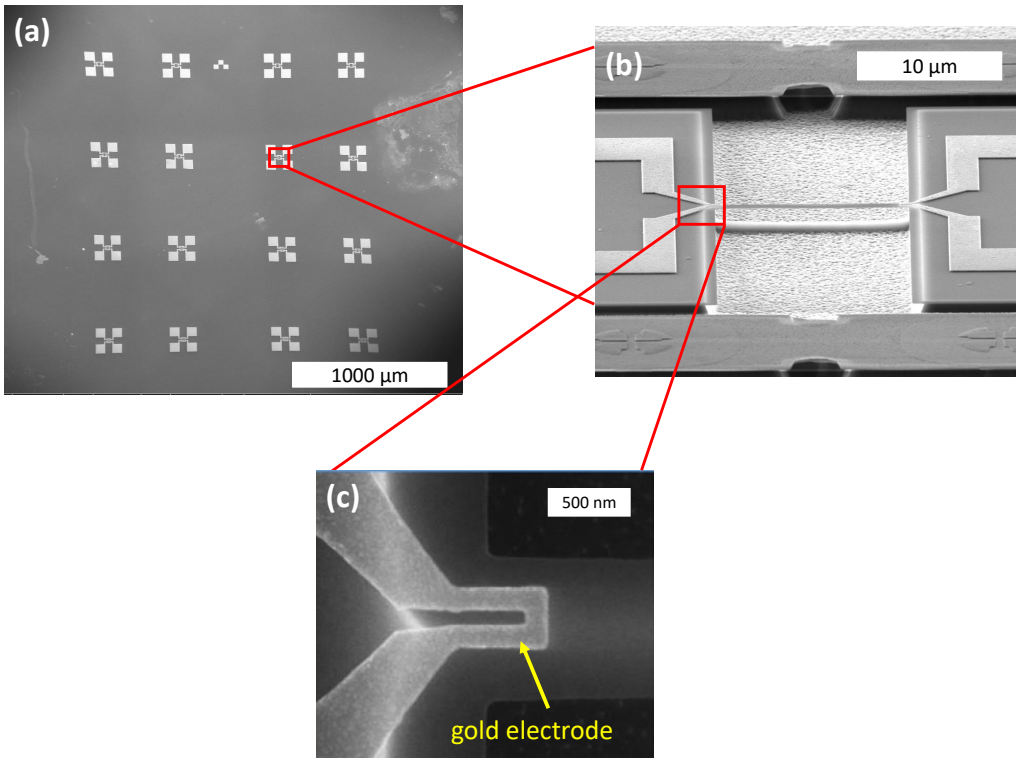

Figure A.1: (a) Scanning electron microscope images of a chip with 16 suspended nano-beams. (b) A single suspended SiN beam. (c) Zoomed area showing one of the gold electrodes at each end of the beam used for actuation.

A.3 Electro-thermal actuation

The devices were actuated exploiting the electro-thermal effect [128]. When a voltage is applied to the gold electrode, a current flows through the metallic layer. This causes Joule heating of the electrode, resulting in a temperature increase and subsequently thermal expansion of the electrode and the beam. Since gold (Au) and silicon nitride (SiN) have different thermal expansion coefficients $\alpha_{thermal}$ ($\alpha_{thermal\ Au} = 12 \cdot 10^{-6}\ \mathrm{K}^{-1}$, $\alpha_{thermal\ SiN} = 3.3 \cdot 10^{-6}\ \mathrm{K}^{-1}$), this differential thermal expansion produces a mechanical deformation of the structure and hence actuates flexural motion of the beam. In this work, we used a double actuation scheme (Fig. 2): the beams were driven by applying two sinusoidal voltage signals, V_1 and V_2, at the two gold electrodes on both ends. The two signals had the same amplitude V_{AC} and their frequency $\omega_0/2$ was varied simultaneously. The phase difference between them was set equal to 0°, 45° or 90°. These particular values of phase difference were chosen because Joule heating actuates mechanical motion at twice the value of the frequency of the applied voltage. Indeed, the dissipated

electrical power P is proportional to the square of the drive voltage:

$$P \propto \left[V_{AC} \cdot \cos\left(\frac{\omega_0 \cdot \tau}{2}\right)\right]^2 = \frac{V_{AC}^2}{2} + \frac{V_{AC}^2 \cdot \cos(\omega_0 \cdot \tau)}{2} \tag{A.1}$$

Hence, 0°, 45° and 90° phase differences in the two drive voltages exert forces to opposite ends of the beam with 0°, 90°and 180° phase difference, respectively, which allow us to observe specific conditions and modes. The dissipated power at each electrode is given by the sum of a DC term and an AC term oscillating at frequency ω_0.

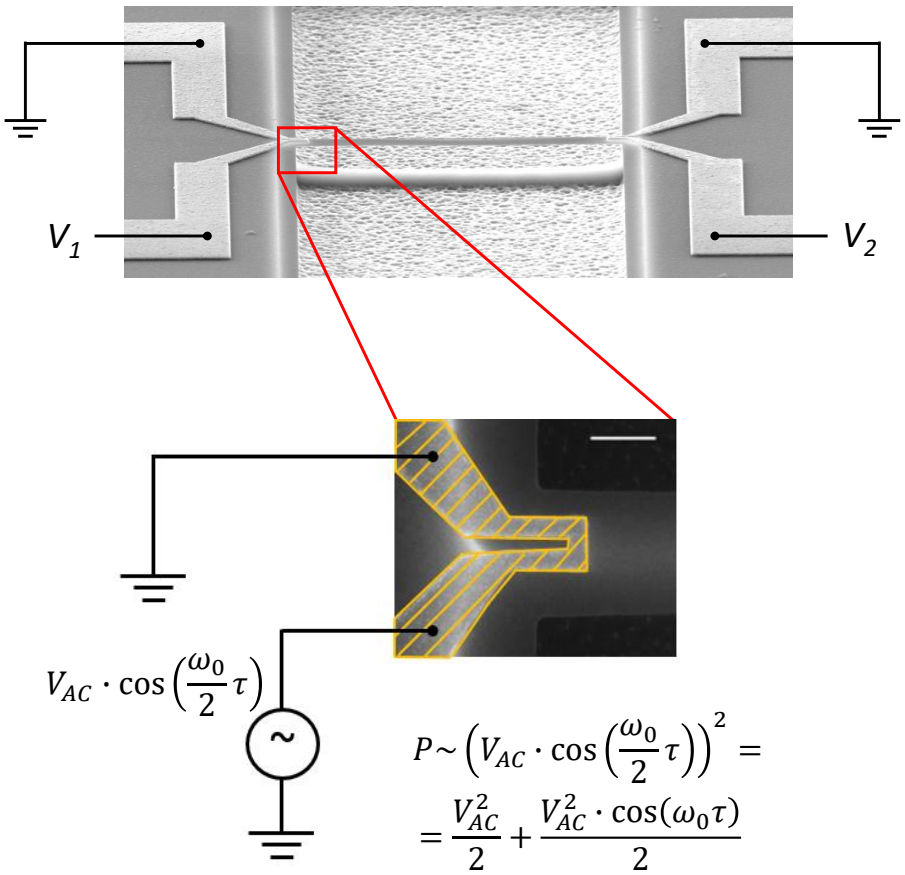

Figure A.2: Double-side electro-thermal actuation. The nano-beams were actuated on both sides by applying two cosinusoidal voltage signals, V_1 and V_2, with equal amplitude, equal frequency, and relative phase of 0, 45 or 90°.

A.4 Homodyne Michelson interferometer

Figure A.3 shows the setup used for the experimental measurements. It is a homodyne free-space Michelson interferometer, where both the measurement and

the reference beam have the same optical frequency. Light from a He-Ne laser (Research Electro-Optics Inc., CO, USA), emitted at a wavelength of 633 nm, is directed through an optical isolator, to protect the source from unwanted back-reflections, a series of beam expander optics and a half-wave plate towards a cube polarized beam splitter (PBS). The plate allows for adjusting the polarization and thus for controlling the fraction of light that is reflected or transmitted by the beam splitter. The reflected beam is redirected along the reference arm of the interferometer. It crosses a quarter-wave plate, and it reflects from a moving mirror mounted on a piezo transducer, connected to a proportional integrative-derivative (PID) controller. Hence, the entire optical interferometer is in a closed feedback loop so that the path length of the reference arm can be adjusted to compensate for slow mechanical and optical path variations and to keep the system in the point of optimal sensitivity. The transmitted beam (measurement beam) crosses a quarter-wave plate, is focused by an objective lens with a magnification of 100X and a numerical aperture of 0.5 onto the sample under test, and it is back reflected to the PBS. The double pass through the quarter-wave plate shifts the polarization so that light can be reflected when it reaches the PBS. A series of lenses, a white light lamp and a camera (CX-ST50, Sony, Japan) are located along the measurement arm: they constitute a microscope system, which allows for monitoring in real-time the location of the laser spot with respect to the NEMS device. The reference and measurement beams are carefully aligned so that they can overlap and be directed towards another PBS. The two light beams are then focused through lenses onto two photodiodes (PD). One (PDA8A, Thorlabs, NJ, USA) carries the signal to the PID controller and is used for feedback stabilization; the other one (NewFocus 1801-AC-FS, Newport, CA, USA) is used to measure the nano-beam displacements and is connected to a spectrum analyzer (FieldFox N9918A, Keysight, CA, USA) for thermal noise measurements or a lock-in amplifier for driven measurements.

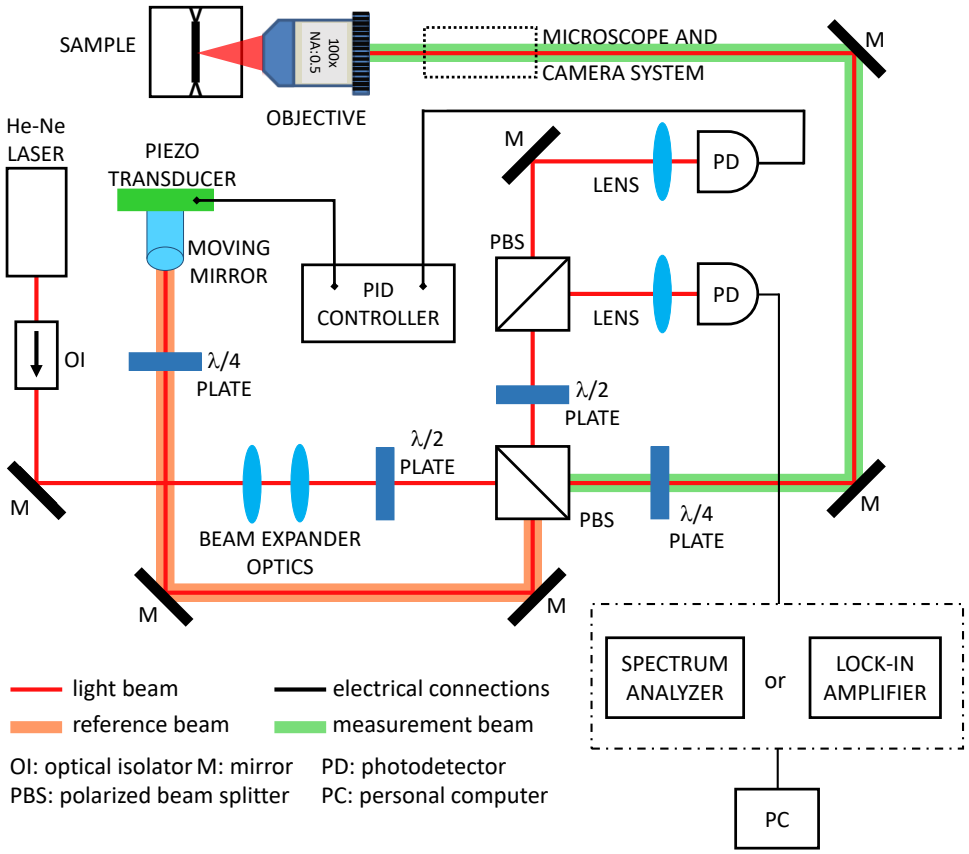

Figure A.3: Homodyne Michelson interferometer used to carry out the experimental measurements. Coherent light emitted by a He-Ne laser is divided by a polarized beam splitter (PBS) between the measurement arm (highlighted in green) and the reference arm (highlighted in orange). After recombination of the two beams, light is splitted by another PBS and directed towards two photodiodes (PD). One is used to carry out the measurement of the nano-beam displacement. The other PD provides the feedback signal for a proportional integrative-derivative (PID) controller for moving the mirror in order to stabilize the optical path.

A.5 Theory of homodyne interferometry

In homodyne interferometry, the reference and the sample beam are at the same wavelength λ, and a change in the optical path of one of the arms results in a change in the interference path and thus the intensity of the light measured by the photodetector. If the reference and measurement arms have total lengths of L_r and $L_m - 2 \cdot d_{sample}$, respectively, the complex electric fields $\overrightarrow{E_{reference}}$ and $\overrightarrow{E_{measurement}}$ at the photodetector are given by

$$\overrightarrow{E_{measurement}} = E_m \cdot e^{i \cdot [\omega \cdot \tau + k \cdot (L_m - 2 \cdot d_{sample})]} \tag{A.2}$$

$$\overrightarrow{E_{reference}} = E_r \cdot e^{i\cdot(\omega\cdot\tau + k\cdot L_r)} \tag{A.3}$$

where E_m and E_r are the electric field amplitudes, i is the imaginary number, ω is the pulsation, k is the wavevector and $2 \cdot d_{sample}$ is the variation in the sample arm length due to the movement of the NEMS device under test. The subscripts "r" and "m" refer to the reference and measurement signals, respectively. Then, the total intensity detected by the photodetector due to the interference between the two light beams is

$$\begin{aligned} I_{ph} &\propto |\overrightarrow{E_{measurement}} + \overrightarrow{E_{reference}}|^2 \\ &= E_m^2 + E_r^2 + 2 \cdot E_m^2 \cdot E_r^2 \cdot \cos[k \cdot (L_r - L_m) + 2 \cdot k \cdot d_{sample}] \end{aligned} \tag{A.4}$$

If the displacement is much smaller than the wavelength (i.e. $2{\cdot}d_{sample} \ll \lambda$, then Equation A.4 can be approximated as

$$\begin{aligned} I_{ph} \simeq (E_m^2 + E_r^2) + 2 \cdot E_m^2 \cdot E_r^2 \cdot \cos[k \cdot (L_r - L_m)] \\ - 4E_m^2 \cdot E_r^2 \cdot k \cdot d_{sample} \cdot \sin[k \cdot (L_r - L_m)] \end{aligned} \tag{A.5}$$

The intensity I_{ph} is thus given by a constant background factor (the two first terms of Equation A.5) and a term that is proportional to the displacement of the device d_{sample} (last term of Equation A.5). Moreover, L_r–L_m = $M \cdot \lambda/4$, with M odd integer number, represents the condition of maximum sensitivity because the background is minimized, and the term proportional to the displacement is maximized. Hence Equation A.5 reduces to:

$$I_{ph} = (E_m^2 + E_r^2) - 8 \cdot \pi \cdot E_m^2 \cdot E_r^2 \cdot \ \lambda \tag{A.6}$$

The path-length stabilization system previously described and constituted by the moving mirror and the PID controller is used to lock the optical path in the interferometer to the condition described by Equation A.6.

A.6 Experimental results

Experimental thermal-noise response and driven response measurements were carried out for a beam with length L_{NEMS} = 40 µm. First, the thermo-mechanical response of the device in air was studied by measuring the displacement fluctuations

of the nano-beam without applying any kind of external force. In this situation, the motion of the beam is caused by the thermal fluctuations in the surrounding fluid due to the finite temperature (Brownian motion). In particular, the air molecules surrounding the beam collide with the beam in a random way and transfer their momentum to the beam, which in turn actuates the beam motion. Results of these experimental measurements are shown in Figure A.4. Mechanical resonant modes up the fifth harmonic were detected at a position of $0.25 L_{NEMS}$. In particular, the first resonant mode is at a frequency $f_{res\,1} = 2.39$ MHz, while higher order modes are located at frequencies that roughly satisfies the condition $f_{res\,m} = m \cdot f_{res\,1}$, where m is the order of the mode ($f_{res\,2} = 4.77$ MHz, $f_{res\,3} = 7.34$ MHz, $f_{res\,4} = 10.23$ MHz and $f_{res\,5} = 13.40$ MHz).

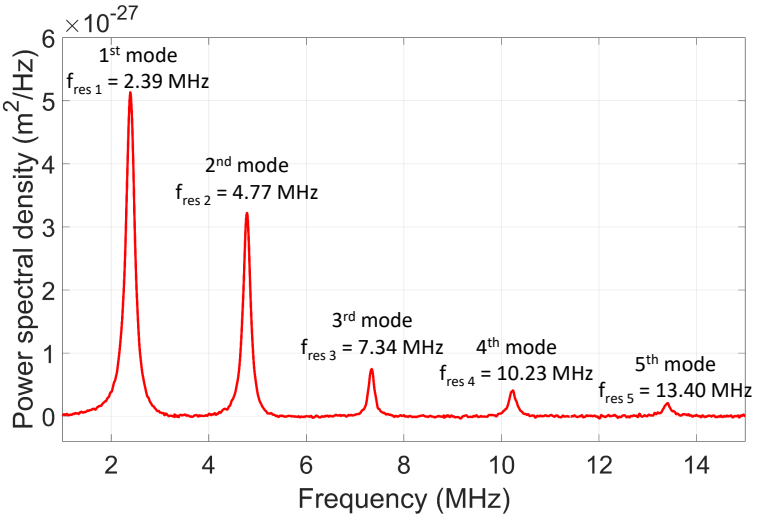

Figure A.4: Spectrum of thermal fluctuations measured in air of a nano-beam with length L_{NEMS} = 40 µm. Mechanical modes up to the fifth were detected.

Afterwards, the nano-beam was electro-thermally driven in air by applying two sinusoidal voltage signals V_1 and V_2, at the two gold electrodes fabricated at the two ends of the beam. V_1 and V_2 both had amplitudes of 200 mV, and their frequencies were varied simultaneously to measure the beam response in the frequency range 1-15 MHz. Moreover, phase difference between the two drive voltages was set to 0°, 45° or 90°, as explained in Section A.3. The experimental results, shown in Figure A.5, were repeated three times by moving the position of the laser spot along the beam as shown in Figure A.5(a). The measurements reported in Figure A.5(b) were performed at the center of the beam (i.e., positioning the laser spot at $0.5 L_{NEMS}$), where it is possible to detect only the odd modes, since the amplitude of the even modes is zero at this position [129]. It is evident that first, third and

fifth mode are strongly excited when the relative phase shift between drive signals is equal to 0° (red trace), while their amplitudes decrease by a factor of 1.5 when the phase difference is set to 45° (green trace). The amplitudes become even smaller when the phase shift is 90° (blue trace). At position $0.25L_{NEMS}$ (Figure A.5(c)), drive signals with phase difference of 0° can excite the odd modes more strongly. On the other hand, when the phase difference is equal to 90°, the second and forth modes have higher amplitude and the first, third and fifth modes have nearly zero amplitude. In the case of a phase shift of 45°, all resonances can be excited with similar amplitude. Finally, measurements were repeated by positioning the beam spot at location $0.33L_{NEMS}$ (Figure A.5(d)). Measurements at this position are similar to those at $0.25L_{NEMS}$ since the two positions are very close. The amplitude of the third mode is very small for every phase shift value because it has a zero-crossing very close to this position.

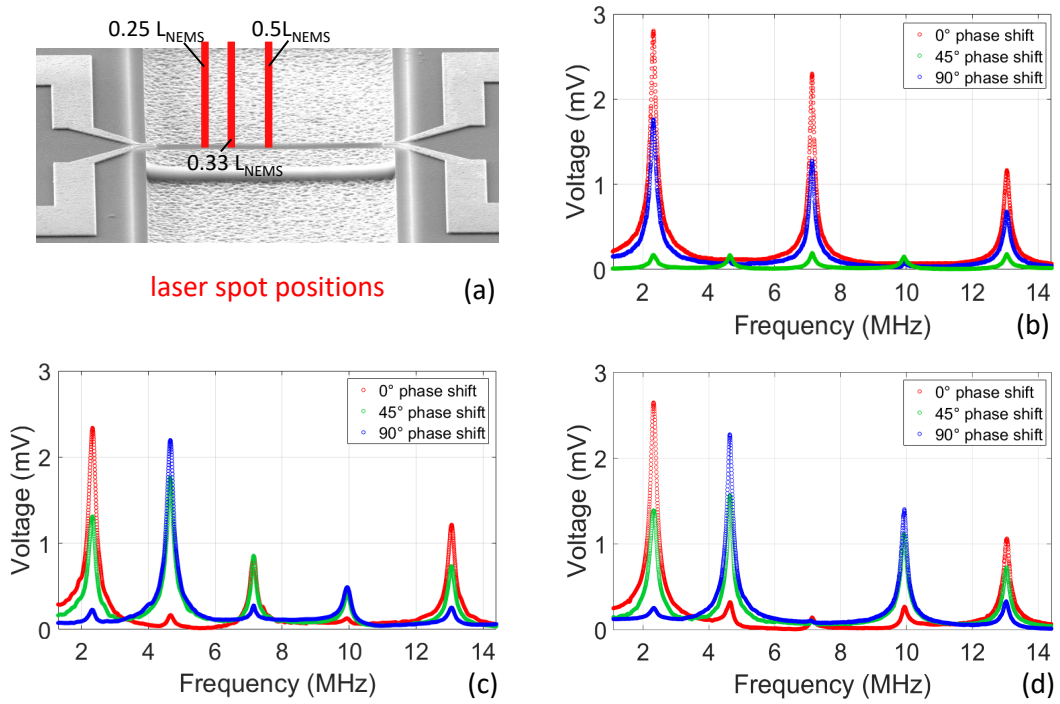

Figure A.5: Results of driven measurements carried out for a beam with L_{NEMS} = 40 µm in air. (a) The three positions where the measurements were performed. Device response was studied at $0.5L_{NEMS}$ (b), $0.25L_{NEMS}$ (c), and $0.33L_{NEMS}$ (d).

A.7 Conclusions

Laser interferometry is a powerful measurement technique that can be exploited to perform contactless, remote, non destructive measurements on NEMS devices.

In this work, a free-space Michelson interferometry was exploited to characterize the mechanical frequency response of doubly clamped nano-beams. In particular, a beam with a length of L_{NEMS} = 40 μm was investigated. From spectral analysis of the thermal motion of the beam, the first five resonant modes were detected. Electro-thermally actuated measurements were also performed in air. The unique contribution of this work was to drive the nano-beam by exploiting a double actuation scheme, where two voltage signals were simultaneously applied, one at each side of the NEMS, with the same amplitude and frequency but with a relative phase difference set to 0°, 45° or 90°. This resulted in actuation forces on two ends of the beam that either enhanced or reduced the motion, depending on the imposed phase difference. It was observed that when the phase difference between the signals was 0°, odd modes were excited more strongly, while with a phase difference of 90° even modes were excited at a higher amplitude. If the phase shift was set to 45°, it was possible to excite all resonant modes simultaneously. Future work could be devoted to carry out other experimental measurements with the nano-beam dipped in fluids with different density and viscosity to study Brownian motion and interaction between particles at a nanometric scale.

Appendix B

Multiwavelength fluidic sensing of water-based solutions in a μ-Slide channel with SWIR LEDs

In the framework of the research activity presented in Chapter 2 and focused on NIR spectroscopy in micro-fluidic devices, another instrumental configuration was designed with the aim of moving towards an amplitude detection scheme that is more compact, cost-effective and integrable in commercial systems. Hence, a multiwavelength instrumental configuration, combining SWIR (short-wave infrared) LEDs (with emission bands centered at λ = 1.3 μm, λ = 1.45 μm and λ = 2.15 μm) and InGaAs amplified photodiodes, has been applied for contactless fluidic sensing by measuring light intensity transmittance across a polymeric microchannel. The sensor was exploited for the measurement of water-based solutions. In particular, the main goal was to provide a proof of principle of urea detection in liquid solutions, exploiting urea absorption band around 2.15 μm. The functionality of the system was tested on solutions with urea concentrations from 0 up to 0.2 g/ml (20%), an interesting range for biomedical applications, with good sensitivity and LoD.

B.1 Introduction

In the last few years, the interest toward the development of sensors for the quantification of fluids composition using short-wave infrared (SWIR) spectroscopy, that refers to the use of radiation in the wavelength region between 1.0 and 2.5 μm, is increasing and widespread for several applications, from pharmaceutics and chemical to food quality and safety [130]. This technique is based on the detection

of transmitted or reflected radiation to study the analytical composition of samples that present absorption peaks at specific wavelengths: indeed, the absorption spectrum as a function of the wavelength is a characteristic "fingerprint" of each molecule and its concentration. Since SWIR spectroscopy is based on relatively weak and broad overtone and combination bands associated with C-H, N-H and O-H vibrational transitions [131], it is an emerging powerful approach to study, both quantitatively and specifically, solutions with water, glucose, ethanol and urea. In addition, the developments of optoelectronic components and the fabrication technology of light sources emitting in the SWIR region are improving, pushing many researchers to work on innovative systems based on SWIR spectroscopy combined with multiwavelength microfluidic sensing for different purposes [132, 133, 134]. For examples, some works focus on control of milk adulteration with water. In 2016, Ribeiro et al. in [135] developed a platform based on diffuse reflectance spectroscopy for the detection of milk adulteration with water by observing the intensity of light, provided by LEDs with specific spectral emission (centered at 1.2 μm and 1.45 μm), reflected by the sample using an InGaAsSb photodiode for the optical detection. In the same year, Moreira et al. developed a portable digital photometer that measures the transmittance of NIR radiation (emitted by three LEDs with emission wavelength centered at 970 nm, 1200 nm and 1450 nm) and observed that the measured light intensities increases with the addition of water to milk, for all the three wavelengths used [132]. Two years later, the authors adapted the prototype to quantify the ethanol content in adulterated gasoline samples, simply modifying the wavelengths of the three LEDs and the values of the resistances of the instrumentation circuit: the wavelength value of 970 nm was selected since it corresponds to a spectral band where there is no information due to absorbance, whereas sources emitting at 1.45 μm 1.53 μm were selected to analyze spectral bands in which there is ethanol absorption [136]. In 2020, Mu et al. measured the ethanol concentration during the glucose fermentation process using an immersion probe and a spectrum analyzer, with the aim to verify the effectiveness of a semi-supervised learning method based on deep learning for spectral modeling. A characteristic peak of ethanol was observed in the wavenumber range of 4790-12000 cm^{-1} and authors observed that the spectral absorption changes with ethanol concentration along the fermentation process [134].

Urea ($CO(NH_2)_2$) is another interesting biomolecule that often needs to be identified with high precising. It is the main nitrogenous end product of the metabolic breakdown of proteins; it is a component of bio-fluids such as blood, sweat, urine, and milk. Measurement of urea levels in body fluids can provide important information on renal function and can be used to diagnose kidney diseases. Con-

ventional analytical techniques for the determination of urea concentration in fluids, such as chromatography and colorimetry, suffer from long time-consuming sample pre-treatment and are mostly laboratory bound, whereas biosensors have the advantages of ease of use, portability, specificity, and are suitable for on-site real time monitoring [137, 138]. Biosensor response is proportional to the concentration of urea in the reaction environment, and the output signal may change based on the transducer type used, such as electro-chemical [139], optical [140], piezoelectric [141], or thermal [142]. Several studies based on spectrophotometric measurements agree to indicate the spectral range between 2.15 μm and 2.2 μm as particularly interesting to determine the amount of urea in solution. In 2019, Lubnow et al. investigated the variations of the absorption spectra as a function of the urea concentration, from 0 up to 40%, in the range 1.25-2.5 μm using a Fourier Transform Infrared (FTIR) spectrometer and a broadband source [143]. For wavelengths around 2.2 μm, the absorption coefficient of urea-water solutions increases with increasing urea concentration, whereas around 1.45 μm and 1.9 μm the absorption coefficient decreases with decreasing water content. In [144], Suzuky et al. aimed to verify the peak of sensitive wavelengths of urea and creatinine by measuring the spectra of the respective single solutions and performing a multiple regression analysis using the combination of 10 LED sources emitting between 1.4 μm and 2.3 μm. Observing the spectra of differential absorbance between pure water (reference sample) and urea and creatinine at different concentrations (measured samples), it was noticed that urea has a strong absorption at 2.2 μm, whereas the absorption of water is stronger at 1.4 μm and 1.9 μm. In the wavelength range between 1.6 μm and 1.8 μm, the spectra are almost superimposed as the urea concentration changes: the flat pattern indicates that the absorption is independent of the analyte concentration. In another work [145], a multiwavelength NIR laser absorption method is proposed with the aim to investigate the thickness, concentration and temperature of aqueous urea solutions between 5 and 40% by measuring the transmittance of NIR laser diodes through a heated thin-film cuvette and a FTIR spectrometer in the range between 5500 and 8000 cm^{-1}.

Despite the wide plethora of methods found in the literature for characterizing water-based solutions, there is still the need to demonstrate simple schemes for specific contactless, label free and noninvasive on-line detection, on fluid volumes of a few hundreds of μL. This work demonstrates an optoelectronic instrumental configuration based on LEDs with three different emission bands in the SWIR region to perform absorption sensing of water-based solutions, with a particular interest towards solutions of urea. A commercial micro-fluidic channel is used, allowing low-cost analyses of ultra-low volumes of sample.

B.2 Instrumental configuration

The instrumental configuration used for experimental testing is reported in Figure B.1. LED_{1300} (LED1300L, Thorlabs, NJ, USA), with emission band centered at 1300 nm and FWHM = 85 nm and LED_{1450} (LED1450L, Thorlabs, NJ, USA), with emission band centered at 1450 nm and FWHM = 105 nm, are combined by means of a 2x1 multimode fiber optic coupler with 50% coupling ratio (FCMM50-50A-FC, Thorlabs, NJ, USA). The coupler single output is then connected to a fiber-pigtailed aspheric lens (LPF-04-1550-50/125-QM-6-26-3.9AS-3S-30-1, OzOptics, Canada. After crossing the micro-fluidic channel with an incident angle of a 4° with respect to the normal, to avoid interference effects due to multiple reflections, the output beam is coupled to another fiber-pigtailed aspheric lens, identical to the input one. The output radiation of LED_{1300} and LED_{1450} can be analyzed in the wavelength domain with an optical spectrum analyzer (OSA Agilent 86142B, Agilent Technologies, CA, USA); spectral data are then processed in MATLAB environment. Moreover, the output radiation of each LED can be detected in time domain with an amplified InGaAs photodiode (PDA20CS2, Thorlabs, NJ, USA) connected to a digital oscilloscope (MDO3034, Tektronix, OR, USA) for data visualization and acquisition; the contributions of LED_{1300} and LED_{1450} are acquired simultaneously. The LEDs are driven with DC current for spectral analyses, whereas for amplitude measurements they are driven with squared pulses at a repetition rate of 5 Hz and duty cycle of 40%, with a relative time delay of 100 ms, providing a current peak of 90 mA corresponding to an emitted peak power of 5 mW (LED_{1300}) and 7 mW (LED_{1450}), approximately. Light is modulated using a two-channel waveform generator (33500B Series, Keysight, CA, USA). LED_{2150} (LED21Sr, Boston Electronics, MA, USA), with emission band centered at 2150 nm and FWHM ≈ 300 nm, is driven by the manufacturer driving board (Universal Photon Source Driver, Boston Electronics, MA, USA), USB connected to a laptop. By means of the software interface, LED_{2150} was driven in pulsed regime with repetition rate of 1 kHz, duty cycle of 2% and emitted peak power of around 1.5 mW. Radiation emitted by LED_{2150} crosses the microchannel and is detected in time domain with an amplified InGaAs photodiode with extended spectral response up to 2500 nm (PDA10D2, Thorlabs, NJ, USA), connected to the oscilloscope. Data are then analyzed in MATLAB environment, to separate the contributions of LED_{1300} and LED_{1450} (acquired simultaneously) and extract the average value and standard deviation of the photodetected signal amplitude in the time intervals when the considered LEDs are actually on. All measurements are performed with the fluid in static conditions.

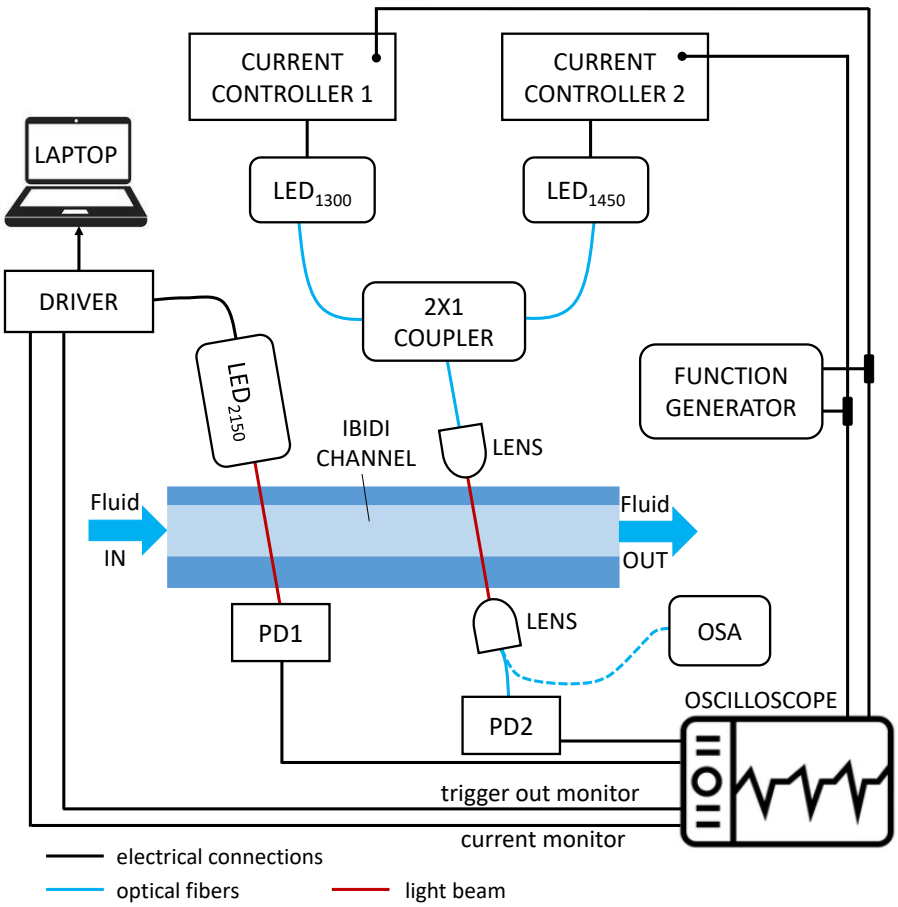

Figure B.1: Instrumental configuration for multiwavelength fluidic sensing. PD: photodiode. OSA: optical spectrum analyzer.

B.3 Theoretical spectral analysis

A theoretical model was developed in MATLAB environment, to obtain analytical results to be compared with the experimental data. Light transmission through the IBIDI channel was described according to the geometrical ray optics approximation (Figure B.2) and by applying the same equations for transmission described in Chapter 2. The only difference is that the IBIDI device is here used in a transmission configuration and not in reflection configuration as the micro-capillary. Hence, no reflectors were exploited in the configuration presented in this Appendix. The IBIDI µ-Slide was considered as a multi-layer structure composed of three layers with finite thicknesses (front polymer layer with t_f = 180 µm, channel with d = 800 µm, and back polymer layer $t_b \simeq$ 1060 µm) in air. Air RI was considered equal to 1 and (constant for every wavelength), while the refractive index of polymer was assumed purely real and equal to 1.52. Absorption losses

and dispersion due to the polymer were neglected.

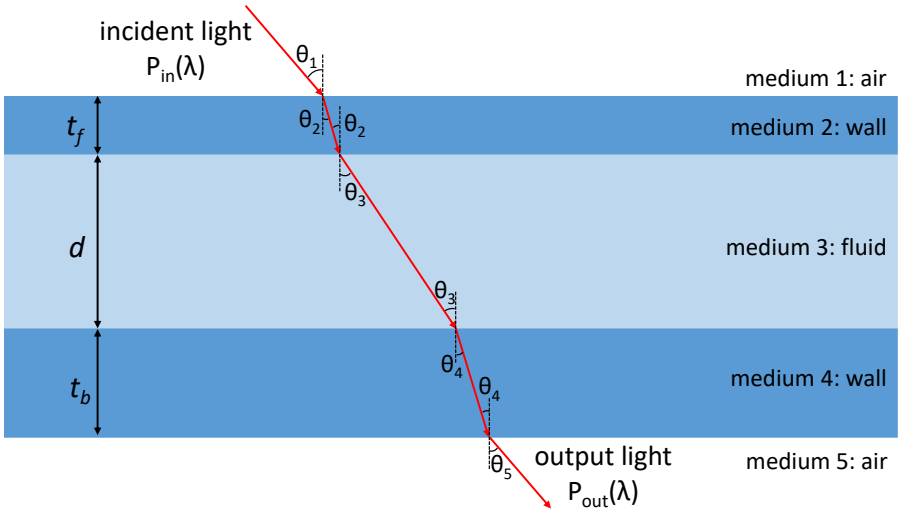

Figure B.2: Schematic representation of the light path through the IBIDI µ-Slide.

The refractive index of the sample filling the channel was modeled as

$$n_3(\lambda) = n'(\lambda) - i \cdot k_{abs}(\lambda) \tag{B.1}$$

where $n'(\lambda)$ is the real part, λ is the wavelength, i is the imaginary unit and $k_{abs}(\lambda)$ is the imaginary part, as expressed by Equation 2.4. The behaviour of k_{abs} as a function of the wavelength determines the absorption properties of each molecule, which are a unique characteristic of every substance. Data about the refractive index dependence on the wavelength in the spectral region of interest for each substance are tabulated in the literature [52, 146]. Then, the path followed by light in the channel and the amount of optical power transmitted at each interface T_{jl} were retrieved by applying the Snell and Fresnel formulas, es expressed by Equations 2.6, 2.7, 2.8, 2.9. The effect of attenuation due to fluid absorption on the transmittance can be calculated by applying the Lambert-Beer relation for the transmittance:

$$T_{abs}(\lambda) = e^{-\alpha(\lambda)\cdot f} \tag{B.2}$$

where α is the absorption coefficient given by $\alpha(\lambda) = [4\cdot\pi\cdot k_{abs}(\lambda)]/\lambda$, as expressed by Equation 2.2 and f is the optical path calculated through Equation 2.10. The wavelength dependence of the overall transmittance is found by multiplying all the contributions, so in presence of the sample in the channel it is given by:

$$T_{sample}(\lambda) = \frac{P_{out\ sample}(\lambda)}{P_{in}(\lambda)} = T_{12} \cdot T_{23} \cdot T_{34} \cdot T_{45} \cdot T_{abs}(\lambda) \tag{B.3}$$

When the channel is empty (i.e. filled with air). the transmittance is given by

$$T_{sample}(\lambda) = \frac{P_{out\ air}(\lambda)}{P_{in}(\lambda)} = T_{12} \cdot T_{23} \cdot T_{34} \cdot T_{45} \tag{B.4}$$

Eventually, we define as spectral response the ratio T_{sample}/T_{air} (as a function of the wavelength, as expressed by Equation 2.19) where additional absorption effects due to the polymer would be canceled out and therefore have been neglected in the model.

B.4 Spectral results

Theoretical spectral analysis was carried out considering ethanol-water mixtures with concentration of ethanol expressed in % of volume of 7.5%, 25%, 86.4% and 96%. Figure B.3(a) shows the theoretical spectral responses T_{sample}/T_{air} in the wavelength range 1000-2500 nm. In the same figure, the measured emission spectra of LED_{1300} (red dashed-dotted trace) and LED_{1450} (blue dashed-dotted trace), both normalized to their maximum value, are also reported. The approximate lineshape of the emission spectrum of LED_{2150} shown in the same graph (black dashed-dotted trace) has been deduced from the typical, nominal behavior reported in the datasheet. A comparison between the results of numerical simulations and experimental measurements carried out by inserting deionized water and ethanol 96% (Dilmoor S.p.A., Italy) in the microfluidic channel, is reported in Figure B.3(b). The measurements were performed by means of the OSA, with resolution bandwidth of 10 nm, using the LED_{1450} as the optical source. The good agreement between theoretical predictions and experimental results, although shown here only in the range 1.35-1.5 μm, but verified in a larger NIR range using a Tungsten lamp as a light source, supports the hypothesis that a similar agreement would be ensured also in other spectral regions.

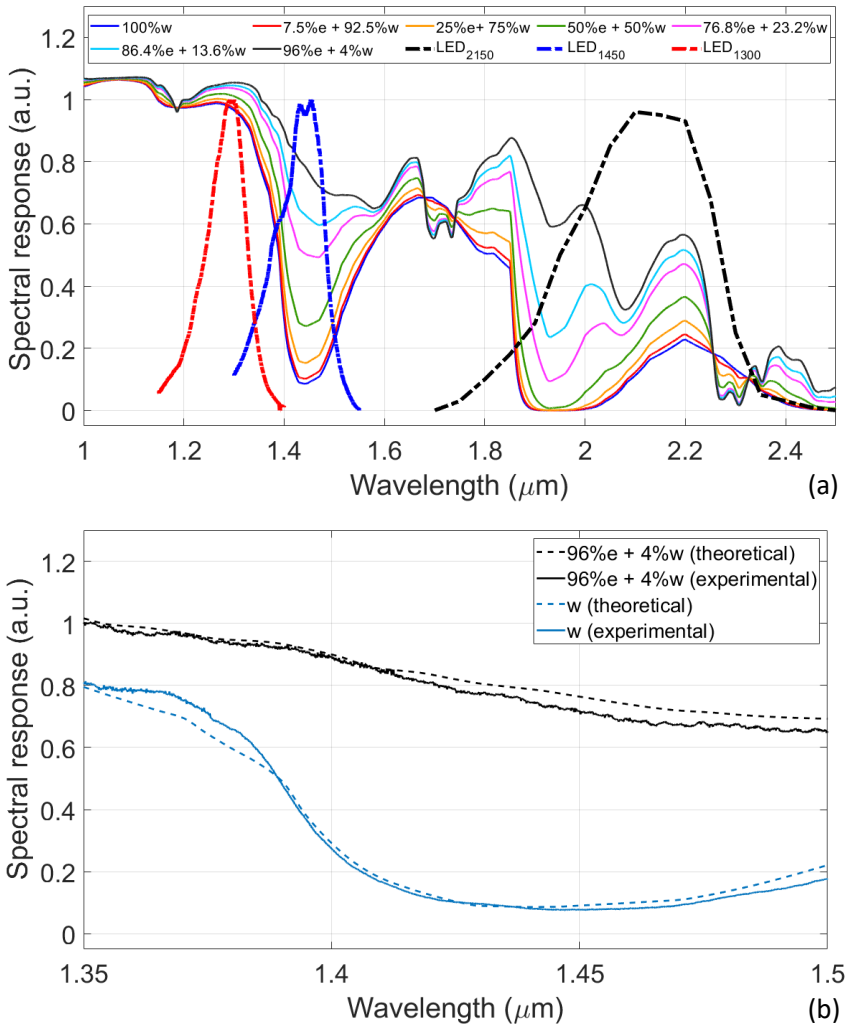

Figure B.3: Spectral results. (a) Theoretical spectral responses T_{sample}/T_{air} considering water-ethanol solutions in different concentrations as filling fluids (solid traces); red dashed-dotted trace: normalized emission spectra of LED_{1300}; blue dashed-dotted trace: normalized emission spectra of LED_{1450}; black dashed-dotted trace: normalized emission spectrum of LED_{2150}. (b) Comparison between the results of numerical simulations and experimental measurements, using LED_{1450} as optical source.

B.5 Experimental results of multiwavelenght sensing

As mentioned in Section B.2, for amplitude transmittance measurements, the LEDs were driven with pulsed waveforms and the photodetected signals were acquired with the oscilloscope. Typical examples of signals collected in the time domain, consisting in a sequence of 15 acquisitions, are reported in Figure B.4. The results

obtained with LED_{1300} and LED_{1450} (turned on and off out-of-phase as follows from the pulsed driving) are shown in Figure B.4(a). Each 2-s-long sample refers to a different filling fluid, namely air, water and ethanol-water solutions with increasing ethanol concentrations. The results obtained with LED_{2150} are shown in Figure B.4(b). Each 20 ms-long sample refers to a different filling fluid, namely air, water and ethanol-water solutions for increasing ethanol concentration. The acquired sets of signals, each one taken by filling the channel with the sample and then discarding it by pushing air, are depicted in the graphs as a continuous sequence, to better highlight the amplitude changes due to the different filling fluids.

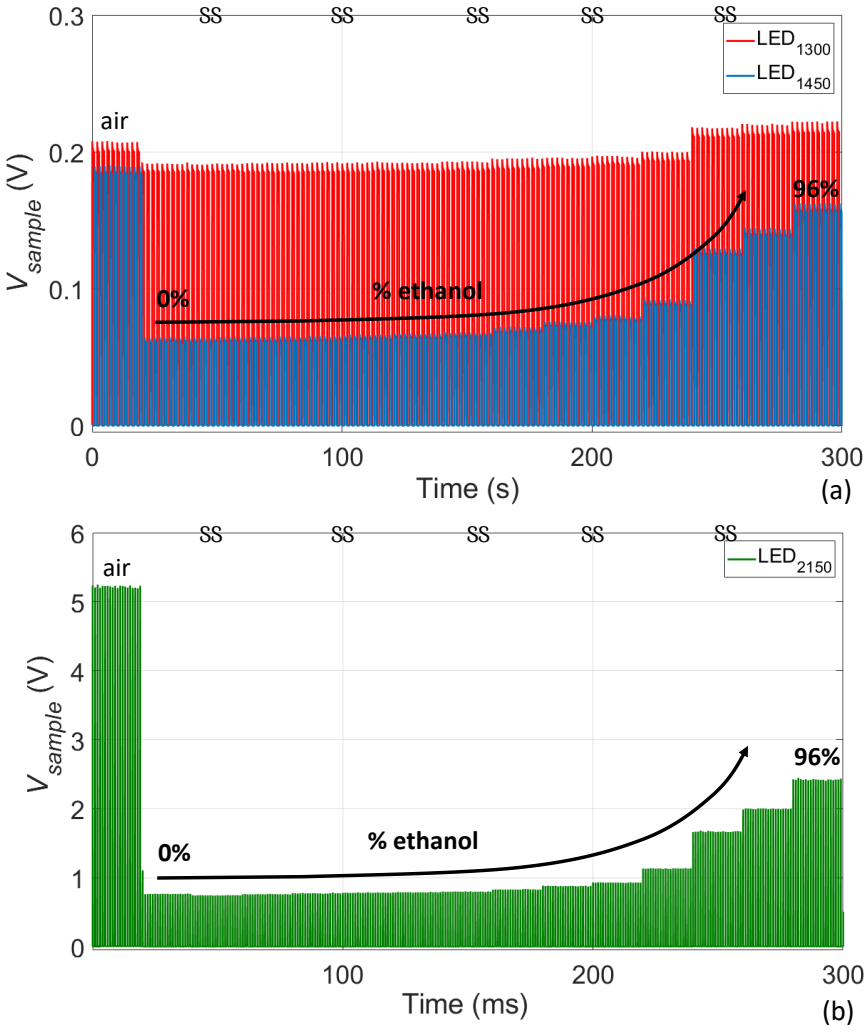

Figure B.4: Photodetected signals in time domain obtained by flowing the channel water-ethanol solutions. (a) Acquisition of LED_{1300} and LED_{1450} signals turned on-off, out of phase. (b) Acquisition of LED_{2150} signals.

Then, the amplitude responsivity

$$\Psi_\lambda(C) = \frac{V_{sample}(C)}{V_{air}} \tag{B.5}$$

was considered for solute concentration detection. The subscript $\lambda = 1300$, 1450, 2150 specifies the considered LED source, V_{sample} and V_{air} are the average amplitude of photodetected signals in the time intervals when the corresponding LED_λ is actually on, in presence of a fluid sample or air in the channel, respectively. V_{sample} depends on the concentration C of the solute (in w/v, weight/volume, g/ml for urea-water and glucose-water solutions, or v/v, volume/volume, ml/ml for ethanol-water solutions) in the tested solution. To relate the amplitude measurements to the spectral transmittances, it is reasonable to suppose that Ψ_λ is proportional to the integral, over the emission bandwidth of the corresponding LED, of the spectral responsivity V_{sample}/V_{air}. Then, the absorbances $A_{s,\lambda}$ and $A_{H2O,\lambda}$ due to the solute and water, respectively, can be expressed as

$$A_{s,\lambda} = \varepsilon_{s,\lambda} \cdot C \cdot F \tag{B.6}$$

$$A_{H2O,\lambda} = \varepsilon_{H2O,\lambda} \cdot C_{H2O} \cdot F \tag{B.7}$$

Moreover, the total attenuation or total transmission losses L_t induced by the presence of the sample in the channel can be expressed as:

$$\begin{aligned} L_t &= -log_{10}\left(\frac{P_{out\ sample}}{P_{out\ blank}}\right) = A_{s,\lambda} + A_{H2O,\lambda} + L_{n'} \\ &= \varepsilon_{s,\lambda} \cdot C \cdot F + \varepsilon_{H2O,\lambda} \cdot C_{H2O} \cdot F + L_{n'} \end{aligned} \tag{B.8}$$

where $P_{out\ sample}$ is the transmitted optical power in presence of the absorbing substance in the solution, $P_{out\ blank}$ is the transmitted optical power in presence of the solvent only or blank solution, C_{H2O} is the water concentration, n' is the real part of the refractive index of the fluid, F is the geometrical path, $\varepsilon_{s,\lambda}$ and $\varepsilon_{H2O,\lambda}$ are the molar extinction coefficients of solute and water, respectively [50, 147]. $L_{n'}$ accounts for the transmission losses at the inner interfaces of the channel microslide due to the refractive index difference between the polymer and the fluid sample. Note that $L_{n'}$ decreases for increasing n', thus for increasing values of C of all tested analytes, since transmittance at the interfaces increases with n'. Losses due

to scattering were here neglected. In order to correlate the theoretical analysis with the experimental results, since

$$\frac{P_{out\ sample}}{P_{out\ blank}} = \frac{V_{sample}(C)}{V_{air}} \tag{B.9}$$

then, transmission losses can be estimated from the experimental measurements as follows:

$$L_t = -log_{10}\left(\frac{P_{out\ sample}}{P_{out\ blank}}\right) = -log_{10}\Psi_\lambda(C) \tag{B.10}$$

Combining Equations B.8 and B.10, the amplitude responsivity can be written as a function of the molar extinction coefficients and concentrations:

$$\Psi_\lambda(C) = 10^{-(\varepsilon_{s,\lambda}\cdot C\cdot F+\varepsilon_{H2O,\lambda}\cdot C_{H2O}\cdot F+L_{n'})} \tag{B.11}$$

Since only two-substance mixtures are analyzed in this work, whose effect is supposed to be independent, it holds that $C_{H2O} \approx 1$ - C , thus

$$\Psi_\lambda(C) = 10^{-(\varepsilon_{H2O,\lambda}\cdot F+L_{n'})}\cdot 10^{-(\varepsilon_{s,\lambda}-\varepsilon_{H2O,\lambda})\cdot F\cdot C)} = B_\lambda\cdot 10^{-(\varepsilon_{s,\lambda}-\varepsilon_{H2O,\lambda})\cdot F\cdot C)} \tag{B.12}$$

where

$$B_\lambda = 10^{-(\varepsilon_{H2O,\lambda}\cdot F+L_{n'})} < 1 \tag{B.13}$$

for $|(\varepsilon_{s,\lambda} - \varepsilon_{H2O,\lambda})\cdot F\cdot C)| < 0.1$, Equation B.13 can be approximated as follows:

$$\Psi_\lambda(C) \simeq B_\lambda - B_\lambda\cdot(\varepsilon_{s,\lambda} - \varepsilon_{H2O,\lambda})\cdot F\cdot C \tag{B.14}$$

where the last term in highlights the linear dependence of $\Psi_\lambda(C)$ on the solute concentration C. Since LED sources are not monochromatic, Lambert-Beer is just an approximation. For example, we cannot recover the exact wavelength dependence of the terms B_λ and $\varepsilon_{s,\lambda} - \varepsilon_{H2O,\lambda}$. Nevertheless, from the experimental measurements of V_{sample} and V_{air} we can obtain the behavior of $\Psi_\lambda(C)$ as a function of the concentration C of the solute, for all three considered wavelength ranges. Figure B.5(a) shows the experimental results of $\Psi_\lambda(C)$ for ethanol-water solutions at different concentrations. Red, blue and black markers refer to the average and standard deviation of the photodetected signals due to LED_{1300}, LED_{1450} and LED_{2150}, respectively, for the following concentration C (ml/ml) of ethanol: 0, 0.005, 0.01,

0.025, 0.05, 0.075, 0.1, 0.165, 0.25, 0.33, 0.5, 0.768, 0.864 and 0.96 ml/ml. The lines with matching colors in Figure B.5(a) are shape-preserving interpolations of the data (cubic spline with adjusted parameters). A linear dependence of $\Psi_\lambda(C)$ on C with high coefficient of determination R^2 is found for $0 < C < 0.5$ ml/ml, thus for low ethanol concentration, as shown in Figure B.5(b), where the lines with matching colors represent the best linear fittings of the experimental data. The linear dependence of $\Psi_\lambda(C)$ on C, for $C < 0.5$, substantially agrees with the linear dependence predicted by Equation B.14. For increasing concentration of ethanol in water, $\Psi_\lambda(C)$ increases with C, i.e. $\Delta\Psi_\lambda(C)/\Delta C > 0$ for all considered wavelength ranges. In particular, $\Psi_{1300} > 1$ V/V for $C > 0.6$ ml/ml since water and ethanol absorbances in that range are very small (see spectral responsivity in Figure B.3(b)), thus have a negligible effect on Ψ_{1300}, while the losses $L_{n'}$ decrease due to the substantial increase of n' with C. In the wavelength bands around 1.45 µm and 2.15 µm, where $\varepsilon_{etoh,\lambda} < \varepsilon_{H2O,\lambda}$ as reported in the literature [148], by augmenting the concentration of ethanol there is a reduction of water concentration, yielding an overall decrease of the absorbance and thus an increase of V_{sample} and hence of the responsivity parameter.

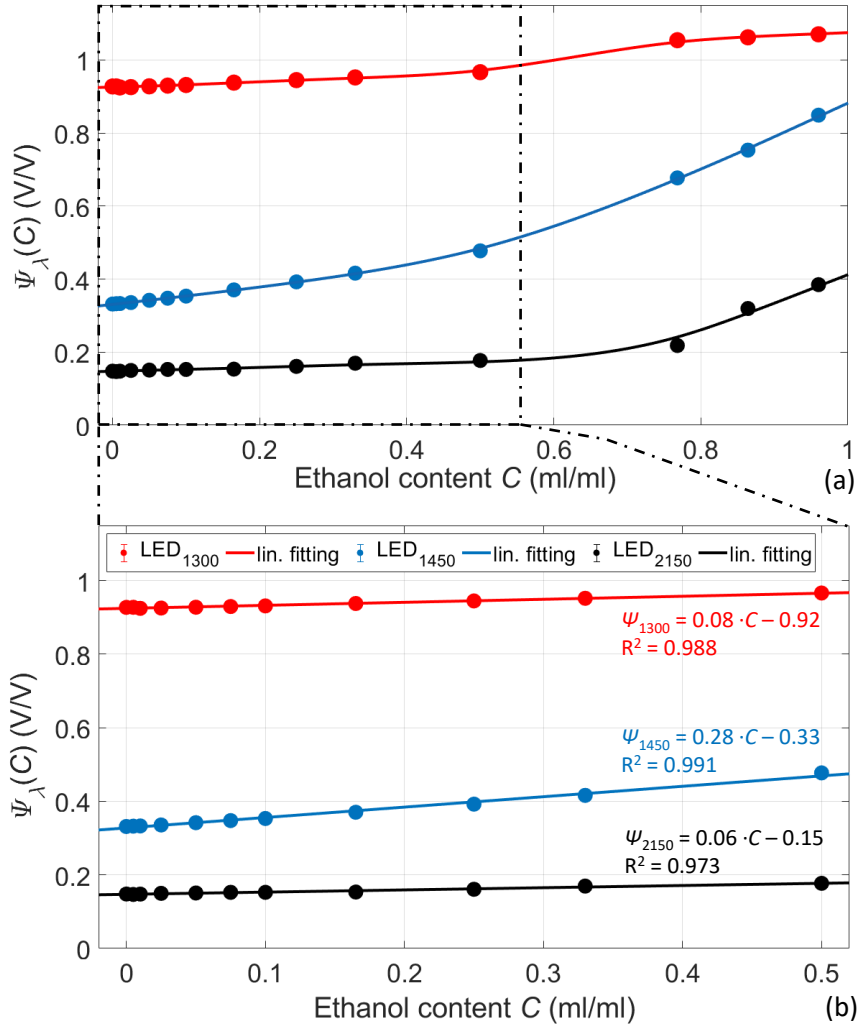

Figure B.5: Experimental results of Ψ_λ for ethanol-water solutions. (a) Signals due to LED_{1300}, LED_{1450} and LED_{2150} (red, blue and black dots), respectively, for different concentration C of ethanol. The lines with matching colors in are shape preserving interpolations of the data. (b) Zoomed view of (a) for $0< C < 0.5$ ml/ml. The lines with matching colors represent the best linear fittings.

Experimental results of Ψ_λ for glucose-water solutions are reported in Figure B.6(a). Red, blue and black markers refer to the average and standard deviation of the photodetected signals due to LED_{1300}, LED_{1450} and LED_{2150}, respectively, for the following concentration C (g/ml) of glucose: 0, 0.005, 0.01, 0.025, 0.05, 0.075, 0.1, 0.165, 0.25, 0.33 and 0.5 g/ml. The solution of glucose 0.01 g/ml is provided by Eurospital S.p.A. (Italy): it is an infusion solution that contains 110 g/l of monohydrate glucose, that correspond to 100 g/l of anhydrous glucose. Glucose 0.33 g/ml and glucose 0.5 g/ml are provided by Fresenius Kabi S.r.l (Italy); they contain 363 g/l and 550 g/l of monohydrate glucose, respectively (that correspond

to 330 g/l and 500 g/l of anhydrous glucose). The other samples are obtained by diluting these solutions with water. The lines with matching colors represent the best linear fittings of the experimental data. From the fittings, it was found that for glucose-water solutions, $\Delta\Psi_{1300}(C)/\Delta C$ = 0.04 (g/ml)$^{-1}$ > 0 and $\Delta\Psi_{1450}(C)/\Delta C$ = 0.14 (g/ml)$^{-1}$ > 0. Since in these bands $\varepsilon_{glucose} \ll \varepsilon_{H2O}$, the increasing concentration of glucose does not compensate for the water absorbance decrease: a higher glucose concentration corresponds to a lower water concentration that yields to an overall decrease of the absorbance [148]. On the other hand, $\Delta\Psi_{2150}(C)/\Delta C$ = – 0.05 (g/ml)$^{-1}$ < 0 since in this range $\varepsilon_{glucose,\lambda} > \varepsilon_{H2O,\lambda}$ and the absorbance increase due to the addition of glucose compensates for the water absorbance decrease. Experimental results of $\Psi_\lambda\lambda$ for urea solutions are summarized in Figure B.6(b). Red, blue and black markers refer to the average and standard deviation of the photodetected signals due to LED_{1300}, LED_{1450} and LED_{2150}, respectively, when testing the following concentration C (g/ml) of urea in water: 0, 0.005, 0.01, 0.1, 0.15 and 0.2 g/ml. The widest range of typical biochemical and biomedical applications was explored. Urea (J75826 Urea, 99.5+%, Molecular Biology Grade, Ultrapure) is provided by Alfa Aesar, ThermoFisher Scientific (MA, USA). The lines with matching colors represent the best linear fittings of the experimental data. Again, for solutions of urea in water, it was observed that $\Delta\Psi_{1300}(C)/\Delta C$ = 0.03 (g/ml)$^{-1}$ > 0 and $\Delta\Psi_{1450}(C)/\Delta C$ = 0.13(g/ml)$^{-1}$ > 0. Since in these wavelength regions (around 1.3 μm and 1.45 μm) $\varepsilon_{urea,\lambda} \ll \varepsilon_{H2O,\lambda}$ the increasing concentration of urea does not compensate for the water absorbance decrease: a higher urea concentration corresponds to a lower water concentration that yields to an overall decrease of the absorbance. Thus, the increase of $\Psi_{1450}(C)$ with C is not specific for urea but it is related to the fact that we are considering water as solvent. As a matter of fact, we have observed the increase of $\Psi_{1450}(C)$ also for previously considered mixtures. Then, it was observed that $\Delta\Psi_{2150}(C)/\Delta C$ = – 0.29 (g/ml)$^{-1}$ < 0, confirming that, in this region, $\varepsilon_{urea,\lambda} \gg \varepsilon_{H2O,\lambda}$ and the absorbance increase due to urea overcompensates the water absorbance decrease. The absolute value of $\Delta\Psi_{2150}(C)/\Delta C$ for urea-water solutions is larger than that found for glucose solutions, since $\varepsilon_{urea,\lambda} \gg \varepsilon_{glucose,\lambda}$ [149]. Concentrations of urea higher than 20 wt% would be easier to detect, since the induced absorption effect would be stronger and the optical power is sufficient to ensure a good signal to noise ratio even for a lower transmittance. However, a linear relationship between urea content and Ψ_λ would not held for much higher urea contents.

The amplitude responsivity Ψ_{2150} was also computed when filling the channel with solutions of urea in dialyzing fluid (also known as dialysate solution), a non-sterile aqueous electrolyte solution for clinical applications [150]. The solution

used in the experiments contains: 138 mmol/L of Na^+, 2 mmol/L of K^+, 1.25 mmol/L of Ca^{++}, 0.5 mmol/L of Mg^{++}, 110.5 mmol/L of Cl^-, 5.55 mmol/L of $C_6H_{12}O_6$, and 33 mmol/L of HCO_3^+. As shown in Figure B.6(b), the results (purple markers and trace) are almost superposed to data obtained when pure water was used as solvent. Thus, the substantial decrease of Ψ_{2150} with C is specifically due to the increasing concentration of urea, though combined with lower water absorption.

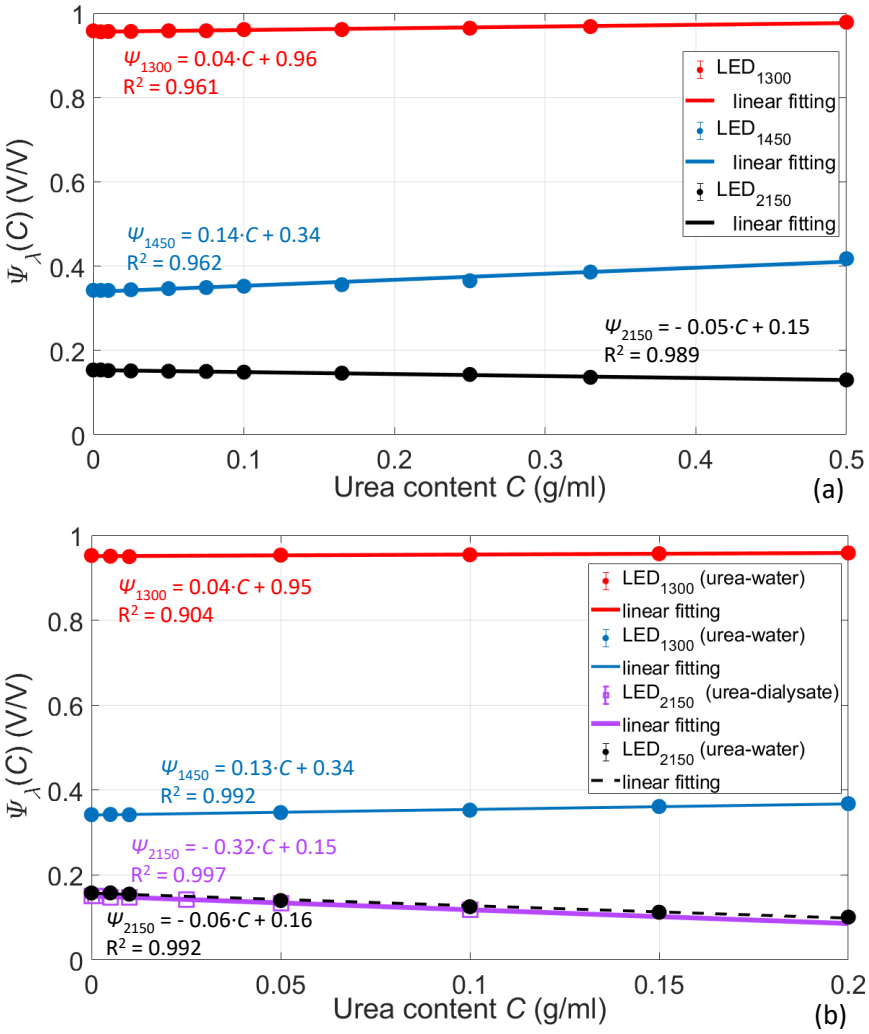

Figure B.6: (a) Experimental results of Ψ_λ for glucose-water solutions. Signals due to LED_{1300}, LED_{1450} and LED_{2150} (red, blue and black dots), respectively, for different concentration C of glucose. The curves with matching colors represent the best linear fittings. (b) Experimental results of Ψ_λ for urea solutions. Signals due to LED_{1300}, LED_{1450} and LED_{2150} (red, blue and black dots), respectively, for different concentration C of urea solutions in water. Violet markers are the experimental data obtained with LED_{2150} for different concentration C of urea in a dialysate solution. The violet trace is the best linear fitting.

The evident correlation between the Ψ_{1450} increase and the Ψ_{2150} decrease, for increasing concentrations C of urea, suggested to identify a parameter $\nu(C)$, as the ratio of the responsivities measured with LED_{1450} and LED_{2150}, that depends on urea concentration C and allows to partially compensate the contribution of water absorption:

$$\nu(C) = \frac{\Psi_{1450}}{\Psi_{2150}} \tag{B.15}$$

$$\nu(C) = \frac{B_{1450} + (\Delta\Psi_{1450}(C)/\Delta C) \cdot C}{B_{2150} + (\Delta\Psi_{2150}(C)/\Delta C) \cdot C} = \frac{0.34 + 0.13 \cdot C}{0.16 - 0.29 \cdot C} \tag{B.16}$$

It is important to stress that Equations B.15 and B.16 holds true for 0 g/ml $< C <$ 0.2 g/ml. Therefore, the concentration C can be derived as:

$$C = \frac{-0.34 + 0.16 \cdot \nu}{0.13 + 0.29 \cdot \nu} \tag{B.17}$$

Figure B.7(a) reports the ν parameter obtained from experimental data as expressed by Equation B.15 as a function of the expected theoretical urea concentration C; Figure B.7(b) reports the detected values of urea concentration C, calculated using Equation B.17 in comparison with the expected concentrations values on the basis of the experimentally prepared mixtures: data are distributed along the bisector with R^2 parameter of 0.995.

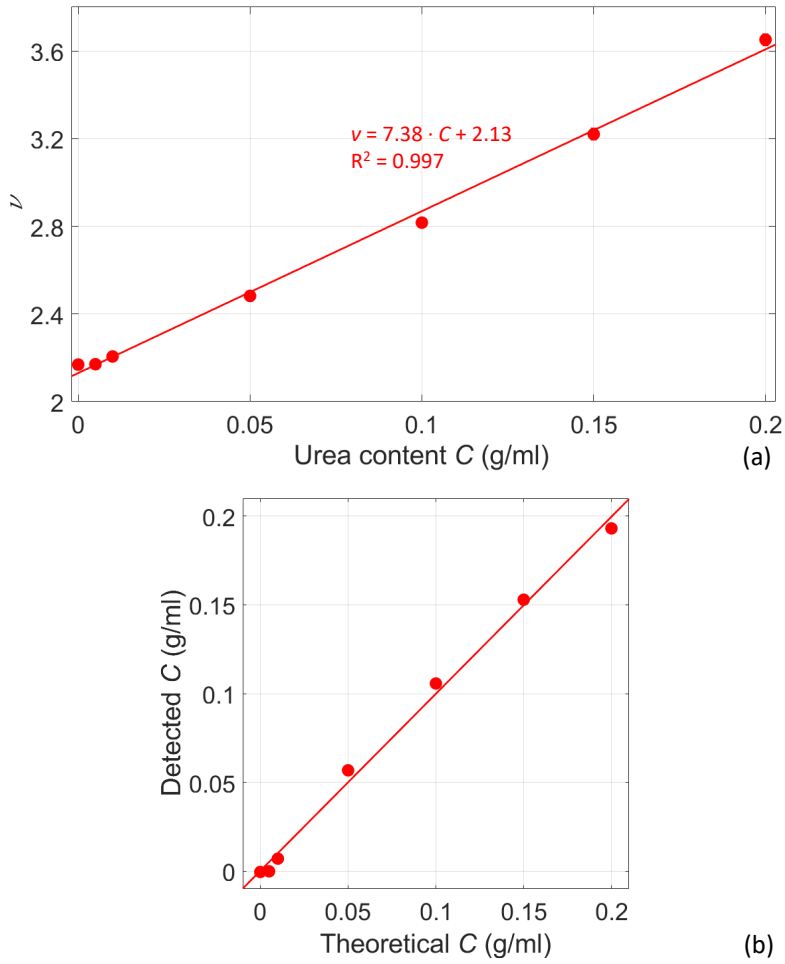

Figure B.7: (a) ν parameter as a function of the expected theoretical urea concentration C used during sample preparation. (b) Detected urea concentration C (calculated computing Equation B.17 versus the expected theoretical values of C; the line represents is the bisector curve.

B.6 Conclusions

In this work, a multiwavelength technique for sensing of solutes in water solutions was demonstrated based optical absorption. The mail goal of the work was to find a direct and specific method for detecting the concentration of urea in water-based solutions, exploiting its absorption SWIR band around $\lambda = 2.15$ µm, measuring the light transmittance across a micro-channel, thus with a contactless and label free approach. Toward this aim, the performances of a simple setup based on three LEDs and two photodiodes have been analyzed and the results have been illustrated. The ν parameter was extracted: it is highly specific for urea detection with sensitivity $S \simeq 7$ (g/ml)$^{-1}$ and limit of detection $LoD \simeq 0.006$ (g/ml). To increase the sensitivity, the optical path could be increased, since absorbance increases with

that parameter. This solution was actually tested by substituting the IBIDI channel with a rectangular glass tubing with 1-mm channel depth, which confirmed that sensitivity could be improved. However, the optical path cannot be substantially increased since strong water absorption within the wide emission band of LED_{2150} would reduce the amplitude of the output signal and, thus, the signal-to-noise ratio. An interesting solution would be to use a diode laser with narrow emission around 2.15–2.20 μm, thus within the absorption band of urea, but at the border of the water absorption band. The fabrication technology of these sources is improving, making them more affordable for specific sensing. Moreover, since semiconductor sources can be easily modulated, detection performed with a lock-in configuration would be able to provide a better signal-to-noise ratio.

Appendix C

Composition of AN mixtures

In Chapter 3, six different AN mixtures were considered for experimental testing. As explained, they are commercial fluids with commercial names CLINIMIX and AMINOMIX, produced by Baxter S.r.l. (Italy) and Fresenius Kabi (Germany), respectively. They were provided by the pharmacy of the San Matteo hospital and they come in plastic bags with different formats (1 L, 1.5 L or 2 L). Each AN mixture is packaged in a plastic bag with two compartments containing an aqueous amino acid solution with electrolytes and a dilution of water with glucose and calcium chloride, respectively. The two compartments are initially divided by a plastic membrane. The mixtures must be administered only after breaking the seal and mixing the contents of both compartments. The appearance of the solution after mixing should be clear and colourless or slightly yellow. The dosage and flow rate of infusion depend on age,sex, metabolism and clinical conditions of the patient. Every type of CLINIMIX and AMINOMIX contains amino acids, electrolytes and glucose in different concentrations. The AN fluids investigated in this Ph.D. tehsis are CLINIMIX N9G15E, CLINIMIX N12G20E, AMINOMIX 12%I, CLINIMIX N14G30E, CLINIMIX N17G35E and AMINOMIX 20%. The following tables report the concentration of every subtsance for every AN mixtures, as it it is reported on the leaflet.

Substance	Concentration (g/L)
L-alanine	5.70
L-arginine	3.17
Glycine	2.84
L-histidine	1.32
L-isoleucine	1.65
L-leucine	2.01
L-lysine	1.60
L-methionine	1.10
L-phenylalanine	1.54
L-proline	1.87
L-serine	1.38
L-threonine	1.16
L-tryptophan	0.50
L-tyrosine	0.11
L-valine	1.60
Sodium acetate, $3H_2O$	2.16
Potassium phosphate dibasic	2.61
NaCl	1.12
Magnesium chlorure, $6H_2O$	0.51
Glucose	75
Calcium chlorure, $2H_2O$	0.33

Table C.1: Composition of CLINIMIX N9G15E.

Substance	Concentration (g/L)
L-alanine	7.25
L-arginine	4.03
Glycine	3.61
L-histidine	1.68
L-isoleucine	2.10
L-leucine	2.56
L-lysine	2.03
L-methionine	1.40
L-phenylalanine	1.96
L-proline	2.38
L-serine	1.75
L-threonine	1.47
L-tryptophan	0.63
L-tyrosine	0.14
L-valine	2.03
Sodium acetate, $3H_2O$	2.58
Potassium phosphate dibasic	2.61
NaCl	0.94
Magnesium chlorure, $6H_2O$	0.52
Glucose	100
Calcium chlorure, $2H_2O$	0.33

Table C.2: Composition of CLINIMIX N12G20E

Substance	Concentration (g/L)
L-alanine	7.00
L-arginine	6.00
Glycine	5.50
L-histidine	1.50
L-isoleucine	2.50
L-leucine	3.70
L-lysine	3.30
L-methionine	2.15
L-phenylalanine	2.55
L-proline	5.60
L-serine	3.25
L-threonine	2.20
L-tryptophan	1.00
L-tyrosine	0.20
L-valine	3.10
Sodium glicerophosphate hydrate	4.59
Acetic acid	4.50
potassium hydroxide	1.981
Hydrochloric acid 25%	1.47
NaCl	1.169
Magnesium chlorure, $6H_2O$	0.61
Glucose	120
Calcium chlorure, $2H_2O$	0.294
Zinc chloride	0.00545

Table C.3: Composition of AMINOMIX with 12% of glucose.

Substance	Concentration (g/L)
L-alanine	8.80
L-arginine	4.89
Glycine	4.38
L-histidine	2.04
L-isoleucine	2.55
L-leucine	3.11
L-lysine	2.47
L-methionine	1.70
L-phenylalanine	2.38
L-proline	2.89
L-serine	2.13
L-threonine	1.79
L-tryptophan	0.77
L-tyrosine	0.17
L-valine	2.47
Sodium acetate, $3H_2O$	2.97
Potassium phosphate dibasic	2.61
NaCl	0.77
Magnesium chlorure, $6H_2O$	0.51
Glucose	150
Calcium chlorure, $2H_2O$	0.33

Table C.4: Composition of CLINIMIX N14G30E.

Substance	Concentration (g/L)
L-alanine	10.35
L-arginine	5.75
Glycine	5.15
L-histidine	2.40
L-isoleucine	3.00
L-leucine	3.65
L-lysine	2.90
L-methionine	2.00
L-phenylalanine	2.80
L-proline	3.40
L-serine	2.50
L-threonine	2.10
L-tryptophan	0.90
L-tyrosine	0.20
L-valine	2.90
Sodium acetate, $3H_2O$	3.40
Potassium phosphate dibasic	2.61
NaCl	0.59
Magnesium chlorure, $6H_2O$	0.51
Glucose	175
Calcium chlorure, $2H_2O$	0.33

Table C.5: Composition of CLINIMIX N17G35E.

Substance	Concentration (g/L)
L-alanine	7.00
L-arginine	6.00
Glycine	5.50
L-histidine	1.50
L-isoleucine	2.50
L-leucine	3.70
L-lysine	3.30
L-methionine	2.15
L-phenylalanine	2.55
L-proline	5.60
L-serine	3.25
L-threonine	2.20
L-tryptophan	1.00
L-tyrosine	0.20
L-valine	3.10
Sodium glicerophosphate hydrate	4.59
Acetic acid	4.50
Potassium hydroxide	1.981
Hydrochloric acid 25%	1.47
NaCl	1.169
Magnesium chlorure, $6H_2O$	0.61
Glucose	200
Calcium chlorure, $2H_2O$	0.294
Zinc chloride	0.00545

Table C.6: Composition of AMINOMIX with 20% of glucose.

Bibliography

[1] P. Minzioni, R. Osellame, C. Sada, S. Zhao, F. G. Omenetto, K. B. Gylfason, T. Haraldsson, Y. Zhang, A. Ozcan, A. Wax, F. Mugele, H. Schmidt, G. Testa, R. Bernini, J. Guck, C. Liberale, K. Berg-Sørensen, J. Chen, M. Pollnau, S. Xiong, A. Q. Liu, C. C. Shiue, S. K. Fan, D. Erickson, and D. Sinton. Roadmap for optofluidics. *Journal of Optics*, 19(9):093003, 2017.

[2] C. Grillet, P. Domachuck, B. Eggleton, and J. Cooper-White. Optofluidics enables compact tunable interferometer. *Laser focus world*, 41(2):100–103, 2005.

[3] P. Domachuk, M. Cronin-Golomb, B. J. Eggleton, S. Mutzenich, G. Rosengarten, and A. Mitchell. Application of optical trapping to beam manipulation in optofluidics. *Optics Express*, 13(19):7265–7275, 2005.

[4] D. Psaltis, S. R. Quake, and C. Yang. Developing optofluidic technology through the fusion of microfluidics and optics. *Nature*, 442(7101):381–386, 2006.

[5] G. M. Whitesides. The origins and the future of microfluidics. *Nature*, 442(7101):368–373, 2006.

[6] X. Fan and I. M. White. Optofluidic microsystems for chemical and biological analysis. *Nature photonics*, 5(10):591–597, 2011.

[7] B. Kuswandi, J. Huskens, and W. Verboom. Optical sensing systems for microfluidic devices: a review. *Analytica Chimica Acta*, 601(2):141–155, 2007.

[8] G. Minas, R. F. Wolffenbuttel, and J. H. Correia. A lab-on-a-chip for spectrophotometric analysis of biological fluids. *Lab on a Chip*, 5(11):1303–1309, 2005.

[9] D. Brennan, J. Justice, B. Corbett, T. McCarthy, and P. Galvin. Emerging optofluidic technologies for point-of-care genetic analysis systems: a review. *Analytical and Bioanalytical Chemistry*, 395(3):621–636, 2009.

[10] T. Yang, P. Paiè, G. Nava, F. Bragheri, R. Martinez Vazquez, P. Minzioni, M. Veglione, M. Di Tano, C. Mondello, and R. Osellame. An integrated optofluidic device for single-cell sorting driven by mechanical properties. *Lab on a Chip*, 15(5):1262–1266, 2015.

[11] N. M. M. Pires, T. Dong, U. Hanke, and N. Hoivik. Recent developments in optical detection technologies in lab-on-a-chip devices for biosensing applications. *Sensors*, 14(8):15458–15479, 2014.

[12] V. Bello and S. Merlo. Phase detection of the NIR optical resonances of rectangular glass micro-capillaries. In *2020 IEEE International Instrumentation and Measurement Technology Conference (I2MTC)*, pages 1–5. IEEE, 2020.

[13] V. Bello, A. Simoni, and S. Merlo. Spectral phase shift interferometry for refractive index monitoring in micro-capillaries. *Sensors*, 20(4):1043, 2020.

[14] V. Bello, A. Simoni, and S. Merlo. Spectral interferometric detection of nir optical resonances of rectangular microcapillaries for refractive index sensing. *IEEE Transactions on Instrumentation and Measurement*, 70:1–9, 2021.

[15] M. Born and E. Wolf. *Principles of optics: electromagnetic theory of propagation, interference and diffraction of light*. Elsevier, 2013.

[16] S. J. Orfanidis. *Electromagnetic Waves and Antennas*. Rutgers University, 2008.

[17] W. Morrish, P. West, N. Orlando, E. Klantsataya, K. Gardner, S. Lane, R. Decorby, A. François, and A. Meldrum. Refractometric micro-sensor using a mirrored capillary resonator. *Optics express*, 24(22):24959–24970, 2016.

[18] G. Rigamonti, M. Guardamagna, V. Bello, S. Marconi, F. Auricchio, and S. Merlo. Flow-through micro-capillary refractive index sensor based on t/r spectral shift monitoring. *Biomedical Optics Express*, 8(10):4438–4453, 2017.

[19] G. Rigamonti, V. Bello, and S. Merlo. Spectral optical readout of rectangular–miniature hollow glass tubing for refractive index sensing. *Sensors*, 18(2):603, 2018.

[20] U. S. Raikar, V. K. Kulkarni, A. S. Lalasangi, K. Madhav, and S. Asokan. Etched fiber bragg grating as ethanol solution concentration sensor. *Optoelectronics and Advanced Material*, 1(4):149–151, 2007.

[21] W. Zhang, D. Webb, and G. Peng. Polymer optical fiber bragg grating acting as an intrinsic biochemical concentration sensor. *Optics Letters*, 37(8):1370–1372, 2012.

[22] M. S. Kwon and W. H. Steier. Microring-resonator-based sensor measuring both the concentration and temperature of a solution. *Optics Express*, 16(13):9372–9377, 2008.

[23] T. Young. Experiments and calculations relative to physical optics, the philosophical transaction, 1803. *A Course of Lectures on Natural Philosophy and the Mechanical Arts II*, pages 639–648, 1803.

[24] M. Norgia, S. Donati, and D. D'Alessandro. Interferometric measurements of displacement on a diffusing target by a speckle tracking technique. *IEEE Journal of Quantum Electronics*, 37(6):800–806, 2001.

[25] W. Drexler and J. G. Fujimoto. *Optical coherence tomography: technology and applications*. Springer Science & Business Media, 2008.

[26] S. Donati. *Electro-optical instrumentation: sensing and measuring with lasers*. Pearson Education, 2004.

[27] B. P. Abbott, R. Abbott, T. D. Abbott, M. R. Abernathy, F. Acernese, K. Ackley, C. Adams, T. Adams, P. Addesso, et al. Observation of gravitational waves from a binary black hole merger. *Physical Review Letters*, 116:061102, Feb 2016.

[28] J. M. Schmitt. Optical coherence tomography (OCT): a review. *IEEE Journal of Selected Topics in Quantum Electronics*, 5(4):1205–1215, 1999.

[29] F. Carpignano, G. Rigamonti, and S. Merlo. Characterization of rectangular glass microcapillaries by low-coherence reflectometry. *IEEE Photonics Technology Letters*, 27(10):1064–1067, 2015.

[30] F. Carpignano, G. Rigamonti, G. Mazzini, and S. Merlo. Low-coherence reflectometry for refractive index measurements of cells in micro-capillaries. *Sensors*, 16(10):1670, 2016.

[31] S. G. Nelson, K. S. Johnston, and S. S. Yee. High sensitivity surface plasmon resonace sensor based on phase detection. *Sensors and Actuators B: Chemical*, 35(1-3):187–191, 1996.

[32] S. Y. Wu, H. P. Ho, W. C. Law, C. Lin, and S. K. Kong. Highly sensitive differential phase-sensitive surface plasmon resonance biosensor based on the mach–zehnder configuration. *Optics Letters*, 29(20):2378–2380, 2004.

[33] Q. Chen, M. Zhang, S. Liu, H. Luo, Y. He, J. Luo, and W. Lv. Refractive index measurement of low concentration solution based on surface plasmon resonance and dual-frequency laser interferometric phase detection. *Measurement Science and Technology*, 28(1):015011, 2016.

[34] M. H. Chiu, S. F. Wang, and R. S. Chang. D-type fiber biosensor based on surface-plasmon resonance technology and heterodyne interferometry. *Optics Letters*, 30(3):233–235, 2005.

[35] K. Gasior, T. Martynkien, P. Mergo, and W. Urbanczyk. Fiber-optic surface plasmon resonance sensor based on spectral phase shift interferometric measurements. *Sensors and Actuators B: Chemical*, 257:602–608, 2018.

[36] RefractiveIindex.INFO. Refractive index of SCHOTT - multiple purpose - BOROFLOAT33. Online: https://refractiveindex.info/?shelf=glassbook=bk7page=schott.

[37] W. M. Zhao and Q. Wang. A high sensitivity refractive index sensor based on three-level gradient structure s-tapered fiber mode-mode interferometer. *Measurement*, 139:49–60, 2019.

[38] C. Zhang, D. Yang, C. Miao, J. Zhao, H. Li, and H. Bai. Large-range refractive index measurement method for open cavity fabry–pérot interferometer. *Measurement Science and Technology*, 30(3):035101, 2019.

[39] Y. Zhao, X. G. Li, L. Cai, and Y. N. Zhang. Measurement of RI and temperature using composite interferometer with hollow-core fiber and photonic crystal fiber. *IEEE Transactions on Instrumentation and Measurement*, 65(11):2631–2636, 2016.

[40] M. Kashif, A. A. B., Ahmad, N. Arsad, and S. Shaari. Development of phase detection schemes based on surface plasmon resonance using interferometry. *Sensors*, 14(9):15914–15938, 2014.

[41] V. Bello and S. Merlo. Micro-opto-fluidic platform for solvents identification based on absorption properties in the NIR region. *Analytical and Bioanalytical Chemistry*, 412(14):3351–3358, 2020.

[42] V. Bello, E. Bodo, and S. Merlo. Near infrared absorption spectroscopy in microfluidic devices with selectable pathlength. *Journal of Lightwave Technology*, 39(12):4193–4200, 2021.

[43] V. Bello, E. Bodo, and S. Merlo. Micro-opto-fluidic platform for spectroscopic identification of water-based fluids. In *Optical Sensors 2021*, volume 11772, page 117720C. International Society for Optics and Photonics, 2021.

[44] V. Bello, E. Bodo, and S. Merlo. Quality control of ethanol-based hand sanitizer gels in micro-opto-fluidic devices. In *CLEO: Science and Innovations*, pages JTh3A–87. Optical Society of America, 2021.

[45] D. L. Pavia, G. M. Lampman, G. S. Kriz, and J. A. Vyvyan. *Introduction to spectroscopy*. Cengage Learning, 2014.

[46] J. M. Hollas. *Modern spectroscopy*. John Wiley & Sons, 2004.

[47] N. V. Tkachenko. *Optical spectroscopy: methods and instrumentations*. Elsevier, 2006.

[48] G. R. Rossman. *Spectroscopic methods in mineralogy and geology*. De Gruyter, 1988.

[49] L. M. Ng and R. Simmons. Infrared spectroscopy. *Analytical Chemistry*, 71(12):343–350, 1999.

[50] D. F. Swinehart. The Beer-Lambert law. *Journal of Chemical Education*, 39(7):333, 1962.

[51] S. Kedenburg, M. Vieweg, T. Gissibl, and H. Giessen. Linear refractive index and absorption measurements of nonlinear optical liquids in the visible and near-infrared spectral region. *Optical Materials Express*, 2(11):1588–1611, 2012.

[52] E. Sani and A. Dell'Oro. Spectral optical constants of ethanol and isopropanol from ultraviolet to far infrared. *Optical Materials*, 60:137–141, 2016.

[53] E. Sani and A. Dell'Oro. Optical constants of ethylene glycol over an extremely wide spectral range. *Optical Materials*, 37:36–41, 2014.

[54] M. Blanco and I. Villarroya. NIR spectroscopy: a rapid-response analytical tool. *Trends in Analytical Chemistry*, 21(4):240–250, 2002.

[55] M. Puyol, M. Del Valle, I. Garcés, F. Villuendas, C. Domínguez, and J. Alonso. Integrated waveguide absorbance optode for chemical sensing. *Analytical Chemistry*, 71(22):5037–5044, 1999.

[56] L. Jiang and S. Pau. Integrated waveguide with a microfluidic channel in spiral geometry for spectroscopic applications. *Applied Physics Letters*, 90(11):111108, 2007.

[57] C. S. Burke, L. Polerecky, and B. D. MacCraith. Design and fabrication of enhanced polymer waveguide platforms for absorption-based optical chemical sensors. *Measurement Science and Technology*, 15(6):1140, 2004.

[58] J. Hu, V. Tarasov, A. Agarwal, L. Kimerling, N. Carlie, L. Petit, and K. Richardson. Fabrication and testing of planar chalcogenide waveguide integrated microfluidic sensor. *Optics Express*, 15(5):2307–2314, 2007.

[59] M. L. Adams, M. Enzelberger, S. Quake, and A. Scherer. Microfluidic integration on detector arrays for absorption and fluorescence microspectrometers. *Sensors and Actuators A: Physical*, 104(1):25–31, 2003.

[60] M. Bai, H. Huang, J. Hao, J. Zhang, H. Wu, and B. Qu. A compact photometer based on metal-waveguide-capillary: application to detecting glucose of nanomolar concentration. *Scientific Reports*, 5(1):1–12, 2015.

[61] L. Wei, K. Fujiwara, and K. Fuwa. Determination of phosphorus in natural waters by long-capillary-cell absorption spectrometry. *Analytical Chemistry*, 55(6):951–955, 1983.

[62] P. Tipparat, S. Lapanantnoppakhun, J. Jakmunee, and K. Grudpan. Determination of ethanol in liquor by near-infrared spectrophotometry with flow injection. *Talanta*, 53(6):1199–1204, 2001.

[63] P. S. Ellis, A. J. Lyddy-Meaney, P. J. Worsfold, and I. D. McKelvie. Multi-reflection photometric flow cell for use in flow injection analysis of estuarine waters. *Analytica Chimica Acta*, 499(1-2):81–89, 2003.

[64] P. S. Ellis, B. S. Gentle, M. R. Grace, and I. D. McKelvie. A versatile total internal reflection photometric detection cell for flow analysis. *Talanta*, 79(3):830–835, 2009.

[65] Y. Xiong, C. Wang, T. Tao, M. Duan, J. Tan, J. Wu, and D. Wang. Fabrication of a miniaturized capillary waveguide integrated fiber-optic sensor for fluoride determination. *Analyst*, 141(10):3041–3049, 2016.

[66] N. Kakuta, H. Yamashita, D. Kawashima, K. Kondo, H. Arimoto, and Y. Yamada. Simultaneous imaging of temperature and concentration of ethanol–water mixtures in microchannel using near-infrared dual-wavelength absorption technique. *Measurement Science and Technology*, 27(11):115401, 2016.

[67] H. Yamashita, N. Kakuta, D. Kawashima, and Y. Yamada. Measurement of temperature-dependent diffusion coefficients of aqueous solutions by near-infrared simultaneous imaging of temperature and concentration. *Biomedical Physics & Engineering Express*, 4(3):035030, 2018.

[68] A. L. Gomez, R. F. Renzi, J. A. Fruetel, and R. P. Bambha. Integrated fiber optic incoherent broadband cavity enhanced absorption spectroscopy detector for near-ir absorption measurements of nanoliter samples. *Applied Optics*, 51(14):2532–2540, 2012.

[69] S. R. T. Neil, C. M. Rushworth, C. Vallance, and S. R. Mackenzie. Broadband cavity-enhanced absorption spectroscopy for real time, in situ spectral analysis of microfluidic droplets. *Lab on a Chip*, 11(23):3953–3955, 2011.

[70] F. B. Xiong and D. Sisler. Determination of low-level water content in ethanol by fiber-optic evanescent absorption sensor. *Optics Communications*, 283(7):1326–1330, 2010.

[71] K. H. Tantawi, W. Gaillard, J. Helton, E. Waddell, S. Mirov, V. Fedorov, and J. D. Williams. In-plane spectroscopy of microfluidic systems made in photosensitive glass. *Microsystem Technologies*, 19(2):173–177, 2013.

[72] K. Bordo and H. G. Rubahn. Effect of deposition rate on structure and surface morphology of thin evaporated al films on dielectrics and semiconductors. *Materials Science*, 18(4):313–317, 2012.

[73] S. Rebsdat and D. Mayer. Ethylene glycol. *Ullmann's Encyclopedia of Industrial Chemistry*, 495, 2000.

[74] H. Yue, Y. Zhao, X. Ma, and J. Gong. Ethylene glycol: properties, synthesis, and applications. *Chemical Society Reviews*, 41(11):4218–4244, 2012.

[75] M. F. Parry and R. Wallach. Ethylene glycol poisoning. *The American Journal of Medicine*, 57(1):143–150, 1974.

[76] D. Pittet, S. Hugonnet, S. Harbarth, P. Mourouga, V. Sauvan, S. Touveneau, T. V. Perneger, et al. Effectiveness of a hospital-wide programme to improve compliance with hand hygiene. *The Lancet*, 356(9238):1307–1312, 2000.

[77] E. L. Larson, P. I. Eke, and B. E. Laughon. Efficacy of alcohol-based hand rinses under frequent-use conditions. *Antimicrobial Agents and Chemotherapy*, 30(4):542–544, 1986.

[78] S. A. Reynolds, F. Levy, and E. S. Walker. Hand sanitizer alert. *Emerging Infectious Diseases*, 12(3):527, 2006.

[79] US Food and Drug Administration FDA. Topical antimicrobial drug products for over-the-counter human use; tentative final monograph (TFM) for health-care antiseptic drug products. *Federal Register*, 59:31402–31452, 1994.

[80] P. B. Price. Ethyl alcohol as a germicide. *Archives of Surgery*, 38(3):528–542, 1939.

[81] World Health Organization. Who guidelines on hand hygiene in health care. In *WHO guidelines on hand hygiene in health care*, pages 270–270. 2009.

[82] T. Cederholm, R. Barazzoni, P. Austin, P. Ballmer, G. Biolo, S. C. Bischoff, C. Compher, I. Correia, T. Higashiguchi, M. Holst, et al. ESPEN guidelines on definitions and terminology of clinical nutrition. *Clinical Nutrition*, 36(1):49–64, 2017.

[83] S. C. Bischoff, J. Escher, X. Hébuterne, S. Kłęk, Z. Krznaric, S. Schneider, R. Shamir, K. Stardelova, N. Wierdsma, A. E. Wiskin, et al. ESPEN practical guideline: Clinical nutrition in inflammatory bowel disease. *Clinical Nutrition*, 39(3):632–653, 2020.

[84] J. Arends, P. Bachmann, V. Baracos, N. Barthelemy, H. Bertz, F. Bozzetti, K. Fearon, E. Hütterer, E. Isenring, S. Kaasa, et al. ESPEN guidelines on nutrition in cancer patients. *Clinical Nutrition*, 36(1):11–48, 2017.

[85] F. Ferrara, F. De Rosa, and A. Vitiello. The central role of clinical nutrition in COVID-19 patients during and after hospitalization in intensive care unit. *SN Comprehensive Clinical Medicine*, 2(8):1064–1068, 2020.

[86] L. Brugliera, A. Spina, P. Castellazzi, P. Cimino, P. Arcuri, A. Negro, E. Houdayer, F. Alemanno, A. Giordani, P. Mortini, et al. Nutritional management of COVID-19 patients in a rehabilitation unit. *European Journal of Clinical Nutrition*, 74(6):860–863, 2020.

[87] T. Johnson and E. Sexton. Managing children and adolescents on parenteral nutrition: challenges for the nutritional support team. *Proceedings of the Nutrition Society*, 65(3):217–221, 2006.

[88] R. M. Beattie. Symposium 6: Young people, artificial nutrition and transitional care nutrition, growth and puberty in children and adolescents with crohn's disease: Conference on 'malnutrition matters'. *Proceedings of the Nutrition Society*, 69(1):174–177, 2010.

[89] A. V. Malinin, A. A. Zanishevskaja, V. V. Tuchin, Y. S. Skibina, and I. Y. Silokhin. Photonic crystal fibers for food quality analysis. In *Biophotonics: Photonic Solutions for Better Health Care III*, volume 8427, page 842746. International Society for Optics and Photonics, 2012.

[90] H. Zhao, P. H. Brown, and P. Schuck. On the distribution of protein refractive index increments. *Biophysical Journal*, 100(9):2309–2317, 2011.

[91] C. Y. Tan and Y. X. Huang. Dependence of refractive index on concentration and temperature in electrolyte solution, polar solution, nonpolar solution, and protein solution. *Journal of Chemical & Engineering Data*, 60(10):2827–2833, 2015.

[92] S. Nemoto. Measurement of the refractive index of liquid using laser beam displacement. *Applied Optics*, 31(31):6690–6694, 1992.

[93] F. Docchio, S. Corini, M. Perini, and R. S. Gasana. A simple and reliable system for measuring the refractive index of liquids using a position-sensitive detector. *IEEE Transactions on Instrumentation and Measurement*, 44(1):68–70, 1995.

[94] Y. Zhao, B. Zhang, and Y. Liao. Experimental research and analysis of salinity measurement based on optical techniques. *Sensors and Actuators B: Chemical*, 92(3):331–336, 2003.

[95] H. Minato, Y. Kakui, A. Nishimoto, and M. Nanjo. Remote refractive index difference meter for salinity sensor. *IEEE Transactions on Instrumentation and Measurement*, 38(2):608–612, 1989.

[96] Y. L. Yeh, C. C. Wang, M. J. Jang, C. H. Chen, S. M. Tzeng, Y. P. Lin, and K. S. Chen. Real-time measurement of glucose concentration using position sensing detector. In *2008 3rd IEEE International Conference on Nano/Micro Engineered and Molecular Systems*, pages 561–565. IEEE, 2008.

[97] F. Jiménez, J. Vázquez, J. L. Sánchez-Rojas, N. Barrajón, and J. Úbeda. Multi-purpose optoelectronic instrument for monitoring the alcoholic fermentation of wine. In *SENSORS, 2011 IEEE*, pages 390–393. IEEE, 2011.

[98] H. Nasibov, A. Kholmatov, and I. Mehmetbeyli. A method for a precise and instantaneous measurement of a refractive index. *IEEE/ASME Transactions on Mechatronics*, 23(4):1886–1896, 2018.

[99] K. Ohtani and M. Baba. Liquid refractive index measurement based on inverse raytracing using an optical angle sensor. In *2019 12th Biomedical Engineering International Conference (BMEiCON)*, pages 1–4. IEEE, 2019.

[100] Y. C. Seow, S. P. Lim, B. C. Khoo, and H. P. Lee. An optofluidic refractive index sensor based on partial refraction. *Sensors and Actuators B: Chemical*, 147(2):607–611, 2010.

[101] IBIDI. µ-Slide I Luer. Online: https://ibidi.com/channel-slides/50–slide-i-luer.html.

[102] G. Rigamonti, M. Guardamagna, and S. Merlo. Non-contact reflectometric readout of disposable microfluidic devices by near infra-red low-coherence interferometry. *AIMS Biophysics*, 3(4):585–595, 2016.

[103] Cheimika S.A.S. Q-VETTES (PS) linea RT. Online: https://www.cheimika.it/it-it/articoli/q-vettes–ps–linea-rt-691.aspx.

[104] SiTek Electro Optics AB. Datasheet of 1L10_SU74_SPC02 Position Sensitive Detector. Online: https://www.lasercomponents.com/fileadmin/user_upload/home/datasheets/sitek/1l10_su74_spc02.pdf.

[105] J. Grant. Recognition, prevention, and treatment of home total parenteral nutrition central venous access comlications. *Journal of Parenteral and Enteral Nutrition*, 26:S21–S28, 2002.

[106] C. M. Dollery, I. D. Sullivan, C. Bull, O. Bauraind, and P. J. Milla. Thrombosis and embolism in long-term central venous access for parenteral nutrition. *The Lancet*, 344(8929):1043–1045, 1994.

[107] N. Meadows. Monitoring and complications of parenteral nutrition. *Nutrition*, 14(10):806–808, 1998.

[108] R. A. Rahim, N. M. Nayan, and M. H. F. Rahiman. Ultrasonic tomography system for liquid/gas flow: frame rate comparison between visual basic and visual C++ programming. *Jurnal Teknologi*, pages 131–150, 2006.

[109] N. S. M. Fadzil, R. A. Rahim, M. S. Karis, S. Z. M. Muji, M. F. A. Sahib, M. S. B. Mansor, N. M. N. Ayob, M. F. Jumaah, and M. Z. Zawahir. Hardware design of laser optical tomography system for detection of bubbles column. *Jurnal Teknologi*, 64(5), 2013.

[110] J. Jamaludin, R. A. Rahim, H. A. Rahim, M. H. F. Rahiman, S. Z. M. Muji, and J. M. Rohani. Charge coupled device based on optical tomography system in detecting air bubbles in crystal clear water. *Flow Measurement and Instrumentation*, 50:13–25, 2016.

[111] M. Lichti, X. Cheng, H. Stephani, and H. J. Bart. Online detection of ellipsoidal bubbles by an innovative optical approach. *Chemical Engineering & Technology*, 42(2):506–511, 2019.

[112] F. De Somer, M. R. Vetrano, J. P. Van Beeck, and G. J. Van Nooten. Extracorporeal bubbles: a word of caution. *Interactive Cardiovascular and Thoracic Surgery*, 10(6):995–1001, 2010.

[113] B. A. Alfarraj, A. M. Alkhedhair, A. A. Al-Harbi, W. Nowak, and S. A. Alfaleh. Measurement of the air bubble size and velocity from micro air bubble generation (MBG) in diesel using optical methods. *Energy Transitions*, 4(2):155–162, 2020.

[114] V. Bello, A. B. Arı, M. S. Hanay, and K. L. Ekinci. Measurement and characterization of nano-electro-mechanical systems using laser interferometry. In *2020 IEEE International Instrumentation and Measurement Technology Conference (I2MTC)*, pages 1–5. IEEE, 2020.

[115] K. L. Ekinci and M. L. Roukes. Nanoelectromechanical systems. *Review of Scientific Instruments*, 76(6):061101, 2005.

[116] T. Kouh, D. Karabacak, D. H. Kim, and K. L. Ekinci. Diffraction effects in optical interferometric displacement detection in nanoelectromechanical systems. *Applied Physics Letters*, 86(1):013106, 2005.

[117] V. Kara, V. Yakhot, and K. L. Ekinci. Generalized knudsen number for unsteady fluid flow. *Physical Review Letters*, 118(7):074505, 2017.

[118] M. S. Hanay, S. Kelber, A. K. Naik, D. Chi, S. Hentz, E. C. Bullard, E. Colinet, L. Duraffourg, and M. L. Roukes. Single-protein nanomechanical mass spectrometry in real time. *Nature Nanotechnology*, 7(9):602–608, 2012.

[119] E. T. Herruzo, A. P. Perrino, and R. Garcia. Fast nanomechanical spectroscopy of soft matter. *Nature Communications*, 5(1):1–8, 2014.

[120] L. M. De Lépinay, B. Pigeau, B. Besga, P. Vincent, P. Poncharal, and O. Arcizet. A universal and ultrasensitive vectorial nanomechanical sensor for imaging 2D force fields. *Nature Nanotechnology*, 12(2):156–162, 2017.

[121] M. S. Hanay, S. I. Kelber, C. D. O'Connell, P. Mulvaney, J. E. Sader, and M. L. Roukes. Inertial imaging with nanomechanical systems. *Nature Nanotechnology*, 10(4):339–344, 2015.

[122] E. Gil-Santos, D. Ramos, J. Martínez, M. Fernández-Regúlez, R. García, Á. San Paulo, M. Calleja, and J. Tamayo. Nanomechanical mass sensing and stiffness spectrometry based on two-dimensional vibrations of resonant nanowires. *Nature Nanotechnology*, 5(9):641–645, 2010.

[123] W. J. Venstra, H. J. R. Westra, and H. S.J Van der Zant. Q-factor control of a microcantilever by mechanical sideband excitation. *Applied Physics Letters*, 99(15):151904, 2011.

[124] V. Annovazzi Lodi, M. Benedetti, S. Merlo, and M. Norgia. Optical detection of multiple modes on resonant micromachined structures. *IEEE Photonics Technology Letters*, 16(7):1703–1705, 2004.

[125] G. Silva, F. Carpignano, F. Guerinoni, S. Costantini, M. De Fazio, and S. Merlo. Optical detection of the electromechanical response of MEMS micromirrors designed for scanning picoprojectors. *IEEE Journal of Selected Topics in Quantum Electronics*, 21(4):147–156, 2014.

[126] V. Annovazzi Lodi, M. Benedetti, S. Merlo, and M. Norgia. Spot optical measurements on micromachined mirrors for photonic switching. *IEEE Journal of Selected Topics in Quantum Electronics*, 10(3):536–544, 2004.

[127] A. B. Arı, M. Ç. Karakan, C. Yanık, İ. İ. Kaya, and M. S. Hanay. Intermodal coupling as a probe for detecting nanomechanical modes. *Physical Review Applied*, 9(3):034024, 2018.

[128] I. Bargatin, I. Kozinsky, and M. L. Roukes. Efficient electrothermal actuation of multiple modes of high-frequency nanoelectromechanical resonators. *Applied Physics Letters*, 90(9):093116, 2007.

[129] A. N. Cleland. *Foundations of nanomechanics: from solid-state theory to device applications*. Springer Science & Business Media, 2013.

[130] L. Rodriguez-Saona, D. P. Aykas, K. R. Borba, and A. Urtubia. Miniaturization of optical sensors and their potential for high-throughput screening of foods. *Current Opinion in Food Science*, 31:136–150, 2020.

[131] J. Chen, M. A. Arnold, and G. W. Small. Comparison of combination and first overtone spectral regions for near-infrared calibration models for glucose and other biomolecules in aqueous solutions. *Analytical Chemistry*, 76(18):5405–5413, 2004.

[132] M. Moreira, J. A. de França, D. de Oliveira Toginho Filho, V. Beloti, A. K. Yamada, M. B. de M. França, and L. de Souza Ribeiro. A low-cost NIR digital photometer based on InGaAs sensors for the detection of milk adulterations with water. *IEEE Sensors Journal*, 16(10):3653–3663, 2016.

[133] R. Hotmartua, P. W. Pangestu, H. Zakaria, and Y. S. Irawan. Noninvasive blood glucose detection using near infrared sensor. In *2015 International Conference on Electrical Engineering and Informatics (ICEEI)*, pages 687–692. IEEE, 2015.

[134] G. Mu, T. Liu, C. Xue, and J. Chen. Semi-supervised learning based calibration model building of NIR spectroscopy for in-situ measurement of biochemical processes under insufficiently and inaccurately labeled samples.

IEEE Transactions on Instrumentation and Measurement, 70:2509912, 2021.

[135] L. de Souza Ribeiro, F. A. Gentilin, J. A. de França, A. L. de Souza Madureira Felício, and Ma. B. de M França. Development of a hardware platform for detection of milk adulteration based on near-infrared diffuse reflection. *IEEE Transactions on Instrumentation and Measurement*, 65(7):1698–1706, 2016.

[136] M. Moreira, A. L. Felício, de Souza Madureira, and J. A. de França. Calibration of a photometer for quantification of ethanol in gasoline: Absorbance determination. *IEEE Transactions on Instrumentation and Measurement*, 67(9):2119–2128, 2018.

[137] C. S. Pundir, S. Jakhar, and V. Narwal. Determination of urea with special emphasis on biosensors: a review. *Biosensors and Bioelectronics*, 123:36–50, 2019.

[138] S. N. Botewad, D. K. Gaikwad, N. B. Girhe, H. N. Thorat, and P. P. Pawar. Urea biosensors: a comprehensive review. *Biotechnology and Applied Biochemistry*, pages 1–17, 2021.

[139] A. K. Singh, M. Singh, and N. Verma. Electrochemical preparation of Fe3O4/MWCNT-polyaniline nanocomposite film for development of urea biosensor and its application in milk sample. *Journal of Food Measurement and Characterization*, 14(1):163–175, 2020.

[140] C. Esmaeili, L. Y. Heng, and T. L. Ling. Nile Blue chromoionophore-doped kappa-carrageenan for a novel reflectometric urea biosensor. *Sensors and Actuators B: Chemical*, 221:969–977, 2015.

[141] Z. Yang and C. Zhang. Single-enzyme nanoparticles based urea biosensor. *Sensors and Actuators B: Chemical*, 188:313–317, 2013.

[142] B. Bjarnason, P. Johansson, and G. Johansson. A novel thermal biosensor: evaluation for determination of urea in serum. *Analytica Chimica Acta*, 372(3):341–348, 1998.

[143] M. Lubnow, T. Dreier, and C. Schulz. NIR sensor for aqueous urea solution film thickness and concentration measurement using a broadband light source. *Applied Optics*, 58(16):4546–4552, 2019.

[144] I. Suzuki, M. Ogawa, K. Seino, M. Nogawa, H. Naito, K. Yamakoshi, and S. Tanaka. Reagentless estimation of urea and creatinine concentrations using near-infrared spectroscopy for spot urine test of urea-to-creatinine ratio. *Advanced Biomedical Engineering*, 7:72–81, 2018.

[145] R. Pan, J. B. Jeffries, T. Dreier, and C. Schulz. Measurements of liquid film thickness, concentration, and temperature of aqueous urea solution by NIR absorption spectroscopy. *Applied Physics B*, 122(1):4, 2016.

[146] K. F. Palmer and D. Williams. Optical properties of water in the near infrared. *Journal of the Optical Society of America*, 64(8):1107–1110, 1974.

[147] T. G. Mayerhöfer, S. Pahlow, and J. Popp. The Bouguer-Beer-Lambert law: Shining light on the obscure. *ChemPhysChem*, 21(18):2029, 2020.

[148] U. Wenzel, S. Princz, L. Gröber, R. Miller, and M. Heßling. L14-datenvorbehandlungsmethoden für präzisere inline-bestimmung von stoffkonzentrationen im bioreaktor aus NIR-absorptions-spektren. *Tagungsband*, pages 450–455, 2013.

[149] A. K. Amerov, J. Chen, and M. A. Arnold. Molar absorptivities of glucose and other biological molecules in aqueous solutions over the first overtone and combination regions of the near-infrared spectrum. *Applied Spectroscopy*, 58(10):1195–1204, 2004.

[150] J. T. Olesberg, M. A. Arnold, and M. J. Flanigan. Online measurement of urea concentration in spent dialysate during hemodialysis. *Clinical Chemistry*, 50(1):175–181, 2004.

List of Publications

International Scientific Journals with Referees

J1. S. Merlo, V. Bello, E. Bodo, S. Pizzurro, "A VCSEL-based NIR transillumination system for morpho-functional imaging", *Sensors*, Vol. 19, No. 4, Article no. 851, (2019). DOI: 10.3390/s19040851

J2. V. Bello, S. Merlo, "Micro-opto-fluidic sensing platform for analytes identification based on absorption properties in the NIR region", *Analytical and Bioanalytical Chemistry*, Vol. 412, No. 14, pp. 3351-3358, (2020). DOI: 0.1007/s00 216-019-02375-z

J3. V. Bello, A. Simoni, S. Merlo, "Spectral phase shift interferometry for refractive index monitoring in micro-capillaries", *Sensors*, Vol. 19, No. 4, Article No. 1043, (2020). DOI: 10.3390/s20041043

J4. V. Bello, A. Simoni, S. Merlo, "Spectral interferometric detection of NIR optical resonances of rectangular refractive index sensing", *IEEE Transactions on Instrumentation and Measurement*, Vol. 70, Article no. 7002609, (2021). DOI: 0.1109/TIM.2021.3055832

J5. V. Bello, E. Bodo, S. Merlo, "Near infrared absorption spectroscopy in microfluidic devices with selectable pathlength", *IEEE/OSA Journal of Lightwave Technology*, Vol. 39, No. 2, pp. 4193-4200, (2021). DOI: 10.1109/JLT.2020.3040488

J6. E. Bodo, V. Bello, V. Asole, S. Merlo, "Multiwavelength fluidic sensing of water-based solutions in a channel microslide with SWIR LEDs", *IEEE Transactions on Instrumentation and Measurement*, Vol. 71, Article no. 7000210, (2022). DOI: 10.1109/TIM.2021.3132090

J7. E. Bodo, S. Merlo, V. Bello, "Spectral fingerprint investigation in the near infra-red to distinguish harmful ethylene glycol from isopropanol in a mi-

crochannel", *Sensors*, Vol. 22, No. 2, Article no. 459, (2022). DOI: 10.3390/s22020459

International Conferences with Proceedings

C1. S. Merlo, V. Bello, E. Bodo, R. Catalano, S. Pizzurro, M. Rossi Borghesano, "NIR transillumination system for in vivo functional imaging", *SPIE Optics + Optoelectronics - Optical Sensors 2019*, April 1st-4th 2019, Prague, Czech Republic. Published in *Proceeding of Optical Sensors 2019*, Vol. 11028, Article no. 1102810, (2019). DOI: 10.1117/12.2520116

C2. V. Bello, E. Bodo, S. Pizzurro, S. Merlo, "Near-infrared transillumination of in vivo biological tissues for functional imaging", *4th International Conference on Biophotonics*, September 15th-18th 2019, Taipei, Taiwan. ISBN 978-1-7281-3837-4. DOI: 10.1109/BioPhotonics.2019.8896750

C3. V. Bello, E. Bodo, S. Pizzurro, S. Merlo, "In vivo recognition of vascular structures by near infra-red transillumination", *6th International Electronic Conference on Sensors and Applications*, November 15th-30th 2019, online virtual conference. Published in *Proceedings*, Vol. 42, No. 1, Article no. 24, (2020). DOI: 10.3390/ecsa-6-06639

C4. V. Bello, S. Merlo, "Phase detection of the NIR optical resonances of rectangular glass micro-capillaries", *I2MTC 2020 IEEE International Instrumentation and Measurement Technology Conference*, May 25th-28th 2020, Dubrovnik, Croatia. DOI: 10.1109/I2MTC43012.2020.912963.

C5. V. Bello, A. B. Ari, M. S. Hanay, K. L. Ekinci, "Measurement and characterization of nano-electro-mechanical systems using laser interferometry", *I2MTC 2020 IEEE International Instrumentation and Measurement Technology Conference*, May 25th-28th 2020, Dubrovnik, Croatia. DOI: 10.1109/I2MTC43012.2020.9129282

C6. V. Bello, E. Bodo, "A NIR-spectroscopy-based approach for detection of fluids in rectangular glass micro-capillaries", *7th International Electronic Conference on Sensors and Applications*, November 15th-30th 2020, online virtual conference. Published in *Engineering Proceedings*, Vol. 2, No. 1, Article no. 43, (2020). DOI: 10.3390/ecsa-7-08250

C7. V. Bello, E. Bodo, S. Merlo, "Micro-opto-fluidic platform for spectroscopic identification of water-based fluids", *SPIE Optics + Optoelectronics Digital Forum 2021*, April 19th-23rd 2021, online virtual conference. Published

in *Proceedings of Optical Sensors 2021*, Vol. 11772, Article no. 117720C, (2021). DOI: 10.1117/12.2589141

C8. V. Bello, E. Bodo, S. Merlo, "Quality Control of Ethanol-Based Hand Sanitizer Gels in Micro-Opto-Fluidic Devices, *CLEO 2021 Virtual Conference*, May 9th-13th 2021, online virtual conference, Article no. JTh3A.87. DOI: 10.1364/CLEO_AT.2021.JTh3A.87

C9. E. Bodo, V. Bello, "Microfluidic devices with selectable optical pathlength for quality control of alcoholic solutions, *8th International Electronic Conference on Sensors and Applications*, November 1st-15th 2021, online virtual conference. Published in *Engineering Proceedings*, Vol. 10, No. 1, Article no. 13, (2021). DOI: 10.3390/ecsa-8-11286

International Conferences without Proceedings

W1. V. Bello, G. Rigamonti, S. Merlo, "Innovative micro-fluidic sensing platform based on glass rectangular micro-capillaries for refractive index detection", *EBS 2019 2nd European Biosensor Symposium 2019*, February 18th-21st 2019, Firenze, Italy

W2. V. Bello, W. Vandezande, D. Daems, J. Lammertyn, "Theoretical investigation, fabrication and experimental testing of dual-channel self-referencing fiber-optic biosensors for biological interaction analysis", *DIATECH 2020*, January 27th-29th 2020, Leuven, Belgium

National Conferences

N1. S. Merlo, V. Bello, E. Bodo, S. Pizzurro, "Valutazione di informazioni morfofunzionali in tessuti biologici in vivo mediante transilluminazione infrarossa", *III Forum Nazionale delle Misure, XXXVI Congresso Nazionale di Misure Elettriche ed Elettroniche*, September 12th-14th 2019, Perugia, Italy

N2. V. Bello, G. Rigamonti, S. Merlo, "Micro-capillary refractive index sensor based on monitoring of T/R ratio spectral shift", *NANO-DAY IV*, December 11th-14th 2019, Milan, Italy

N3. V. Bello, E. Bodo, S. Pizzurro, "Morpho-functional in vivo imaging of biological tissues based on NIR transillumination", *ICOP 2020 Italian Conference on Optics and Photonics*, September 9th-11th 2020, Parma, Italy

N4. V. Bello, A. Simoni, “Spectral interferometry-based detection of optical resonances of micro-capillaries”, *ICOP 2020 Italian Conference on Optics and Photonics*, September 9th-11th 2020, Parma, Italy

N5. V. Bello, E. Bodo, S. Merlo “Interferometria spettrale per rivelazione di risonanze ottiche e misure di indice di rifrazione ad alta sensibilità”, *V Forum Nazionale delle Misure*, September 16th-18th 2021, Giardini Naxos, Italy

N6. V. Bello, E. Bodo, S. Merlo, “Rilevazione di fluidi senza contatto mediante spettroscopia ad assorbimento nel vicino infrarosso in dispositivi microfluidici multipasso”, *V Forum Nazionale delle Misure*, September 16th-18th 2021, Giardini Naxos, Italy

Book Chapters

B1. V. Bello, E. Bodo, S. Merlo, “Optical readout techniques for smart detection of fluids in the near infrared wavelength region by means of rectangular glass micro-capillaries”, Chapter in *Sensors and Microsystems, Series: Lecture Notes in Electrical Engineering*, G. Di Francia, C. Di Natale, Springer Nature Switzerland, (2022). In press